

INVESTIGATION OF  
HECTOMETRIC AND KILOMETRIC RADIO EMISSIONS FROM  
JUPITER AND NEPTUNE

By

LIYUN WANG

A DISSERTATION PRESENTED TO THE GRADUATE SCHOOL  
OF THE UNIVERSITY OF FLORIDA IN PARTIAL FULFILLMENT  
OF THE REQUIREMENTS FOR THE DEGREE OF  
DOCTOR OF PHILOSOPHY

UNIVERSITY OF FLORIDA

1994

To my mother, wife, and lovely daughter  
for their love, encouragement and endless support

献给我亲爱的母亲、妻子宗彬和女儿培娟



## ACKNOWLEDGEMENTS

First of all, I would like to express my deepest gratitude to Dr. Thomas D. Carr, chairman of my supervisory committee, for his guidance and support during my years at the University of Florida. He suggested this topic and was a major influence in its development.

I would wish to thank Dr. Alex G. Smith, Dr. John P. Oliver, Dr. George R. Lebo, and Dr. Henri A. Van Rinsvelt, members of my supervisory committee, for their advice and many helpful suggestions. I also wish to acknowledge valuable help from Dr. Kwan-yu Chen.

Further, I would like to thank the entire Department of Astronomy for the encouragement, support and friendships they have provided.

My deepest love and gratitude go to my family, especially to my mother and wife, for their tremendous encouragement, understanding, patience, support, and sacrifice during all these years of my study. I should also express my appreciation to my lovely daughter, Christine, for filling my family with all the joy and happiness.

This research project has been supported primarily by grants from the National Aeronautics and Space Administration, and has been benefited from the support of low frequency planetary radio astronomy research by the National Science Foundation at the University of Florida.

## TABLE OF CONTENTS

	Page
ACKNOWLEDGEMENTS . . . . .	iii
ABSTRACT . . . . .	vii
CHAPTERS	
1 INTRODUCTION . . . . .	1
2 THE VOYAGER PRA EXPERIMENT AND ITS ANTENNA CALIBRATION . . . . .	6
2.1 Description of the Voyager PRA Experiment . . . . .	8
2.2 Calibration of the PRA Antenna for Polarization Sense Measurement	9
2.2.1 Polarization Response of the PRA Antenna . . . . .	9
2.2.2 Antenna E-plane Calibration for Sources in a Particular Azimuth Region . . . . .	16
2.2.3 Full Calibration Based on all Usable Events . . . . .	24
2.2.4 Discussion . . . . .	28
2.3 The PRA Data Base at the University of Florida . . . . .	29
3 A BRIEF REVIEW OF JUPITER'S RADIO EMISSIONS . . . . .	33
3.1 The Synchrotron Radiation (DIM) . . . . .	35
3.2 Decametric Radiation . . . . .	36
3.3 Hectometric Radiation . . . . .	39
3.4 Kilometric Radiation . . . . .	40
3.5 Power Spectrum . . . . .	41
4 JUPITER'S HECTOMETRIC RADIO EMISSIONS . . . . .	43
4.1 Characteristics of the HOM Emission . . . . .	43
4.1.1 Frequency Coverage . . . . .	44
4.1.2 Intensity Profile in CML . . . . .	46

4.1.3	Magnetic Latitudinal Beaming . . . . .	54
4.1.4	Polarization . . . . .	62
4.1.5	Solar Wind Control . . . . .	68
4.1.6	Propagation Effect from the Io Plasma Torus . . . . .	69
4.2	Emission Mechanisms . . . . .	70
4.2.1	The CMI Theory . . . . .	71
4.2.2	Indirect Emission Mechanisms . . . . .	73
4.3	Modeling . . . . .	74
4.3.1	Equatorial Beaming Models . . . . .	74
4.3.2	Model Assumptions . . . . .	80
4.3.3	The Beaming Geometry . . . . .	84
4.3.4	Modeling Procedures and Results . . . . .	87
4.3.5	Discussion . . . . .	90
5	STUDY OF THE HOM EMISSIONS VIA RAYTRACING . . . . .	98
5.1	The Necessity of Raytracing Studies of the Jovian HOM Emission . . . . .	98
5.2	Early Raytracing Studies on the HOM Emissions . . . . .	99
5.3	Formulation of Ray Equations . . . . .	103
5.4	Procedures of Solving the Ray Equations . . . . .	106
5.5	Magnetic Field Model and Magnetospheric Plasma Model . . . . .	110
5.6	Two-dimensional Raytracing Result . . . . .	112
5.6.1	R-X Mode . . . . .	115
5.6.2	L-O Mode . . . . .	123
5.7	Three-dimensional Raytracing Result . . . . .	127
5.8	HOM Source Localization via Raytracing . . . . .	128
6	A MODEL OF NEPTUNE'S SMOOTH RADIO COMPONENT . . . . .	139
6.1	Introduction . . . . .	139
6.2	The Neptunian Magnetic Field Models . . . . .	145
6.3	Plasmasphere Model . . . . .	149
6.4	Modeling . . . . .	153
6.5	Discussion . . . . .	161
7	SUMMARY AND CONCLUSIONS . . . . .	163
APPENDICES		
A	REFRACTIVE INDEX AND RAY EQUATIONS . . . . .	168
A.1	Refractive Index and the Appleton-Hartree Formula . . . . .	168
A.2	Ray Equations and Relevant Terms . . . . .	173

B	THE JOVIAN AND NEPTUNIAN MAGNETIC FIELD MODELS . . . .	181
B.1	Models Without External Terms . . . . .	182
B.2	Models With External Terms . . . . .	187
C	TRANSFORMATION OF SPACECRAFT COORDINATE SYSTEMS . .	191
C.1	Transformation at a Given Catalog Time . . . . .	192
C.2	Transformation at any Given Time . . . . .	195
	REFERENCES . . . . .	199
	BIOGRAPHICAL SKETCH . . . . .	209

Abstract of Dissertation Presented to the Graduate School  
of the University of Florida in Partial Fulfillment  
of the Requirements for the Degree of  
Doctor of Philosophy

INVESTIGATION OF  
HECTOMETRIC AND KILOMETRIC RADIO EMISSIONS FROM  
JUPITER AND NEPTUNE

By

LIYUN WANG

August 1994

Chairman: Thomas D. Carr  
Major department: Astronomy

This dissertation concerns radio emissions at hectometric and kilometric wave lengths from the planets Jupiter and Neptune, as observed with the Planetary Radio Astronomy (PRA) experiment on board the two Voyager spacecraft.

The PRA antenna system is found to be incorrectly calibrated in early work, and the system is recalibrated for polarization sense determination. It is concluded that the PRA antenna E-surface is not a plane as had previously been supposed — that its tilt can be significantly different at different azimuths. It is suggested that a tilt of  $27^\circ$  and  $45^\circ$  of the “E-plane” be used when the observed radiation arrives from the front and back sides of the antenna system, respectively.

New observational results of the Jovian hectometric (HOM) emission are presented. Characteristics of the HOM emission are thoroughly discussed. It is found that the HOM emission at different frequencies is beamed into different magnetic latitudes. The beaming profile is shown to contradict the generally accepted belief that

refraction of rays passing through the Io plasma torus is solely responsible for the beaming. A beaming model of the HOM emission is established that can account for the major characteristics of the HOM observation. Raytracing (both two-dimension and three-dimension) is performed over the *entire* frequency range of the HOM emission, and it is concluded that the presence of the Io plasma torus can affect only to a certain extent the propagation of the HOM emission, but it is not responsible for the magnetic equatorial beaming and for the shadowing of the emission. A special spacecraft maneuver event is used in searching for the HOM source location with help of the raytracing technique; the result is found to be consistent with those predicted by our beaming model.

Finally, the Voyager 2 observation of the Neptune kilometric radiation (NKR) is reviewed. A similar modeling process is applied to the NKR modeling, but a more realistic magnetic field model is used in the modeling process. Results that fit the observation of the NKR smooth component are presented. A plasmaspheric model based on the source location as determined in the beaming model is also presented.



## CHAPTER 1 INTRODUCTION

Among the nine known planets of the solar system, Jupiter, Saturn, Uranus, and Neptune are classified as the *giant* or *Jovian* planets. They are strikingly similar, and are very much different from the *terrestrial* planets (Mercury, Venus, Earth and Mars). Next to the Sun, Jupiter is by far the most massive object in the solar system, and the combined mass of all the Jovian planets is over 200 times that of terrestrial planets. In contrast to the terrestrial planets, which are relatively small and light and are composed mainly of rock, the Jovian planets are huge and massive, yet their average mass densities are surprisingly low (in the range of 0.7 to 1.8 g/cm<sup>3</sup>). Their chemical compositions are mainly hydrogen and helium, mixed with much smaller amounts of methane (CH<sub>4</sub>), ammonia (NH<sub>3</sub>), water (H<sub>2</sub>O) and other compounds. Each of the Jovian planets probably has a relatively small rocky core and a mantle composed of either liquid metallic hydrogen or liquid water, ammonia, and methane, but does not have a solid surface. Although the Jovian planets are much larger and more massive than Earth, they all rotate faster than Earth and in the same direction, with the exception of Uranus (due to some ancient impact that tilted its rotation axis past 90°). An outstanding feature of the Jovian planets is their powerful global magnetic moments (among the terrestrial planets only Earth has an appreciable magnetic field). The main type of markings on the visible disks of the Jovian planets are the bands of clouds that run parallel to the equator. As a result of complex and variable patterns of atmospheric winds, the cloud bands at different latitudes indicate

slightly different planetary rotation periods (which is approximately 10 hours in the case of Jupiter). Before the discovery of the Jovian radio emissions and through them the Jovian magnetic field, it was customary to specify the central meridian longitudes of Jupiter's visible markings in terms of one or the other of two standard longitude systems based on assumed rotation periods differing by about 5 minutes (although the visible features never remained stationary in longitude in either system for long at a time). Radio astronomy, however, made possible the measurement of the highly stable rotation period of the Jovian interior, because it is believed that episodic radio emissions are locked in phase with the rotation of Jupiter's magnetic field and therefore the electrically conducting deep interior of the planet. It is the magnetic fields the Jovian planets possess that are responsible for most of the phenomena with which this dissertation is concerned.

The accidental discovery in 1955 of non-thermal radio emissions from Jupiter in the decametric wavelength band (nominally 3 to 30 MHz) [*Burke and Franklin, 1955; Franklin and Burke, 1956*] marked the beginning of planetary radio astronomy. Since this discovery, the Jovian decametric radiation has been studied intensively from ground based radio observatories and from spacecraft. No emission in the decametric band has been observed from any other planets, except for the so-called Saturn Electrostatic Discharges or SEDs (presumably lightning transients) that were observed by the Voyager spacecraft. Radiation from the Jovian planets at lower frequencies, in the hectometer and kilometer wavelength bands, is blocked out by the Earth's ionosphere and was not detected until observations from Earth orbiting satellites and other spacecraft became available. These lower frequency emissions from all four of the Jovian planets were first investigated by the two Voyager spacecraft.

Soon after the 1955 discovery of the Jovian decametric emission (DAM), several investigators found that the probability of detecting Jovian activity was dependent

upon the central meridian longitude (CML) of the observer. It was found that histograms of Jovian activity as a function of CML remain relatively stationary in longitude over a time span of a decade or more if a rotation period about 0.5 minutes longer than the so-called *System II* period (based on an early estimate of the mean rotation period of visible features outside the equatorial zone) is invoked. The *System III* longitude ( $\lambda_{\text{III}}$ ) rotation period,  $9^{\text{h}}55^{\text{m}}29^{\text{s}}.71$ , is based in part on such decametric observations. This is the period of rotation of the Jovian magnetic field. The DAM source longitude regions were named A, B, and C, according to their relative strengths at an intermediate decametric frequency. The two main sources, A and B, have now been recognized to be due to the two edges of a hollow cone beam originating from a common location.

*Bigg* [1964] discovered that the orbital phase of the Galilean satellite Io ( $\phi_{\text{Io}}$ ), measured from the *superior geocentric conjunction*, also had a profound effect on the occurrence of the Jovian DAM emission: A very large enhancement in the detection probability for Io phase angles of  $90^\circ$  and  $240^\circ$  was found. In the two-dimensional picture of dynamic interaction between the planet and the satellite Io, the regions of  $(\lambda_{\text{III}}, \phi_{\text{Io}})$  configuration space which showed dependence on both parameters were named Sources Io-A, Io-B, Io-C and Io-D; those regions showing no Io dependence become non-Io-A, non-Io-B, non-Io-C, etc. [*Carr et al.*, 1983]. Also from long term ground-based observations, it was learned that the occurrence of DAM varies with the 12-year periodicity of the observer's Jovicentric declination or  $D_{\text{E}}$  [*Carr et al.*, 1970].

The first detection of radio emission from Jupiter at frequencies higher than those of the DAM bursts was in the centimeter-wavelength band, at about 9500 MHz [*Mayer et al.*, 1958]; this continuous emission was later shown to be thermal radiation from the Jovian atmosphere. Subsequently, a non-thermal component of continuous emission was discovered in the decimetric-wavelength band at frequencies considerably

higher than the 40 MHz upper limit of the DAM bursts (see *Berge and Gulkis* [1976] and references therein). As a result of extensive observational and theoretical investigations, it was shown that this non-thermal component was synchrotron emission from high energy electrons trapped in Jovian Van Allen belts, located between 1.6 and 3  $R_J$  ( $1R_J = 71,372$  km) at equatorial latitudes. This was the first positive proof that any planet other than Earth has a magnetic field, although it had been suggested earlier that a Jovian field is involved in the emission of the DAM bursts [*Carr*, 1959].

Before the spacecraft age, Jupiter's magnetic field could be studied only remotely, from groundbased observations of the radio emissions. Other Jovian planets' magnetic fields were not known until the *in situ* measurements from spacecraft were made. The first *in situ* measurements of Jupiter's (and Saturn's) magnetic fields were made by four spacecraft: Pioneer 10 in 1973, Pioneer 11 in 1974, Voyager 1, and Voyager 2 (both in 1979). The first indication that Uranus and Neptune also possess magnetic fields was from the Voyager 2 observation of the non-thermal radio emission, and then from the *in situ* measurements during Voyager 2's flyby of these two planets in early 1986 and 1989, respectively.

In this dissertation I will present results from my research on the radio emissions from Jupiter in the hectometric and the adjacent part of the kilometric bands, and those from Neptune in the kilometric band, observed mainly from the Voyager spacecraft. I will first present in Chapter 2 the result of our Voyager PRA antenna calibration which will be used in later chapters to correctly interpret the polarization sense of the observed radiation and to locate the Jovian radio sources at hectometric wavelengths. An overview of various components of Jupiter's radio emissions will be made in Chapter 3 before I discuss in great details the Jovian hectometric radiation. Chapter 4 will be devoted solely to the study of the Jovian hectometric radio emission. Various characteristics of this emission component will be discussed; many data analysis results that have never been seen in the literature will be presented.

Theoretical models that account for many, if not all, observational characteristics of this emission component will be then presented. In Chapter 5, I will continue to investigate in detail the propagation of Jupiter's hectometric radio waves in the Jovian magnetosphere by using a raytracing program that I developed. Results of source localizations via the raytracing technique will be presented and compared with those obtained in Chapter 4. In Chapter 6, results of observation and modeling of the Neptune smooth kilometric emission will be presented. I will conclude this dissertation in Chapter 7 with some discussions and a summary.

## CHAPTER 2

### THE VOYAGER PRA EXPERIMENT AND ITS ANTENNA CALIBRATION

The passage of Voyager 2 by Neptune in late August 1989 marked the end of an amazingly successful program of exploration of the outer planets. During the missions of the two Voyagers, the Planetary Radio Astronomy (PRA) measurement system recorded spectral intensity distributions of low frequency radio emissions from Jupiter, Saturn, Uranus, and Neptune. The PRA observations yielded a huge amount of data which has been and will long continue to be of great importance in developing an understanding of source locations and beaming geometry, emission mechanisms, and relationships of the radio sources to their magnetospheric environments. The PRA data bank is an invaluable scientific resource. It may remain the only such data we have for decades to come, particularly in the case of Uranus and Neptune.

The PRA experiment on board both Voyagers is identical and is designed to receive whatever decametric, hectometric, or kilometric radio signals might be observed from the vicinity of each of the radio planets Jupiter, Saturn, Uranus, and Neptune. Its primary goals were of course to locate the radio sources, to determine their emission beaming patterns, and to ascertain the magnetoionic mode of the radiation. Unfortunately, the PRA antenna was not designed for direction finding. Since the spacecraft was three-axis stabilized, the antenna beam could not execute the repeated scans across the source that might have provided direction information. However, in the vicinity of each planet the spacecraft was occasionally made to execute a complete or partial rotation in a relatively short time, usually causing the antenna beam to

be scanned once across the source direction. Although the moving antenna beam in such cases was much too broad to produce a sufficiently sharp pattern of intensity modulation of the received radiation from which useful source directional information could be derived, the sweeping of the electric plane<sup>1</sup> of the antenna system across a source direction sometimes produced a relatively abrupt reversal of the indicated sense of elliptical polarization. Measurements have previously been made of the antenna E-plane orientation relative to the spacecraft as deduced from the observed times of occurrence of polarization reversals during spacecraft maneuvers, using an assumed location of the calibration source (which was at Saturn in some cases and at Uranus in others) [*Ortega-Molina and Daigne*, 1984; *Lecacheux and Ortega-Molina*, 1987; *Ortega-Molina and Lecacheux*, 1990; *Sawyer et al.*, 1991]. In this chapter I will demonstrate that when the best of these previous E-plane orientation calibrations are used to obtain directional information from other sources, impossible results can be obtained. From previously unused spacecraft-maneuver observations of a Jovian source made under particularly favorable conditions, I will derive a corrected value of the relative orientation of the antenna E-plane which is much different from the currently accepted value. I will make other determinations from observations obtained during other spacecraft rotation-maneuvers that suggest that the tilt of an assumed antenna E-plane is different when the source is to the rear of the plane formed by the PRA orthogonal monopole pair than it is when the source is forward of this plane. Calibration data will be provided in the form of the tilt angles of the effective E-plane as a function of the azimuth of the source (in the antenna monopole coordinate system). I believe that the new calibration data can make possible correction of previous

---

<sup>1</sup>The electric plane, or “E-plane”, of an antenna is that plane upon which is projected the component of the incident-wave electric field vector that is effective in exciting the antenna. In the present case it is also the plane dividing the directions of incident rays for which the indicated elliptical polarization sense is correct from those for which it is reversed.

erroneous conclusions regarding the true polarization sense of a significant amount of the radiation received by the Voyagers from Jupiter, Saturn, Uranus, and Neptune, from direction angles greater than  $45^\circ$  with respect to the normal to the monopole antenna plane. The result of this newly calibrated data will be applied in Chapter 5 to locate the Jovian HOM emission source.

## 2.1 Description of the Voyager PRA Experiment

The Voyager PRA Experiment consists of a pair of 10-m orthogonal monopoles connected to a high sensitivity broadband stepped-frequency receiver covering the range 1.2 kHz to 40.2 MHz. The signals from the two antennas are added in phase quadrature by two switchable quarter wave hybrids in order to send alternately the apparent right hand (RH) and left hand (LH) circularly polarized components of the observed emission to the receiver. There were actually two receivers on each spacecraft, for the lower and higher frequency ranges, respectively. The low-frequency (LF) band receiver had 70 channels of 1.0 kHz bandwidth each, with center frequencies spaced at 19.2 kHz intervals from 1.2 kHz to 1326 kHz. The high-frequency (HF) band receiver consisted of 128 channels of 200 kHz bandwidth each, with center frequencies spaced at 307.2 kHz intervals from 1.2 MHz to 40.4 MHz. The HF band receiver was designed especially for the observation of Jovian decametric radio emissions.

The PRA experiment can be operated in six modes but only three of them were operated to a large extent in the mission during each of its encounters with a planet. One of the basic routine modes is called the POLLO sweeping mode, in which the receiver sweeps and samples all its 198 frequency channels in 6 seconds, dwelling at each frequency channel for a total of 30 msec and measuring alternately flux densities of RH and LH circular polarizations. (There are additional 2 channels being used to store “housekeeping” data describing the experiment’s status.) From one step to



the next during the channel switching sequence, the antenna polarization sense is reversed, *i.e.*, it is changed from RH to LH or vice versa. At a given frequency the left and right circular components are not observed simultaneously but alternately at consecutive (6-sec interval) frequency sweeps; in other words, measurements of both polarizations can be obtained in opposite polarizations at two adjacent frequencies in 30 msec or at the same frequency in 6 seconds. The time required for making a measurement of both the RH and LH intensity components at both senses of elliptical polarization at a given frequency was therefore 12 sec. The PRA experiment can be also operated in other special high-rate modes. For example, in FIXLO mode, the receiver performs over an integer number of telemetry frames (48 sec), with a high time resolution (30 ms), on selected groups of three channels, each frequency being sampled consecutively with alternated polarization state during 6 seconds. In so-called PHIEX mode, which is designed for high time resolution, fixed-frequency observations and is operated only at selected times, the instrument simultaneously observes signals in two adjacent channels. The resolution of the data obtained in this mode is 140  $\mu$ s. Much more detailed descriptions of the PRA experiment are given by *Warwick et al.* [1977] and by *Lang and Peltzer* [1977].

## 2.2 Calibration of the PRA Antenna for Polarization Sense Measurement

### 2.2.1 Polarization Response of the PRA Antenna

Since the Voyager spacecraft was three-axis stabilized, and the only signals obtained from the PRA experiment were the intensity outputs from the receiver, the PRA experiment was not able to completely determine the polarization status (the four Stokes parameters) of the incoming radio waves. Ideally, however, if the two monopoles together with the spacecraft body were equivalent to a pair of orthogonal dipoles in free space and if a source being observed were located in the positive

direction of the axis perpendicular to the two dipoles, the indicated RH and LH receiver outputs (background-subtracted) would actually be the RH and LH circularly polarized intensity components of the radiation, and the apparent polarization ratio (defined as  $[I_L - I_R]/[I_L + I_R]$ , where  $I_L$  and  $I_R$  are the indicated LH and RH intensity outputs of the receiver) would be the true degree of circular polarization. The sources that were actually observed, however, were almost always considerably offset from the axis perpendicular to the equivalent dipoles. Furthermore, unwanted coupling between the two monopoles due to other structures projecting from the spacecraft had resulted in a certain amount of contamination of both the RH and LH outputs. Thus the measured Voyager RH and LH elliptically polarized intensity components uniquely define neither the polarization ellipse of the incident radiation nor its true RH and LH circularly polarized intensity components. The only Voyager polarization measurement that can be made unambiguously is the sense of elliptical or circular polarization, and only if it is known on which side of the E-plane the source lies. The indicated sense becomes incorrect when a source direction crosses the E-plane in passing to the lower side. That is, the sign of the apparent polarization ratio is opposite from that of the true degree of circular polarization on the lower side of the antenna E-plane, but is correct on the upper side.

The two orthogonal 10-meter monopoles are insulated from the spacecraft body. As previously indicated, each monopole together with the spacecraft body, including its projecting structures, acts as a dipole. Since each monopole resonates as a quarter-wave element at about 7.5 MHz, and the spacecraft body together behave more or less like a free-space half-wave dipole in the vicinity of this frequency. Thus for all frequency channels of the low-band receiver, *i.e.*, at 1326 kHz and below, the equivalent dipole corresponding to each monopole has approximately the “short dipole” frequency-independent directional E-field pattern (for which the field strength of a transmitted signal at a fixed distance is proportional to the sine of the direction

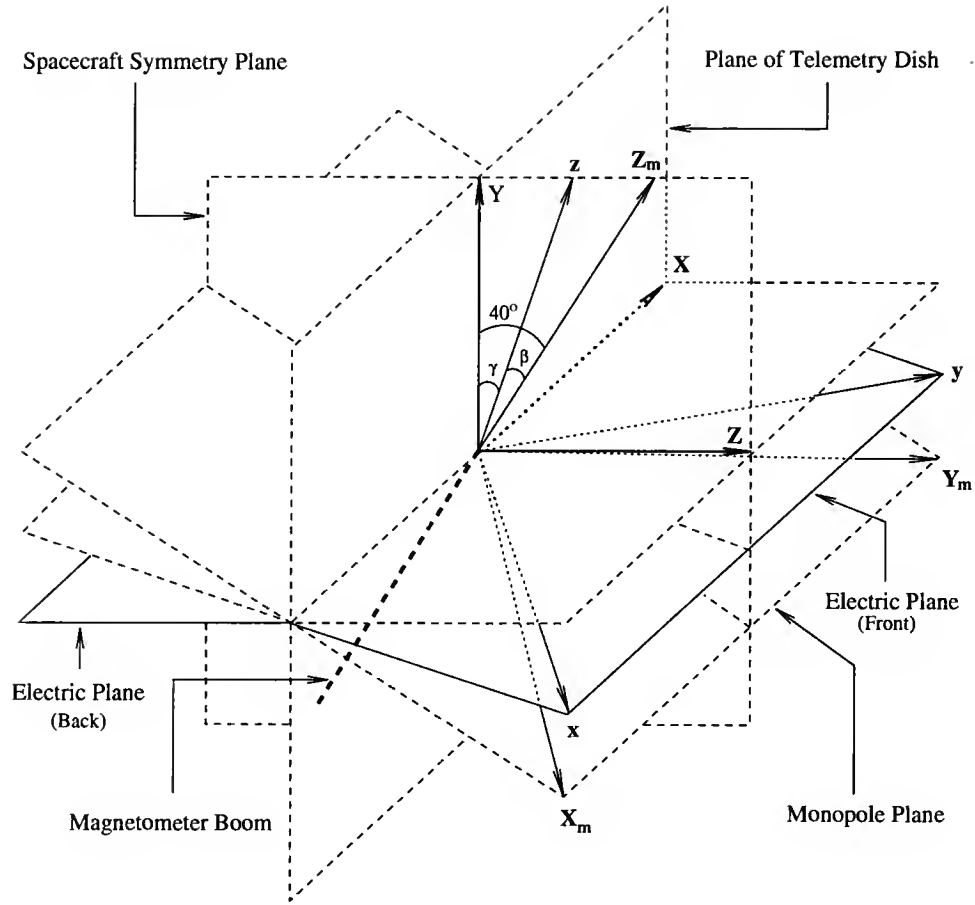


Figure 2.1. Coordinate systems used in the PRA experiment on board the Voyager spacecraft. The  $X_m$  and  $Y_m$  axes correspond to the directions of two monopoles, and the negative direction of the  $Z_m$  axis is that of the magnetometer boom.

angle with respect to the dipole). The longest of the projecting structural features of the spacecraft body is the 13-meter magnetometer boom, which is perpendicular to both monopoles. The spacecraft is approximately bilaterally symmetrical about the plane that contains the magnetometer boom and bisects the  $90^\circ$  angle between the two monopoles. The aperture plane of the paraboloidal telemetry dish (3.7 m in diameter) is perpendicular to the symmetry plane.

To make our description easier, we establish some relevant coordinate systems which are shown in Figure 2.1. The Voyager structural geometry is also illustrated in figures in papers by *Warwick et al.* [1977] and by *Ortega-Molina and Daigne* [1984].

In the spacecraft coordinate system,  $[X, Y, Z]$ , the  $Y$  axis lies along the intersection of the spacecraft symmetry plane and the telemetry dish plane, its positive direction being the one which is farther from the magnetometer boom<sup>2</sup>. The  $Z$  axis is perpendicular to the dish aperture plane, its positive direction being the farther one from the magnetometer boom. This coordinate system is used in the Voyager SEDR (Supplementary Experimental Data Record) ephemeris files for expressing spacecraft-centered positions and directions. In the PRA antenna coordinate system,  $[X_m, Y_m, Z_m]$ , the  $X_m$  and  $Y_m$  axes are defined by the directions of the two monopoles, and the negative direction of the  $Z_m$  axis is that of the magnetometer boom.

Unfortunately, it was not feasible to measure the directional and polarization characteristics of the PRA antenna system prior to the Voyager launchings. However, while the system was under development, *Sayre* [1976] approximated its directional characteristics at frequencies of 0.25, 0.5, and 2.5 MHz by numerical modeling and simulating the shape of the spacecraft body and its projecting structures. Sayre's report, which was not published, contains PRA antenna directional patterns that are relevant to our investigation. These plots have apparently not been used in related investigations, except for being briefly mentioned by *Ortega-Molina and Daigne* [1984]. We reproduce in Figure 2.2 Sayre's unpublished Voyager PRA antenna directional E-field patterns at 0.5 MHz for the  $X_m$  monopole (in combination with the spacecraft body) in the  $X_m Z_m$  and  $Y_m Z_m$  planes, and also for the  $Y_m$  monopole in these two planes. The sharply defined diametrically opposite minima in each of these patterns are in the directions closest to the line along which the equivalent dipole lies. The following information can be deduced from the plots of Figure 2.2: (1) Each monopole pattern is approximately that of a short dipole which is tilted from the

---

<sup>2</sup>The boom supporting the instrumentation platform extends about 4.5 m approximately in the positive  $Y$ -axis direction, and the nuclear-electric power supply boom extends about the same distance in the opposite direction; these features are not indicated in Figure 2.1.

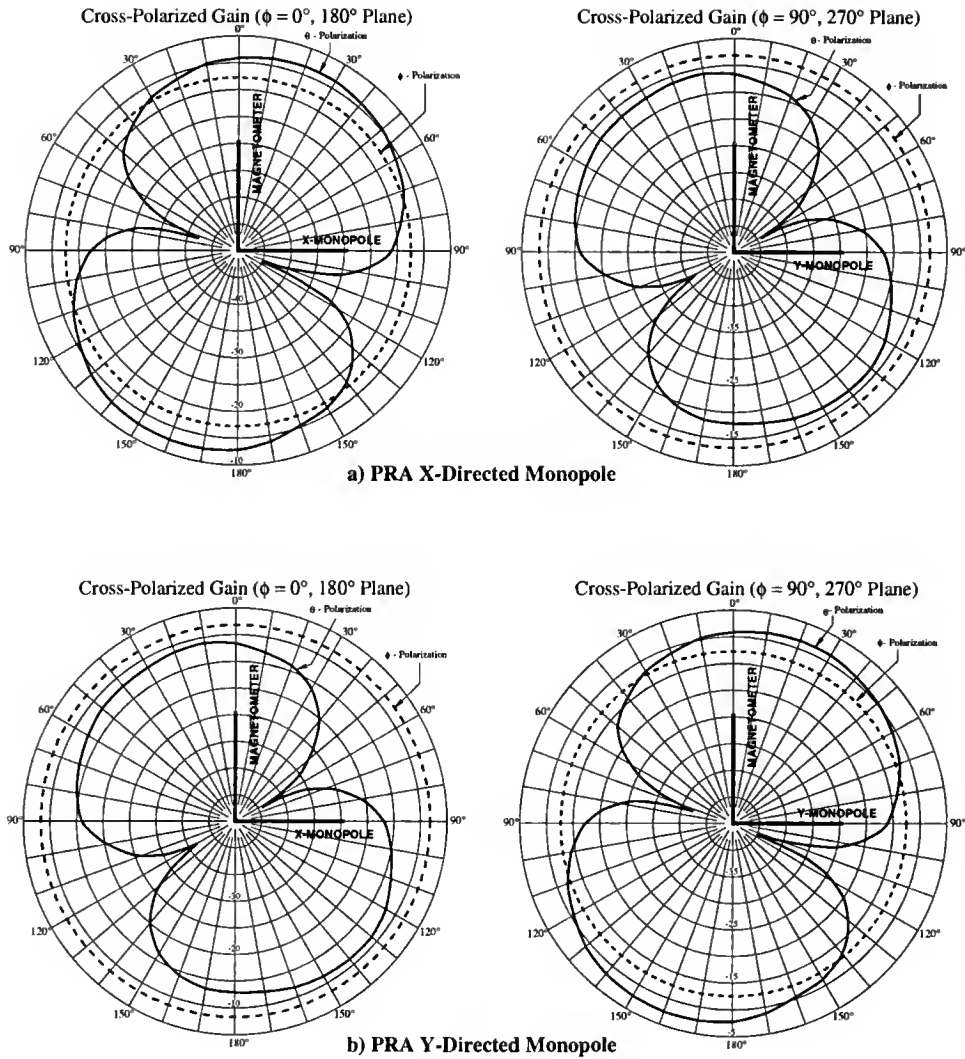


Figure 2.2. The PRA antenna directional patterns at 0.5 MHz for the  $X_m$  monopole in the  $X_m Z_m$  and  $Y_m Z_m$  planes (a), and for the  $Y_m$  monopole in these two planes (b), reproduced from a numerical simulation modeling by Sayre [1976].

monopole direction, the dipole centers being approximately at the intersection of the two monopoles. (2) The two equivalent dipoles are not perpendicular, but intersect in the present case at an angle of about  $137^\circ$ ; this intersection angle is bisected by the spacecraft symmetry plane. (3) The normal to the plane (on its “front” or positive side) that is defined by the two equivalent dipoles lies within a degree of the spacecraft symmetry plane, and is tilted  $55^\circ$  from the normal to the monopoles, in the direction away from the telemetry dish aperture plane.

In Figure 2.1, the orientation of the  $[x, y, z]$  coordinate system is determined by that of the assumed equivalent crossed free space dipoles, which are not necessarily orthogonal. These dipoles, the positive half of each of which is indicated by a dotted line in the figure, determine the  $xy$  plane. The dipole nearest the  $x$  axis will be referred to as the  $x$  equivalent dipole, and that nearest the  $y$  axis as the  $y$  dipole. They correspond, respectively, to the  $X_m$  and  $Y_m$  monopoles. The  $x$  and  $y$  axes are symmetrical about the spacecraft symmetry plane, as are the  $x$  and  $y$  equivalent dipoles. The angle of intersection of the E-plane ( $xy$ ) with the monopole plane ( $X_m Y_m$ ) is  $\beta$ , as is the intersection angle of the  $z$  axis with the  $Z_m$  axis. The direction of a radio source can be expressed by the colatitude and azimuth with respect to either the  $[X_m, Y_m, Z_m]$  system or the  $[x, y, z]$  system. Transformation from the  $[X_m, Y_m, Z_m]$  system to the  $[x, y, z]$  system can be done through the matrix  $\mathbf{M}$ :

$$\mathbf{M} = \mathbf{R}_3(-45^\circ) \mathbf{R}_2(-\beta) \mathbf{R}_3(45^\circ) ,$$

where  $\mathbf{R}_2$  and  $\mathbf{R}_3$ , which are rotation matrices about the  $y$  and  $z$  axes, are expressed as:

$$\mathbf{R}_2(\alpha) = \begin{pmatrix} \cos \alpha & 0 & -\sin \alpha \\ 0 & 1 & 0 \\ \sin \alpha & 0 & \cos \alpha \end{pmatrix}, \quad \mathbf{R}_3(\alpha) = \begin{pmatrix} \cos \alpha & \sin \alpha & 0 \\ -\sin \alpha & \cos \alpha & 0 \\ 0 & 0 & 1 \end{pmatrix}.$$

*Ortega-Molina and Daigne* [1984] developed an analytical model of the Voyager PRA antenna system, based on equivalent tilted and not necessarily orthogonal crossed dipoles. *Leblanc and Daigne* [1984], *Lecacheux and Ortega-Molina* [1987], and *Leblanc et al.* [1987] identified a number of instances of purely instrumental polarization reversals that occurred during spacecraft maneuvers when radiation was being received from Jupiter, Saturn, and Uranus. Although it had long been known that a reversal of the indicated sense of polarization would occur if the antenna E-plane swept across an elliptically or circularly polarized source, the first quantitative demonstration of such instrumental reversals (and the first actual measurement of

the relative orientation of the E-plane) was provided by *Lecacheux and Ortega-Molina* [1987]. They found from the analysis of a set of such events, that had been observed with the low-band receiver channels during the Saturn and Uranus encounters, that regardless of the initial state of polarization of the radiation, the instrument has a null-polarization response for a set of source directions that lie approximately within a plane. In each case the polarization sense became reversed from its initial sense as the plane was crossed by the source direction vector. They interpreted this plane as the E-plane of the equivalent crossed short dipoles. Assuming the Saturnian source to be located as proposed by *Kaiser and Desch* [1982], which was later confirmed by *Lecacheux and Genova* [1983], and the Uranian source to be located at the center of the planet, they calculated the approximate orientation of the E-plane in the coordinate system of the spacecraft. They found the E-plane tilt angle  $\beta$  in Figure 2.2 to be about  $23^\circ 3$  and the equivalent dipole intersection angle to be  $90^\circ \pm 10^\circ$ . We note that this value of  $\beta$  is less than half that found by Sayre, but that our initial and most accurately determined value, to be presented below, is in general agreement with Sayre's.

*Ortega-Molina and Lecacheux* [1990] deduced from a combined analytical study and statistical investigation of a considerable amount of kilometric radiation data from Saturn that the equivalent dipole intersection angle is  $82^\circ 6 \pm 1^\circ 8$ . Their method required the assumption that the Saturnian kilometric radiation is always 100 percent circularly polarized, in opposite senses for two assumed polar sources. They presented evidence that this assumption is correct. In their analysis, the E-plane tilt angle  $\beta$  could not be measured. There is a large difference in the Ortega-Molina and Sayre values of the equivalent dipole intersection angle.

*Ortega-Molina and Lecacheux* [1991] and *Pedersen et al.* [1992] have subsequently attempted to use the foregoing E-plane orientation calibration data to deduce source location information from spacecraft-maneuver polarization-reversal events occurring

during the Jupiter and Neptune encounters. As I have stated previously, however, I will demonstrate that the directional calibration used by these investigators can lead to improbable results. It is attributed to their use of spacecraft-maneuver polarization reversal (referred to as SMPR hereafter) events for the E-plane calibration that did not meet the selection criteria that are outlined below.

### 2.2.2 Antenna E-plane Calibration for Sources in a Particular Azimuth Region

Choosing optimum spacecraft-maneuver polarization reversal events I have initially attempted to recalibrate the relative orientation of the PRA antenna E-plane using particularly favorable and previously unused SMPR events that occurred near Jupiter. For these events I was able to derive enough independent information about the magnetospheric location of the sources so that their offset from the center of the planet could be estimated with the required accuracy. (The SEDR ephemeris tape provided precise locations of the center of the planet at regular intervals.) In choosing suitable SMPR events with which to make the calibration, the following conditions were favored: (*a*) the ratio of the intensity of the received radiation to the spacecraft background noise level must be relatively high; (*b*) the received radiation must have a relatively high degree of circular polarization; (*c*) the geometry must be such that the spacecraft maneuver produces large changes in the angle between the radius vector to the planet and the antenna E-plane both before and after this angle passes through zero; (*d*) the radiation must have been emitted from only one source, as indicated by the uniqueness and sharpness of the transition from the initial apparent polarization sense to the opposite one, and the uniformity of this reversal over a wide range of frequencies. During the Voyager flybys of Jupiter, Saturn, Uranus, and Neptune many spacecraft maneuvers were made, but only a few of them that satisfy the above criteria were found. The three best events for E-plane calibration took place during



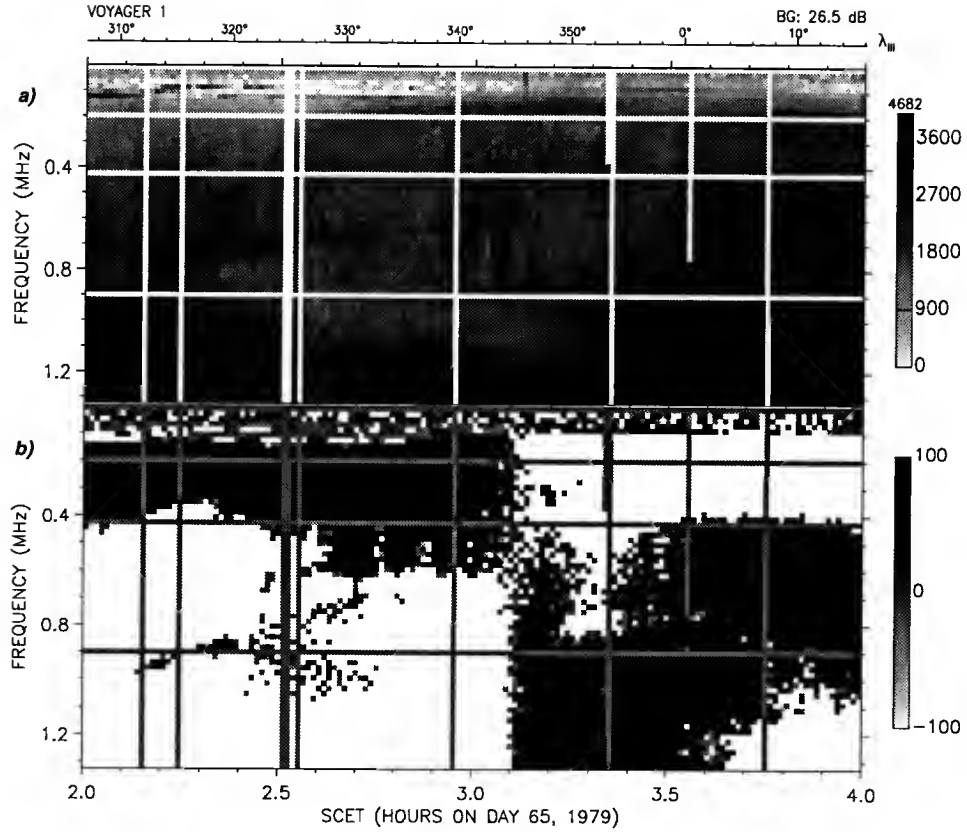


Figure 2.3. A spacecraft-manuever polarization reversal (SMPR) event recorded by the Voyager 1 PRA experiment in the low-frequency-band channels on March 6 (day 65), 1979. Panel (a) is the total flux density as a function of time and frequency, with darker shades of gray indicating higher intensities. Panel (b) indicates the apparent sense of elliptical or circular polarization as a function of time and frequency, with the LH sense represented by black and the RH by white; gray regions are for other cases.

the encounter with Jupiter; they are the ones upon which our initial calculations are based.

Initial E-Plane Calibration from Three Selected Events The best of the three above-mentioned SMPR events was a near-perfect one that occurred between about 02:54 and 03:19 SCET (spacecraft event time) on March 6 (day 65), 1979, when Voyager 1 was about  $15 R_J$  from Jupiter's center. This is illustrated in Figure 2.3. Panel (a) shows the total intensity as a function of time and frequency (darker shades of gray indicate higher intensities). Panel (b) indicates the apparent sense of elliptical

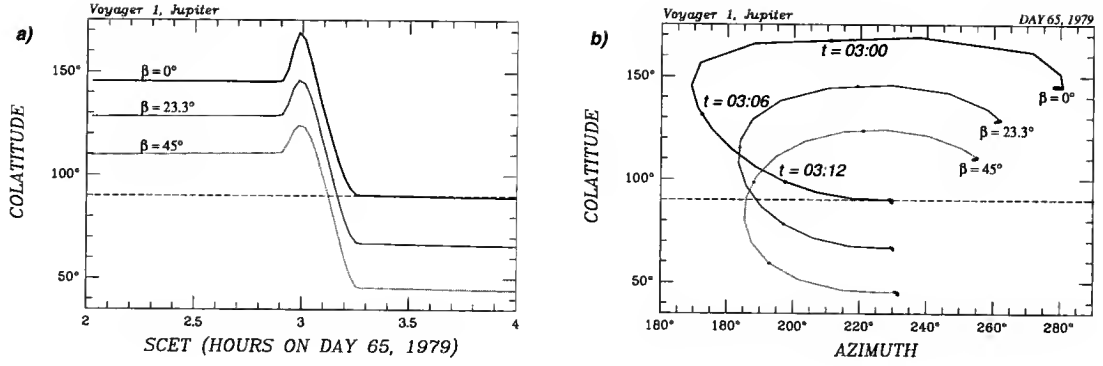


Figure 2.4. (a) Colatitude of the center of Jupiter with respect to the positive normal to each of three planes associated with the PRA antenna, as a function of Spacecraft Event Time (SCET) during the SMPR event of Figure 2.3. The indicated values of  $\beta$  are the tilt angles of the three planes from the monopole plane, for which  $\beta = 0^\circ$  (see Figure 2.1). (b) The above colatitudes have been replotted as functions of the azimuths about the respective positive normals to the above three planes; the symmetry plane lies at  $45^\circ$  azimuth in each case.

polarization as a function of time and frequency. In this panel the polarization sense as indicated by the PRA receiver is left-handed in the black regions and right-handed in the white regions. Gray regions can indicate linearly polarized radiation, unpolarized radiation (not believed to occur in the Voyager data), no radiation at all, or radiation having two components (from separate sources) of approximately equal intensities and axial ratios but opposite senses of elliptical or circular polarization. During the spacecraft maneuver, Jupiter's direction angle in the monopole coordinate system  $[X_m Y_m Z_m]$  changed more than  $70^\circ$  in colatitude and more than  $100^\circ$  in longitude. Figure 2.4a shows the time variation of the colatitude of Jupiter's center as expressed in the equivalent-dipole coordinate system  $[xyz]$  for each of three assumed values of the tilt angle  $\beta$  of the  $xy$  plane (E-plane) with respect to the  $X_m Y_m$  plane (monopole plane). The upper curve, for  $\beta = 0^\circ$ , is the one that would apply if the E-plane coincided with the monopole plane. The middle curve should be used if  $\beta = 23.3^\circ$  as found by *Lecacheux and Ortega-Molina* [1987]. The lower curve is applicable if a value of  $\beta$  calculated below,  $45^\circ$ , is the correct one. It is apparent that before the spacecraft maneuver began, Jupiter's center and also all possible positions of the radio source

were far south of the assumed E-plane for each of the curves. Thus at every frequency in Figure 2.3*b* the indicated polarization sense was opposite to the true sense before the maneuver began, but was correct after the maneuver. We can rule out the  $\beta = 0^\circ$  curve without consideration of the actual source location relative to Jupiter's center. For any reasonable assumed offset of the source from the center of the planet the polarization sense reversal as indicated in Figure 2.4*a* for  $\beta = 0^\circ$  would have been marginal if it had occurred at all, whereas the actual reversal shown in the figure is not at all marginal. The three curves in Figure 2.4*b* are plots of colatitude (from the  $z$  axis) as a function of azimuth (in the  $xy$  plane) for the  $\beta$  values  $0^\circ$ ,  $23^\circ 3'$ , and  $45^\circ$ . It is apparent that for the  $\beta$  values  $23^\circ 3'$  and  $45^\circ$  the azimuths at which the polarization reversals take place (*i.e.*, at which the curves cross  $\theta = 90^\circ$ ) differ by only  $10^\circ$ , and the times of the reversals differ by slightly more than a minute.

The event displayed in Figure 2.3 clearly demonstrates that the lower limit of Jupiter's predominantly hectometric component can be as low as 100 kHz, extending deep into the kilometric band. It also shows that there is an actual reversal of polarization sense at a frequency near 500 kHz. The true polarization sense was LH for frequencies above a somewhat variable boundary in the vicinity of 500 kHz and was RH for frequencies below this boundary. The spacecraft was in the southern Jovian magnetic hemisphere at the time of the event. If we make the usual assumption that the radiation is emitted in the X mode simultaneously from magnetically conjugate sources in opposite auroral zones, and we assume that in this case the contribution of the nearer southern hemisphere source to the received radiation was greater than that of the northern source, then the observed polarization sense at frequencies above about 500 kHz is correctly explained. Two possible explanations of the reversed polarization sense below 500 kHz are that (*a*) although the emission from the conjugate sources is still in the X mode, the frequency dependence of their emission beams has caused the intensity contribution from the northern source to exceed that from the

southern one despite the latter being the closer, or (*b*) the lower-frequency emission from the two conjugate sources was predominantly in the O mode. We are not concerned here with the true polarization sense of radiation at frequencies less than 500 kHz.

Figure 2.3 clearly shows that the reversal of the apparent polarization sense at most frequencies between 100 and 1300 kHz occurred simultaneously to within one 48-sec pixel width. The reversal time was 03:06 SCET. If the source were located at the position of the center of the planet, the polarization reversal times for assumed E-plane tilts of  $23^{\circ}3'$  and  $45^{\circ}$  would be the times at which the corresponding curves cross the  $90^{\circ}$  colatitude line in Figure 2.4. Although the fact that the  $\beta = 23^{\circ}3'$  curve crosses this line considerably after 03:06 SCET suggests that this value of the E-plane tilt angle is unrealistic, such a conclusion is not yet justified because the effect of the offset of the true source position from the center of the planet has not been taken into consideration. However, Figure 2.5 shows clearly that this is indeed the case. The four oval-shaped curves in Figure 2.5 represent the colatitude of the radio horizon as a function of azimuth (in the monopole coordinate system) at a frequency of 1 MHz as seen from the spacecraft at the SCETs of 03:03, 03:06, 03:09, and 03:12, respectively. By radio horizon we mean the set of directions of the locus of the points of tangency of the straight lines<sup>3</sup> from the spacecraft to the surface at which the electron cyclotron frequency  $f_c$  equals the frequency of observation. The OTD magnetic field model was used in the horizon calculations. At a given time the points representing the directions of the radio source at 1 MHz must lie on or inside the corresponding horizon oval. The dotted curves intersecting the ovals are plots of colatitude versus azimuth for assumed E-planes having tilt angles  $\beta$  (from

---

<sup>3</sup>The ray tracing investigations presented in Chapter 5 indicate that refraction of rays penetrating the Io plasma torus can be neglected at the relatively high frequency of 1 MHz; straight-line propagation can be assumed in this case.

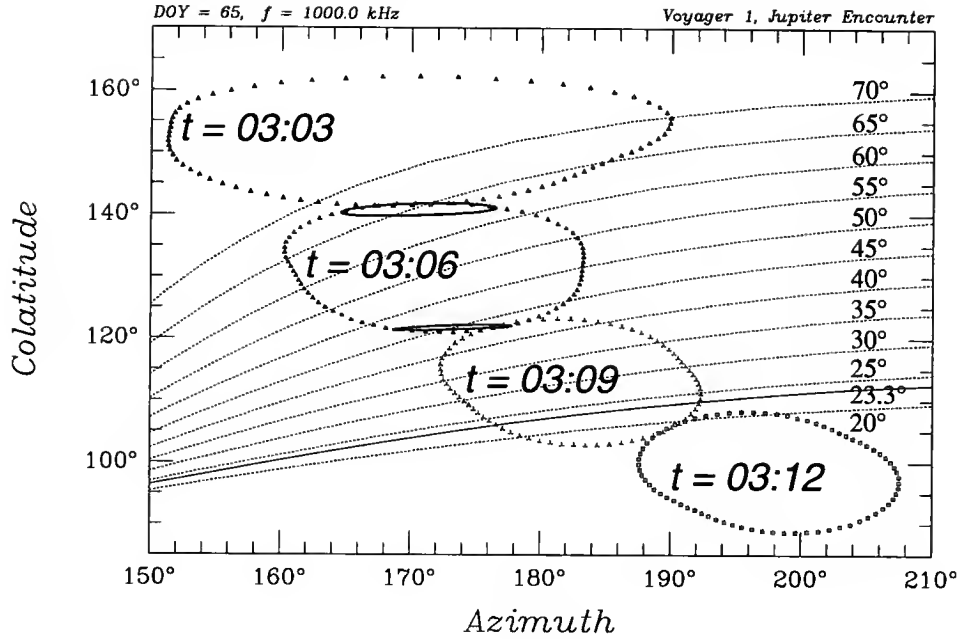


Figure 2.5. Colatitude versus azimuth (in the monopole antenna coordinate system) for the radio horizons at 1 MHz as seen from the spacecraft (zero refraction assumed) at SCETs of 03:03, 03:06, 03:09 and 03:12, respectively, on day 65 of 1979. The finely dotted curves indicate the possible directions of arrival of rays lying within assumed antenna E-planes having the indicated tilt angles, in  $5^\circ$  increments. The two thick solid-line curves near the top and bottom of the radio horizon at the time of the apparent polarization reversal (03:06 SCET) represent the directions of all points along two possible conjugate source regions at the northern (upper) and southern (lower) intersections of the  $L=20$  magnetic shell with the  $f_c=1$  MHz surface.

the monopole plane) in  $5^\circ$  increments. The thin solid curve at  $\beta=23.3^\circ$  represents the E-plane as determined by *Lecacheux and Ortega-Molina* [1987]; I shall hereafter refer to it as the L-OM E-plane. It is obvious that at the time of the apparent polarization reversal (03:06 SCET), all possible source regions intersected by the extended L-OM E-plane were beyond the radio horizon. At this time the lower edge of the horizon oval was still  $20^\circ$  below the L-OM E-plane. If this had been the true E-plane, it would have taken another 2 to 4 minutes for the reversal to occur. (Our mean timing error is less than 24 sec, *i.e.*, half the interval between the Voyager data points.) Figure 2.5 indicates that the true E-plane was tilted at least  $43^\circ$  from the monopole plane.

It is generally believed that the Jovian HOM sources are located within magnetically conjugate regions in the two auroral zones having  $L$ -shell values of approximately 10 to 20, at altitudes at which the electron cyclotron frequency ( $f_c$ ) is nearly equal to the wave frequency [Carr and Wang, 1989, 1990; Ladreiter and Leblanc, 1989, 1990; Barrow, 1991]. The extent to which these sources are distributed in magnetic longitude is still in question; they may extend around the full  $360^\circ$  or they may be limited to a sector of longitude. I have plotted in Figure 2.5 for the time of the apparent polarization reversal (03:06 SCET) two closed (thick) solid-line curves representing the directions of all points in the two possible source regions along the northern and southern intersections of the  $L = 20$  magnetic shell with the  $f_c = 1$  MHz surface. On the basis of the oval-like curves in Figure 2.5 alone it can be stated that (a) the  $\beta$  value for the true E-plane is between  $42^\circ$  and  $48^\circ$  if the source was in the southern hemisphere, (b) the true  $\beta$  is between  $62^\circ$  and  $67^\circ$  if the source was in the northern hemisphere, and (c) the L-OM  $\beta$  value  $23^\circ 3'$  defines a plane that passes no closer than  $23^\circ$  from the southern hemisphere source (the nearer one). From the solid curves superimposed on the oval for 03:06 SCET one can decide in which hemisphere the source was located. Since the true polarization sense was LH at the time of the reversal of the apparent polarization, the predominant source region must have been the southern-hemisphere one (lower curve). Thus, on the basis of this best SMPR event alone, one would have concluded that the E-plane tilt,  $\beta$ , was  $45^\circ \pm 3^\circ$ . This is twice the L-OM value, but agrees more closely with the value deduced from Sayre's numerical modeling results shown in Figure 2.2.

Next, similar calculations of  $\beta$  were made from each of the other two of the three best SMPR events, for which the planet-to-spacecraft distances were  $35 R_J$  and  $60 R_J$ , respectively. Figure 2.6 shows three ovals representing the radio horizon directions at the time ( $t = 18:50$ ) of the  $35 R_J$  event and also at times one minute earlier and one minute later. Superimposed on the  $t = 18:50$  oval are the possible source points along

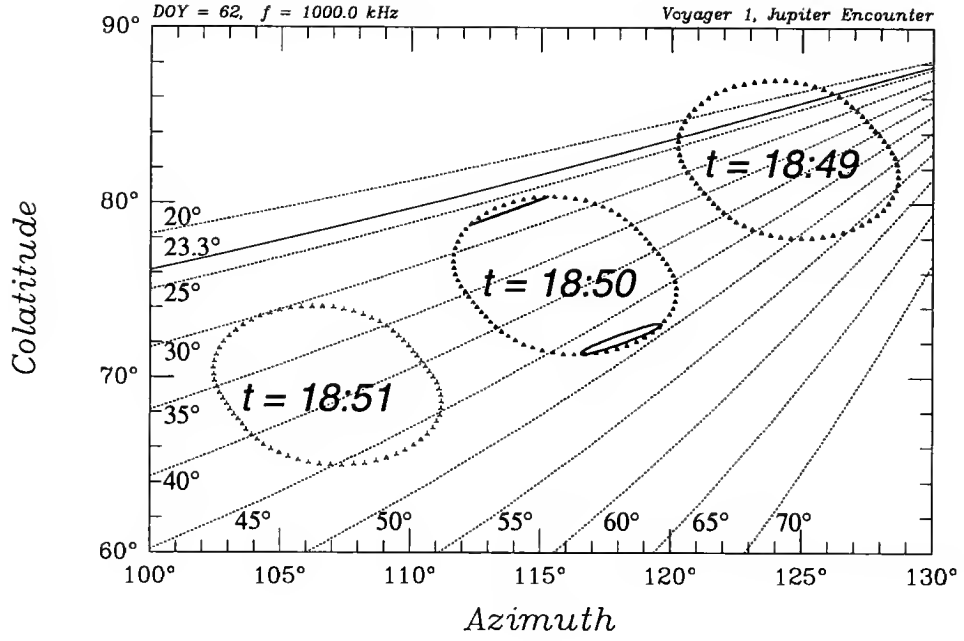


Figure 2.6. Three ovals representing colatitude versus azimuth (in the monopole antenna coordinate system) for the radio horizons at 1 MHz for SCETs of 18:49, 18:50, and 18:51 on day 62 of 1979. The two solid-line curves near the top and bottom of the middle oval (at  $t = 18:50$ , the time nearest the SMPR event) represent the directions of all points along two possible conjugate source regions at the northern (lower) and southern (upper) intersections of the  $L = 20$  magnetic shell with the  $f_c = 1$  MHz surface.

the northern (lower) and southern (upper) intersections of the  $L = 20$  magnetic shell with the  $f_c = 1$  MHz surface. Since the true polarization sense for this event was LH, the source must have been on the upper curve. The corresponding  $\beta$  value is  $27^\circ \pm 2^\circ$ . Corresponding plots for the  $60 R_J$  event are very similar in appearance to those for  $35 R_J$ , and also give  $27^\circ \pm 1^\circ$  for  $\beta$ . I believe that the apparent large discrepancy between this  $\beta$  value and the previous value of  $45^\circ$  is not due to measurement error, but instead is an indication that the assumption of a single E-plane for source directions at all azimuths about the antenna is an oversimplification. This is borne out by the results presented in the next section.

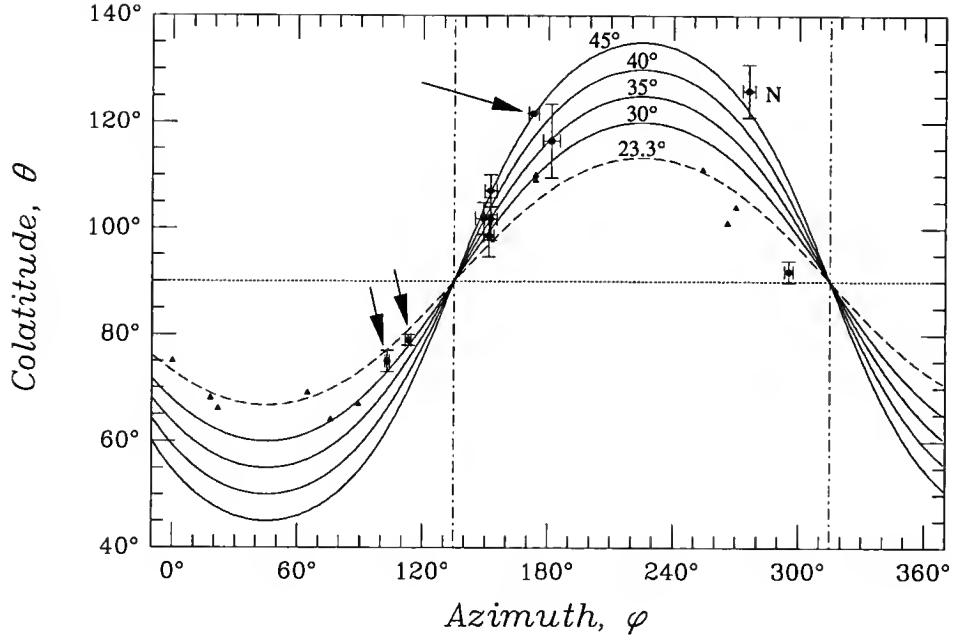


Figure 2.7. Estimated source colatitude and azimuth (in the monopole antenna coordinate system) for all usable SMPR events listed in Table 2.1. The three highest-quality events are indicated by arrows, with the longest arrow at the near-perfect event. The point marked “N” is for Neptune; all the rest of the points with error bars are for Jupiter. A family of quasi-sinusoidal curves representing colatitude versus azimuth for incident rays lying within assumed E-planes having the indicated tilt angles are also plotted. The small triangular points without error bars represent the measurements by *Lecacheux and Ortega-Molina* [1987].

### 2.2.3 Full Calibration Based on all Usable Events

There were a number of SMPR events that occurred at greater distances from Jupiter from which some information is obtainable despite the fact that they were of poorer quality than the three above. For these poorer-quality events the measurement error had become so large due to the increased distance from the planet that the source could be assumed to be located at the center of the planet without appreciably increasing the error. (This was the case for *all* the measurements made for the L O-M paper.) The measurements for all usable SMPR events used in this study are displayed in Figure 2.7, with the three high-quality events that were considered in the previous section being indicated by arrows (the longest arrow for the near-perfect event). Each



event provides one measurement of the antenna E-plane tilt,  $\beta$ , together with the colatitude and azimuth (in the  $X_m Y_m Z_m$  coordinate system) the source point would have if it lay within this E-plane. The family of quasi-sinusoidal curves give colatitude versus azimuth for assumed E-planes having the indicated tilt angles (at  $5^\circ$  intervals). The vertical and horizontal error bar lengths represent mean errors due to the fact that measurements were made only at 48-sec intervals, rather than continuously. There are probably other sources of appreciable error that cannot be represented here. All of the points having error bars are for Jupiter except the one labeled “N”, which is measured from an SMPR event during the Neptune encounter. The small triangles without error bars indicate the L O-M results, obtained from SMPR events at Saturn and Uranus. Unfortunately, insufficient information was provided in the L O-M paper for the determination of error bars for their measurements.

The data associated with all SMPR events, from which the measured points in Figure 2.7 were derived, are summarized in Table 2.1. In this table, V1 and V2 indicate Voyagers 1 or 2; HOM is hectometric or combined hectometric-kilometric radiation from Jupiter; NKR represents kilometric radiation from Neptune; SCET is spacecraft event time (*i.e.*, UT at the spacecraft);  $r$  is distance from the center of the planet to the spacecraft in planetary radii ( $R_J$  and  $R_N$  for Jupiter and Neptune, respectively);  $\varphi$  and  $\theta$  are the azimuth and colatitude in the monopole coordinate system  $[X_m, Y_m, Z_m]$ ; and  $\beta$  is the tilt angle of the equivalent E-plane with respect to the monopole plane.

If the Voyager PRA antenna had been an isolated orthogonal pair of short dipoles, it would have possessed an E-plane with a tilt angle that would be independent of the direction of the radiation source used to measure it. It is clear from Figure 2.7, however, that the Voyager PRA antenna does not have such a unique E-plane. Significantly different values of  $\beta$  can occur for different azimuths of the source. We attribute this to the effect of the highly irregular conducting surface of the spacecraft

Table 2.1. The SMPR events used in the study. Entries marked with  $\dagger$  are measurement based on source location.

S/C	Source	Year/Day	SCET (hh:mm)	$r$ ( $R_P$ )	$\varphi(^{\circ})$	$\theta(^{\circ})$	$\beta(^{\circ})$
V1	HOM	1979/062	18:49.8	35.3	$117.7 \pm 5.0$	$77.1 \pm 4.0$	$36.0 \pm 2.0$
			18:49.8 $\dagger$	35.3	$113.0 \pm 1.5$	$79.0 \pm 1.0$	$27.0 \pm 2.0$
V1	HOM	1979/065	03:06.2	15.5	$172.7 \pm 1.0$	$130.2 \pm 2.0$	$56.0 \pm 2.5$
			03:06.2 $\dagger$	15.5	$173.0 \pm 2.5$	$121.7 \pm 1.0$	$45.0 \pm 2.5$
V1	HOM	1979/067	18:00.0	60.3	$104.9 \pm 5.0$	$73.1 \pm 4.0$	$30.5 \pm 1.5$
			18:00.0 $\dagger$	60.3	$103.0 \pm 1.0$	$75.0 \pm 2.0$	$27.0 \pm 1.0$
			18:36.6	60.7	$152.5 \pm 3.0$	$107.1 \pm 3.0$	$45.0 \pm 10.0$
V1	HOM	1979/069	15:23.4	89.3	$152.3 \pm 3.0$	$101.8 \pm 4.0$	$35.0 \pm 11.0$
			12:55.2	131.7	$149.0 \pm 4.0$	$101.9 \pm 3.0$	$41.0 \pm 12.0$
			03:49.2	140.7	$151.5 \pm 2.5$	$98.6 \pm 4.0$	$28.0 \pm 12.0$
V1	HOM	1979/096	03:06.6	456.3	$295.3 \pm 2.0$	$91.9 \pm 2.0$	$7.0 \pm 13.0$
V2	HOM	1979/195	23:18.6	72.5	$181.5 \pm 4.0$	$116.5 \pm 7.0$	$34.5 \pm 7.0$
V2	NKR	1989/237	10:03.0	16.8	$276 \pm 3.0$	$126 \pm 5.0$	$48.0 \pm 5.0$

and its various projecting members. In Figure 2.7, the two nodal points in the family of quasi-sinusoidal curves are located at the  $(\theta, \varphi)$  points  $(90^{\circ}, 135^{\circ})$  and  $(90^{\circ}, 315^{\circ})$ , *i.e.*, in the two directions of sources lying in the plane of the orthogonal monopoles. The front side of the antenna system, which is the side for which both  $Z_m$  and  $Z$  in Figure 2.1 are positive, lies between the nodal points in the region for which  $\theta < 90^{\circ}$  in Figure 2.7; the back side is the  $\theta > 90^{\circ}$  region. In Figure 2.8, I have plotted the same  $\beta$  values that appear in Figure 2.7 as a function of azimuth,  $\varphi$ . Here again, the three points calculated from the three relatively high-quality SMPR events are indicated by arrows, with the longest arrow indicating the near-perfect event. The point marked “N” is for data obtained during the Neptune encounter, the only one that is not for Jupiter. Point “N” is ranked as the fourth-highest in quality. Our conclusions are drawn almost entirely from these four points.

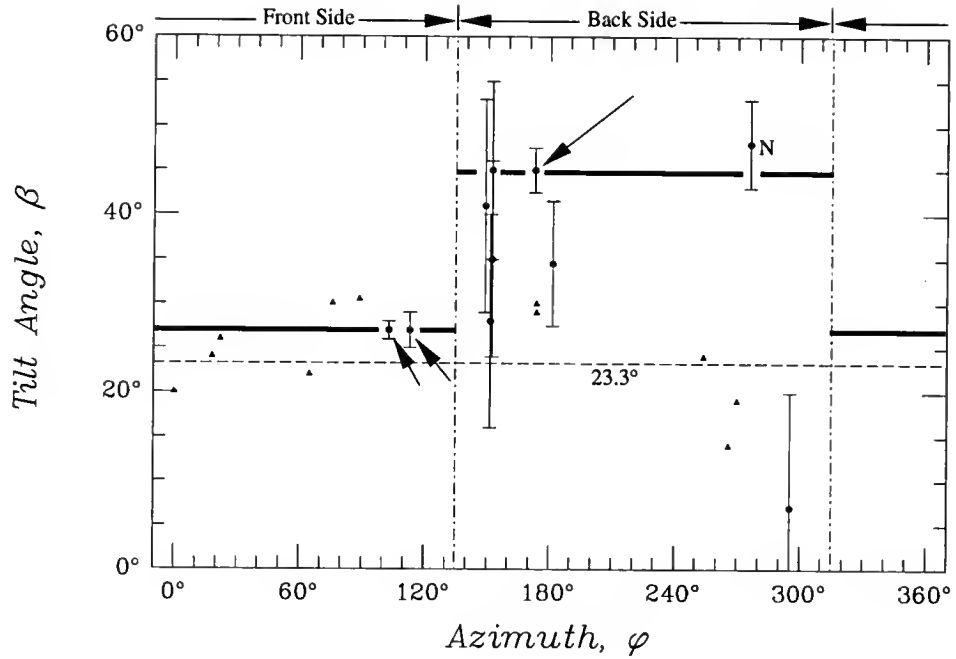


Figure 2.8. Measured E-plane tilt angle plotted as a function of source azimuth for the SMPR events of the previous figure. The composite E-surface is approximated here by two half-planes, one with tilt angle of  $27^\circ$  for sources on the front side of the monopole plane, and the other with a  $45^\circ$  tilt for sources to the rear, as indicated by the two horizontal heavy lines.

One can now assume that the antenna does not have an E-surface that is a single tilted plane. This E-surface can be best approximated by two half-planes of different tilt angles intersecting along the  $X$  axis, one for sources on the front side of the monopole plane and the other for sources to the rear, as depicted in Figure 2.1 (the front and rear half-planes are indicated by solid rather than dashed lines). The two horizontal heavy lines in Figure 2.8 represent this best estimate of the tilt angle of the E-surface as a function of azimuth,  $\varphi$ . The two tilt angles obtained in this way are  $\beta_f = 27^\circ$  and  $\beta_b = 45^\circ$  for sources on the front and back sides of the antenna, respectively. The L O-M value of the tilt angle for all azimuths is  $23.3^\circ$ ; it is indicated by the horizontal dotted line. Our value  $\beta_f$  for the front side is in reasonable agreement with the L O-M value but our  $\beta_b$  for the back side differs from the L O-M value by  $21^\circ$ . Our  $\beta_b$  agrees more closely with the value calculated from Sayre's numerical

model of the antenna-spacecraft system than with the L O-M value; however, the Sayre E-plane tilt, unlike ours, appeared to be about the same at all azimuths. I have to point out that this bent E-plane model is at best a very rough approximation. The actual E-surface dividing the arrival directions, for which the indicated polarization sense is correct from those for which it is reversed, probably has a more complex shape than the bent E-plane.

#### 2.2.4 Discussion

We conclude that the PRA antenna E-surface is not a single plane — its tilt can be significantly different at different azimuths. Our results indicate that there are certain azimuths at which the L O-M (Lecacheux Ortega-Molina) E-plane tilt angle of  $23^\circ 3'$  is in error by as much as  $20^\circ$ , although at other azimuths the L O-M tilt value appears reasonable. We believe that the error bars associated with our four best points in Figure 2.8 (*i.e.*, the three with arrows and the one marked “N”) are realistic. We are less sure that our two horizontal solid lines in the figure indicate the correct tilt angles at *all* azimuths, but they represent the best approximation we can make from the presently available data. It is our opinion that a significant amount of Voyager data exists for which the use of the L O-M E-plane tilt angle would lead to an incorrect interpretation of the polarization sense of the received radiation. There is also the possibility that when observed times of the reversal of the indicated polarization sense (as the true E-surface sweeps across a source) are employed to obtain information related to source direction, the assumption of the L O-M tilt value can sometimes lead to a grossly inaccurate result. In order to minimize the possibility of such errors it is advised that the L O-M tilt of  $23^\circ$  (or our value of  $27^\circ$ ) be used when the observed radiation is incident on the front of the monopole

antenna plane, and that tilt of  $45^\circ$  be used when the radiation arrives from the back side of this plane.

It is unfortunate that the quantity of suitable data was insufficient to yield more conclusive results on the variation of  $\theta$  with  $\varphi$  in Figure 2.8. I searched all of the 48-sec-average Voyager data from Jupiter and Neptune in locating the usable SMPR events, and found no other events in these two data sets that meet the requirements (as listed in Section 2.2.2 on page 16). However, some of the Jovian events which I was forced to reject because the 48-sec sampling rate did not provide sufficient time resolution could perhaps be salvaged if the same data sampled at 12 sec intervals (in both senses of apparent polarization) were available. Other sources of additional unused data are the Saturn PRA data sets obtained by the two Voyagers and the Uranus data set of Voyager 2. If additional points obtained from these unused data sets could be added to the plot of Figure 2.8, the variation of E-surface tilt as a function of azimuth might be much better defined.

### 2.3 The PRA Data Base at the University of Florida

The Voyager PRA data of the Jupiter observations archived at the University of Florida are processed POLLO data (12-sec averages nominally) obtained directly from the Goddard Space Flight Center in the original, unedited, and unsmoothed form. The data set was later edited and cleaned with the removal of the recognizable solar interference and abnormal noise, and was smoothed by taking averages over a 48-sec interval. Data in a few channels have been also removed due to heavy contamination by interference. The overall coverage of the PRA data for the Jupiter observation available at the University of Florida is shown in Figure 2.9, in terms of channel number and the day number in the year 1979. On a specific day, if a channel contains usable data points, it is considered to be a “good” one and is represented by a dot in

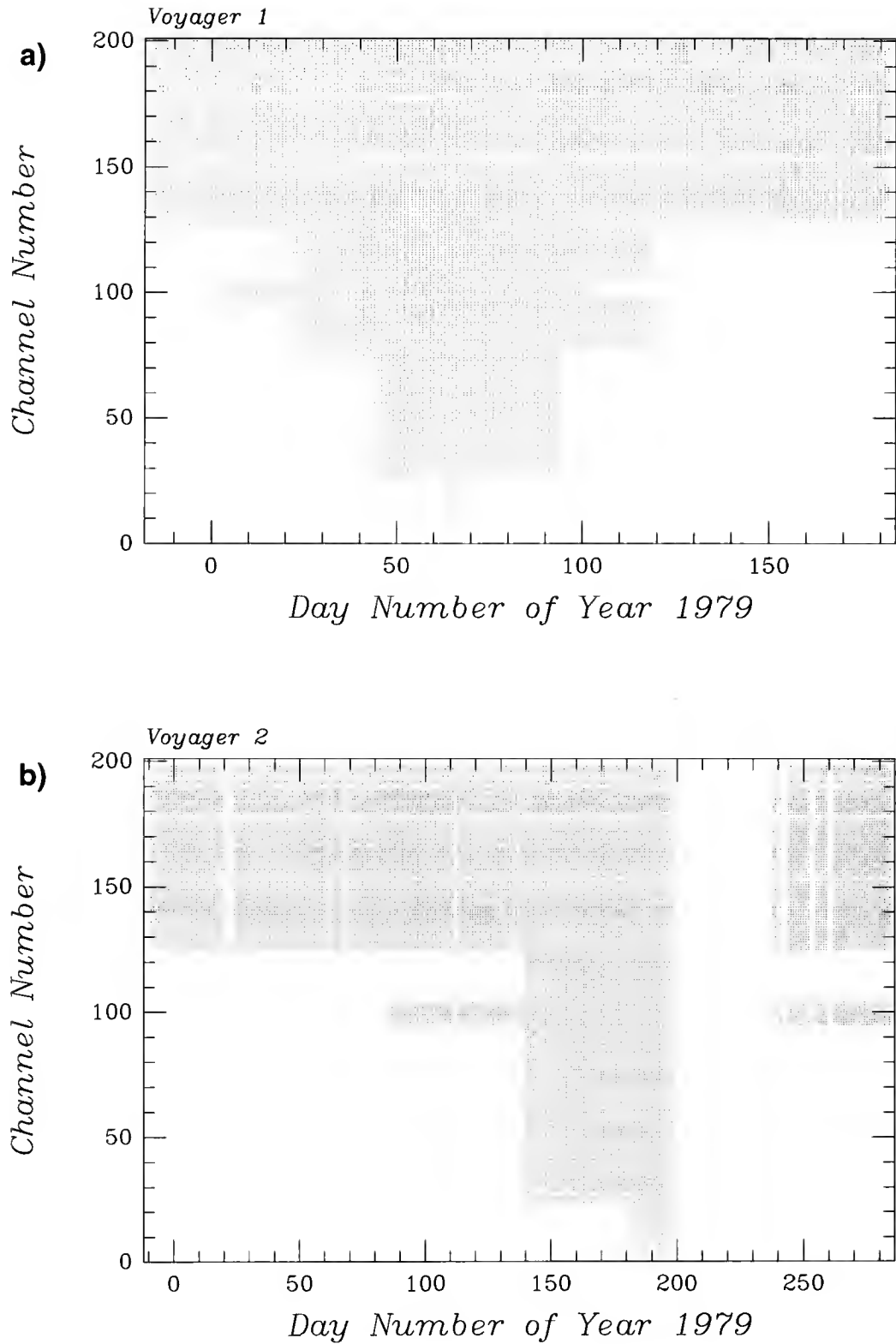


Figure 2.9. A map of availability of the Voyager PRA data base for Jupiter encounters at the University of Florida. Channels which contain usable data points on a specific day are represented with dots. Upper and lower panels are for Voyager 1 and Voyager 2 data respectively.

the figure. Notice that the data for Voyager 2 after encounter from day 199 to day 238 are not available in our data base. Also note that the LF band observations were made for a much longer period than the HF band observations. Meaningful HF band data were only obtained during a period of about one and a half months before and after Jupiter encounter. This is due to an extremely high level of noise in the HF band related to Voyager spacecraft high-speed switching logic which greatly reduces its effective sensitivity. The excellent spacecraft noise rejection design employed in the LF band permitted detection of Jupiter's HOM emission almost immediately after launch.

The PRA data from the Neptune observation was also processed POLLO-mode data obtained directly from the Goddard Space Flight Center. It covers data collected by Voyager 2 during its Neptune encounter period, from Day 219 (August 7) to Day 248 (September 5) of the year 1989. Like the data from Jupiter, the data from Neptune are also subject to intermittent spacecraft-generated interference and other instrumental abnormalities, and contamination to the data sets is far more severe than for the Jupiter case. Cleaning by the removal of all recognizable interference and effects of receiver channel malfunctioning while preserving the good data points becomes very necessary before analyzing and drawing conclusions from the PRA Neptune data. Procedures and methods employed for the data cleaning and editing are described in detail by *Wang et al.* [1991]. To maintain the maximum time resolution, no smoothing process is performed, which means that the time resolution is 12 sec for both LH and RH intensity outputs. My PRA data analyzing and modeling are based on cleaned data sets.

The importance and advantage of using edited, cleaned data set are obvious. Both Voyagers were very noisy spacecraft. The background noise generated within the spacecraft itself greatly exceeds the galactic background and internally generated receiver noise, which can limit the sensitivity of the system for detecting weak radio

signals. Intermittent episodes of greatly increased and sometimes violently fluctuating background noise often occur. Removing this kind of noise along with other types of interference (such as solar wind interference) can maximize the information potential of the data set by minimizing the probability of misidentification. As will be seen in later chapters, the main component of the Jovian HOM emission and the smooth component of the Neptunian kilometric emission are rather stable and persistent, having almost the same appearance from one rotation to the other. Time averaged quantities such as flux density and occurrence probability are suitable to describe some aspects of the HOM emission characteristics. This requires an interference-free data sets to avoid misleading results.



### CHAPTER 3

#### A BRIEF REVIEW OF JUPITER'S RADIO EMISSIONS

Jupiter, by far the largest and most massive planet in our solar system, possesses a complex magnetosphere which would appear from Earth, if it emitted visible light, to be larger than the full moon. This magnetosphere is driven by the rotational energy of the planet, coupled through an intense magnetic field which deflects the solar wind incident upon it. The Galilean satellite Io with its volcanic activity provides perhaps the most prodigious plasma source in the solar system short of the Sun. Each of these is a factor in generating intense and multifaceted radio emissions.

It was by accident that *Burke and Franklin* [1955] discovered Jupiter to be emitting sporadic, strongly polarized decametric radio emission. This discovery was the first observational evidence of any kind that indicated that Jupiter possesses a strong magnetic field. Although the fact was not recognized until several years later, the discovery proved to be a landmark in solar system exploration, preceding such historical events as the discovery of Earth's radiation belts, the determination of the nature of the solar wind, and the discovery of magnetospheres around the magnetized planets.

Prior to the great increase in our knowledge of the Jovian planets made possible by observations from spacecraft, a considerable amount of information on the Jovian magnetic field and magnetosphere had been deduced from groundbased radio observations in the decametric and decimetric wavelength bands. It was known, for example, (a) that Jupiter has a very strong, predominantly dipolar, magnetic field oppositely oriented, relative to the rotational angular velocity vector, from that of Earth, (b)

that there is an extensive Van Allen belt composed of trapped particles with relativistic energies, (c) that contrary to the indications of optical observations, Jupiter's rotation period is constant to a high degree, (d) that a unique electrodynamic interaction between the Galilean satellite Io and the Jovian magnetospheric plasma plays an important role in the physics of this magnetosphere, and (e) that there are strongly localized wave-particle interactions taking place at the northern foot of the tube of magnetic flux passing through Io. Observations of Jupiter's radio spectrum from Earth are restricted at low frequencies by effects of the terrestrial ionosphere. The lowest frequency at which such observations are feasible from Earth ranges from about 25 MHz down to 5 MHz, depending on the state of the ionosphere. Jupiter's hectometric component (nominally at frequencies from 3 MHz down to 300 kHz) and kilometric component (300 to 30 kHz) were not discovered until the 1970's, when Earth-orbiting satellites from which radio observations could be made well above the densest part of the ionosphere became available. Although Jovian radio emissions down to 1 MHz had been detected from the satellites RAE-1, IMP-6, and ISEE-3, most of our knowledge of the hectometric and kilometric components has come from the data provided by the Planetary Radio Astronomy (PRA) on board Voyagers 1 and 2, and more recently by the Unified Radio and Plasma Wave (URAP) experiment on board Ulysses. Now, Jupiter's radio emissions have been observed over the entire spectral region from the lowest frequency which can propagate through the interplanetary medium (20 kHz more or less) up to frequencies of about 300 GHz, where the radio and infrared spectral regions merge. Thermal emission from the Jovian cloud-tops dominates the radio spectrum above about 5000 MHz, and it peaks well inside the infrared region. Jupiter's three low-frequency radio emission components (occurring below 40 MHz), that will be discussed briefly in the remainder of this chapter, are the decametric (abbreviated DAM), hectometric (HOM), and kilometric (KOM) components; the latter is subdivided into the broad-band kilometric (bKOM) and the

narrow-band kilometric (nKOM) components. For the sake of completeness, I will also briefly discuss the much higher frequency Jovian decimetric radio component (DIM), even though it is not directly related to my research.

### 3.1 The Synchrotron Radiation (DIM)

The Jovian synchrotron radiation, referred to as the decimetric radiation in the early literature, was first detected at wavelengths of 10 cm and longer in 1958 [McClain, 1959]. Distinguishing characteristics of this radiation component are its non-thermal spectrum, the relatively large extent and distinctive shape of the emitting region, the relatively high degree of linear polarization, the very small degree of circular polarization, and the beaming effect. This radiation is due to synchrotron emission by high energy electrons trapped in the Jovian Van Allen belt between  $1.6 \sim 3 R_J$ . Such emission consists of extremely high and closely-spaced integral harmonics of  $f_c / \sin \alpha$ , where  $f_c$  is the electron cyclotron frequency and  $\alpha$  is the pitch angle of the magnetically trapped relativistic electrons. Although the early observations of the Jovian synchrotron radiation were in the decimetric wavelength band (hence the abbreviation DIM), it has since been observed over the entire frequency range from 80 MHz to 300 GHz. Its spectrum has a broad maximum centered at about 800 MHz. At about 4000 MHz the synchrotron and thermal radiation components are equal, and above that frequency the latter increases in intensity while the former decreases. Because of the beaming of the radiation together with the fact that the Jovian magnetic dipole axis is tilted about  $10^\circ$  with respect to the rotation axis, the flux density observed at Earth varies periodically as the planet rotates, generally with two maxima and two minima during each rotation. A related effect is the rocking of the polarization plane of the linearly polarized component back and forth by  $\pm 10^\circ$  relative to the rotational equatorial plane as the planet rotates. Because the Jovian

synchrotron radiation was relatively well understood from the Earth-based observations (together with the fact that the frequency coverage of the receivers would have had to be greatly extended), the Voyager PRA instrumentation was not designed for observing the synchrotron component as well as the lower frequency components.

### 3.2 Decametric Radiation

The Jovian decametric radiation (DAM) is the first component of radio emissions from Jupiter discovered in 1955 from ground-based observatories. It has been observed from the ground and from space ever since its discovery (see, for example, *Carr and Desch* [1976], *Carr et al.* [1983], and references therein). This radiation is by far the most powerful radio emission from planets. Both ground and space borne observations of DAM emission show that there is a high frequency cut-off at about 39.5 MHz which is known as the magnetic cut-off because it represents the maximum electron cyclotron frequency occurring in the emission region. The lower end of this emission component is at about 2 MHz. A typical DAM storm can last several hours and the emission shows drifting features in a frequency-time spectrogram.

Soon after the 1955 discovery of the DAM emission, several investigators found that the probability of detecting Jovian activity was dependent upon the central meridian longitude (CML),  $\lambda_{III}$ , and the Jovicentric declination of the observer. Histograms of Jovian activity, as a function of CML, appear similar from apparition to apparition when a planetary rotation rate of  $9^h55^m29^s.71$  is invoked. This period is approximately 5 minutes longer than that obtained from the visible features at the equator and is believed to represent the intrinsic rotation rate of the planet (Jupiter's magnetic field is believed to be generated by the so-called dynamo effect). The DAM

sources were named A, B, and C, according to their relative strengths at an intermediate decametric frequency. Those sources have now been recognized to be due to multiple beams originating from a common location.

*Bigg* [1964] reported that the orbital phase of the Galilean satellite Io,  $\phi_{\text{Io}}$ , measured from the superior geocentric conjunction, had a profound effect on the occurrence of the Jovian DAM emission: A very large enhancement in the detection probability for Io phase angles of  $90^\circ$  and  $240^\circ$  was found. In the two dimensional picture of dynamic interaction between the planet and the satellite Io, the regions of  $(\lambda_{\text{III}}, \phi_{\text{Io}})$  configuration space which showed dependence on both parameters were named Sources Io-A, Io-B, Io-C and Io-D; those regions showing no Io dependence become non-Io-A, non-Io-B, non-Io-C, etc [*Carr et al.*, 1983]. Also from long term ground-based observations, it was learned that the occurrence of DAM varies not only with the CML and Io-phase of the observer, but also with the observer's Jovicentric declination. This was first pointed out by *Carr et al.* [1970] as the well known “ $D_E$ ” effect.

Frequency-time dynamic spectra of Jupiter's emissions display a high degree of complexity, exhibiting intricate structure on several widely different time scales. It also shows at least two distinct types of emission: the “greater arcs” extending from as low as 1 MHz up to the 39.5 MHz cutoff, and the “less arcs” limited in frequency extent. The dynamic spectra of DAM are often organized into individual storms which can last up to several hours separated by long periods of complete radio silence. The L-bursts, with durations usually between 1 and 10 sec, are the most common type observable from Earth. It has long been known that the modulation envelope characterizing individual L-bursts is impressed upon Jovian bursts of much longer intrinsic durations by scintillation due to the rapidly drifting inhomogeneities in the interplanetary plasma along the ray path [*Douglas and Smith*, 1961; 1967]. This

modulation pattern is disordered, and its frequency dependence is hardly apparent in relatively narrow band dynamic spectra [*Genova et al.*, 1981].

There is an additional modulation component known as the modulation lanes, which were discovered by *Riihimaa* [1968; 1970]. The characteristic spectral pattern of this modulation, in contrast to those of L-bursts, is relatively well ordered and is strongly frequency dependent, even when relatively narrow bandwidths are observed. *Imai et al.* [1992] showed that the major component of the Jovian modulation lane structure is probably impressed upon escaping Jovian radiation by constructive and destructive interference due to some type of regular striational structure in the part of the Io plasma torus through which the radiation passes, and that the frequency drifts of the modulation lanes are due to the relative inclination and motion of this interfering structure with respect to the radio-emitting part of the active flux tube.

The DAM radiation from Sources A and B is predominantly right hand (RH) but more left hand (LH) polarization becomes apparent outside the A-B longitude region when the frequency is below about 20 MHz. Most RH polarization occurs within the  $\pm 90^\circ$  CML range while most LH occurs in the other  $180^\circ$  CML range.

The emission is generally believed to be produced by a mechanism related to the cyclotron maser plasma instability [*Wu and Lee*, 1979] that is apparently responsible for the terrestrial kilometric radiation. There is considerable evidence indicating that the Jovian radiation originates in the northern auroral zone (and perhaps to a much lesser extent in the southern zone) at altitudes above the cloud tops at which the electron cyclotron frequencies are only slightly less than the frequencies being emitted.

It is generally accepted that Io related emissions are emanating from sources located within the Io flux tube at magnetospheric altitudes where the local electron gyrofrequency is slightly less than the observed wave frequency. The emission is beamed in a hollow cone with the cone symmetry axis being tangent to the magnetic

field at the source. The non-Io DAM is believed to be generated elsewhere, possibly at higher magnetic latitudes near the tail field auroral zones or the north and south polar cusps.

It has long been supposed that the DAM radiation patterns are due to the rotation with the planetary magnetic field of a complex set of emission beams. *Dulk* [1967] and *Goldreich and Lynden-Bell* [1969] first proposed that Io-B and Io-C sources result from the two sides of a bilobed beam: the DAM radiation is beamed within a thin conical sheet where the flux tube passing through Io meets the top of the ionosphere. Source B is seen when this sheet first crosses the direction of the Earth, and Source C when the other side of the cone sweeps past. *Carr* [1972] showed that both the longitude oscillations and the variations in overall occurrence probability of Io-A source are consistent with a rotating beam having a leading edge parallel to the spin axis and a wedge-shaped trailing edge.

### 3.3 Hectometric Radiation

The Jovian hectometric (HOM) radio emission was not discovered until observations from spacecraft became available. The first observations of Jovian radiation at frequencies below the ionospheric critical frequency were made by *Desch and Carr* [1974] using data from the RAE-1 satellite, and by *Brown* [1974a] using IMP-6 data. Most of our knowledge on the HOM emission has come from the observations by the Planetary Radio Astronomy (PRA) experiment on board Voyager 1 and 2 [*Warwick et al.*, 1979a, 1979b], and only recently by the Unified Radio and Plasma Wave (URAP) experiment on board Ulysses [*Stone et al.*, 1992].

The hectometric radio band nominally extends from about 100 to 1000 meters, corresponding to frequencies from 3 MHz down to 300 kHz. Emission in this waveband from Jupiter fairly well delimits a rather distinctive region of Jupiter's radio spectrum

that lies between the well known decametric radiation above 3 MHz and the kilometric radiation, most of which is below 300 kHz.

The activity of the HOM emission was observed mainly in the frequency range between 400 kHz and about 2 or 3 MHz, with a broad spectral peak centered at about 800 kHz, but sometimes it can be observed down to about 40 kHz, especially near the Voyager encounters. Its upper frequency limit was somewhat unclear, but it can be as high as 8 MHz, as will be shown in the next chapter. The appearance of the HOM emission in a dynamic spectrum plot always shows up as a “block” of emission with a well defined gap centered near  $200^\circ$  CML; another gap can appear near  $25^\circ$  CML, depending on the observer’s latitude. In later chapters, various characteristics of the HOM emission will be discussed in details, and models that best fit those observational characteristics will be established.

### 3.4 Kilometric Radiation

Two kilometric (KOM) components were detected for the first time by the Voyager PRA experiment: a broad-band emission (bKOM) and a narrow-band emission (nKOM). The bKOM recurs favorably when the Jovian north magnetic pole points toward the observer. The emission is RH dominated when seen in the northern magnetic hemisphere and LH dominated when seen in the southern hemisphere. The bKOM is generally observed between about 20 and 400 kHz, and occasionally events may occur up to some 1 MHz. It is believed that sources of the bKOM are probably located at the edge of the Io plasma torus near the magnetic equator. The nKOM, on the other hand, is very narrow in bandwidth (around 20~60 kHz), and confined to a narrow band of frequencies between about 60 and 140 kHz. The nKOM is a quite smooth emission in contrast to the bKOM. The sources of nKOM are believed also



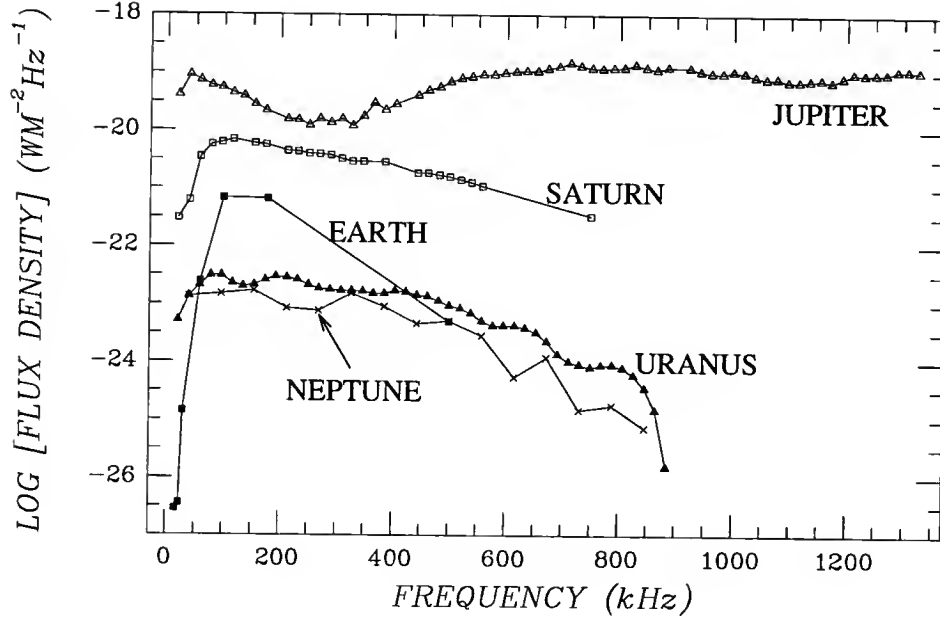


Figure 3.1. Peak flux density of the four giant planets (Jupiter, Saturn, Uranus, and Neptune) and Earth, all normalized to a standard distance of 4 AU.

to lie near the Io plasma torus but distinct from the bKOM sources. It is believed that the same CMI mechanism is responsible for the KOM emissions.

### 3.5 Power Spectrum

Having briefly reviewed Jupiter's radio emission components, we are now ready to take a look at them in a bigger picture. Taking the PRA data from Voyager 1 recorded from February 9 to February 11, 1979, I calculated the peak flux density spectrum for the Jovian radio emission, normalized to a standard distance of 4 AU ( $1 \text{ AU} = 1.496 \times 10^8 \text{ km}$ ). The result is shown in Figure 3.1. To make comparisons with other radio planets, I also plotted in the figure the peak flux density spectrum curves for Earth, Saturn, Uranus and Neptune, all normalized to the distance of 4 AU. They are all calculated from the Voyager PRA observations, except that for Earth. The curves for Earth, Saturn, and Uranus are from *Gurnett [1974]*, *Carr et al. [1981]*, and

*Gulkis and Carr* [1987], respectively; and that for Neptune was calculated recently by me from the Voyager 2 data. As can be seen, radio emissions from Earth, Saturn, Uranus and Neptune do not reach 1 MHz, and curves for these planets are similar, suggesting that they may share a common emission mechanism. Jupiter, on the other hand, emits up to nearly 40 MHz (not shown in Figure 3.1), much higher than other planets. *Brown* [1974*b*] and *Desch and Carr* [1974] reported from the observations of the RAE-1 spacecraft a power spectral peak of the HOM emission near 1 MHz. The Voyager observation, however, shows a broader peak centered somewhat lower than 1 MHz, at about 800 kHz. The power spectrum curve displays no well-defined peak in the KOM and HOM frequency range. This, however, does not necessarily mean that different types of emission mechanisms are involved. Jupiter's magnetic field is at least ten times stronger than those of other planets so that plausible Jovian magnetospheric source locations could be found having electron cyclotron frequencies from a few tens of kilohertz to nearly 40 MHz. Thus, generally speaking, Jupiter's entire spectrum, as well as those of other magnetized planets, could possibly result predominately from a single type of emission mechanism. One of most probable mechanism candidates might be the cyclotron maser instability (CMI), which is well established as the source of Earth's auroral kilometric radiation (AKR) [*Wu and Lee*, 1979].

## CHAPTER 4

### JUPITER'S HECTOMETRIC RADIO EMISSIONS

The successful Voyager mission enabled the exploration of the magnetospheres of the outer planets: Jupiter, Saturn, Uranus, and Neptune. The mission has become one of the most exciting and successful explorations in the history of space flights. One of many exciting results made by Voyager 1 and 2 in their missions to Jupiter was the detection of the intense Jovian radio emission at hectometric wavelengths by the Planetary Radio Astronomy (PRA) experiment [*Warwick et al.*, 1979*a*, 1979*b*] on board the spacecraft. My investigation of the Jovian hectometric (HOM) emission is mainly based on observations from the PRA experiment. Detailed discussion of the PRA experiment and the PRA data has been given in Chapter 2. In this chapter, I will first discuss various properties of the Jovian HOM emission, followed by a presentation of a model that accounts for most of the observational phenomena. Comparison of this model with others being proposed in the literature will be discussed.

#### 4.1 Characteristics of the HOM Emission

Before the Voyager observations are discussed, it is helpful to get an idea about the Voyager trajectories during their encounters with Jupiter. Both Voyager spacecraft were launched in 1977 and flew over Jupiter in 1979. The closest approaches to Jupiter occurred on March 5 (Day 64) and July 9 (Day 190) for Voyager 1 and Voyager 2, respectively. The trajectories during the encounter period for both Voyagers are shown in Figure 4.1. The two Voyagers approached Jupiter at different Jovigraphic

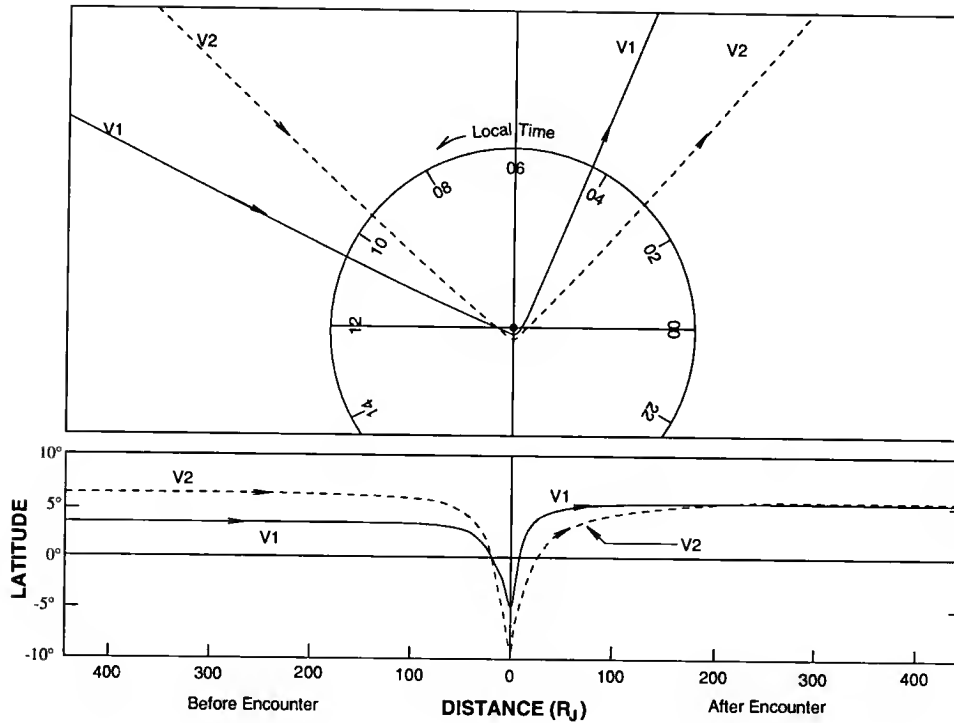


Figure 4.1. Trajectory of both Voyagers during their mission to Jupiter. The local time is defined as the angle of observer-Jupiter-Sun.

latitudes (at about  $3.2^\circ$  and  $7^\circ$  for Voyager 1 and 2, respectively) and at different local times (at about 10:30 and 9:40 for Voyager 1 and 2, respectively). They flew away from Jupiter at almost the same Jovigraphic latitude (about  $5^\circ$ ) but at different local times (about 04:15 and 03:00 for Voyager 1 and 2, respectively).

#### 4.1.1 Frequency Coverage

Let us begin our discussion of the characteristics of the HOM emission with a typical dynamic spectrum plot, shown in Figure 4.2, of Jupiter's radio emissions observed with both low- and high-frequency band receivers of the PRA experiment of Voyager 1 after the encounter on March 21 (Day 80), 1979. The dynamic spectrum is a plot of received total intensity as a function of frequency (or channel number) and spacecraft event time (SCET). This plot is made such that the darkness in the plot

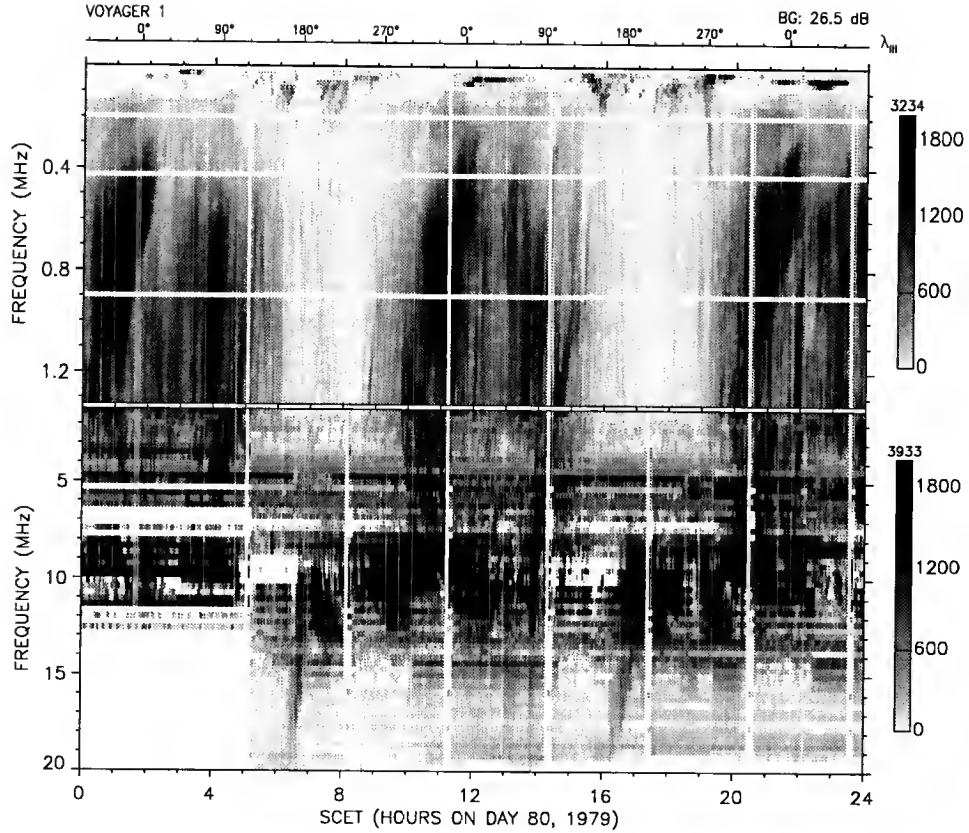


Figure 4.2. A typical dynamic spectrum plot of the Jovian radio emissions in the low- and high-frequency bands recorded by Voyager 1 on March 21 (Day 80), 1979. The CML of the spacecraft,  $\lambda_{III}$ , is plotted on the top of the figure.

is proportional to the logarithmic intensity of the signal above a selected background (labeled as BG in the figure) as shown in the scale bar with numerical labels in units of millibels (the number on the top of the scale bar for each panel is the maximum intensity reading in the panel). The *System III* (1965) central meridian longitude (CML) of the spacecraft,  $\lambda_{III}$ , is also plotted on the top of the figure. The presence of the horizontal streaks is due to the problem of spacecraft interference which made some of the channels permanently unusable. White blanked regions correspond to bad data points being removed.

The HOM emissions were observed when the CML of the spacecraft was between about  $280^\circ$  and  $120^\circ$ . Radiation occurring elsewhere in the LF panel (mainly in low frequency regions) is the kilometric emission. Clearly, this figure shows that the HOM

emission occurs mainly from a lower frequency of about 350 kHz and extends to the high-frequency band receiver up to about 8 MHz. Radiation at frequencies as low as 40 kHz was observed in the same CML range when Voyager was very close to Jupiter. The decrease in the power spectrum near 400 kHz shown in Figure 3.1, as well as occurrence probabilities (to be discussed next), indicate that 400 kHz is an average of the lower frequency limit of the HOM emission. The upper frequency limit is not as clear as the lower frequency limit, because the HOM emission merges into the decametric emission (DAM). *Barrow and Desch* [1989] suggested it to be as high as 7 MHz. Our dynamic spectrum (Figure 4.2) shows clearly that the HOM emissions can reach the frequency as high as 8 MHz.

#### 4.1.2 Intensity Profile in CML

From Figure 4.2 and other dynamic spectrum plots similar to it, one can see that the HOM emission appears to be strongly modulated as Jupiter rotates. Radiation at about 1 MHz reaches its peak in every rotation when the observer is near  $330^\circ$  and  $90^\circ$  CML. Such emission peaks shift as the frequency decreases. For example, at 500 kHz, the main emission peak has shifted from  $330^\circ$  to  $350^\circ$ . It is a persistent feature that is unique to the HOM emission. When fixed-frequency-channel plots of the emission intensity as a function of time from a single channel in the vicinity of 1 MHz are made, there is a strong tendency for a characteristic signature, which is either bilobed or monolobed, to occur with each rotation of the planet as is shown in Figure 4.3. In this figure, the observed right-hand (RH) and left-hand (LH) intensity outputs<sup>1</sup> at 1 MHz, taken over four successive Jovian rotations for each Voyager, are plotted against the SCET, and are compared before encounters when the Jovigraphic latitudes of

---

<sup>1</sup>The corresponding plot of the apparent polarization ratio in the same periods will be shown in Figure 4.11 on page 66.

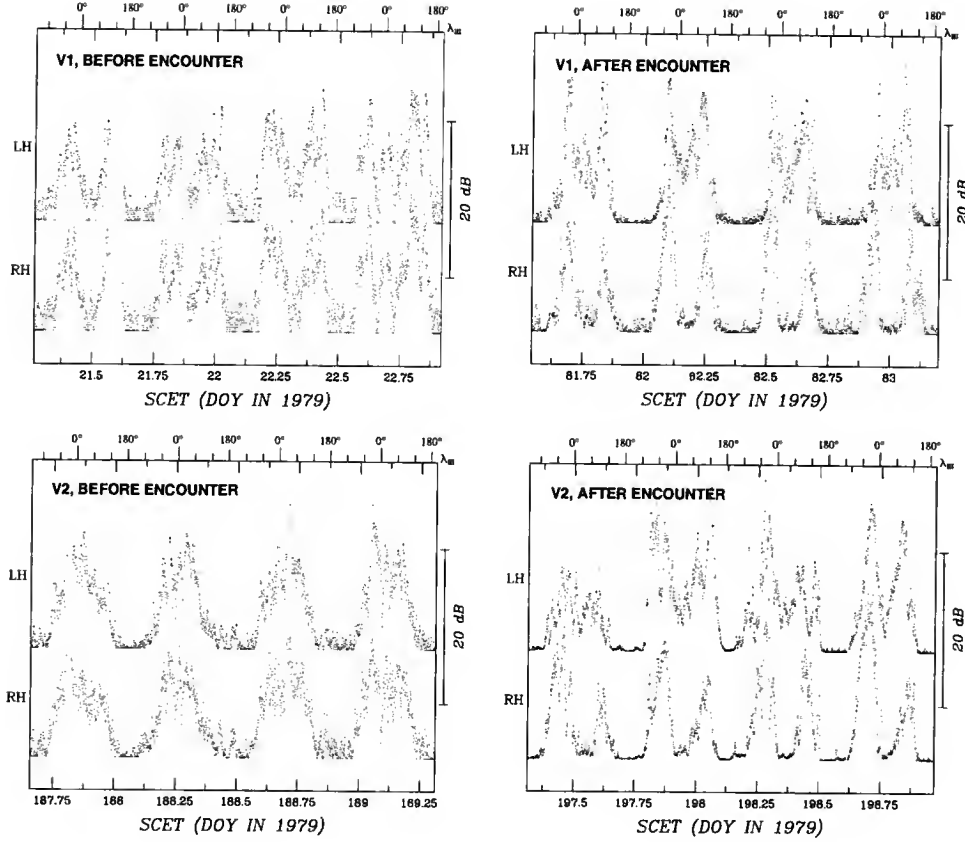


Figure 4.3. Intensity plots for both the LH and RH components at 1 MHz as a function of spacecraft event time (SCET) in units of Day of Year (DOY) in 1979 for data from Voyager 1 and 2 before and after encounters, for four consecutive rotations each. Plotted on the top of each panel is the CML ( $\lambda_{III}$ ) of the spacecraft.

Voyager 1 and Voyager 2 were 3°2 and 7°1, respectively, and after encounters when the Jovigraphic latitudes of Voyager 1 and Voyager 2 were 5°2 and 4°2, respectively. In preparation of the intensity-time plots, the intensity is normalized by a factor that is proportional to the square of the distance. The ordinate in Figure 4.3 is the logarithm of the normalized intensity.

The most conspicuous feature of the apparent corotating emission pattern shown in Figure 4.3 is a deep and relatively wide null centered around 200° CML, which is the approximate longitude of the northern magnetic pole (when a tilted dipole magnetic field model is assumed). Furthermore, the emission gap of pre-encounter data is wider for Voyager 2, which was at higher latitudes, than for Voyager 1, which approached

Jupiter at lower latitudes. The monolobed response for Voyager 2 before encounter differs from the bilobed response for the three other cases due to the difference in spacecraft's Jovigraphic latitude. There is also a narrow gap centered around  $30^\circ$  CML between the leading and trailing maxima in a bilobed feature, and this gap in each cycle is more widely separated for the RH data than for the LH data. Such a repeating structure appears to be quite stable except during the period of close encounter. The apparent activity of the HOM emission varies with the latitude of the observer; it is very similar to the behavior of the Jovian decametric radio emission (DAM), known as the " $D_E$  effect" [Carr *et al.*, 1970; Carr and Desch, 1976]. Plots similar to Figure 4.3 at all frequencies from about 0.7 to 1.3 MHz show the same characteristics, but the repeating structure is best displayed at about 1 MHz.

It has been argued that the wide gap around  $200^\circ$  CML and the narrow gap around  $30^\circ$  CML, where low or no HOM emission was detected by the PRA receiver, is due to the drop-out of emission intensities near these longitudes below the threshold that the receiver can detect. It was suggested that the HOM source is still active but its emission is just too weak to be detected by the PRA receiver [Ladreiter and Leblanc, 1989]. However, it is important to note that the intensity readings recorded near  $90^\circ$  and  $330^\circ$  CML (where the HOM emission reaches its peak) are at least 15 dB higher than those recorded near  $200^\circ$  CML (the center of the wide gap). This means that the peak intensity of the HOM emission is at least 30 times stronger than the intensity that could have been detected in the wide gap. Recent observations from the Unified Radio and Plasma Wave (URAP) experiment, which is at least one order of magnitude more sensitive than the PRA experiment, on board the spacecraft Ulysses also showed a gap near  $200^\circ$  CML when Ulysses was at about  $1.5^\circ$  Jovigraphic latitude [Lecacheux *et al.*, 1992b]. All these facts indicate that the gap near  $200^\circ$ , and probably that near  $30^\circ$  CML, are true gaps. A successful HOM model should be able to produce such gap(s). I will come to this point later in Section 4.3 regarding modeling.



As can be seen from Figures 4.2 and 4.3, the HOM emission is strongly modulated by the rotation of Jupiter. The emission appearance as a function of CML of the observer is quite stable, although rapid changing of HOM activity on a time scale of minutes is also obvious. Such a stable character is best described by the *averaged total flux density* or the *occurrence probability* as a function of CML and frequency for data over many rotational cycles. The occurrence probability is calculated by dividing the number of activity counts by the total number of observing counts. Only the activity that exceeds a certain threshold above the background level is counted. The appearance of stronger emissions can be best described by using a larger threshold value when the occurrence probability is calculated. Weaker emissions are emphasized by plotting flux density values in a logarithmic scale above the background level. The averaged total flux density as a function of CML of the spacecraft and emission frequency before and after encounters is presented in Figure 4.4 for each of the two Voyagers. Data for over 70 rotational cycles were used for the calculation except for the Voyager 2 after-encounter case, where only 12 rotational cycle data were used. The observed intensity for both RH and LH components was normalized to a distance of  $200 R_J$  before it was added and its average was taken. The HOM emission appears clearly as two maxima concentrated near the  $330^\circ$  and  $90^\circ$  CML for Voyager 1 pre- and post-encounters and for Voyager 2 post encounter. For Voyager 2 pre-encounter, the emission is seen near  $350^\circ$  as a single broad maximum. It is worth noting that the intensity peak near  $330^\circ$  became more intensive after encounter, a sign of local time effect. This is most obvious for the case of Voyager 1 after encounter. Figure 4.5 shows the occurrence probability from Voyager 1 and 2 observations over 70 rotational cycles (except for Voyager 2 after encounter, in which 12 cycles are considered) before and after encounter with Jupiter with a threshold value of 10 dB. As can be seen in the figure, the HOM emission occurs in every rotation of the planet with almost 100% occurrence probability when the spacecraft is near  $90^\circ$  and  $330^\circ$  CML, and the

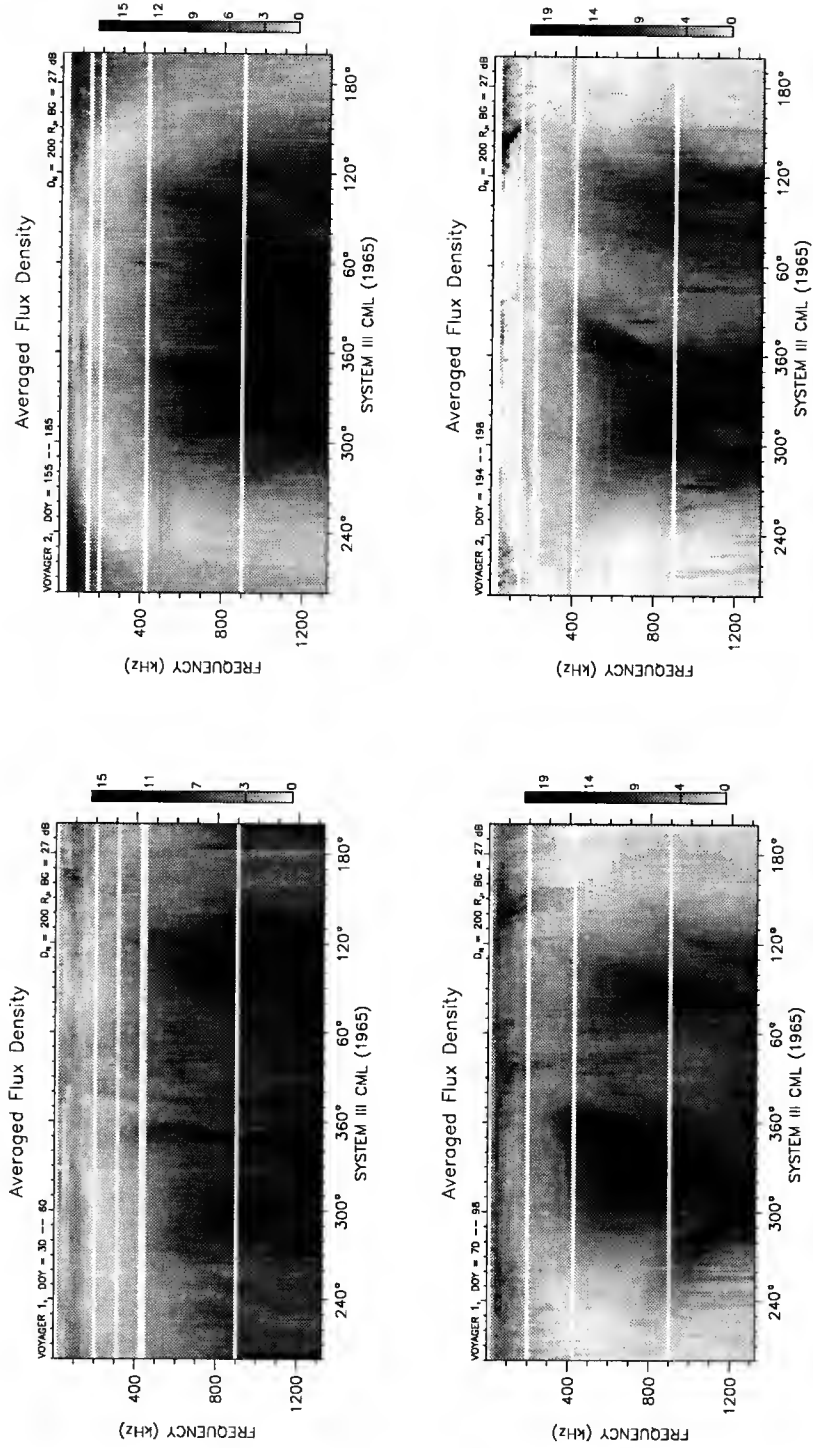


Figure 4.4. The averaged total flux density (above the background level) of the HOM emission as a function of CML of the spacecraft and the emission frequency calculated for both Voyagers before the Jupiter encounter (upper panels) and after (lower panels).

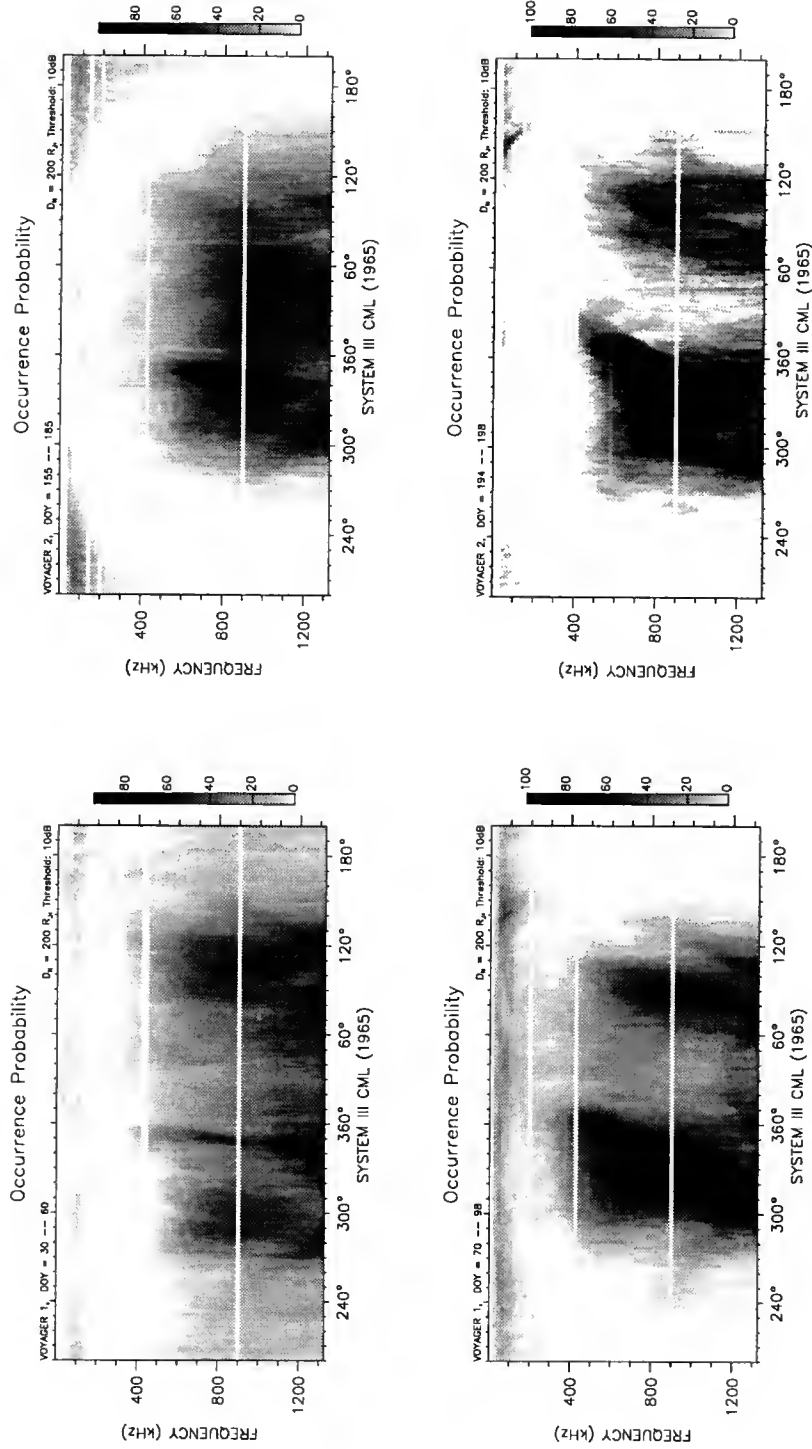


Figure 4.5. Occurrence probability as a function of CML of the spacecraft and the emission frequency, calculated for both Voyagers before the Jupiter encounter (upper panels) and after (lower panels). The threshold value is set to 10 dB.

Table 4.1. Measurements of longitude associated with the midpoints of the wide and narrow gaps.

	Wide gap			Narrow gap		
	CML	N	SSL	CML	N	SSL
Voyager 1 before encounter	$203^{\circ}8 \pm 1^{\circ}9$	47	$180^{\circ}$	$31^{\circ}0 \pm 2^{\circ}0$	32	$7^{\circ}$
Voyager 1 after encounter	$203^{\circ}0 \pm 1^{\circ}4$	74	$87^{\circ}$	$30^{\circ}4 \pm 1^{\circ}8$	59	$275^{\circ}$
Voyager 2 before encounter	$199^{\circ}1 \pm 1^{\circ}7$	48	$166^{\circ}$	$30^{\circ}5 \pm 4^{\circ}1$	12	$1^{\circ}$
Voyager 2 after encounter	$201^{\circ}6 \pm 2^{\circ}8$	11	$56^{\circ}$	$32^{\circ}2 \pm 1^{\circ}7$	8	$249^{\circ}$
Weighted mean	$202^{\circ}0 \pm 0^{\circ}9$			$31^{\circ}6 \pm 1^{\circ}0$		

occurrence probability near  $200^{\circ}$  CML is almost zero. There is a trend that emissions at higher frequencies occurs a little earlier than those at lower frequencies, causing the shift in CML of the emission peaks. Part of such shifting is a stable spectral feature which appears as lanes of decreasing intensity within the otherwise persistent HOM emission. Such lane features have been studied by *Green et al.* [1992] and by *Higgins et al.* [1993], who suggest that the lane phenomenon may be intrinsic to the source of the HOM emission and is unlikely to originate from the propagation effect. The lane feature is most obvious for the peak near  $330^{\circ}$  CML. It is important to note that the HOM emission in its broad frequency range (from about 450 kHz to 1.3 MHz) has almost the same occurrence probability distribution. It means that the HOM emission in its frequency range is observed almost simultaneously. This implies that the HOM emission at different frequencies experiences the same propagation effect from the Jovian magnetosphere on its way out. Of course, the averaged flux density or occurrence probability only describes the stable part of the HOM emission.

A close examination of the overall stability of the HOM emission appearance has been made as a function of CML from observations obtained by both Voyagers. The midpoint longitudes of the wide and narrow gaps are measured, and the results are given in Table 4.1. In this table, *CML* is the average central meridian longitude

(System III) of the midpoint of the gap;  $N$  is the number of values averaged;  $SSL$  is the average of the subsolar longitudes occurring when the gap midpoints were on the central meridian. The CML indicated error is the standard deviation of the mean. The standard deviation of a single measurement ranged from  $5^\circ$  to  $14^\circ$ . The mean of the mid-longitude of the wide gap centered near  $200^\circ$  CML was measured for 180 rotational cycles, and the result  $(202^\circ 2 \pm 0^\circ 9)$  turned out to be quite close to the mean of the north magnetic pole longitudes for the four tilted dipole models discussed by *Acuña et al.* [1983]. The mean of the mid-longitudes of the narrow gap was found to be  $31^\circ 6 \pm 1^\circ 0$ , which differs by  $9^\circ 1$  from the longitude  $(22^\circ 2)$  diametrically opposite the wide gap midpoint. The fact that the midpoint longitude of the wide gap can be accurately measured makes it an extremely good candidate as a fiducial point for the precise measurement of the mean Jovian magnetospheric rotation period. *Carr and Wang* [1990] first proposed that the long-term monitoring of the Jovian HOM emission at a frequency of about 1 MHz from a high-orbit satellite or from the surface of the moon would eventually provide a record of rotation period changes revealing secular variations in the Jovian magnetic field, with a sensitivity and accuracy higher than could be achieved from terrestrial observatories. The Jovian hectometric observations will be made by the spacecraft Galileo in 1995, and when such observations are used in conjunction with those of the Voyagers obtained in 1979, a mean rotation period measurement with an accuracy of 0.01 sec can be achieved [*Wang and Carr*, 1990].

The HOM emission profiles shown in Figures 4.3, 4.4, and 4.5 indicate that there are some differences for data recorded by both Voyagers before and after their Jupiter encounters. This can be due to (1) difference of the spacecraft's Jovigraphic latitude and (2) difference in local time (*i.e.*, the observer-Jupiter-Sun angle) during which the observation was made. As shown in Figure 4.1, Voyager 1 and Voyager 2 approached Jupiter at local times of 10:30 and 9:40 on the day side, and after encounter they traveled away at local times of 4:20 and 3:00 on the night side, respectively.

When on the day side (before encounter), radiation received at about  $330^\circ$  CML was on the average weaker than that received at  $90^\circ$  CML; after encounter, the opposite result became dominant. Previous study by *Alexander et al.* [1979] from combined observations of the two Voyager spacecraft and two other spacecraft (PRE-1 and IMP-6) provided a strong evidence that the HOM profile changes with the observer's latitude, an effect similar to that long observed DAM emission, known as the " $D_E$ " effect [*Carr et al.*, 1970]. However, the difference shown in Figures 4.4 and 4.5 of pre- and post-encounter observations does show a local time effect. From those figures it is clear that the HOM emission undergoes some changes in intensity level and occurrence probability between the pre- and post-encounter observing intervals. Apparently, the leading beam ( $\lambda_{III} < 360^\circ$ ) becomes more intense and more common after encounter for both Voyagers. Such variation cannot be explained by the change of the spacecraft's latitude, because the Voyager 1 observation was made at a lower latitude before encounter and at a higher latitude after encounter, while the Voyager 2 observation was made at a higher latitude before encounter and at a lower latitude after encounter. Both observations lead to the same change in intensity level and occurrence probability. We conclude that the difference in the HOM emission profiles before and after encounter is mainly due to the local time effect.

It is interesting to note that Figures 4.5 and 4.2 clearly show an anti-correlation between the broad kilometric (bKOM) and the HOM occurrences in CML.

#### 4.1.3 Magnetic Latitudinal Beaming

Figures 4.3, 4.4 and 4.5 show that the HOM emission occurrence varies with the latitude of the observer. Based on their study, *Alexander et al.* [1979] suggest that the HOM emission is beamed to a constant magnetic latitude,  $3^\circ$  north of the magnetic equator with a beam width of about  $10^\circ$ .

We notice that the magnetic latitude of a “stationary” observer consistently changes as the planet rotates, due to the tilt of the Jovian magnetic field. The HOM emission occurs just before and after the observer reaches its minimum magnetic latitude. To see how the HOM emission at all frequencies occurs as a function of the magnetic latitude, it is best to calculate the occurrence probability or average flux density in terms of frequency and magnetic latitude of the observer. As the planet rotates, an observer experiences increasing and decreasing changes in his magnetic latitude, depending on the CML position of the observer. Figure 4.6 shows the averaged total flux density of the HOM emission calculated from both Voyagers before and after their encounters with Jupiter for over 70 rotational cycles, except for the Voyager 2 observation of 12 rotational cycles taken after the encounter. This calculation indicates that the HOM emission as a whole occurs when the observer is near the magnetic equator, a strong evidence of magnetic latitudinal beaming. However, the HOM emission at different frequencies is *not* beamed to a constant magnetic latitude, as *Alexander et al.* [1979] suggested; beaming widths are also different for emissions at different frequencies, depending on the observer’s Jovigraphic latitude. For example (see Figure 4.6), at 800 kHz the emission is beamed to about  $3^\circ$  with about  $5^\circ$  width for Voyager 1 before encounter ( $\delta \approx 3.2$ ), but is to about  $-1^\circ$  with  $7^\circ$  width after encounter ( $\delta \approx 5.2$ ). Another important feature to note is that the emission at lower frequencies ( $< 600$  kHz) is actually beamed to a lower magnetic latitude after encounter than before encounter. As will be seen next, after encounter with Jupiter, each Voyager was oriented in the position such that the PRA antenna behaved like an almost perfect circular polarimeter, and the outputs of the PRA polarization channels are nearly proportional to the true left and right circular components of the source(s) [see Equation (4.6) on page 64]. It is therefore possible to determine how the LH and RH circularly polarized emissions are beamed to the magnetic latitude from the

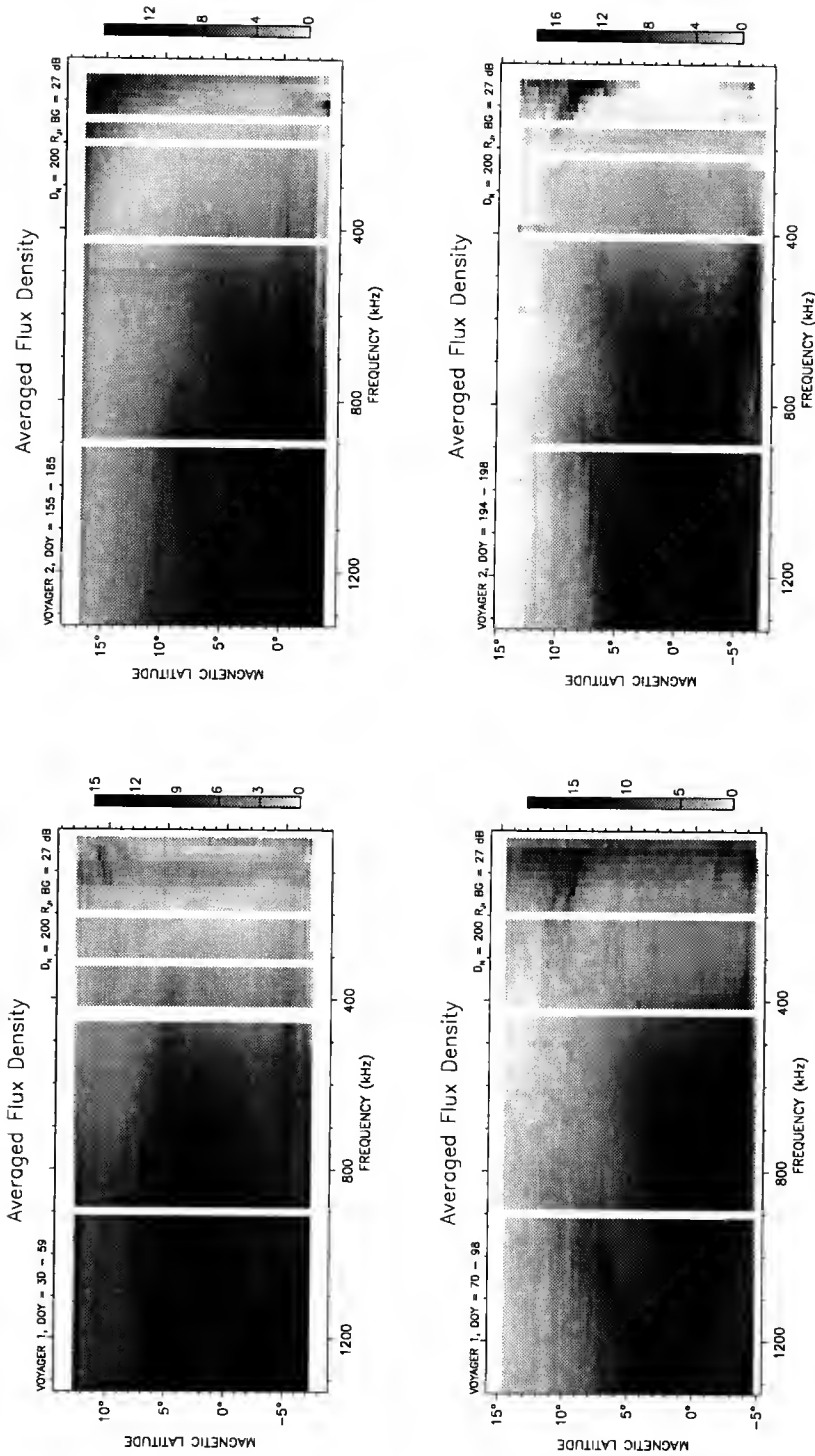


Figure 4.6. The averaged total flux density as a function of the emission frequency and the magnetic latitude of the spacecraft. The upper panels are for before encounter observations, while the lower panels are for after encounter observations. The darkness in each panel represents the intensity above the background (BG) level in a logarithmic scale shown in the scale bar in units of dB.



post-encounter observations. I made similar calculations, shown in Figure 4.7, of occurrence probabilities for the LH and RH components from after encounter data of Voyager 1 (left panels) and Voyager 2 (right panels). These calculations once again show that radiation at different frequencies is beamed in different magnetic latitudes. The most obvious feature shown in such calculations is that for RH (LH) components, radiation is beamed toward lower (higher) magnetic latitudes as the frequency goes down. Such a shifting feature is not caused by the lane feature as described by *Green et al.* [1992]. This is quite a surprising feature that has never been investigated or reported before, quite contrary to what would be expected by the traditional source modelings, especially when the role of the Io plasma torus for reshaping the beaming of the HOM emission is considered to be appreciable. It is generally believed that the HOM emission originates from high magnetic latitude regions in both (magnetic) hemispheres, propagating in the R-X mode [*Carr and Wang*, 1989; *Ladreiter and Leblanc*, 1989; *Ladreiter*, 1990]. It was suggested that the propagation path of the HOM emission is altered heavily due to the presence of the Io plasma torus [*Ladreiter and Leblanc*, 1989, 1990a, 1990b; *Barrow*, 1991]. However, if this were true, one would expect that RH (LH) polarized component from the northern (southern) hemisphere would be refracted by the Io torus, and the result of this would be that the HOM beaming would be shifted to a higher (lower) magnetic latitude for lower frequencies.

To investigate the magnetic latitudinal beaming of the HOM emission further, I calculated the occurrence probability, as a function of magnetic latitude and frequency, for both RH and LH components of the HOM emission by using only the data taken while the spacecraft's magnetic latitude was increasing and decreasing, respectively. In other words, I investigated the magnetic latitudinal beaming in two longitudinal regions separately in which the spacecraft's magnetic latitude is monotonically increasing or decreasing. I refer to these two longitudinal regions as region

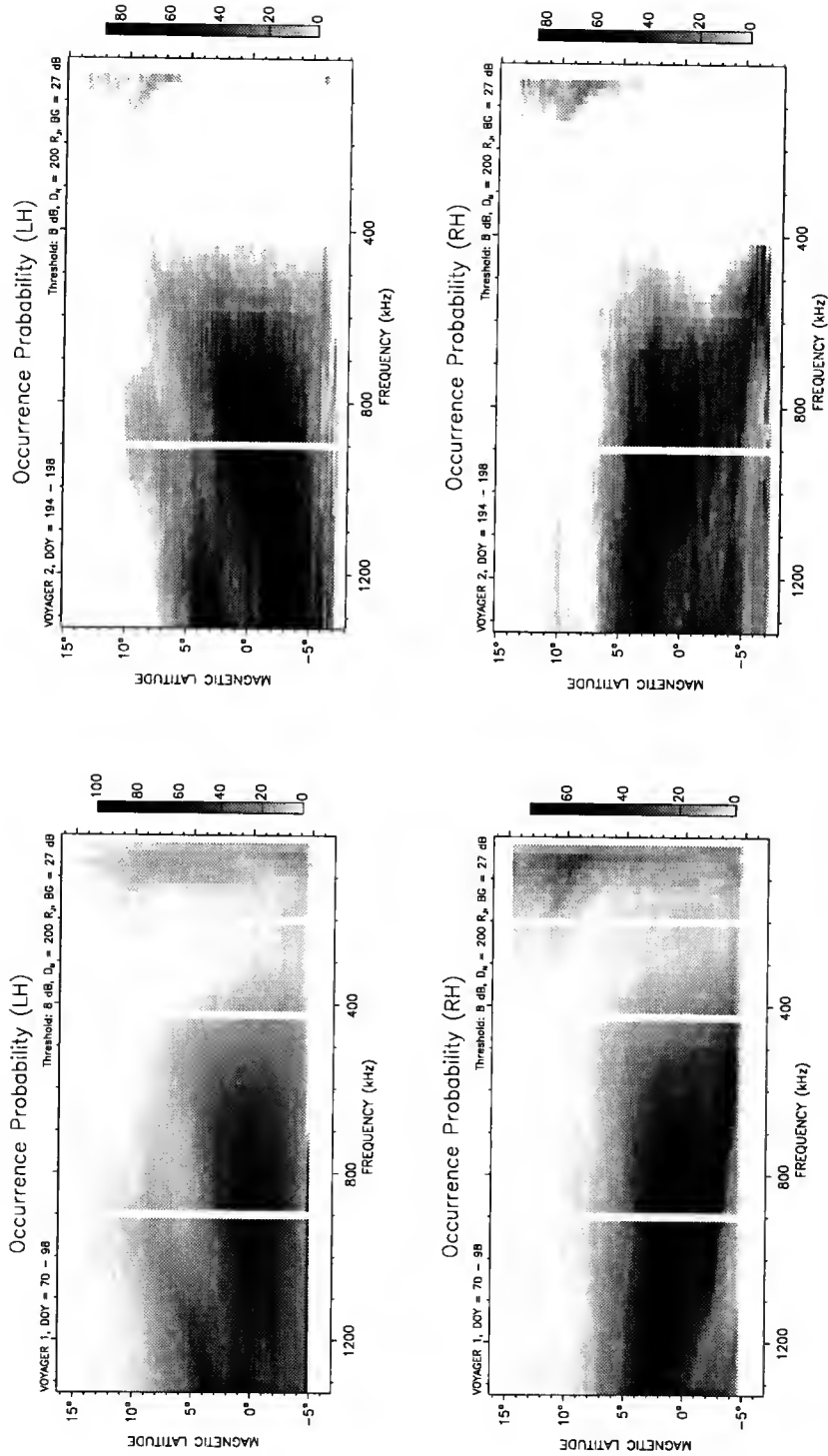


Figure 4.7. Occurrence probability, represented with the darkness at the scale shown in the scale bar, as a function of the emission frequency and the magnetic latitude of the spacecraft calculated from post encounter data of Voyager 1 (left panels) and Voyager 2 (right panels) for LH components (upper panels) and RH components (lower panels).

“I” (for increasing magnetic latitude) and region “D” (for decreasing magnetic latitude), respectively. The CML range for the “I” region is  $22^\circ \sim 202^\circ$ , and is  $202^\circ \sim 22^\circ$  for the “D” region. The results are shown in Figure 4.8 for the “I” region and in Figure 4.9 for the “D” region. Figures 4.8 and 4.9 reveal several features of the HOM emission. The occurrence probability of HOM emission is higher for the “D” region than for the “I” region. The LH component of the HOM emission is beamed roughly at a constant magnetic latitude in the “I” region, although the shifting feature still is obvious. The beam shifting is most obvious for the “D” region, in which the RH (LH) beam is shifted toward lower (higher) magnetic latitude. The beaming width is wider for Voyager 2 than for Voyager 1. The lanes that “interrupt” the HOM beam appear to have a steeper slope for the “D” region than for the “I” region. It is also obvious, especially for emission at lower frequencies, that the RH component is beamed considerably to a lower latitude in the “D” region than in the “I” region. For example, the RH component at 500 kHz is beamed to a magnetic latitude as low as  $-6^\circ$ , while that at 1 MHz is beamed to  $0^\circ$ . For the LH component, emission at 1 MHz is beamed to about  $-2^\circ$ , while that at 700 kHz is beamed to about  $1^\circ$ . Different magnetic beamings at different frequencies in different regions may be an indication of a distorted beam pattern or a curved magnetic equator. The existence of the Io plasma torus usually leads to an anticipation that the HOM emission would be affected differently at different frequencies (such effect is greater the lower the frequency). The fact that the presumed R-X mode emission from the northern (southern) hemisphere is beamed more southward (northward) seems to contradict the role of the Io plasma torus on altering paths of the HOM emission. There are two possible ways for this to happen: (1) the HOM emission does not go through the dense part of the torus on its way out; or (2) the plasma torus is not as dense as has been reported, so that it does not have too much refraction effect on the HOM emission. No evidence was found in the Voyager and Ulysses observations to support the idea that the Io torus would be

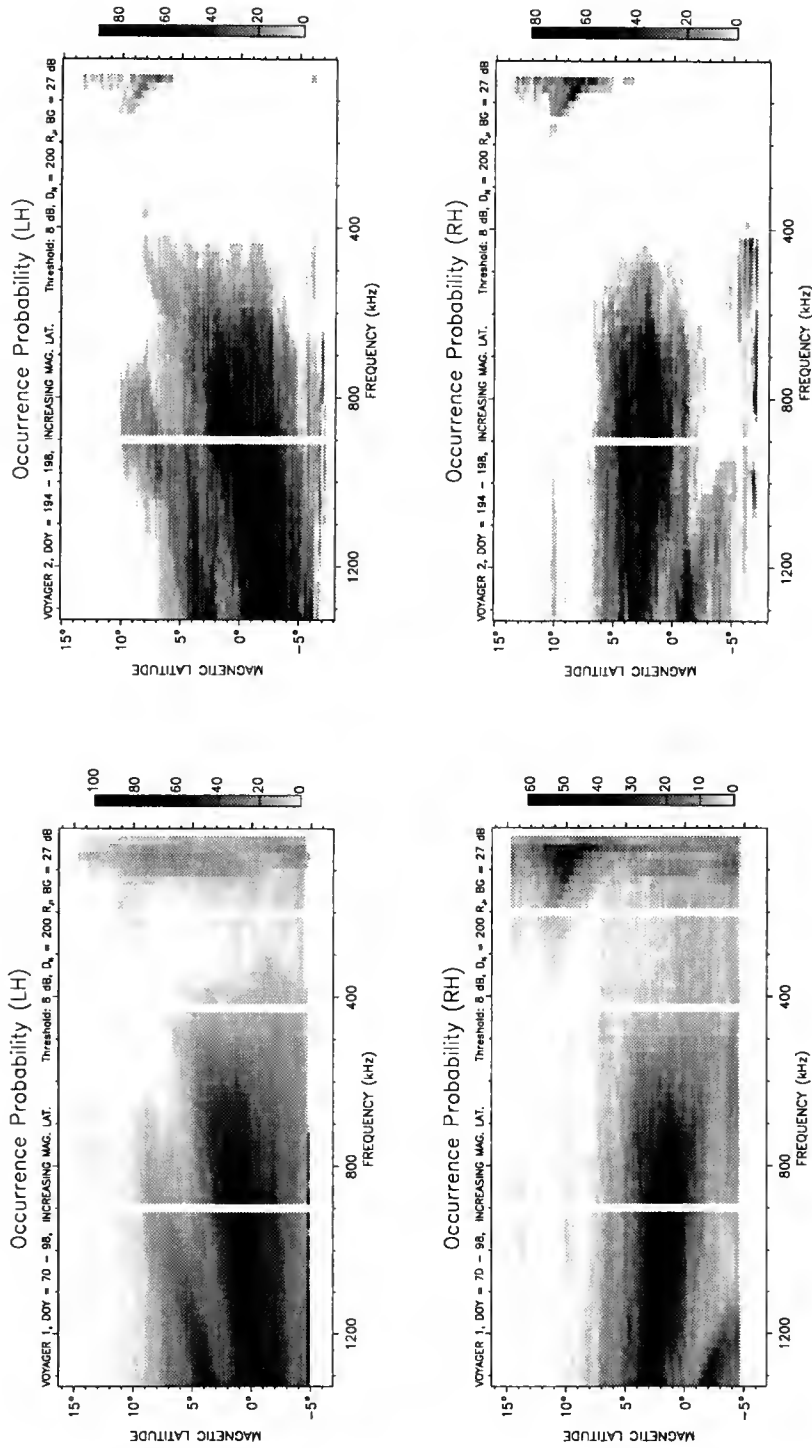


Figure 4.8. Occurrence probability, represented with the darkness at the scale shown in the scale bar, of both the LH and RH polarization components calculated as a function of the magnetic latitude of the spacecraft and the emission frequency from post encounter observations by Voyager 1 (left panels) and Voyager 2 (right panels). Only data points in the “I” region are included for which the spacecraft’s magnetic latitude is increasing.

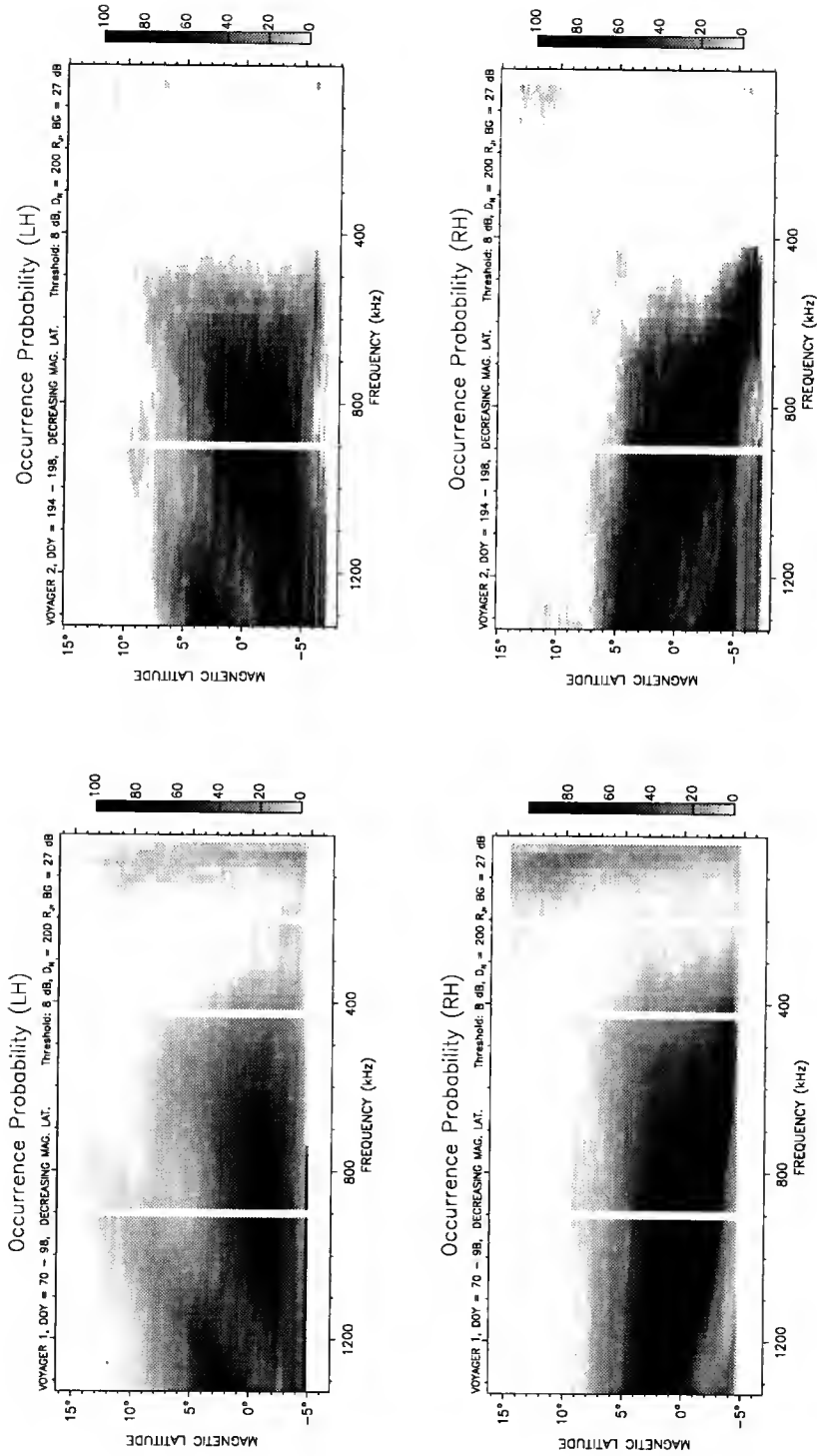


Figure 4.9. Occurrence probability, represented with the darkness at the scale shown in the scale bar, of both the LH and RH polarization components calculated as a function of magnetic latitude of the spacecraft and the emission frequency from post encounter observations by Voyager 1 (left panels) and Voyager 2 (right panels). Only data points in the “D” region are included for which the spacecraft’s magnetic latitude is decreasing.

so dense. The only plausible explanation is therefore that the HOM emission does not propagate deep inside the Io torus.

#### 4.1.4 Polarization

The polarization status of radio emissions is of great importance in revealing physical processes involved in wave generation and propagation. The only polarization measurements of Jupiter's radiation below 2 MHz are those of the Voyager PRA experiment and the recent Ulysses URAP experiment. As has been described in Chapter 2, the Voyager receiver was designed only to provide two intensity measurements on each frequency channel, which would be the RH and LH circularly polarized intensity components if the source lay on the antenna axis.

The only unambiguous polarization information provided by the Voyager PRA receiver is the polarization sense (*i.e.*, whether the RH or LH circular component is the larger one) because the RH and LH outputs were contaminated by the unwanted coupling between the two monopoles due to the interference effect of the spacecraft structures. In addition, Jupiter was never in a direction perpendicular to the antenna plane during the whole encounter period. Polarization of the HOM emission observed by Voyager was investigated previously by *Warwick et al.* [1979*a*, 1979*b*], *Alexander et al.* [1981], and *Ladreiter and Leblanc* [1989]. Their work was all based on the apparent polarization calculated from the LH and RH outputs without taking actual antenna response into account. *Lecacheux and Ortega-Molina* [1987] and *Ortega-Molina and Lecacheux* [1990, 1991] studied, based on an early calibration results of *Ortega-Molina and Daigne* [1984], the polarization properties of the Jovian HOM emission observed by the PRA experiment. They showed that the apparent degree of circular polarization measured by the PRA instrument is the result of fluctuations in the relative intensities of the two HOM circular components, and therefore they

concluded that the complex morphology of the HOM emission can be explained by simultaneous radiation from two independent, oppositely circularly polarized sources with 100% polarization degree. Linear polarization in HOM was found to be extremely rare; the maximum percentage of linear polarization was less than 10%. Observations from the Ulysses URAP experiment, which is capable of measuring all four Stokes parameters, also confirmed that the linear polarization component is insignificant in the HOM emission [Reiner *et al.*, 1993a].

In this section, I will make a new determination of average polarization sense, taking into account the newly calibrated antenna response (see Chapter 2). For each set of the PRA data taken at a given time, Jupiter's directions with respect to the spacecraft at that moment will be calculated. According to *Ortega-Molina and Lecacheux* [1990, 1991], once the direction angle of Jupiter (and hence the HOM source) relative to the E-plane (front side or back side) is calculated, the normalized Stokes parameters of the antenna system,  $q, u, v$ , can be deduced:

$$q = \frac{q_{\perp} + a}{1 + q_{\perp} a} \quad u = \frac{v_{\perp} b}{1 + q_{\perp} a} \quad v = \frac{v_{\perp} c}{1 + q_{\perp} a}, \quad (4.1)$$

where

$$q_{\perp} = \frac{\sin^2 \Theta}{1 + \cos^2 \Theta} \quad u_{\perp} = 0 \quad v_{\perp} = \frac{2 \cos \Theta}{1 + \cos^2 \Theta} \quad (4.2)$$

are the Stokes parameters of an orthogonal dipole antenna system, and

$$a = \cos \alpha \sin 2\Theta \quad b = \cos \alpha \cos 2\Theta \quad c = \sin \alpha, \quad (4.3)$$

$\alpha$  is the opening angle of the equivalent dipole. The apparent total intensity  $S_{app}$  and degree of circular polarization  $V_{app}$  can be obtained:

$$S_{app} = I_L + I_R = s S (1 + qQ + uU), \quad (4.4)$$

$$V_{app} = \frac{I_L - I_R}{I_L + I_R} = \frac{vV}{1 + qQ + uU}. \quad (4.5)$$

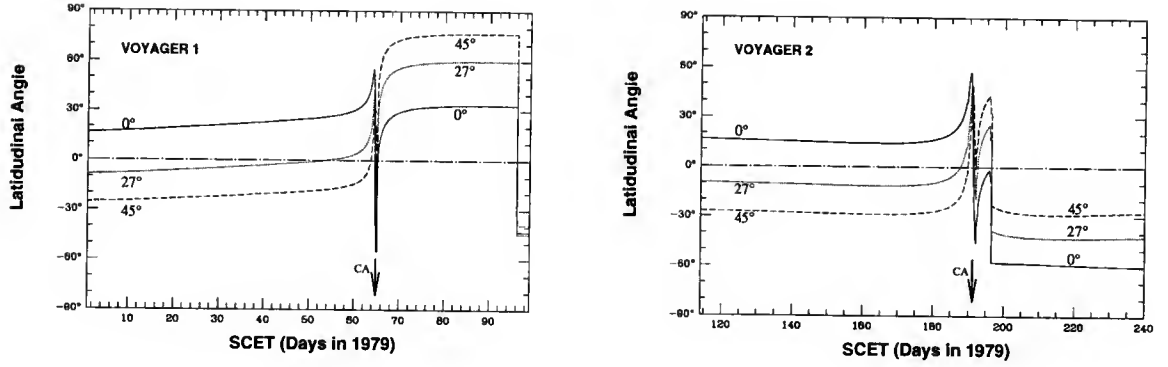


Figure 4.10. Jupiter's latitudinal angles as a function of spacecraft event time (SCET), seen from the Voyager spacecraft with respect to the monopole plane (solid line), front-side E-plane (dotted curve), and back-side E-plane (dashed curve). Left panel and right panel are for Voyager 1 and Voyager 2, respectively.

where  $(S, SQ, SU, SV)$  are the Stokes parameters of the incoming wave. Consequently, two incoherent circular components and their relative intensities can be separated:

$$\left. \begin{aligned} S_A &= \frac{(v+1)I_L + (v-1)I_R}{2sv} \\ S_B &= \frac{(v-1)I_L + (v+1)I_R}{2sv} \end{aligned} \right\}, \quad (4.6)$$

where  $S_A$  and  $S_B$  are the true intensities of the two incoherent circularly polarized sources;  $I_L$  and  $I_R$  are the apparent left- and right-circular intensity components of the receiver, and  $s = \sqrt{q^2 + u^2 + v^2}$ . When the antenna-source geometry is such that  $|v| \lesssim 1$ , the apparent left and right intensity levels ( $I_L$  and  $I_R$ ) will be proportional to the true intensities of two left- and right-handed circularly polarized sources ( $S_A$  and  $S_B$ ). Formulation of calculating the  $\Theta$  value of a radio source or planet center at any given time based on the *Supplementary Experimental Data Record* (SEDR) is presented in Appendix C. Shown in Figure 4.10 are the latitudinal angles of Jupiter's center, measured from the E-plane (see Chapter 2) tilted  $0^\circ$ ,  $27^\circ$  and  $45^\circ$  from the monopole plane, as a function of Spacecraft Event Time (SCET). Short-time variations of the spacecraft's position and orientation were not included in the figure. The



solid curves (for  $0^\circ$ ) are therefore Jupiter's latitude relative to the monopole plane, dotted (for  $27^\circ$ ) and dashed (for  $45^\circ$ ) curves are Jupiter's latitude relative to the E-plane when Jupiter is seen from the spacecraft in the front side and in the back side, respectively. Before their encounters with Jupiter, both Voyagers saw Jupiter to be on their front side (with azimuthal angles of about  $25^\circ$  and  $27^\circ$  respectively) and they were oriented such that Jupiter (and therefore all radio sources) was actually quite close to the direction of null-polarization response, which led to a poor PRA sensitivity to the circular polarization ( $v \sim 0$  and therefore  $|S_A| \approx |S_B|$ ). Calculations of polarization ratio (referred to as PR hereafter) for pre-encounter data would be very questionable. After encounter with Jupiter, both Voyagers were in an orientation which led to a very good PRA sensitivity ( $|v| \lesssim 1$ ). Thus only calculations of PR for the post encounter period are meaningful. Also note that after its encounter with Jupiter, Voyager 2 was oriented such that Jupiter was seen below the E-plane (*i.e.*,  $v < 0$ ), which means that the polarization sense detected after encounter was false and opposite to the true polarization sense. Taking into account the PRA antenna's actual response to circularly polarized incoming radio waves, I plotted in Figure 4.11 the apparent PR for both Voyagers before and after encounters with Jupiter for the same periods as those shown in Figure 4.3 (on page 47) for the total intensity plots. The apparent PR (*i.e.*, the apparent degree of circular polarization) is defined by  $(I_L - I_R)/(I_L + I_R)$ . Since the LH and RH intensity measurements made by the PRA instrument were recorded in a logarithmic scale, uncertainties can be introduced when calculating the PR for weak intensity readings. To minimize such uncertainty, only data points that exceed a certain threshold level (5 dB for plots shown in Figure 4.11) above the background are used in the PR calculation. Clearly, the PR is poorly determined before encounter because during such time Jupiter was quite close to (the front side of) the E-plane, and both intensity components are almost the same. It

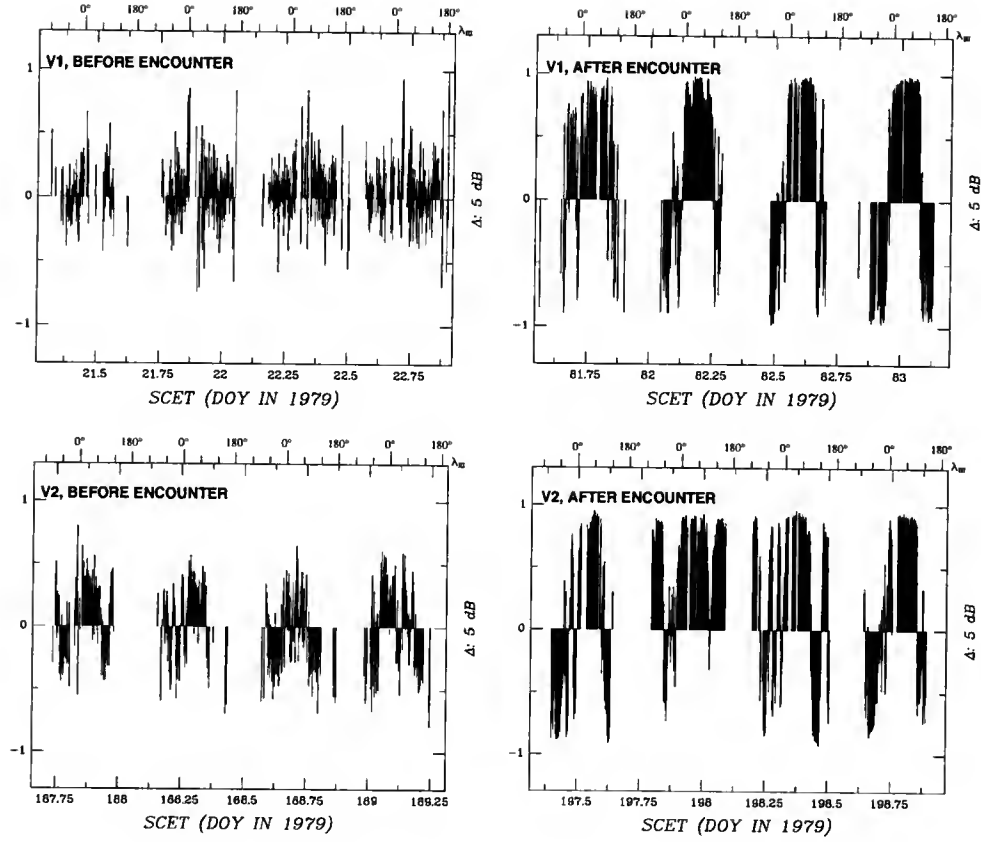


Figure 4.11. Plots of apparent polarization ratio at 1 MHz as a function of spacecraft event time (SCET) in units of day of year (DOY) for data from Voyager 1 and 2 before and after encounter, for four consecutive rotations each.

is evident, however, that the LH polarized radiation (with positive PR) was dominant when Voyager was at its lowest magnetic latitude (close to  $22^\circ$  CML), and the RH polarized radiation (with negative PR) became dominant when Voyager got into the northern magnetic hemisphere. After encounters, both Voyagers were in favorite orientations for the PR measurement ( $|v| \lesssim 1$ ). It is evident (see Figures 4.3 and 4.11) that intensities of the two polarization components have a similar global profile and occurrence appearance. However, any correlation of the detailed structures of the spectral patterns are not apparent. This is an indication of the presence of two independent, oppositely polarized sources.

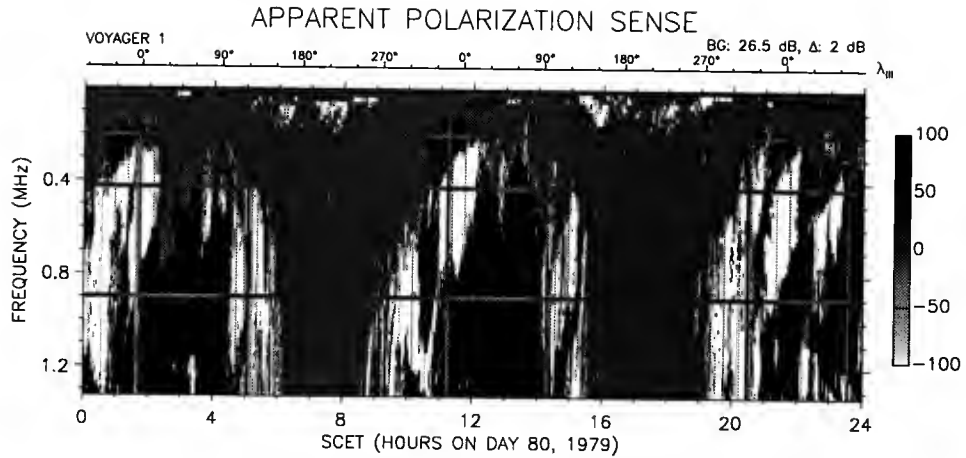


Figure 4.12. Polarization sense as a function of frequency and SCET during the same period of time for Figure 4.2. Black, white and grey features correspond respectively to the left-handed, right handed and unpolarized (or no) emissions.

To see the polarization pattern for all frequency channels of the low-frequency band receivers, I present in Figure 4.12 the calculation of the polarization sense (sign of PR) as functions of frequency and SCET for Voyager 1 during the same period of time as in Figure 4.2 of the dynamic spectral plot. Black, white and grey features correspond to RH polarized, LH polarized and unpolarized (or no) emissions, respectively. This figure shows a great complexity with alternating left and right circular polarizations at a time scale of hours. Apparently, as has been shown in Figure 4.11, the polarization is, in the entire HOM frequency range, predominantly right hand at the beginning and end of a HOM storm and predominantly left hand when the spacecraft is near  $30^\circ$  CML, *i.e.*, when the spacecraft reaches its lowest magnetic latitude. There is often an abrupt reversal of the observed circular polarization when the spacecraft crosses the magnetic equator. From the intensity profiles of both LH and RH components (Figure 4.3) it is clearly seen that the polarization pattern depends on the relative strengths of the RH and LH emissions. It can be expected that when the spacecraft is in the northern magnetic hemisphere it receives stronger emission

originating from the northern hemisphere; likewise, it receives stronger emission originating from the southern hemisphere when it is in the southern magnetic hemisphere. The polarization profile of the HOM emission suggests that the majority of the HOM emission is in the R-X mode originating from both hemispheres.

#### 4.1.5 Solar Wind Control

It is well known that the solar wind strongly affects planetary radio emissions, such as the auroral kilometric radiation (AKR) from Earth [*Gallagher and D'Angleo*, 1981], the Saturnian kilometric radiation (SKR) [*Desch*, 1982; *Desch and Rucker*, 1983], and the DAM and HOM from Jupiter [*Desch and Barrow*, 1984; *Rabl et al.*, 1990]. In the case of HOM, it was found that the arrival of high density solar wind streams at Jupiter can enhance the HOM energy output, activate low frequency HOM sources located at  $6\sim 7 R_J$ , and widen the HOM beam to higher magnetic northern latitudes and possibly to higher magnetic southern latitudes.

The linear cross correlation between the HOM energy and the fluctuations of the solar wind density and velocity at Jupiter was investigated by *Desch and Barrow* [1984]. They found significant correlation only between variations in the HOM energy and the solar wind density; the solar wind velocity did not seem to correlate with the HOM energy output. The solar wind influence on the HOM emission indicates that the solar wind particles must have direct or indirect access to the HOM source region. There are two ways that the solar wind particles can enter the Jovian magnetosphere, one is from the tail region, and the other from the two cusp regions near the magnetic poles. When modeling the HOM emissions, the solar wind influence must be taken into consideration.

#### 4.1.6 Propagation Effect from the Io Plasma Torus

It is well known that the Jovian satellite Io has a tremendous influence on Jupiter's DAM emissions, whose sources have been identified as Io-A, Io-B, and Io-C, etc. (see, e.g., *Carr et al.* [1983]). No evidence was found for Io itself to control Jupiter's activity below 1300 kHz from the RAE-1 observation [*Desch and Carr*, 1978] nor from the Voyager PRA observation [*Kaiser et al.*, 1979]. One aspect of the uniqueness of the Jovian magnetosphere is the existence of the Io plasma torus in which the (electron) plasma frequency was reported to be as high as 500 kHz from the Voyager 1 observation [*Bagenal et al.*, 1980; *Divine and Garrett*, 1983; *Bagenal et al.*, 1985]. This plasma torus could undoubtedly affect the observed radiation by refracting those rays that must pass through it. The amount of this refraction is greater the lower the frequency. In the case of the Voyager HOM observations, if the HOM sources are in a high Jovigraphic latitude auroral region, some of the rays can indeed pass through a part of the torus, although not through the densest central part, before they reach the observer. If the HOM sources are in a low Jovigraphic latitude region (for example close to the magnetic equator), radiation from those sources would definitely have to pass through the torus to reach the distant observer near the equator. In this case, radio waves would be subject to strong refraction or reflection by the torus, depending on the actual electron density distribution in the torus. Ray paths at a given frequency can be modeled by using a ray-tracing computer program if a source location and an electron density distribution are assumed. One of the objectives of this study is to determine, using the raytracing techniques, the lowest HOM frequency at which we can neglect refraction altogether. At frequencies lower than this, an HOM emission model should include raytracing calculations to account for the HOM source locations and radiation beaming patterns. The propagation of the HOM emission

as a whole may be affected by the Io torus (see page 52). The detailed modeling including the Io torus effect will be investigated in Chapter 5.

## 4.2 Emission Mechanisms

The purpose of studying radio emissions from the magnetospheres of planets is to understand the relevant physical emission processes and conditions at these planets. Radiative energy is produced in plasma by the action of any of several types of emission mechanisms. If this radiation can propagate to reach the observer, information about the physical processes, energy exchange, and plasma environment can be obtained in a coded way. The high intensities, limited bandwidths, short time scales, and sporadic nature of the low-frequency radio emissions indicate that they are due to stimulated emission from plasma micro-instabilities. The remarkable repeatability of many of the decameter, hectometer, and kilometer wavelength spectra implies a long term stability of at least some of the plasma parameters. The variations in intensity and frequency band reflect the changes of the propagation characteristics of the medium and/or physical processes that are involved in generating the free energy. The repeatability of the DAM, HOM and KOM spectra suggests that the wave frequencies are related to the characteristic frequencies of the plasma. Among all characteristic frequencies, only the electron cyclotron frequency and the upper-hybrid frequency appear to be directly related to the observed spectra. This leads to the expectation that the maximum frequency of the Io controlled DAM (39.5 MHz) corresponds to the maximum magnetic field at the foot of the Io flux tube. The strength of that magnetic field was inferred from the Pioneer 11 observations [*Smith et al.*, 1976; *Acuña and Ness*, 1976] to be approximately 14 gauss in the northern hemisphere. All radio waves observed so far are of the *high frequency* type in the

sense that they appear at frequencies higher than the local electron cyclotron frequency at the source. According to *Stix* [1962], there are two high frequency normal modes in a magnetized plasma: the ordinary (O) mode and the extraordinary (X) mode. The X mode consists of two branches separated by a stop band where the electromagnetic wave becomes evanescent and cannot propagate. In the low frequency side of the stop band is the slow mode for which the phase velocity is less than the velocity of light; in the high frequency side, on the other hand, is the fast mode for which the phase velocity is greater than the velocity of light. Far from a planet that emits radio radiation, the observed radiation must be in either the fast X mode or the O mode. Observations from Jupiter, Uranus, and Neptune indicate that most radio emissions are in the X mode. Theories of radio emission mechanisms address how the plasma distribution is modified so that its free energy is converted with adequate efficiency into the electromagnetic waves near the local electron cyclotron frequency, and how this radiation propagates through the intervening plasma to a distant observer. Such theories are distinguished by whether they depend on direct or indirect emission processes.

#### 4.2.1 The CMI Theory

Since the discovery of radio emissions from planets with magnetic fields, many theories have been proposed and developed to explain possible mechanisms and processes involved in the generation of the planetary radio emissions. Among those theories, the cyclotron maser instability (CMI) theory proposed by *Wu and Lee* [1979] has gained significant popularity and proved to be the most promising one. The CMI theory was developed to explain the generation mechanism of the auroral kilometric radiation (AKR, also called the terrestrial kilometric radiation or TKR) from Earth, and has been applied to the generation mechanism of radio emissions from other

planets. According to the theory, the emission mechanism of the AKR is attributed to a maser effect associated with the trapped energetic electrons which originate in the plasma sheet during a substorm. The free energy of the electrons is transferred to electromagnetic waves via a relativistic normal Doppler resonance process. Specifically, it is assumed that the energetic electron distribution function contains more free energy in velocity components perpendicular to the magnetic field than in those parallel to the magnetic field. *Wu and Lee* [1979] showed that a kinetic instability exists when the population of suprathermal electrons possess a loss-cone distribution function; such an instability can lead to the direct amplification of the extraordinary and ordinary mode radiation. The loss-cone distribution function results from the fact that injected electrons (from the plasma sheet) travel downward along the convergent magnetic field lines, those with sufficiently small pitch angles can precipitate into the upper atmosphere and therefore are lost (by collision with atmospheric particles); those with pitch angles outside the atmospheric loss cone will be reflected at their mirror points. It is found that those ascending electrons (due to the reflection at mirror points) play a decisive role in the amplification of electromagnetic waves which can propagate (or escape) from Earth. Although radiation in both the X and O modes can be generated, the CMI theory predicts that the X-mode radiation prevails over the O-mode radiation [*Lee and Wu*, 1980]. The growth rate of the emission is found to be related with the angle  $\vartheta$  of the wave normal with respect to the magnetic field direction; it reaches a maximum when  $\vartheta$  is at some large value, leading to a hollow cone of emission and the radiation is confined to the edges. Later work on CMI theory [*Wong et al.*, 1982; *Wu et al.*, 1982] shows that the angle  $\vartheta$  at the source is a strong function of both the ratio of the electron plasma frequency ( $f_p$ ) to the cyclotron frequency ( $f_c$ ), and the ratio of the energetic electron density ( $n_e$ ) to the background electron density ( $n_b$ ). Radiation triggered by the loss-cone distribution will propagate upward and escape into free space. However, *Le Quéau et al.* [1984a,



1984b] showed that such initially propagating waves would be heavily damped when penetrating regions of decreasing magnetic field, while initially downward propagating waves, on the other hand, can be amplified till they are reflected as a consequence of the increasing magnetic field, eventually travelling upward and escaping the magnetosphere. Beside the loss-cone instability, there can be other types of instabilities which also lead to freely escaping emissions. The hole-like electron distribution function is an example of such instability; it is caused by the accelerated down-going electrons and trapped electrons, which are suggested to be trapped throughout a time-varying (or space-varying) parallel electric field [Luoarn *et al.*, 1989], near the  $v_{\perp}$  axis in the  $(v_{\parallel}, v_{\perp})$  space. The AKR is believed to be excited by the loss-cone and hole-like feature instabilities.

#### 4.2.2 Indirect Emission Mechanisms

The CMI mechanism described above is a type of direct emission mechanism, *i.e.*, the electromagnetic waves are generated directly by the interaction of particles with the magnetosphere.

It has been suggested, however, that the Jovian decametric radiation can arise from indirect processes where the energetic electrons first excite electrostatic waves, which then combine to produce the observed electromagnetic radiation. The indirect emission mechanisms start with an assumption that the distribution function of energetic electrons is essentially that of a beam; the excess free energy is parallel to the magnetic field. Roux and Pellat [1979] suggested that both upper- and lower-hybrid waves can be excited by beam driven instabilities, which in turn could couple to produce the electromagnetic radiation. In the Jovian magnetosphere, where  $f_p/f_c \ll 1$ , the coupling  $f \simeq f_{\text{LHR}} + f_{\text{UHR}}$  can produce radiation above  $f_{R=0}$ , the right hand cut-off frequency, thus giving a freely escaping electromagnetic wave with a frequency close

to the local gyrofrequency. It is not yet clear which of these somewhat contradictory mechanisms produces the observed low frequency magnetospheric emissions. At the present time, however, the *Wu and Lee* [1979] theory is the most popular.

### 4.3 Modeling

I have described characteristics of the Jovian HOM emission, mostly based on the Voyager PRA observations. The fact that the HOM emission is strongly modulated as the planet rotates suggests that the radiation is beamed in a way that only when such beam is aligned with the observer can the radiation be received. This is usually depicted as a rotating lighthouse or searchlight beam. Depending on the Jovigraphic latitude of the observer, the HOM emission can be received twice (or once) during each rotation of Jupiter. In this section, I will first briefly discuss some equatorial beaming models that were proposed in the literature and show the difficulties that those models face. I will describe in detail a beaming model that can account for the beaming effects. The key point for a successful model is that it should be able to simulate the intensity variations observed by the two Voyagers, namely the two radiation peaks near the CML of  $330^\circ$  and  $90^\circ$ , and a true wide gap around  $200^\circ$  CML, and a narrow gap around  $30^\circ$  CML.

#### 4.3.1 Equatorial Beaming Models

By comparing observations from four spacecraft (RAE-1, IMP-6, Voyager 1 and Voyager 2), which covered Jovigraphic latitudes from  $-3.2^\circ$  to  $6.5^\circ$ , *Alexander et al.* [1979] first pointed out that a magnetic latitudinal beaming pattern could very well account for HOM emission behavior. Although they did not provide any proposal or hypothesis regarding the HOM source location and mechanism of generation of the HOM emission that can form such a beaming pattern, they concluded that the HOM

emission is confined in a curved thin sheet with a thickness of about  $10^\circ$  centered at a constant magnetic latitude of  $2^\circ \sim 4^\circ$  north of the magnetic equator at about  $2R_J$ .

One of the attempts to model such an equatorial beaming pattern was made by *Ladreitner and Leblanc* [1989, 1990b] who used the raytracing technique to locate the HOM source(s) and tried to simulate the HOM beam. According to them, the equatorial beam of the HOM emission was formed by the HOM sources distributed all over the longitudinal region around an auroral zone, each of the source points emits radiation in the hollow cone fashion. By adjusting the source location and the beaming cone angle, they argued that the combination of all such beaming cones would produce an equatorial beam with about  $10^\circ$  thickness and centered at about  $+3^\circ$  magnetic latitude, as proposed by *Alexander et al.* [1979]. If one closely studies the latitudinal profile produced in such manner, one can indeed see at least one maximum close to the magnetic equator that is formed by the contribution from equatorial edges of all beaming cones. What is ignored in both the Ladreitner and Leblanc model (referred to as the LL model hereafter) and a more qualitative model by *Barrow* [1991] is the contribution from overlaps of side edges of all beaming cones. It will be shown following that side edges of beaming cones of all sources can make up to 50% of contribution to the received radiation. Such a side-edge contribution was subtracted as a background noise in the LL model, for which they did not give any justification. To demonstrate how significant the side-edge contribution can be, let us assume, as the LL model suggests, that the HOM sources are distributed on a certain  $L$ -shell ( $\sim 20$ ) along all (magnetic) longitudes around the auroral zone (in either the northern or the southern hemisphere, depending on the polarization component being concerned). The continuously distributed source can be replaced by an arbitrary number of point sources (or sub-sources). Each subsource emits radiation and the radiation is beamed into a hollow cone with a half-angle of  $\beta_0$  and thickness of  $\Delta\beta$ . The normalized beam pattern is given by Equation (4.7). Radiation

from all subsources received by an observer at a given magnetic latitude are incoherent and are summed together to yield the final intensity for each latitude position of the observer. Once the received intensity for an observer at a broad range of latitudes is calculated, an intensity profile as a function of magnetic latitude is obtained and normalized to the peak intensity values. The latitudinal intensity profile so calculated is shown in Figure 4.13 for the emission at 1 MHz located at  $L = 20$ . The cone half angles ( $\beta_0$ ) for each subsurface are assumed to be identical and are adjusted so that a maximum is formed near  $3^\circ$  magnetic latitude. In panels (a) and (b), the HOM source is approximated by 360 point sources distributed uniformly on the  $L = 20$  shell along the magnetic longitude all over the auroral zone and the beam thickness,  $\Delta\beta$ , is assumed to be  $5^\circ$  and  $1^\circ$ , respectively; while in panels (c) and (d) the number of subsources are reduced to 25 for emissions at  $f = 1$  MHz and  $f = 500$  kHz for the same beam thickness. In order to make an intensity profile with a maximum near the magnetic equator which is independent of observer's longitude, the number of subsources must be large enough. Only 9 subsources were used in the LL model used to simulate the assumed continuously distributed HOM sources. One can see clearly from Figure 4.13 that contributions from side edges of emission cones of subsources can be 50% that of the equatorial edges and therefore cannot be ignored in the equatorial beaming model suggested by Ladreiter and Leblanc.

Even when the wall of the emission cone is very thin ( $1^\circ$  shown in Figure 4.13b), the side edge contribution is still more than 20% that of the peak value of the equatorial beam (however, the resultant beam width of  $5^\circ$  is too narrow to account for the HOM beam). One of the strong arguments made by *Ladreiter and Leblanc* [1989, 1990b] with regard to the HOM source locations is that the HOM emission was also detected near the CML region of  $200^\circ$  where the wide gap usually occurs, when Voyager was very close to Jupiter and was at lower Jovigraphic latitudes. The wide gap occurred, as suggested in the LL model, when the observer was too far away

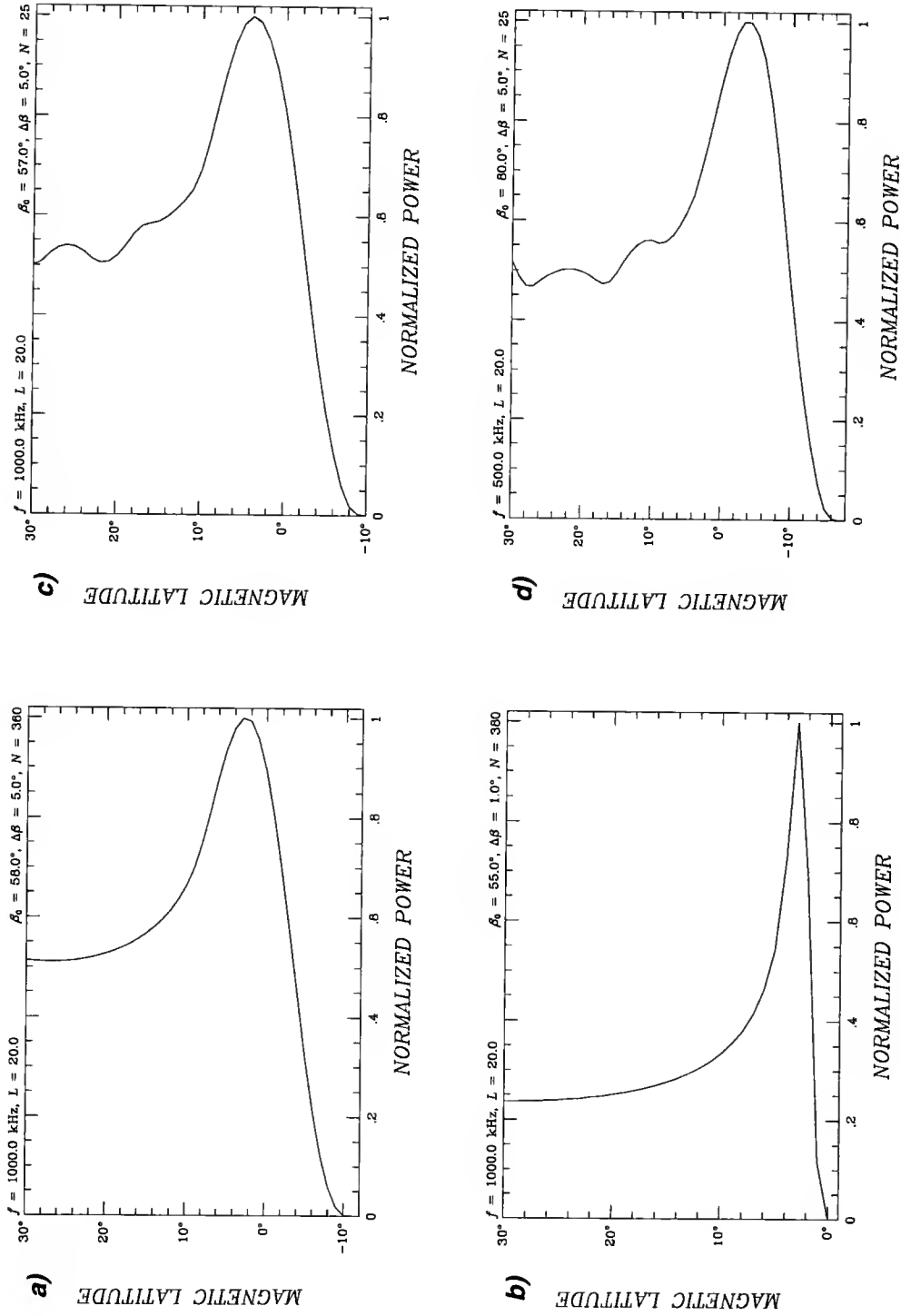


Figure 4.13. Magnetic latitude intensity profiles formed by a number of subsources distributed on a given  $L$ -shell along all magnetic longitudes over the auroral zone. Wave frequency ( $f$ ),  $L$  shell number, half-angle of the hollow cone ( $\beta_0$ ), beam thickness ( $\Delta\beta$ ), and number of subsources used ( $N$ ) are indicated on the top of each panel.

from the source such that the intensity of the radiation arrived at the receiver had dropped below the detectable limit of the receiver. There is no doubt that very weak emissions could not be detected by the Voyager PRA experiment until the spacecraft was very close to Jupiter. However, the peak intensity values obtained near  $330^\circ$  and  $90^\circ$  CML just four or five rotations before and after the closest approach are at least 15 dB above the background level, while the intensity readings near the wide gap region centered at  $200^\circ$  CML are virtually the same as that of the background level. In other words, the intensity values near the two peaks are at least 30 times stronger than that which would have been detected near  $200^\circ$  CML. If the equatorial beaming model of Ladreiter and Leblanc were correct, the intensity readings of the Voyager PRA receiver near  $200^\circ$  CML would have been much higher than that of the background level due to contributions from side edges of subsources. Furthermore, recent observations made by the URAP experiment on board Ulysses also indicate a true gap near  $200^\circ$  CML [*Lecacheux et al.*, 1992b]. The fact that the URAP receiver is at least one order of magnitude more sensitive than that of PRA's strongly suggests that the gap at  $200^\circ$  is a true one.

Another strong argument which does not favor the LL equatorial model is that there is no clear mechanism that would make the HOM emission at *all* frequencies (from 300 kHz up to 7 or 8 MHz) from high latitude region to be all beamed parallel to the magnetic equator. Since the HOM emission is believed to originate from the place close to the local electron cyclotron frequency, the source radial distances and the magnetic field directions at the sources are very different for different frequencies. It is hard to imagine that the beaming geometry is set so coincidentally that radiation at different frequencies would eventually be in the same latitudinal direction. It will be demonstrated with the raytracing technique in the next chapter that the presence of the Io plasma torus does not play this magic role either.

I have demonstrated above that the proposed equatorial beaming pattern cannot be constructed by simply overlaying emission hollow cones from subsources located in not-so-large  $L$ -shells ( $L < 30\sim 50$ ) distributed along a broad range of longitudes. It is possible, however, to construct such equatorial beams from sources at other locations with different beaming properties. For example, if the HOM sources are located on the  $R = 0$  cutoff frequency surface (or  $f_c$  surface) at the places where the local magnetic field direction is nearly parallel (or anti-parallel) to the magnetic equator, then filled-cone beaming would provide a true equatorial beaming pattern. In this case, an observer near the equator would indeed detect a lack of radiation near  $200^\circ$  CML. For this model to work, it is required that radiation at different frequencies originates from different  $L$ -shells (the higher  $f$  is, the smaller  $L$  value will be) and source (magnetic) latitude for all frequencies would be roughly the same value close to  $53^\circ$  (if an OTD magnetic field model is assumed). The problem is that there has been no physical mechanism supporting such a filled-cone beaming model.

The other possible model that can produce the proposed equatorial beaming pattern can be that radiation beamed in a single, wide-open hollow cone comes from a very high latitude (cusp) region. If the HOM emission does originate in a small region at very high latitude (*i.e.*, very large  $L$ -shell) in the cusps in both hemispheres and beamed into a large angle hollow cone, one can expect that the resultant beaming would be close to the magnetic equator. Figure 4.14 shows the intensity profile similar to those shown in Figure 4.13 as a function of magnetic latitude of an observer, produced by a single source located on the  $L = 100$  shell with radiation beamed into a hollow cone of half-angle of  $\beta_0 = 85^\circ$ . The emission beam is correctly produced near the magnetic latitude of  $3^\circ$  with width of about  $10^\circ$ . This is the kind of beaming pattern that *Alexander et al.* [1979] had proposed. The cusp region is one that the solar wind particles have the direct and the easiest access along the opened magnetic field lines, giving rise to particles that could trigger the HOM emission. In this region,

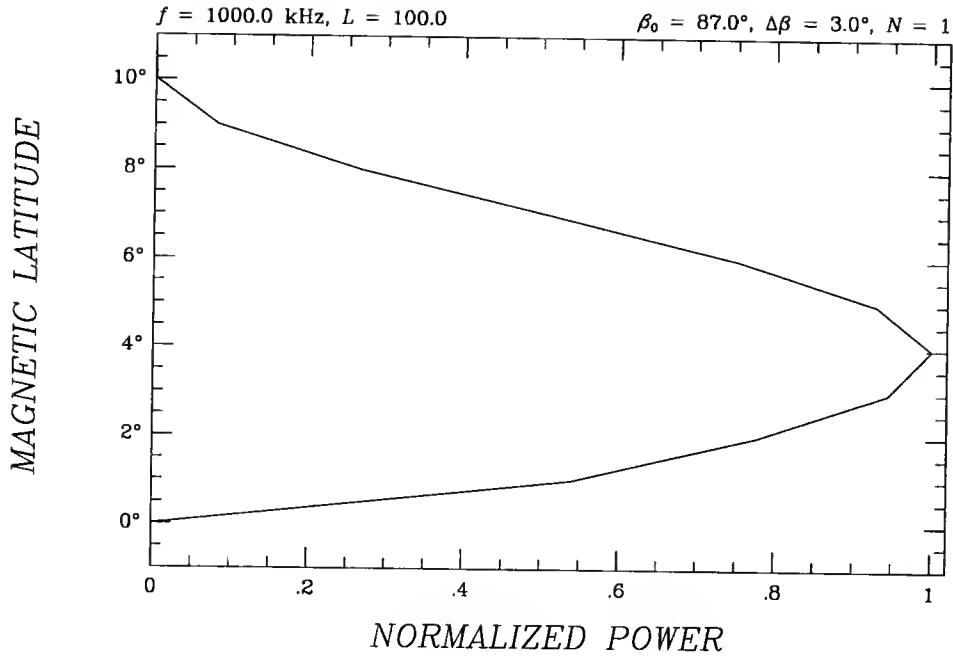


Figure 4.14. Intensity profile created with a single source located near the northern cusp region with radiation beamed into a  $85^\circ$  half-angle emission cone. A latitudinal beam near the magnetic equator is correctly produced.

the plasma density might be low enough that would make the CMI mechanism easy to work [Dulk *et al.*, 1992; Lecacheux *et al.*, 1992a; Zarka, 1992].

#### 4.3.2 Model Assumptions

Hollow cone beaming models have been previously proposed to explain the DAM emissions from Jupiter (see, e.g., Goldstein *et al.* [1979] and Thieman and Smith [1979]), and kilometric emissions from Uranus (e.g., Gulkis and Carr [1987], Carr and Gulkis [1987]). The similarity of the power spectrum of the Jovian HOM and KOM emissions to those of other giant planets suggests that they may share a common emission mechanism. Based on the exceptional intensity profile and other characteristics of the HOM emission observed by both Voyagers, a hollow cone beaming



originating from a confined source region is chosen for the model to explain the HOM emission's bilobed and monolobed pattern.

The following assumptions will be made in my HOM emission modeling process.

(1) The emission mechanism is similar to that of the auroral kilometric radiation (AKR) from Earth, namely the cyclotron maser instability (CMI) [*Wu and Lee, 1979; Omidì et al., 1984; Lyons and Williams, 1984*]. The AKR spectrum is characterized by lower and upper cutoff frequencies at about 50 and 500 kHz, respectively [*Lyons and Williams, 1984*]. If it is assumed that the Jovian kilometric, hectometric, and decametric components are distinct (Io control is observed only in the case of the DAM emission), then the hectometric cutoff frequencies appear to be about 300 and 2000 kHz [*Carr et al., 1983*]. If it is further assumed that the Jovian hectometric radiation is emitted within regions having the same range of values of the ratio  $f_p/f_c$ , ( $f_p$  and  $f_c$  are the plasma and cyclotron frequencies, respectively) as does the AKR [*Lyons and Williams, 1984*], it follows that  $f_p$  as well as  $f_c$  are about 4 times higher in the Jovian than in the terrestrial source regions. The indicated values of the electron number density of Jupiter would thus be from approximately  $0.3$  to  $30 \text{ cm}^{-3}$ . These values are in good agreement with those predicted by the Jovian ionosphere modeled by *Divine and Garrett [1983]*.

(2) The radiation is generated from a pair of conjugate cyclotron resonant sources on the same magnetic field line in both (magnetic) hemispheres, and is in the R-X mode at frequencies which is determined by the relativistic Doppler-shifted cyclotron resonance condition. Consequently it is near the local electron cyclotron frequency,  $f_c$ . This implies that the northern and southern conjugate sources will emit right and left elliptically or circularly polarized radiation, respectively. This assumption is supported by the fact that the HOM emission is RH polarization dominated when it is observed from the northern magnetic hemisphere and LH polarization dominated when it is observed from the southern magnetic hemisphere. It is also supported by the fact shown in Figure 4.3 that intensities from the

two polarization channels have a similar global profile and occurrence appearance. *Ortega-Molina and Lecacheux* [1991] provided the evidence that the two HOM components are emitted in different source regions and very likely from the conjugated source regions with similar beaming properties. (3) The radiation is beamed into a hollow cone whose axis is tangent to the local magnetic field at the source and whose vertex is located at the source. Such a beaming cone or cones is fixed to the magnetic field and rotating with the planet. (4) The emitted power from each point in the source region is gyrotropic, *i.e.*, it is azimuthally symmetrical about the tangent of the magnetic field at the source point. The normalized power pattern at a constant azimuth is specified by

$$p(\beta) = \begin{cases} \frac{1}{2} + \frac{1}{2} \cos[k(\beta_0 - \beta)], & \text{if } |k(\beta_0 - \beta)| \leq 180^\circ; \\ 0, & \text{for other } \beta \text{ values,} \end{cases} \quad (4.7)$$

where  $\beta_0$  is the half opening angle of the hollow cone defined by the azimuthal directions for which  $p(\beta)=1$  (its maximum),  $\beta$  is the angle between the magnetic field at the source and the observer,  $k$  is a parameter that determines the beam thickness. An equivalent term, the half-power beamwidth  $\Delta\beta$ , where  $\Delta\beta = 180^\circ/k$ , is also used to measure the beam thickness. The second condition ( $|k(\beta_0 - \beta)| > 180^\circ$ ) in Equation (4.7), approximately, is a necessary one. It simply indicates that no radiation would propagate toward and pass through the stop zone surface. The stop zone surface is determined by  $f \equiv f_{R=0}$  (and therefore  $f \approx f_c$ ) and is normal to  $\nabla B$  (and therefore approximately normal to  $\mathbf{B}$  at high latitude regions); inside this surface no radio wave in the R-X mode is allowed to propagate. (5) The local magnetic field vector of the magnetic field line that connects the pair of conjugate cyclotron resonant sources is pointed toward the longitude of the narrow gap ( $\approx 30^\circ$  CML). The narrow gap occurs, therefore, as the radial vector from the source to the spacecraft comes closest to the axis of the hollow cone beam (when the spacecraft is traversing the inside of the hollow emission cone); while the wide gap occurs when the hollow cone beam is

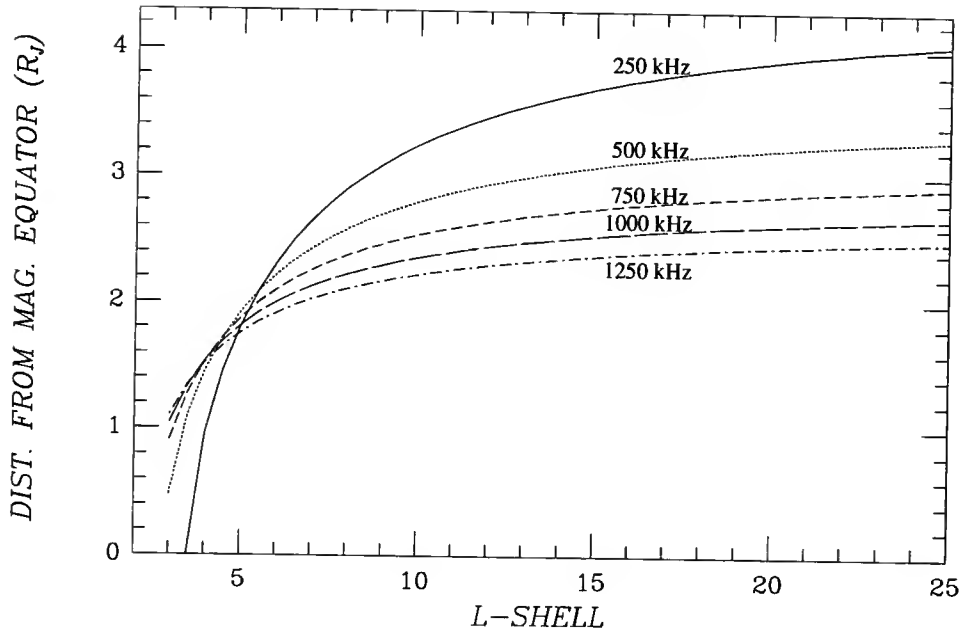


Figure 4.15. Distance of sources to the magnetic equator at indicated frequencies as a function of the  $L$ -shell value.

turning away from the spacecraft. The longitude of this field line connecting both the northern and southern sources is an adjustable parameter of the model. (6) The initial wave refraction, if any, occurs only in a small localized region near the source and the final directions of wave propagation is confined in the hollow beaming cone. Refraction by other sources such as the Io plasma torus will be neglected. This is not totally true, because the presence of the Io plasma torus will certainly alter propagation direction of waves that pass through the central, dense region of the torus. However, since all the HOM sources are at least  $1.5 R_J$  above the cloud-tops of Jupiter, and they have relatively large distance from the magnetic equator, radiation received by a distant observer would barely go through the Io plasma torus and therefore would not be affected by the torus. To demonstrate this, I calculated, as is shown in Figure 4.15, distances to the magnetic equator of many different potential source positions at frequencies of 250 kHz, 500 kHz, 750 kHz, 1000 kHz and 1250 kHz as a function of the  $L$ -shell values. This figure clearly shows that if the HOM radiation is from

the  $f_c = f$  surface on  $L$ -shells with  $L > 5$ , the source will be at least  $2 R_J$  from the magnetic equator. Even if the Io plasma torus extends  $\pm 1 R_J$  above and below the (centrifugal) equator, radiation from given source locations can reach an observer at a magnetic latitude as low as  $-11^\circ$  without passing through the Io torus. Refraction from the Io plasma torus can be therefore, to the first approximation, ignored. This assumption will be justified in Chapter 5 where raytracing calculations indicate that radiation from high magnetic latitude region can reach a distant spacecraft near the magnetic equator without being affected by the Io torus.

### 4.3.3 The Beaming Geometry

Figure 4.16 shows the geometry of our corotating hollow cone beaming model and how the model could produce the observed results. In panel (a),  $(X, Y, Z)$  are the axes of the Jovicentric equatorial system (not to be confused with the  $XYZ$  system in Chapter 2), and the source (southern source not shown) is located at the point  $P(r, \theta, \lambda)$  at which the magnetic field vector is  $\mathbf{B}$ . The longitudes of the spacecraft and the sun are indicated in each of four diagrams in panel (b). The leading-lobe and trailing-lobe maxima of the intensity-time plot occur in the diagrams for which the Jovigraphic longitudes of the spacecraft are assumed to be  $323^\circ$  and  $83^\circ$ , respectively. The CML locations of the apparent sources corresponding to these edges can be found with this model. The midpoint of the narrow gap occurs when spacecraft's longitude is midway between these values, at  $23^\circ$ . The wide gap occurs when the longitude of the spacecraft is  $203^\circ$  (*i.e.*,  $180^\circ$  opposite) which is actually the observed mean midpoint of the wide gap for the Voyager 1 data after encounter (see Table 4.1). It is also the longitude of the north magnetic pole for the tilted dipole field. If the emission cone is inclined such that only the equatorial edge of the cone reaches the observer, then only one radiation event will occur, resulting in monolobed intensity profile.

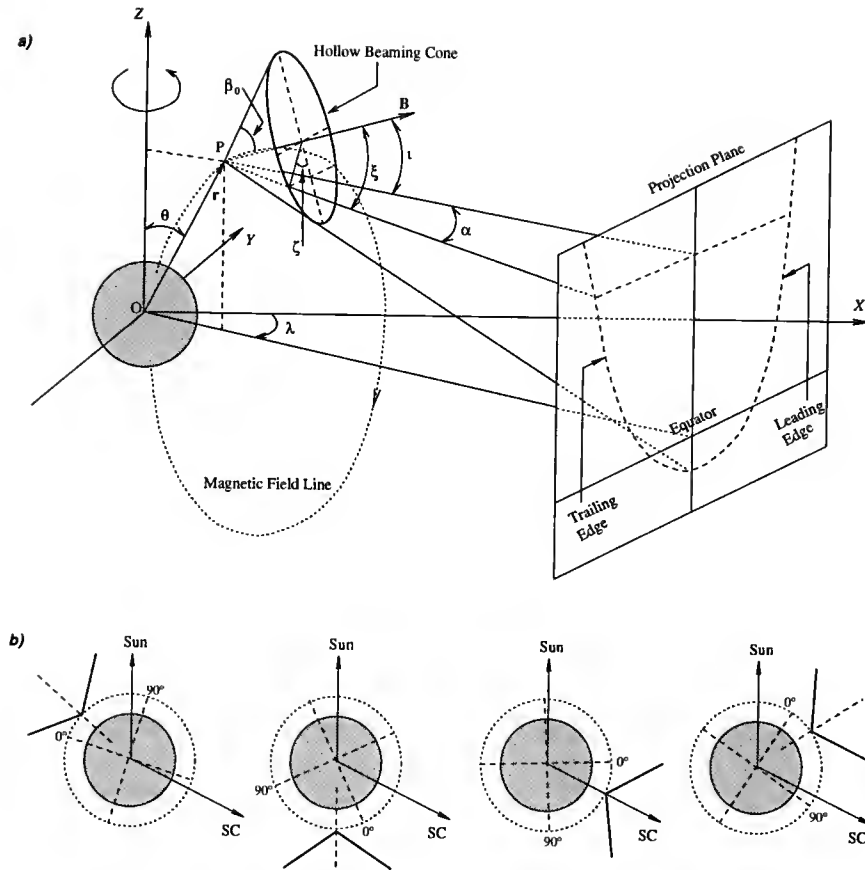


Figure 4.16. (a) Geometry of the hollow cone beaming model. Only one “sub-source” point is shown. Source(s) in the southern hemisphere are not shown. (b) A sequence of rotation seen from top of the north pole during the post-encounter period. The “V” shape beaming pattern is the intersection of the beaming cone defined by the beam-maximum directions with the plane containing the observer and the vertex of the cone. The angle between the leading edge and the trailing edge is about  $120^\circ$ , which is the angular separation of the two HOM emission peaks.

When the axis of the emission cone is inclined by an angle  $\iota$  to the plane passing through the cone vertex and the spacecraft, then the emission cone will intersect this plane along a curve whose asymptotes are two straight lines intersecting at an angle  $2\alpha$ , where  $\alpha$  has a relationship with  $\iota$  and the cone opening angle  $\beta_0$ :

$$\cos \alpha = \frac{\cos \beta_0}{\cos \iota} \quad (0^\circ \leq \beta_0 \leq 90^\circ, 0^\circ \leq \iota < 90^\circ), \quad (4.8)$$

or equivalently,

$$\tan^2 \alpha = \tan^2 \beta_0 \cos^2 \iota - \sin^2 \iota .$$

This formula was actually used first by *Goldreich and Lynden-Bell* [1969] and later by *Goldstein et al.* [1979] and *Thieman and Smith* [1979] in their modeling of Jupiter's decametric radio emissions. Equation (4.8) immediately leads to the following important implications. First, the minimum cone opening angle will be  $\beta_{0\min} = \alpha$  when the tilting angle  $\iota$  is  $0^\circ$  (i.e., when the cone axis is parallel to the plane on which the spacecraft lies). Also, in order for the emission cone to reach the observer ( $\alpha \geq 0^\circ$ ), the tilt angle  $\iota$  has to be smaller than the cone opening angle  $\beta_0$ . Since the tilting angle  $\iota$  is measured from the magnetic field direction at the source, it can be expressed in terms of the magnetic colatitude of the source ( $\theta_m$ ) and the magnetic latitude of the spacecraft ( $\delta_m$ ):

$$\cos(\iota + \delta_m) = \frac{3 \sin 2\theta_m}{2\sqrt{1 + 3 \cos^2 \theta_m}} . \quad (4.9)$$

From the second assumption of the model (on page 81), the radio source is located on the surface of cyclotron frequency  $f_c$  which is only slightly smaller than the radio wave frequency. The magnetic field intensity at the source is thus determined by  $B = 2\pi m_e f_c / e$ , which at the magnetic colatitude  $\theta_m$  on a specified  $L$ -shell is expressed as

$$B = \frac{\mathcal{M} \sqrt{1 + 3 \cos^2 \theta_m}}{L^3 \sin^6 \theta_m} ,$$

where  $\mathcal{M}$  is the dipole moment. On the  $f_c$ -surface, the  $L$ -shell value and the magnetic colatitude  $\theta_m$  are therefore related such that

$$L^3 = \frac{e \mathcal{M} \sqrt{1 + 3 \cos^2 \theta_m}}{2\pi m_e f_c \sin^6 \theta_m} . \quad (4.10)$$

Equations (4.8), (4.9) and (4.10) provide a guideline for us to set the adjustable parameters of our model. The most important parameters that would affect fitting

quality are the  $L$ -shell values of the source and the opening half-angle of the emission cone,  $\beta_0$ . The Voyager observations after Jupiter encounters show that the HOM emission reaches two peaks when the spacecraft is at about  $330^\circ$  and  $90^\circ$  CML. This means that the angular separation of the two peaks is about  $120^\circ$ . This leads to  $\alpha \approx 60^\circ$ . Equation (4.10) indicates that sources at larger  $L$ -shells will be at higher magnetic latitude (smaller  $\theta_m$ ), and therefore the cone axes will be tilted further away ( $\iota$  increases) from the spacecraft. This naturally will require a larger cone opening angle to maintain the angle  $\alpha$  unchanged.

#### 4.3.4 Modeling Procedures and Results

Based on the model assumptions and the geometry considerations, I simulated the Jovian HOM emission as detected by the Voyager spacecraft with a pair of modeled conjugate source regions which are located in the northern and southern hemispheres, respectively. The following adjustable model parameters for each considered radio wave frequency are used: (1) central longitude of the source region,  $\lambda_c$ ; (2) longitudinal width of source region,  $\Delta\lambda$ ; (3)  $L$ -shell value,  $L$ , of the magnetic field line passing through both source regions; (4) half-angle of the hollow beaming emission cone,  $\beta_0$ ; (5) thickness of the emission cone,  $\Delta\beta$ ; and (6) intensity scaling factor,  $S$ . The actual source is continuously distributed within the specified region just outside the stop zone, and is located above one, or each, auroral zone. The distributed source can be approximated by a group of equally incoherently-emitting point sources, or “sub-sources”. Locations of each of the subsources are determined by radiation frequency,  $L$ -shell value, and longitude of the field line.

In the modeling process, models that best fit to the observed curves of the radiation intensity at 1 MHz, and at other frequencies, were made as a function of time. The criteria to measure the goodness of fitting are: (1) positions of the emission peaks

in terms of CML or SCET; (2) duration of each emission peak; (3) relative strength of the emission peak. These criteria are mainly used for visual examination of the modeling process. In addition to the criteria, the standard deviation of the modeled intensity curve from the observed, smoothed intensity curve is used for a quantitative measurement along with the visual examination. The fitting was first done separately for each of several groups of subsources equally spaced at  $1^\circ$  interval along the lines of constant  $L$ -shell value. The magnetic field assumed was the  $O_4$  model [Acuña and Ness, 1976] plus a contribution due to the current sheet [Connerney, 1981]. For each of assumed sets of positions of the subsources, initial values were assumed for the cone angle ( $\beta_0$ ) and the beam thickness parameter ( $k$ ). Then a normalized power  $p(\beta)$ , as defined by Equation (4.7), for each subsurface was multiplied by the subsurface-to-spacecraft distance squared, and the intensity contributions were summed. After adding a constant background value to the summed intensity and finding the most suitable scale factor, the computed curve was visually compared with the observed intensity curve. The process was repeated, systematically varying the adjustable parameters  $\beta_0$ ,  $k$ , and scale factor  $S$ , until a best fit was obtained. Then the process was again repeated for new sets of positions of the subsources until the latitude and longitude range within which acceptable fits of modeled-to-observed intensity curves could be obtained were determined. This was done for assumed source regions in the northern and southern auroral zones separately, and also for conjugate pairs of simultaneously emitting sources located in the two hemispheres. In the latter case, models were investigated for which the adjustable parameters  $\beta_0$  and  $k$  were identical for the two conjugate sources, and others were investigated for which they were different.

The cone parameters, the source location, and the source width in longitude (in each hemisphere) that would best fit to the observed data were determined for a series of groups of subsources, with each group at a constant  $L$ -shell value. The RH and



Table 4.2. Model parameters that result in best fit to the observational emissions at 1 MHz, 0.75 MHz and 0.5 MHz for a pair of conjugate sources in the northern and southern hemispheres.

	Northern source					Southern source				
	$L$	$\lambda_c$	$\Delta\lambda$	$\beta_0$	$\Delta\beta$	$L$	$\lambda_c$	$\Delta\lambda$	$\beta_0$	$\Delta\beta$
$f = 1 \text{ MHz}$	4	35°	10°	64°	26°	4	30°	9°	60°	48°
	6	30°	10°	68°	20°	6	30°	10°	65°	40°
	10	25°	10°	73°	11°	10	30°	10°	70°	31°
	15	35°	9°	76°	13°	15	30°	9°	73°	26°
	20	35°	10°	78°	10°	20	30°	10°	75°	23°
	30	40°	10°	80°	7°	30	30°	10°	78°	20°
	50	30°	10°	83°	8°	50	30°	10°	80°	16°
$f = 750 \text{ kHz}$	4	37°	10°	60°	29°	4	25°	10°	59°	48°
	6	37°	10°	65°	22°	6	25°	10°	63°	38°
	10	37°	10°	70°	16°	10	25°	10°	69°	30°
	15	37°	10°	73°	12°	15	20°	10°	73°	26°
	20	37°	10°	75°	9°	20	20°	10°	75°	23°
	30	40°	10°	78°	7°	30	20°	10°	78°	20°
$f = 500 \text{ kHz}$	4	40°	10°	60°	42°	4	30°	10°	58°	54°
	6	40°	10°	66°	32°	6	30°	10°	64°	43°
	10	40°	10°	68°	20°	10	30°	10°	70°	34°
	15	40°	10°	70°	13°	15	30°	10°	73°	28°
	20	40°	10°	73°	11°	20	30°	10°	76°	26°
	30	40°	10°	76°	8°	30	30°	10°	80°	24°

LH intensity components (from assumed conjugate source locations of the same set of field lines) were modeled independently. For radiation at 500, 750, and 1000 kHz, the parameters leading to a good fit to after encounter observational RH and LH intensity curves are listed in Table 4.2. Seven locations of the sources were considered for 1 MHz, and six locations each for 750 kHz and 500 kHz. If the sources are in lower latitudinal regions (smaller  $L$ -shell values), the magnetic field direction at the source is more toward the observer, as has been predicted. In this case the inclination angle of the emission cone relative to the observer would be smaller, which would lead to a

smaller cone opening angle ( $\beta_0$ ). Calculations shown in Table 4.2 also show that for sources at high latitudes (and therefore larger  $L$ -shell value and greater emission cone opening angle  $\beta_0$ ), the cone thickness becomes narrower (smaller  $\Delta\beta$ ). Examples of comparison of the modeling results and the observed ones are shown in Figures 4.17 for radiation of both LH and RH components at 1 MHz and 750 kHz. These results indicate that our model correctly simulated the occurrence of the HOM emission, with a wide gap near  $200^\circ$  CML and a narrow gap near  $30^\circ$ . The wider separation of the leading and trailing maxima for each rotation cycle for the RH data than for the LH data was also correctly simulated.

We have already seen, from the calculation of the averaged flux density and the occurrence probability shown in Figures 4.4 and 4.5, that radiation received near  $330^\circ$  CML are usually stronger in intensity or have higher occurrence probability than those received near  $90^\circ$  CML. An additional parameter, ratio of the peak intensity of the trailing lobe to that of the leading lobe, could be introduced to account for such intensity variation. The best value of this ratio was usually about 0.5. This intensity reduction might be attributed to the loss of energy of the group of radiating trapped particles between the times the leading and trailing lobes were observed, as will be discussed below. The other reason for this uneven intensity profile is probably that the gradients in magnetic field strength  $B$  are asymmetric about the emission cone axis, the amount of radiation beamed into the emission cone can be different on the two sides.

#### 4.3.5 Discussion

We have modeled the HOM emission at different frequencies originating on the magnetic field lines with various  $L$ -shell values. Computation results with a variety of parameter sets fit the observation almost equally well, and predict a wide range of

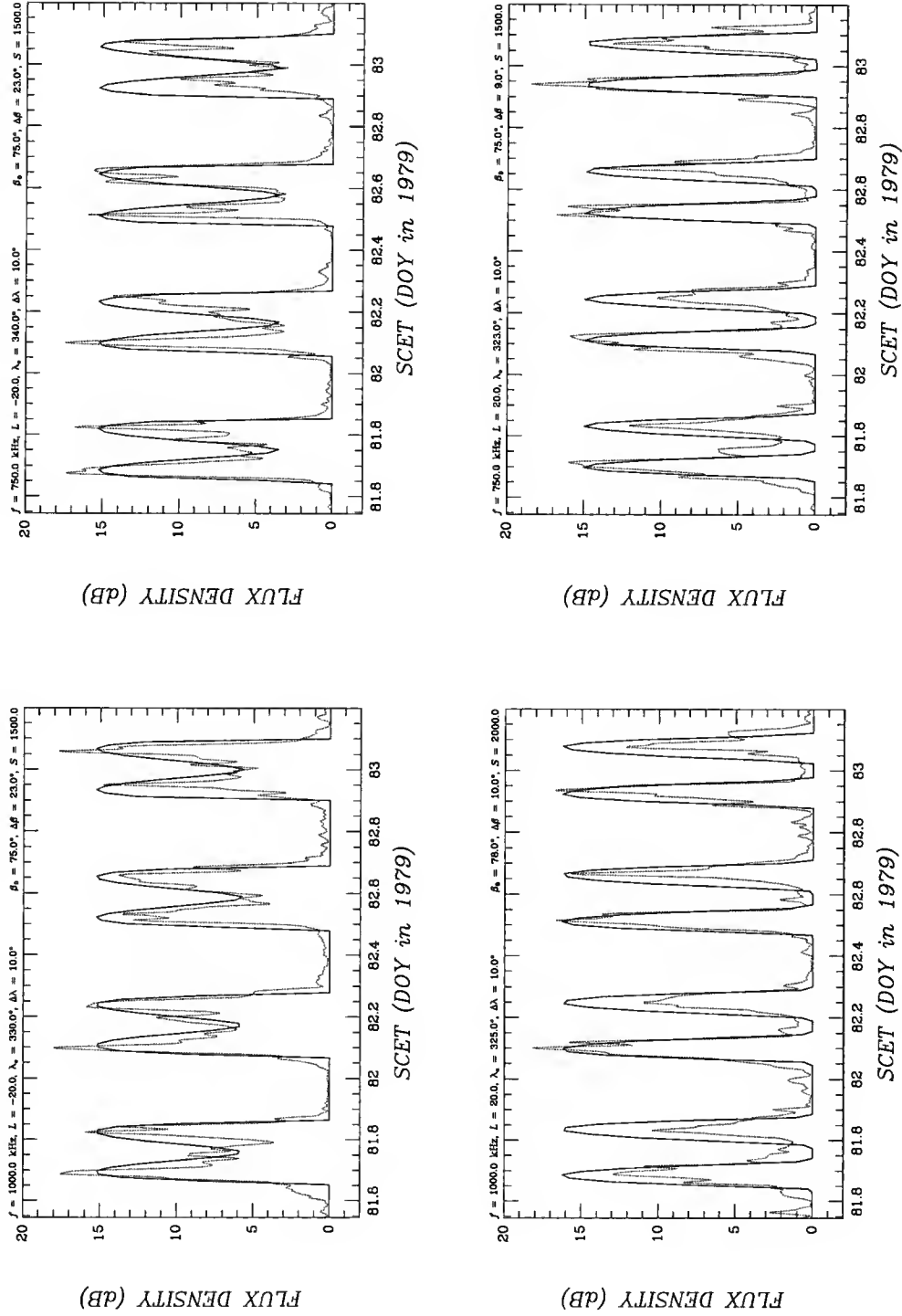


Figure 4.17. Comparison of modeled (solid line) LH and RH components (top and bottom panels, respectively) of the HOM emission at frequencies of 750 kHz (right panels) and 1000 kHz (left panels) as a function of spacecraft event time (SCET) with observed (dotted line) Voyager 1 data after encounter. Model parameters are indicated on the top of each plot. Sources in the southern hemisphere are specified with negative  $L$ -shell values.

$L$ -shells for possible locations of the source. The question as to whether the HOM sources are located on lower or higher  $L$ -shell magnetic field lines has been controversial in the literature. One consideration in this regard is that the reported solar wind control of the HOM favors large  $L$ -shell values, which would permit easier access of solar wind electrons than would the small  $L$ -shell locations. Recent observations from a new spacecraft, however, suggest otherwise.

In early 1992, the spacecraft Ulysses encountered Jupiter from a high latitude orbit. The URAP experiment on board Ulysses is the first radiometer that has the capability of direction finding. Preliminary results [Reiner *et al.*, 1993*a*, 1993*b*] indicate that the HOM sources are located in a low  $L$ -shell region with  $L \approx 4 \sim 8$ , assuming that radiation is emitted near the  $f_c = f$  surface and propagates along straight lines without being affected by the Io plasma torus. This result appears to be in direct support of the low  $L$ -shell source origin, but it cannot be relied upon because the assumption of straight line propagation is almost surely incorrect. A better model is needed to locate the source region by raytracing the observed radio waves back to the source region.

If the HOM sources really are located on the low ( $4 \sim 7$ )  $L$ -shells, the natural electron source would be the trapped electrons that cross the magnetic equator within the cold plasma torus. The cold torus is about 5 to 5.8  $R_J$  from the center of the planet, located in the inner part of the toroidal distribution of relatively dense plasma surrounding Jupiter near the orbit of Io. The distribution of the cold torus is highly asymmetrical in longitude with the highest densities occurring approximately within the range of  $250^\circ \pm 90^\circ$  and the lowest at diametrically opposite longitudes. Trafton [1980] found that the ratio of the highest to lowest plasma densities can be as large as 5, and other observers found longitudinal variations almost as high. According to our results, the HOM emission originates at a magnetically conjugate pair of sources close to the Jovigraphic longitude of the south magnetic pole. The reason for the absence of

similar emission from the vicinity of the Jovigraphic longitude of the north magnetic pole would be the much higher density of the cold plasma torus there. The increased plasma density in that part of the torus in some way renders the trapped particles passing through it incapable of causing the emission of radiation when (and if) they reach auroral latitudes. One way might be for pitch angle scattering of the particles as they cross the torus to cause their subsequent precipitation. Another possibility is that as a result of the increased torus density, the ambient plasma density in the radio emitting regions may also be increased sufficiently to raise the plasma-to-cyclotron frequency ratio above the upper limit for cyclotron maser emission to occur. The scale height of the cold torus above the magnetic equator is much too small for this to occur directly. But it could perhaps result from photoionization of neutral particles in the dense sector of the torus, with subsequent migration of heated ionospheric plasma to the source region.

Of course, if sources are on low  $L$ -shells, the required half-angle of the beaming cone would be relatively small ( $\sim 60^\circ$ ), as has been shown in our model. Since the CMI is assumed to be the HOM emission mechanism and such mechanism favors larger values for the initial wave normal angle ( $\approx 90^\circ$ ), sources on small  $L$ -shells do not seem to be favored by the CMI mechanism. Our beaming model predicts the resultant beaming angle *after* the initial refraction (if any) of the radiation at the source region, thus a  $60^\circ$  half-angle of the beaming cone seems to be quite reasonable. *Ladreiter* [1991] argued that since the refractive index  $n$  at the radiation source must be near unity for the required low ratio of  $f_p/f_c$  (*i.e.*,  $f_p/f_c < 0.1$ ) for the CMI mechanism to operate, not much refraction is experienced by the radiation. I disagree with this conclusion. I believe that the true situation may be that suggested by *Le Quéau et al.* [1984a, 1984b], in which initially downward propagating waves triggered by hole-like electron distribution can be amplified till they are reflected (actually strongly refracted) as a consequence of the increasing magnetic field. The reflected

wave eventually travels upward and escapes the magnetosphere; consequently the outgoing waves can have smaller beaming angles with respect to the local magnetic field. In any event, more study is needed on the emission mechanism in order to clear these arguments.

We also see that our model works for sources located on large  $L$ -shells ( $>20$ ). In this case, the beaming angle is much larger than that for sources on small  $L$ -shells, in closer agreement with the CMI theory. As has already been stated, the other point in support of the sources being on large  $L$ -shells is the easy access to the source regions by the solar wind particles, explaining at least partially why the HOM emission is correlated with the solar wind activity and shown local time effect. In their modeling of the HOM emission, *Ladreiter and Leblanc* [1989, 1990b] concluded that the HOM emission must be from  $L$ -shells larger than 20. One of their considerations is also the easy access of the solar wind particles to the source region. Large  $L$ -shell is particularly required in their model for radiation at lower frequencies ( $\sim 500$  kHz), so that radio waves would initially propagate toward the central part of the Io torus and could then be bent toward, with the aid from the Io plasma torus, the direction parallel to the magnetic equator. However, for radiation at higher frequencies ( $>800$  kHz), such scenario no longer works unless the electron density in the Io torus is increased two or three times higher than the value currently modeled from the *in situ* observations by *Bagenal et al.* [1980], *Bagenal and Sullivan* [1981], and *Divine and Garrett* [1983].

Our models correctly simulates, for the whole HOM emission frequency range, the observed radiation with two peaks near  $330^\circ$  and  $90^\circ$  CML, a break near  $200^\circ$  CML, and a minor gap near  $30^\circ$  CML. The received radiation near the magnetic equator in a broad range of frequencies does not depend on the presence of the Io plasma torus, and the HOM emission appears as a group of broad band emissions. Also our model is compatible with some of the non-Io DAM emission models. Since

there are many similarities in properties between the HOM and the non-*Io* DAM emissions, it has been suggested by many researchers that the HOM emission might be the extension in low frequency part of the non-*Io* DAM emission. On the other hand, our model predicts no detected radiation near  $200^\circ$  CML at all times. The PRA receiver did observe some emissions at this longitude when the spacecraft was very close to Jupiter and was at low Jovigraphic latitudes ( $< -2^\circ$ ). It is very likely, however, that the radiation observed near Jupiter has a different origin than that observed far away from Jupiter. This is supported by recent observations made with the URAP experiment of Ulysses [*Reiner et al.*, 1993a]. We can say that our model correctly accounts for the HOM emission received by the two Voyagers when they are at Jovigraphic latitudes  $> 0^\circ$ . Close field observations need special treatment such as raytracing and other knowledges on plasmasphere and magnetosphere. I will briefly address this issue in Chapter 5.

When and how the particles originating the radiation become trapped at the meridian of the south magnetic pole is another issue that our model needs to address. Two observational phenomena may give us some clue to the answer. The first is that the emission patterns most often observed in the pre-encounter Voyager 1 data (from the sunward side) are chaotic, while those of the post-encounter data (from the dark side) are relatively regular. Although it is generally believed that solar wind particles enter the Jovian magnetosphere from the tail region, this evidence could be interpreted to suggest transient magnetospheric disturbances associated with the entry of particles from the sunward side. If this were indeed true, such entry through the southern cusp at the time the subsolar point is near the magnetic south polar meridian would be indicated. The cusp region is likely to be active with the precipitation of the solar wind particles, which is necessary to produce a particle distribution function with a loss-cone that is usually assumed as the free energy source of the cyclotron maser instability. Although particles would equally well enter the

northern cusp, for some reason the ambient plasma density in the source regions might have been increased sufficiently, due to the asymmetry of plasma density distribution in longitude, to raise the plasma-to-cyclotron frequency ratio above the upper limit for cyclotron maser emission to occur. The second observed feature that provides some information on the time of particle entry is the drop in the calculated average post-encounter source power from about 130 to 50 kW/Hz during the 3.3 hour interval between the times of alignment of the leading-lobe and trailing-lobe beam maximum directions with the spacecraft direction. These alignments occur at the times shown in the diagrams in Figure 4.16*b* (on page 85) for the spacecraft longitudes about  $323^\circ$  and  $83^\circ$ , respectively. According to our interpretation, no net particle replenishment occurs during this interval; if it did, the source power would have been observed to increase instead of decreasing. There is no problem with this observational constraint if entry is assumed to be from the sunward side. If particles are assumed to enter from the tail, however, their entry must occur before the anti-solar point reaches the magnetic south polar meridian (*i.e.*, before the second diagram in Figure 4.16*b*).

*Barrow* [1991] followed an early model of *Carr and Wang* [1988] and suggested, purely from a geometry approach, that the Carr-Wang model can be modified such that the HOM sources are distributed in a broad longitudinal region and therefore the difficulty of finding a good physical reason why the HOM emission sources are confined in a small region near the meridian plane of the south magnetic pole can be avoided. However, this would cause other questions that are even harder to address. I have discussed such problems in Section 4.3.1.

So far, the HOM (and radio emission components at other frequencies) source locations can only be deduced indirectly with various models that are made to fit observational data. The reason is simply that all space borne observations, except that of the Ulysses URAP experiment, are incapable of finding directions of the incoming radio waves. The URAP experiment is the first one that has such a direction finding



feature and can be in principle used to determine all four Stokes parameters of the incoming wave. However, so far only limited work has been done in determining the HOM and KOM source locations, and the results are still rather controversial. To understand fully the emission mechanism, propagation effects, and source locations of the Jovian HOM and KOM emissions, more observation and analysis are needed. I will discuss in the next chapter the propagation effects on the Jovian HOM emission in the Jovian magnetosphere. These results will justify my assumption in the above modeling effort that the HOM emission received by the two Voyagers did not experience extensive refraction from the Io plasma torus after leaving the source region. It is expected that further analysis of the URAP data from Ulysses and from the observations to be made from the spacecraft Galileo in 1995 will provide new information needed in the ongoing effort to find the answers to the mysteries of Jupiter's low-frequency radio emissions.

## CHAPTER 5

### STUDY OF THE HOM EMISSIONS VIA RAYTRACING

#### 5.1 The Necessity of Raytracing Studies of the Jovian HOM Emission

Since the discovery of radio emissions from planets with magnetic fields, most of the work on modeling such emissions has been based on the assumption that radio waves propagate within the planetary magnetosphere along straight lines on their way out; any refraction or even reflection of the waves by highly concentrated plasma (e.g., the Jovian ionosphere and the Io torus in the case of Jupiter), or by the close approach to a stop zone boundary at which  $f_c \simeq f$ , is partially or completely ignored. In many cases such an assumption is valid, especially when the frequency of the radio wave is several orders of magnitude higher than the local electron plasma frequency ( $f_p$ ) and when the local electron cyclotron frequency ( $f_c$ ) is well below the wave frequency everywhere along the path. However, there are a number of examples in the literature for which it is clear that inadequate correction for ray refraction, or no correction at all, lead to potentially erroneous conclusions. Correction for ray refraction certainly requires the raytracing calculation.

Correction for refraction by means of raytracing is essential when modeling the Jovian HOM and KOM emissions in Jupiter's unique magnetospheric environment: globally strong magnetic field and the Io plasma torus where the electron plasma frequency is believed to be on the order of dozens or hundreds of kilohertz, comparable to frequencies of the concerned radio waves. Tracing radio rays outward from

within the Jovian magnetosphere is therefore an important and powerful tool for investigating the process of radio emissions from Jupiter. The raytracing technique involves the understanding of the magnetic and the plasma environment of the planetary magnetosphere in which the radio waves propagate. It can therefore be very helpful in determining and confirming many important details about the origin of a radio wave (source location and extension). In addition, the modes and polarization status of the wave can be inferred by matching raytracing calculations with the observations. Raytracing is a particularly useful tool in that it can provide insight into the propagation effects. These include refraction and reflection, and shadow zones for regions where radiation can not be reached due to the intervening plasma between the source region and the spacecraft. As a diagnostic tool along a computed ray path, wave growth rates and estimates of plasma densities can also be calculated to provide rigorous tests for theories of wave generation and amplification. In the case of Jovian radio emissions in the KOM and HOM frequency range, the existence of the Io plasma torus, which is the most viable source for any propagation effects, can alter the behavior of waves propagating through it; the raytracing calculation can therefore be of great help in investigations of any possible influence of the Io torus on the HOM emission.

## 5.2 Early Raytracing Studies on the HOM Emissions

The raytracing technique was used to investigate the AKR from Earth by many people such as *Jones and Grard* [1976], *Green et al.* [1977], *Hashimoto* [1984], just to name a few. It was also applied to the study of the Jovian DAM emission by *Hashimoto and Goldstein* [1983], *Green* [1984], *Menietti et al.* [1984] and to the Jovian KOM emission by *Green and Gurnett* [1980], and *Jones* [1980, 1981]. The first raytracing work on the Jovian HOM emission was done by *Lecacheux et al.* [1981],

who used an oversimplified Io torus plasma model and an OTD magnetic field model to trace rays in a meridian plane in an effort to identify possible source regions. However, the absence of any model for the emission mechanism combined with insufficient knowledge of the plasma distribution in the torus at that time explain why the tracing results from arbitrary source locations failed to contribute to plausible source localization. The only important conclusion that can be drawn from the calculation by *Lecacheux et al.* [1981] is that the Io plasma torus can appear opaque to the incident radiation at frequencies below 300 kHz, and it can still affect appreciably the radiation at higher frequencies (depending on the source locations). The study of the Jovian HOM emission via raytracing was later independently conducted by *Wang and Carr* [1990] and by *Ladreitner and Leblanc* [1990b]. Both performed two- and three-dimensional raytracing on a specified meridian plane from a source location designated by its  $L$ -shell value and the electron cyclotron frequency, using the identical magnetic field model and plasmasphere model.

The raytracing by *Wang and Carr* [1990] was done to test a hypothesis of an early HOM emission beaming model of *Carr and Wang* [1988] that the Io plasma torus does not play a crucial role on the magnetic equatorial beaming of the Jovian HOM emission originating from high latitude regions, especially for the high frequency ( $> 800$  kHz) part of the HOM emission. The well known Runge-Kutta method, a relatively simple and fast way of solving a set of first order ordinary differential equations was used in the study. A qualitative conclusion of their raytracing study is that, as long as the HOM sources are located in high latitude regions (*i.e.*, on large  $L$ -shells) and the emission is beamed into a moderately wide opened hollow cone (with a cone opening angle of around  $60^\circ$  or a little larger), the HOM emission will not follow a path that passes through the central part of the Io torus and therefore will not be affected appreciably by the Io torus. However, due to the complicated distribution of the plasma in the inner magnetosphere and the inflexibility of the integral method in

the raytracing, radio wave rays that follow complicated paths can sometimes lead to large errors, preventing one from investigating how those rays propagate inside the Io plasma torus.

*Ladreiter and Leblanc [1990b]* performed raytracing calculation in their modeling of the Jovian HOM emission. What they tried to simulate is a magnetic equatorial beam that was postulated by *Alexander et al. [1979]*. Two constraints were taken into consideration in their model assumptions: (1) The CMI mechanism required a large initial wave normal angle, *i.e.*, the hollow cone must have a large opening angle (close to  $90^\circ$ ); (2) the radiation must eventually propagate parallel to the magnetic equator to reach the spacecraft. From a purely geometric approach and considering only the radiation propagating in the magnetic equatorial direction in the meridian plane of the spacecraft, they concluded that the HOM emission cannot come from low  $L$ -shell field lines because otherwise the opening angle of the beaming cone would be too small ( $< 30^\circ$ ) for the CMI mechanism to work. In their two-dimensional model, the HOM emission from both hemispheres is not initially beamed toward the magnetic equator, but rather toward the Io plasma torus. The Io torus naturally becomes the only refractor that can alter the propagating direction of the radio waves that pass through it. This idea worked rather well for radiation at low frequencies ( $< 500$  kHz). Radio waves at  $f < 500$  kHz initially propagating toward the Io torus are indeed refracted by the torus to produce a relatively large change in direction. They concluded that the Io plasma torus must play a key role in reshaping the emission beam of the HOM radiation. The implication is that the HOM emission would not show the magnetic equatorial beaming if there were no Io plasma torus. However, if their conclusion were true, one would expect the HOM emission at lower frequencies to be refracted and beamed to directions farther away from the magnetic equator. This is obviously contradictory to what was observed by the Voyager PRA experiment (see Section 4.1.3, page 57).

*Ladreiter and Leblanc* [1990b] then extended their conclusion to the higher frequency part ( $\geq 1$  MHz) of the HOM emission. Although they believe that the Io plasma torus plays the same crucial role of refraction for these higher HOM frequencies, their model encountered a great difficulty in this case. As I will show next, the plasma density in the Io torus is not high enough to affect high-frequency HOM emission to the extent required by their model. In order to have appreciable refraction effect on the high-frequency HOM emission, the actual Io plasma torus must have a greatly enhanced density distribution, at least 3 times higher than is given by the standard model of *Divine and Garrett* [1983]. Such a highly enhanced torus would, as will be shown below, block out the HOM emission at 500 kHz and below that would have passed through it. One of the objectives of this chapter is to investigate how the Io plasma torus would affect the HOM emission in its entire frequency range originating at presumed source locations.

We will see below that the raytracing involves the integration of a set of first-order ordinary differential equations (the so-called ray equations) upon a given magnetic field model and plasmasphere model (including an ionospheric model and the Io plasma torus model in the case of Jupiter). The *in situ* measurement by Voyager 1 and the later model of the Io plasma torus density show that the plasma density distribution is complicated and in many regions shows a large gradient. When integrating the ray equations the integral step length should be adjusted carefully and properly, especially in the regions where a large density gradient occurs, to minimize computation errors. The integration method used for solving the ray equations is therefore very crucial. According to *Ladreiter* [1990], the method being used in the *Ladreiter and Leblanc* [1990b] raytracing work is Euler's method, a straightforward yet often very inaccurate method in most cases of solving ordinary differential equations. In their independent raytracing work, *Wang and Carr* [1990] used an improved

differential-equation solving method, the fourth-order Runge-Kutta method, and obtained a more reliable result in support of an early model of the HOM emission [*Carr and Wang, 1988*].

Although the Io plasma torus is well known to be capable of effectively affecting propagations of radio waves at lower frequencies (in the hectometric and kilometric range) that pass through it, no work has been done on how it would affect radio emissions in the entire HOM frequency range from any plausible source locations. It was seen in Chapter 4 that the intensity profiles of the HOM emission at broad range frequencies are very similar. I will investigate to what extent the Io plasma torus can appreciably affect the radio emission at different frequencies originating from different places.

### 5.3 Formulation of Ray Equations

The first formulation of ray tracing equations that are suitable for integration by standard numerical methods was done by *Haselgrove* [1954]. This method does not have a restriction that the plasma in the magnetosphere be stratified and it can therefore be used with more realistic models of plasma density and magnetic field. Six first order differential equations that describe the motion of energy in electromagnetic waves propagating in an anisotropic medium in three dimensions were developed [*Haselgrove, 1954*]:

$$\left. \begin{aligned} \dot{r} &= \frac{c}{\tilde{n}^2} \left( n_r - \tilde{n} \frac{\partial \tilde{n}}{\partial n_r} \right) \\ \dot{\theta} &= \frac{c}{r \tilde{n}^2} \left( n_\theta - \tilde{n} \frac{\partial \tilde{n}}{\partial n_\theta} \right) \\ \dot{\varphi} &= \frac{c}{r \sin \theta \tilde{n}^2} \left( n_\varphi - \tilde{n} \frac{\partial \tilde{n}}{\partial n_\varphi} \right) \end{aligned} \right\}, \quad (5.1)$$

$$\left. \begin{aligned} \dot{n}_r &= \frac{c}{\tilde{n}} \frac{\partial \tilde{n}}{\partial r} + n_\theta \dot{\theta} + n_\varphi \dot{\varphi} \sin \theta \\ \dot{n}_\theta &= \frac{1}{r} \left( \frac{c}{\tilde{n}} \frac{\partial \tilde{n}}{\partial \theta} - n_\theta \dot{r} + n_\varphi r \dot{\varphi} \cos \theta \right) \\ \dot{n}_\varphi &= \frac{1}{r \sin \theta} \left( \frac{c}{\tilde{n}} \frac{\partial \tilde{n}}{\partial \varphi} - n_\varphi \dot{r} \sin \theta - n_\varphi r \dot{\theta} \cos \theta \right) \end{aligned} \right\}, \quad (5.2)$$

where  $\tilde{n}$  is the (complex) refractive index:  $\tilde{n} = n - i\chi$ , whose real and imaginary part,  $n$  and  $\chi$ , describe the phase velocity ( $c/n$ ) and attenuation rate of a wave travelling in a medium, respectively. Also,  $n_r$ ,  $n_\theta$  and  $n_\varphi$  are three components of  $n$  along the direction of the wave normal and they satisfy the following *normalization relation*:

$$n_r^2 + n_\theta^2 + n_\varphi^2 = \text{real} \{ \tilde{n}^2 \} = n^2. \quad (5.3)$$

The equations in (5.1) describe the time rate of change in the position of a ray, while those in (5.2) describe the time rate of change of the three components of the refractive index with respect to the position ( $r, \theta$ , and  $\varphi$ ), which express the motion of the energy of the wave in spherical coordinates.

One characteristic quantity in a magnetosphere (determined by the electron number density  $N_e$  and the superimposed magnetic field with flux density  $\mathbf{B}$ ) is the refractive index  $\tilde{n}$ . It is generally given as the solutions of the dispersion relation in a plasma, which, according to *Stix* [1962], is obtained from the condition for nontrivial solutions of a homogeneous set of field equations (see Appendix A). The dispersion equation is in a simple form:

$$A\tilde{n}^4 - B\tilde{n}^2 + C = 0, \quad (5.4)$$

where  $A$ ,  $B$ , and  $C$  are usually expressed in terms of ratios of some characteristic frequencies (plasma frequency  $\Pi_k$ , cyclotron frequency  $\Omega_k$ , and collision frequency  $\nu_k$  for all kinds of particles involved) to the wave frequency given by Equations (A.6) on page 170 and (A.10) on page 172 in Appendix A. However, for radio waves travelling through the planetary magnetosphere, these characteristic frequencies for particles



other than electrons are usually so small that their contribution to the refractive index can be completely ignored. Furthermore, the effective collision frequency,  $\nu$ , of electrons with other particles is very small in the magnetosphere (in the order of  $100 \text{ s}^{-1}$  or lower) compared with the frequency of radio waves being investigated, and can also be neglected in our study (assumption of cold plasma). Under these conditions, the refractive index  $\tilde{n}$  becomes either real (*i.e.*,  $\chi = 0$ , corresponding to propagating waves) or pure imaginary ( $n = 0$ , corresponding to evanescent waves) and is given by the Appleton-Hartree formula (see Appendix A for derivation):

$$\tilde{n}^2 = 1 - \frac{X(1-X)}{1-X - \frac{1}{2}Y^2 \sin^2 \xi \pm \sqrt{\frac{1}{4}Y^4 \sin^4 \xi + Y^2 \cos^2 \xi (1-X)^2}}, \quad (5.5)$$

where  $X$  and  $Y$  are the usual magnetoionic parameters that characterize the plasma and magnetic field distributions. In a cold plasma, they are defined by:

$$\begin{aligned} X &= \frac{f_p^2}{f^2}, & f_p &= \frac{1}{2\pi} \sqrt{\frac{e^2 N_e}{\epsilon_0 m_e}}, \\ Y &= \frac{f_c}{f}, & f_c &= \frac{1}{2\pi} \frac{eB}{m_e}, \end{aligned} \quad (5.6)$$

where  $f_p$  is the electron plasma frequency,  $f_c$  is the electron cyclotron frequency,  $f$  is the frequency of the wave,  $e$  and  $m_e$  are the charge and mass of the electron,  $\epsilon_0$  is the permittivity of free space,  $N_e$  is the electron number density of the plasma, and  $B$  the static magnetic field.

Equation (5.5) corresponds to two solutions,  $n_O$  and  $n_X$ , of the dispersion relation, representing two different modes of the wave (with different phase velocities in the medium): the upper sign (+) and lower sign (−) in the denominator of this equation refer to the ordinary (O) mode and the extraordinary (X) mode, respectively. These two branches of the refractive index are normally associated with different wave polarizations as well. For the R-X mode free escaping waves, they can only propagate

down to the  $R = 0$  cutoff frequency,  $f_{R=0}$ , where  $R$  is given by Equation (A.1) in Appendix A in general, and  $f_{R=0}$  is given by

$$f_{R=0} = \frac{1}{2}f_c + \sqrt{f_p^2 + \frac{1}{4}f_c^2} \quad (5.7)$$

for the cold plasma environment. For an R-X mode wave at frequency  $f$ ,  $f_{R=0}$  represents the region in which the R-X mode wave can propagate. Usually, the local electron plasma frequency  $f_p$  is very small compared with the local electron cyclotron frequency  $f_c$ ,  $f_{R=0}$  is therefore very close to the local electron cyclotron frequency  $f_c$ . On the other hand, the electron plasma frequency  $f_p$  marks the limit for which the L-O mode wave can propagate. Near the ionosphere, this limit is usually far below the altitude of the electron cyclotron frequency.

For a wave at frequency  $f$ ,  $\hat{n}$  is a function of  $N_e$ ,  $B$  and the direction angle  $\xi$  of the wave normal with respect to  $\mathbf{B}$ . The wave normal direction and the associated ray direction (the direction of energy flow) are in general different, because the refractive index  $n$  depends on the direction of the wave normal with respect to  $\mathbf{B}$ .

#### 5.4 Procedures of Solving the Ray Equations

The ray equations and the initial conditions form a system of six first-order ordinary differential equations, which can be expressed in a generic form as

$$\frac{d\mathbf{y}}{dx} = \mathbf{f}(x, \mathbf{y}) \quad (5.8)$$

with the initial condition  $\mathbf{y}(x_0) = \mathbf{y}_0$ , where  $\mathbf{y}$ ,  $\mathbf{y}_0$ , and  $\mathbf{f}$  are column vectors with 6 components. Various methods can be used to solve such a differential equation system; among those that we used, the Hamming modified predictor-corrector (MPC) method [Hamming, 1959] proved to be the most suitable one in the ray tracing problem. This method can achieve a satisfactory accuracy (in the order of  $h^5$ , where  $h$  is the integral

step length), and maintains a considerably faster speed because there is no iteration involved during integration and error estimation. This method is also stable, *i.e.*, the error measured by the difference between the true solution and the numerical one decreases in magnitude on the average as the integration proceeds step by step. The formulation of the Hamming MPC method is as follows:

$$\left. \begin{array}{ll} \text{Predictor:} & p_{i+1} = y_{i-3} + \frac{4h}{3} (2y'_i - y'_{i-1} + 2y'_{i-2}) \\ \text{Modifier:} & m_{i+1} = p_{i+1} - \frac{112}{121} (p_i - c_i) \\ & m'_{i+1} = f(x_{i+1}, m_{i+1}) \\ \text{Corrector:} & c_{i+1} = \frac{1}{8} [9y_i - y_{i-2} + 3h(m'_{i+1} + 2y'_i - y'_{i-1})] \\ \text{Final value:} & y_{i+1} = c_{i+1} + \frac{9}{121} (p_{i+1} - c_{i+1}) \end{array} \right\} . \quad (5.9)$$

Obviously, the Hamming MPC method is not a self-starting method. That is, each step of the integration in this method requires the knowledge of past values of the solution which are not available at the start of the integration. To obtain the values required to start the solution, the fourth-order Runge-Kutta integration formula is used. This is so done because starting values  $y_i$  calculated with the fourth-order Runge-Kutta method are as accurate as the Hamming MPC method; errors in the first few values will not be so large as to degrade the later accuracy or to increase the tendency toward instability.

The Jovian magnetosphere has a very complex environment. Ray tracing through such an environment requires not just a fast and accurate integration method, but properly adjusted integration increment steps. Computation speed is not a major concern nowadays, but to maintain required accuracy without slowing down the computation speed, it is desirable that the integration increment step  $h$  be decreased when the estimated per step truncation error grows too large to be tolerable, and be increased when estimated per step error is much smaller than necessary. It is

generally practical to double the value of  $h$  if the interval is to be increased, and to halve the value of  $h$  when decreasing the size of the interval. When this scheme of varying integral step lengths is applied to the Hamming MPC method, one can expect accurate integral results at an optimized speed. In my calculation, a standard IBM library FORTRAN subroutine, DHPCG, has been modified to carry out the integration of the ray equations. The computation procedure was originally developed by *Ralston* [1960]. To achieve the required accuracy, the following criteria are imposed when doubling and halving the increment step: whenever the relative error of *either one* of the integral variables is greater than the tolerable error limit, the increment step is halved; the increment step is doubled only when the relative errors of *all* integral variables are smaller than  $1/50$  of the tolerant error limit. In addition, double precision variables are used in all core subroutines of the program to ensure the necessary accuracy.

Before one starts integrating the ray equations, initial values of  $r$ ,  $\theta$ ,  $\varphi$ ,  $n_r$ ,  $n_\theta$ , and  $n_\varphi$  are needed.  $r$ ,  $\theta$ , and  $\varphi$  are given by the problem concerned; to get  $n_r$ ,  $n_\theta$ , and  $n_\varphi$ , the wave normal direction specified by  $\xi$  and  $\zeta$  as an initial condition is used. The program checks to see if a wave at the given frequency can propagate from a given point toward the given direction. At the given point in the space, the program calculates the refraction index surface for waves propagating in a given mode (either the X or O mode) based on the assumed magnetic field model and the plasma model of the magnetosphere. The program then takes an incremental step perpendicular to the surface of the refraction index (which indicates the direction of the group velocity and energy flow) so that a new point is found, where the refraction index surface can be calculated, and the steps are repeated.

Various efforts have been made to minimize computation error. For example, terms associated with the ray equations are arranged such that evaluation of multi-value functions (square root, arc sine, arc cosine, etc.) are avoided wherever possible.

The advantage of doing this, as has been suggested by *Jones and Stephenson* [1976], is that one can avoid discontinuous changes of those multi-value functions from one point on the ray path to the next. See Appendix B for details on how the ray equation terms are grouped. Also, during calculation, round off error may be introduced in calculating  $n^2$  (via the Appleton-Hartree formula) and in integrating  $\dot{n}_r, \dot{n}_\theta, \dot{n}_\varphi$ , which may result in  $n_r^2 + n_\theta^2 + n_\varphi^2 \neq n^2$ . For this reason, after each integral step is achieved,  $n_r, n_\theta$ , and  $n_\varphi$  are adjusted to make sure that the normalization relation (5.3) is kept valid.

Several methods of testing and validating the computer codes were performed. One of them is to trace rays from a specified source location toward various directions, especially those toward which the rays would be expected to be refracted heavily. The ray is then traced backward at a certain point and deviation of the returned ray from its origin is calculated. Figure 5.1 presents an example of such a test for rays traced with different methods of integration. In the figure, radio wave rays at a frequency of 500 kHz from  $L=20$  magnetic field line are traced starting at the point where the cyclotron frequency is equal to the wave frequency. The left panel is the result of the fourth-order of the Runge-Kutta method, and the right panel is from the Hamming MPC method. The result shows that the Runge-Kutta method is accurate enough only for ray paths along which the gradient of plasma density is small. For the region where large plasma density and gradient occur, the calculation leads to larger errors than the Hamming MPC method. The Euler method, which is used by *Ladreitner and Leblanc* [1990b], leads to an even larger error (not shown in the figure) for the rays traced with the same initial conditions. The Hamming MPC method, however, does a much better job when dealing with rapidly changing gradient of plasma torus.

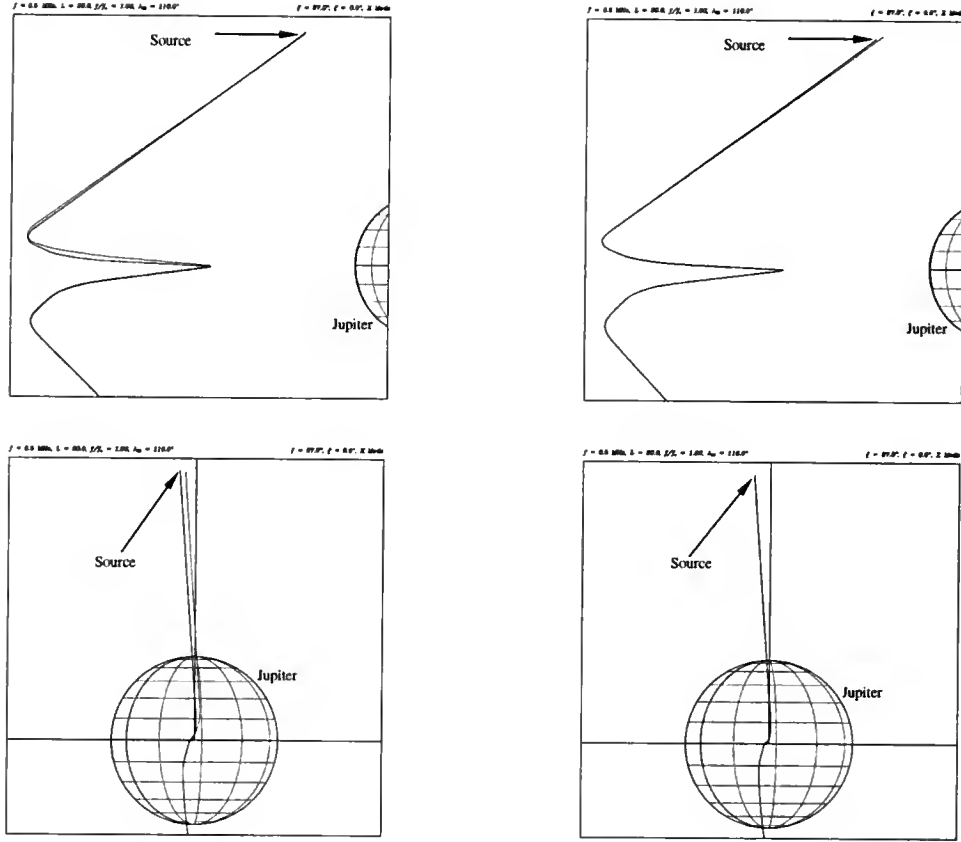


Figure 5.1. Testing of raytracing code. Integration method used in left panels is the fourth-order Runge-Kutta method, while that in right panels is the Hamming MPC method. Upper panels are plotted from the point of view perpendicular to the tracing meridian plane, and lower panels are plotted from the point of view facing the tracing meridian plane.

### 5.5 Magnetic Field Model and Magnetospheric Plasma Model

Propagation of radio waves inside a planetary magnetosphere is highly dependent on the distribution of plasma in the ionosphere and in other regions like the Io plasma torus in the case of the Jovian magnetosphere. It also depends on the distribution of the planetary magnetic field. A good knowledge of the strength and geometry of the planetary magnetic field and plasma distribution within the magnetosphere is both required and crucial in the raytracing process. The magnetic field and plasmasphere models must be acceptable representations of the physical magnetospheric environment which affects the radiation. The raytracing technique itself provides a way of

testing models of the planetary plasmasphere and magnetosphere. In the case of the Jovian magnetosphere, the *in situ* measurement of the Jovian magnetic field in the inner and outer Jovian magnetosphere was made first by the Pioneer 11 spacecraft and later by the two Voyagers. Models based on such observations were made [Davis *et al.*, 1975; Acuña and Ness, 1976; Connerney *et al.*, 1981; Connerney, 1992]. Observations of the plasma distribution in the Jovian ionosphere and in the vicinity of the Io plasma torus were also made by the two Voyagers, and modeled by several researchers [Bagenal *et al.*, 1980; Divine and Garrett, 1983; Bagenal *et al.*, 1985]. These models are so far the best ones that are available and have been used successfully in the study of various phenomena in the Jovian magnetosphere.

In our raytracing calculation, the  $O_4$  magnetic field model of Acuña and Ness [1976] is used. The  $O_4$  model provides spherical harmonic coefficients corresponding to the dipole, quadrupole and octopole terms. A contour map and field vector map of the magnetic field strength on Jupiter's surface calculated from this model are shown in Figure 5.2 (Jupiter's dynamic flattening of 1/15.4 has been taken into account). Other magnetic field models such as the P11(3,2)A model [Davis *et al.*, 1975] and the  $O_6$  model [Connerney, 1992] are also used for comparison.

As for the plasmasphere model, the one made by Divine and Garrett [1983] is used. The electron density contours calculated from the model are shown in panel (a) of Figure 5.3. The peak electron density in the torus is about  $3500 \text{ cm}^{-3}$ , corresponding to a plasma frequency of 530 kHz. However, this highly concentrated region is very small as can be seen in the figure. Also shown in Figure 5.3 are the contour curves of the electron plasma frequency  $f_p$  (panel b), the ratio of  $f_p/f_c$  (panel c), and the  $R=0$  cutoff frequency  $f_{R=0}$  (panel d), where  $f_{R=0}$  is given by Equation (5.7). Necessary modifications to the Io plasma torus model will be made in the raytracing calculation for further investigation of the electron distribution in the Io plasma torus.

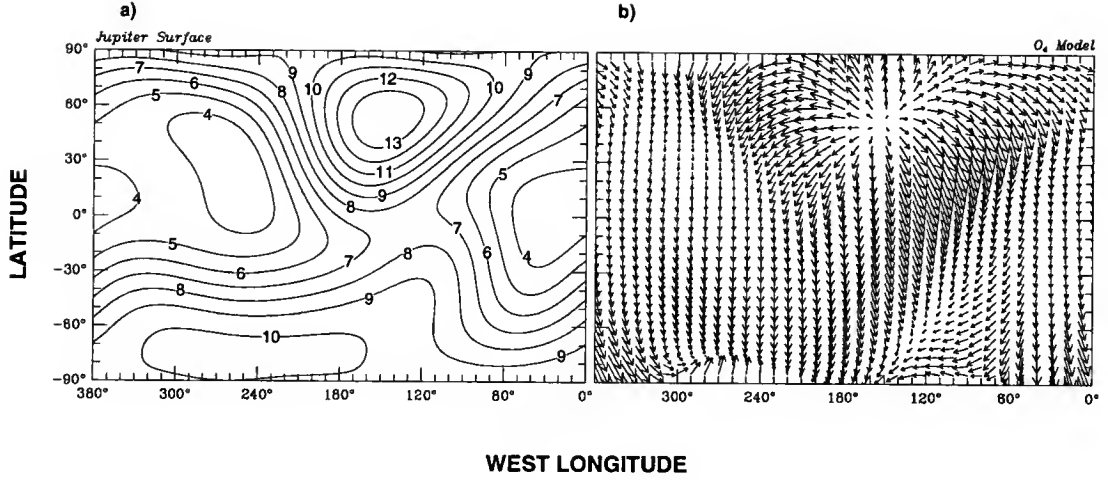


Figure 5.2. The Jovian O<sub>4</sub> magnetic field model [Acuña and Ness, 1976]. (a) Contours of the magnetic field strength on the surface in the form of Mercator projection. Contour levels are labeled in units of gauss. (b) Projection of the magnetic field vector onto the surface. Jupiter's dynamic flattening of 1/15.4 has been taken into account in the plots.

### 5.6 Two-dimensional Raytracing Result

To show generally how the HOM emission rays are affected by the Io plasma torus, I traced rays propagating from a specified source location in the meridian plane of the source in a wide frequency range. The Voyager observations indicate that the HOM emission is dominated by the right hand (RH) polarization when the spacecraft is in the northern magnetic hemisphere, and is left hand (LH) dominated when the spacecraft is in the southern hemisphere [Ortega-Molina and Lecacheux, 1991; Section 4.1.4, this dissertation]. This suggests that the RH polarized radiation is associated with the northern hemisphere, while the LH polarized radiation is associated with the southern hemisphere. Emissions excited in the R-X mode from both hemispheres seem to fit this scenario. On the other hand, the L-O mode waves from one or both hemispheres can also be excited and freely escape from the Jovian magnetosphere. As a matter of fact, the new observation from the Ulysses URAP experiment does indicate that both RH and LH circularly polarized emissions originate from the same



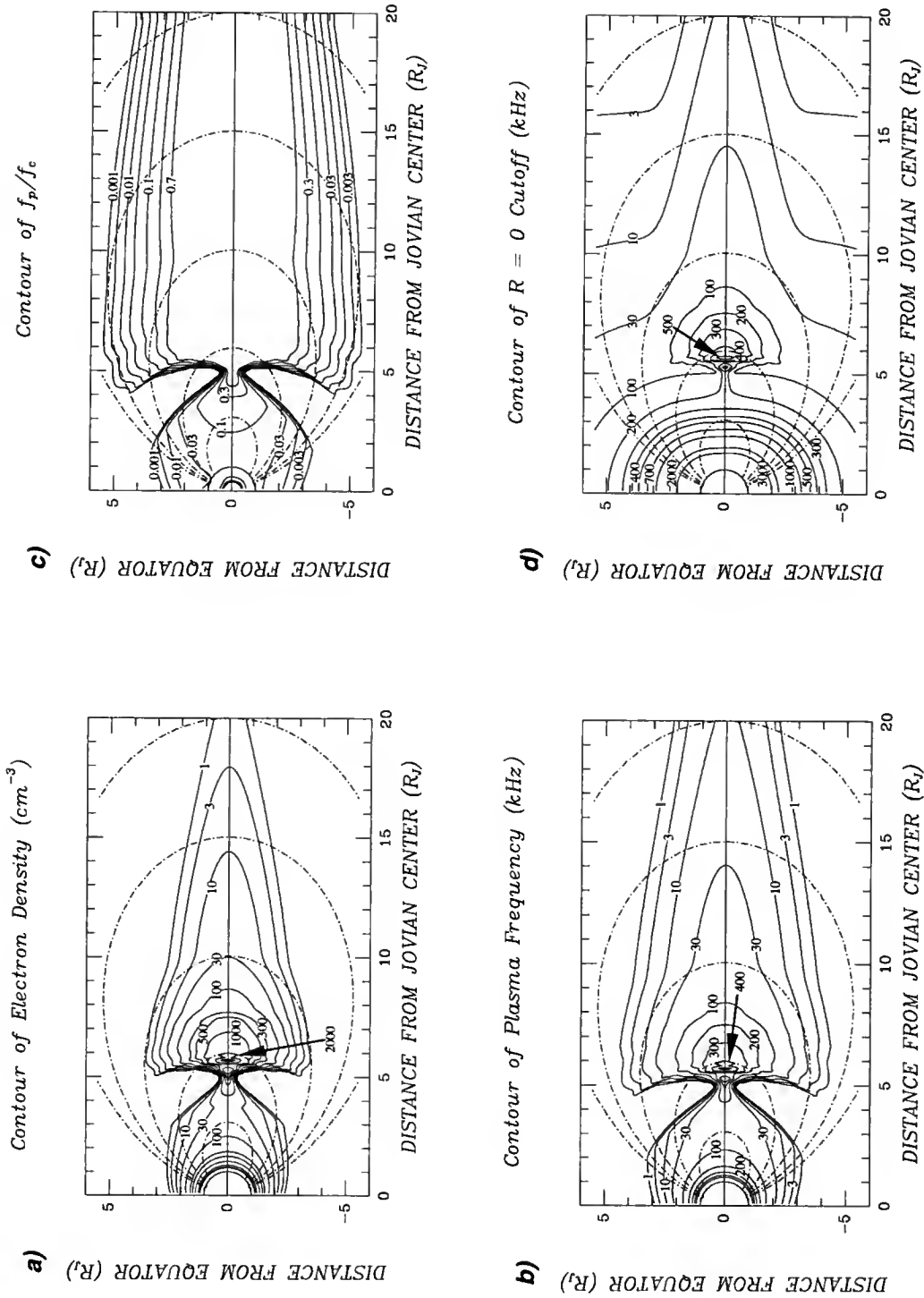


Figure 5.3. Plasma parameters of the Jovian inner magnetosphere. (a) Contours of the electron number density in units of  $\text{cm}^{-3}$ . The maximum electron density near the torus center is  $3500 \text{ cm}^{-3}$ . (b) Contours of the electron plasma frequency  $f_p$ . (c) Contours of ratio of  $f_p$  to the electron cyclotron frequency,  $f_c$ . (d) Contours of  $R=0$  cutoff frequency,  $f_{R=0}$ . Over-plotted are also magnetic field lines for  $L$ -shells of 6, 10, 15, and 20, calculated with an OTD model.

hemisphere [Reiner *et al.*, 1993a]. Since the polarization sense is determined as a result of computation of both RH and LH components received by the Voyager PRA receivers, it is likely that the PRA receiver also detected weaker radiation in the L-O mode. Waves in both the R-X and L-O modes were therefore investigated, and some implications for the HOM source locations were considered.

The three quantities used to specify a source location are (a) the  $L$ -shell value of the field line that passes through the source, (b) the east longitude of the field line at the equator, and (c) the ratio of the wave frequency ( $f$ ) to a characteristic frequency of the wave. For waves in the R-X mode, the characteristic frequency is the electron cyclotron frequency  $f_c$ , and the frequency ratio will be  $f/f_c = \sigma$ , where  $\sigma$  is a constant. For the fundamental emission in R-X mode,  $\sigma$  is just above unity (in this case, it is an indication of how close the source is to the  $f_c = f$  surface); for harmonic emissions,  $\sigma = 2, 3, \dots$ . For waves in the L-O mode, the characteristic frequency can be either the electron plasma frequency ( $f_p$ ) or the electron cyclotron frequency ( $f_c$ ). According to the CMI theory, the L-O mode waves can also be excited at the place where the R-X waves are excited (*i.e.*, just above the  $f_c = f$  surface). Usually, this place is far above the stop zone surface ( $f = f_p$ ) of the L-O mode wave (below which the L-O mode wave cannot propagate). The L-O mode radiation can be therefore excited and propagate anywhere above the  $f = f_p$  surface. Since both the magnetic equator and the torus plane are tilted from Jupiter's rotational equator, for the purpose of two-dimensional investigation, it is best to place sources on the field line whose longitude is  $90^\circ$  or  $-90^\circ$  from the tilting direction of the dipole moment and to trace rays propagating in the direction close to that meridian plane. In that meridian plane, the Io plasma torus is almost symmetric about the rotational equator. In this way, rays from a source in the southern hemisphere are roughly symmetric about those from its conjugate source in the northern hemisphere. (The raytracing calculation is actually done in the frame of the Jovigraphic coordinate system.) Tracing results for rays from such sources at

this longitude can be applicable to sources at other longitudes as long as the results are presented in the magnetic coordinate system.

### 5.6.1 R-X Mode

The raytracing results for waves in the R-X mode at frequencies of 300, 500, 750, and 1000 kHz for  $L = 20$  are presented in Figure 5.4. In the figure, only rays with zero degree azimuth angle ( $\zeta = 0^\circ$ , cf. Figure 4.16a on page 85 for illustration) and the initial wave normal angles in the range between  $\xi_{\min}$  and  $\xi_{\max}$  at a  $2^\circ$  interval are traced. These rays propagate approximately in the meridian plane of the source. The traced rays and the magnetic field line that passes through the source are projected onto the meridian plane of the source. For waves at a given frequency, there is a stop zone boundary determined by the  $R=0$  cutoff frequency curves inside which no propagation of waves at that frequency or lower is allowed. Rays at a given frequency are reflected just before reaching the stop zone surface for that frequency. This is the most obvious for those rays at  $f = 300$  kHz that were launched initially toward the torus center (see Figure 5.4a). Multi reflections at the stop zone surfaces between the Io torus and the Jovian ionosphere occurred.

The following important conclusions can be drawn based on the raytracing results shown in Figure 5.4: (1) The refraction effect from the Io plasma torus begins to diminish for radiation at frequencies above 750 kHz. For radiation at frequencies higher than 1 MHz, such refraction effect has virtually disappeared. (2) The Io plasma torus only affects the low frequency rays that propagate through the region close to the central part of the torus. The torus can keep low-frequency radiation originating from the northern source regions from propagating far south of the magnetic equator; likewise, the low-frequency radiation from the southern source regions can be blocked by the torus from reaching further north. (3) Rays at all frequencies that initially

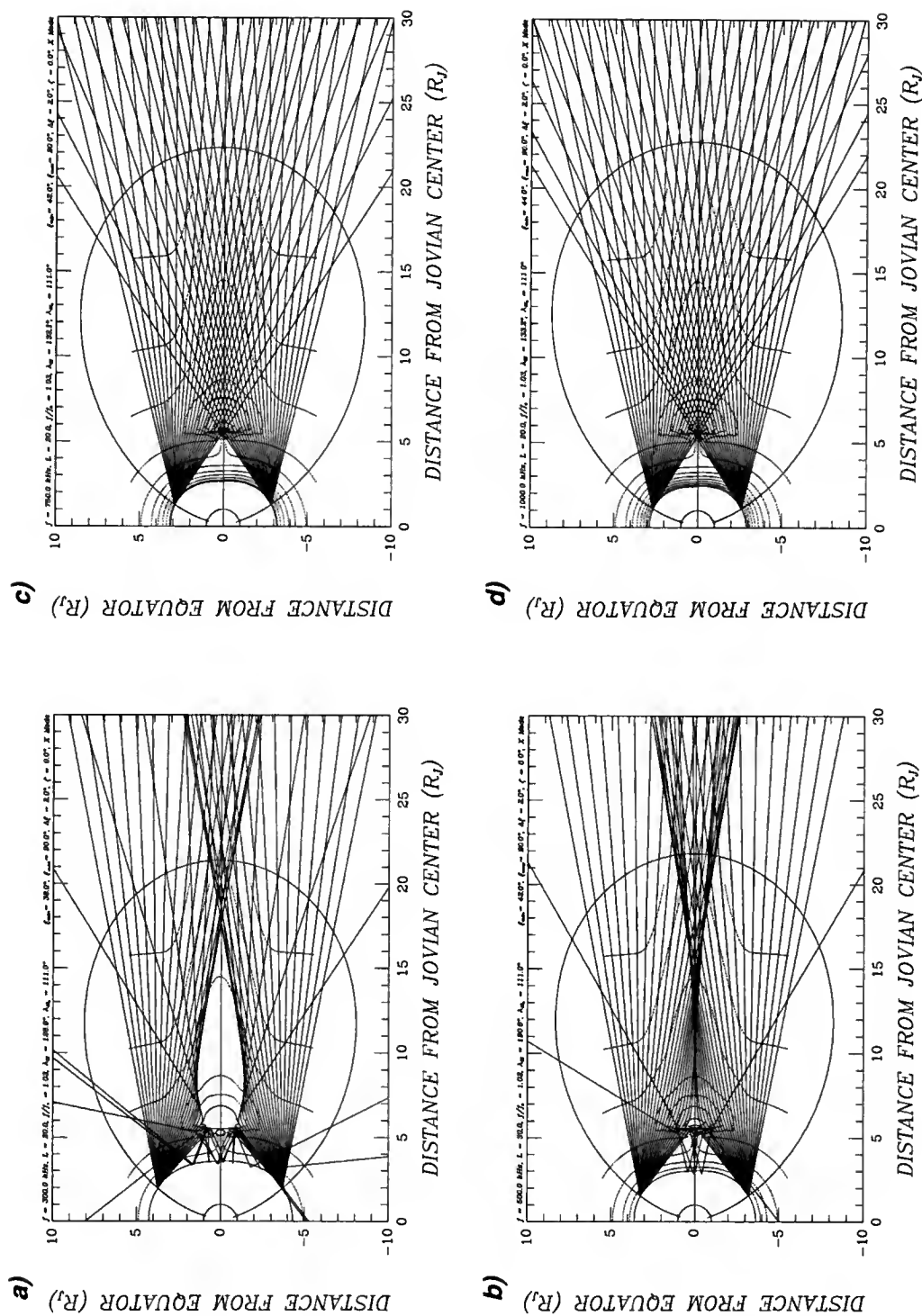


Figure 5.4. Two-dimensional raytracing of the HOM emission propagating in the X mode at frequencies of 300 kHz (panel *a*), 500 kHz (panel *b*), 750 kHz (panel *c*), and 1000 kHz (panel *d*) from  $L = 20$  field line close to the meridian plane whose longitude is  $111^\circ$ . All rays and the magnetic field line that passes through the source are projected onto the meridian plane on which the source lies. Also over-plotted are contour curves of the  $fR=0$  cutoff frequency surface for frequencies 3 kHz, 10 kHz, 30 kHz, 100 kHz, ... and up to the wave frequency concerned (see Figure 5.3).

propagate toward or above the magnetic equator are *not* affected by the Io torus. These rays have relatively smaller initial wave normal angles. Since the emission received by an observer near the equator may not necessarily come from the equatorial edges of the emission cone, these rays directly reaching the observer can still have large initial wave normal angles. This justifies our assumption of straight line propagation of the HOM emission in my modeling in Chapter 4 in which emissions beamed into the side edges of hollow cones can also reach the observer. (4) The Io plasma torus is *not* responsible for the formation of the so-called shadow zone near the equator at least for emissions above 500 kHz. This is quite contradictory to what *Ladreiter and Leblanc* [1990b] had concluded. The shadow zone described by them was observed not just in the low frequency part of the HOM emission, but in the other (high) frequency part as well. I believe that the shadow zone must be due to other causes such as source geometric configuration and probably refraction near the source region. (5) It was suggested that the HOM emission is the low-frequency extension of the non-Io DAM emission [*Lecacheux and Moller-Pedersen*, 1980; *Alexander et al.*, 1981; *Genova et al.*, 1987; *Barrow and Desch*, 1989]. However, the observed peak near 1 MHz [*Brown*, 1974b] distinguishes the HOM from the non-Io DAM. *Ladreiter* [1990] and *Ladreiter and Leblanc* [1990b] suggested that such a spectral peak near 1 MHz can be produced by the focusing of the radiation due to refraction effects of the Io torus. Our calculation shows however, if there were such a focusing effect, it would occur at frequencies much lower than 1 MHz.

The above conclusions still hold for rays originating from different  $L$ -shells at different frequencies, as are shown in Figures 5.5 and 5.6. In these figures, deviations of the ray's final direction from the initial propagating direction (the would-be direction if there were no refraction effect) are plotted as a function of the initial wave normal angle. Figure 5.5 gives the raytracing results for the radiation at different frequencies originating on a given  $L$ -shell. It shows that for radiation at  $f = 300$  kHz, rays do

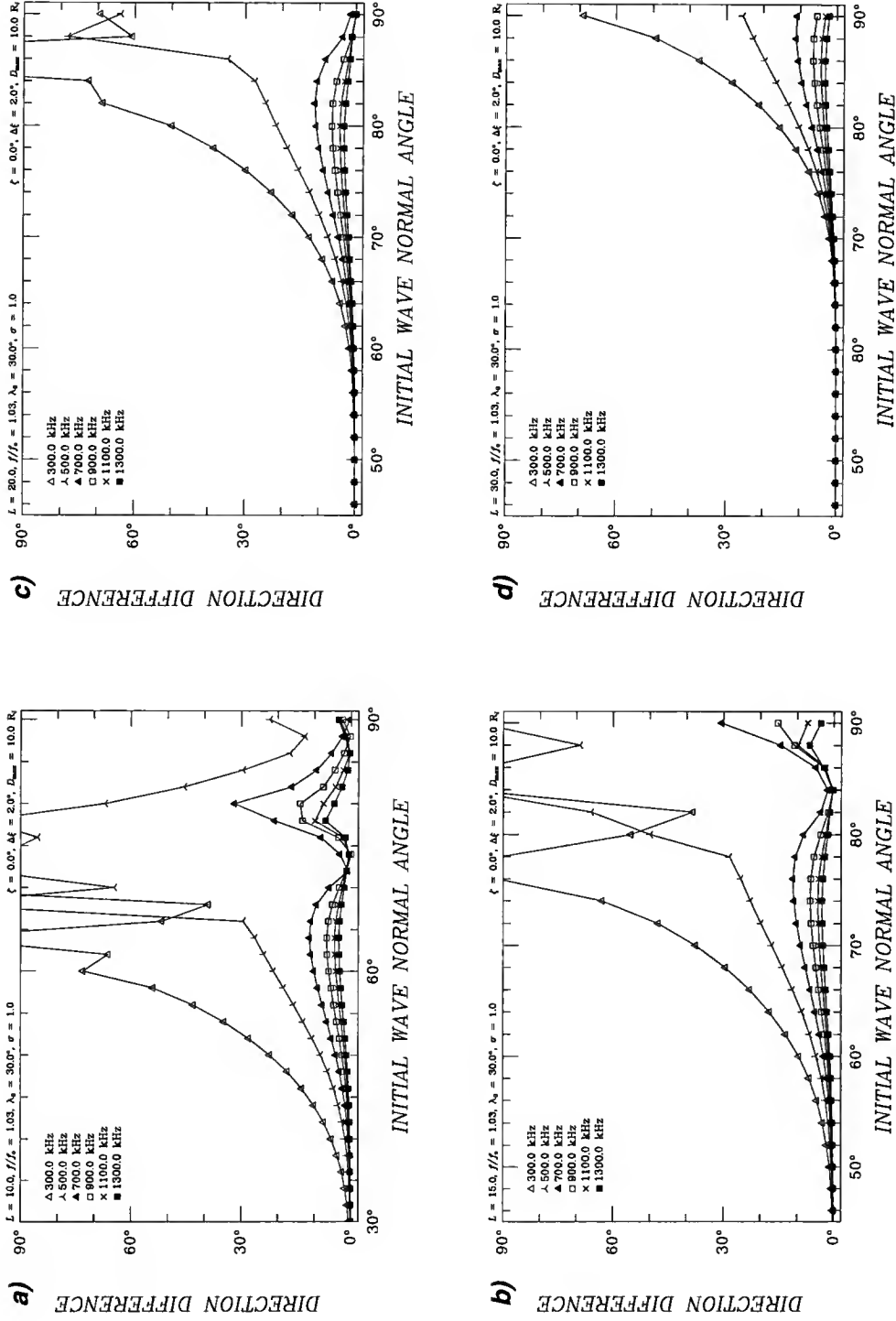


Figure 5.5. Direction difference of traced rays from their initial direction for radiation at different frequencies (300, 500, 700, 900, 1100, and 1300 kHz), originating close to the  $f_c = f$  surface ( $f/f_c = 1.03$ ) on the magnetic field lines with  $L=10$  (panel a),  $L=15$  (panel b),  $L=20$  (panel c), and  $L=30$  (panel d).

not start deviating until the initial wave normal angle  $\xi$  is more than  $30^\circ$  for  $L = 10$ , and more than  $60^\circ$  for  $L = 20$ . Only the emissions below 500 kHz can be refracted appreciably from their original directions when the initial wave normal angle becomes larger (in this case rays are initially propagating directly toward the dense part of the torus); emissions above 900 kHz do not change their propagation directions significantly (with a maximum deviation of  $5^\circ$  or less) even when the propagation direction is initially toward the torus center. The double peaks in panels (a) and (b) in Figure 5.5 for the radiation above 700 kHz are caused by the joint refraction effect near the torus and at the source region. For sources on higher  $L$ -shell field lines, emitted waves that can reach the torus must have larger initial wave normal angles, and the refraction effect from the Io torus is significant *only* for lower frequency ( $< 500$  kHz) emissions, no matter what the initial wave normal angle is.

Figure 5.6 compares raytracing results for the emission at for four given frequencies but originating on different  $L$ -shells. It shows that for the low frequency ( $\lesssim 500$  kHz) HOM emission, if its source is on low  $L$ -shells ( $< 10$ ), rays near the meridian plane can be completely blocked out by the Io torus, especially if the initial wave normal angle is large enough such that the rays are directly launched toward the torus center. As the frequency increases, the amount of refraction by the Io torus becomes smaller and smaller, even for rays that directly hit the torus center.

All of above calculations are based on the assumption that the Jovian  $O_4$  magnetic field model [Acuña and Ness, 1976] and the Jovian ionospheric and Io plasma torus model [Divine and Garrett, 1983] are realistic representations of the Jovian magnetosphere. As has been stated, these models, especially the magnetic field models, are the best available to date. Similar calculations were made when the magnetic field model was switched to the P11(2,3)A and to the  $O_6$  models, and the results are similar to those calculated with the  $O_4$  model. Modification to the Io torus model of Divine and Garrett [1983] can, however, lead to different results. The current torus

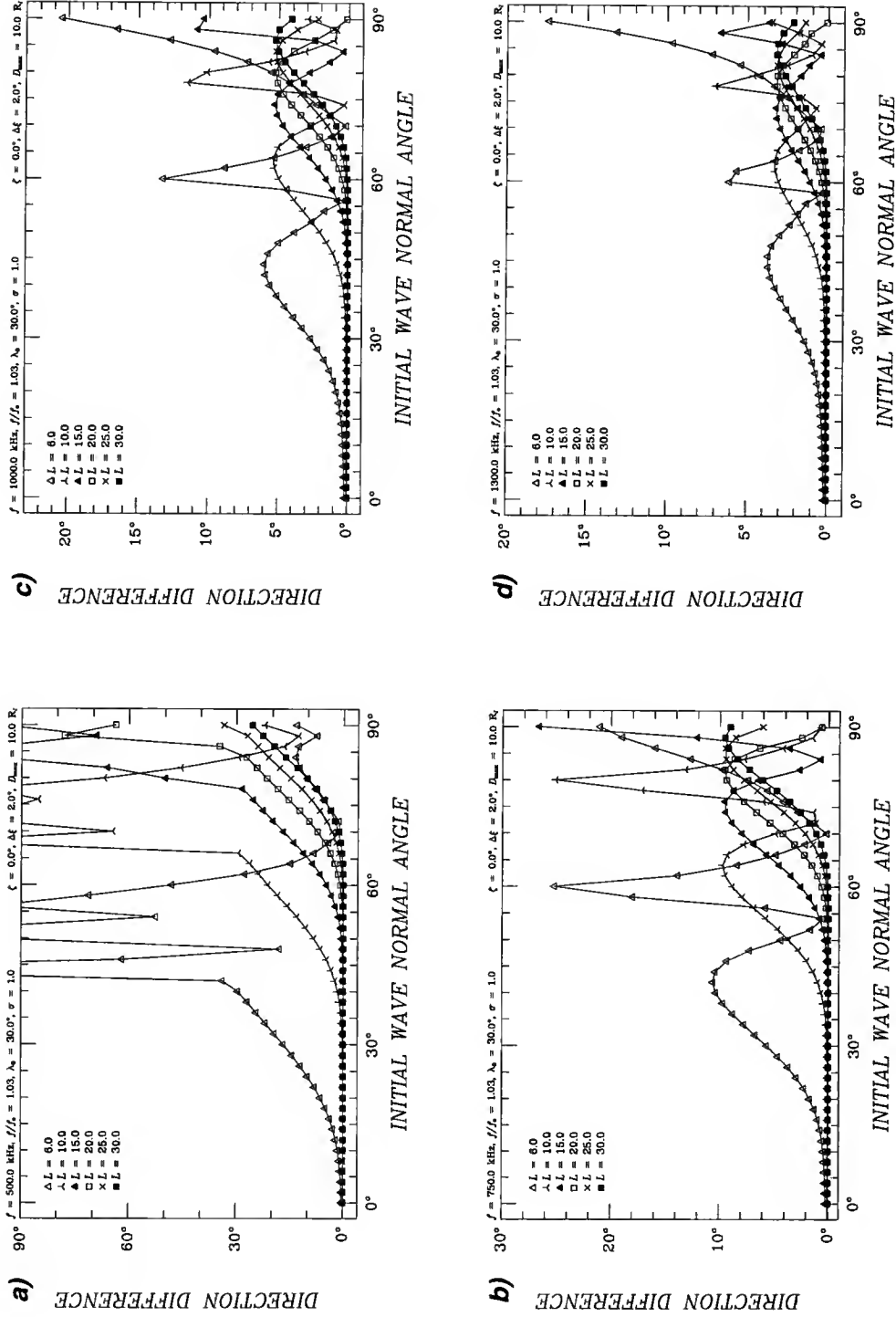


Figure 5.6. Direction difference of traced rays from their initial direction for the radiation emitted close to the  $f_c = f$  surface on different magnetic field lines ( $L = 6, 10, 15, 20, 25, 30$ ) at frequencies  $f = 500$  kHz (panel a),  $f = 750$  kHz (panel b),  $f = 1000$  kHz (panel c), and  $f = 1300$  kHz (panel d). Notice the different scales in the coordinate axes.



model was made mainly based on a single *in situ* measurement during the Jupiter encounter by Voyager 1, which covered only a limited longitudinal region. This model implies that the plasma distribution in the torus is longitudinally symmetric (*i.e.*, independent of longitude of any meridian plane). There are, however, evidences that the temperature and the radial extent of the torus plasma are longitudinally asymmetrical [Pilcher *et al.*, 1981; Hill *et al.*, 1983]. Also, the maximum electron density in the torus center could be over- or under-estimated.

In an effort to reconcile the Io torus' incapability of altering propagation directions for the high frequency HOM emission, Ladreiter and Leblanc [1990b] speculated that the torus might be much denser than what was observed and modeled. There are two aspects in the Ladreiter and Leblanc [1990b] model that demand the torus to be much denser. The first is that at least 25% enhancement of the electron density in the torus is needed for the torus to create a shadow zone for the HOM emission. The other is that the torus density must be at least three times higher than what the Divine and Garrett [1983] model predicts for the torus to alter the high frequency HOM ray paths toward the magnetic equator. I investigated the plausibility of such scenarios by enhancing the electron density of the torus to a level that would put a similar refraction effect on radiation at 1 MHz to that on radiation at 500 kHz when the torus plasma is not modified. Results are shown in Figure 5.7 for radiation at 300, 600, 800, and 1000 kHz with  $L = 20$ , when the electron density in the torus is enhanced 3 times higher than that of the Divine and Garrett [1983] model. It is shown that only such a highly enhanced torus can appreciably affect propagation of the radio waves at 1 MHz. Shadow zones begin to form even for the radiation at 800 kHz, and become larger for radiation at lower frequencies. Rays at lower frequencies that were bent toward the (magnetic) equator under the Divine and Garrett [1983] model are now blocked out by the enhanced torus. If the radio sources are on low  $L$ -shells ( $L < 20$ ), they will be closer to the equator, and more rays at lower frequency

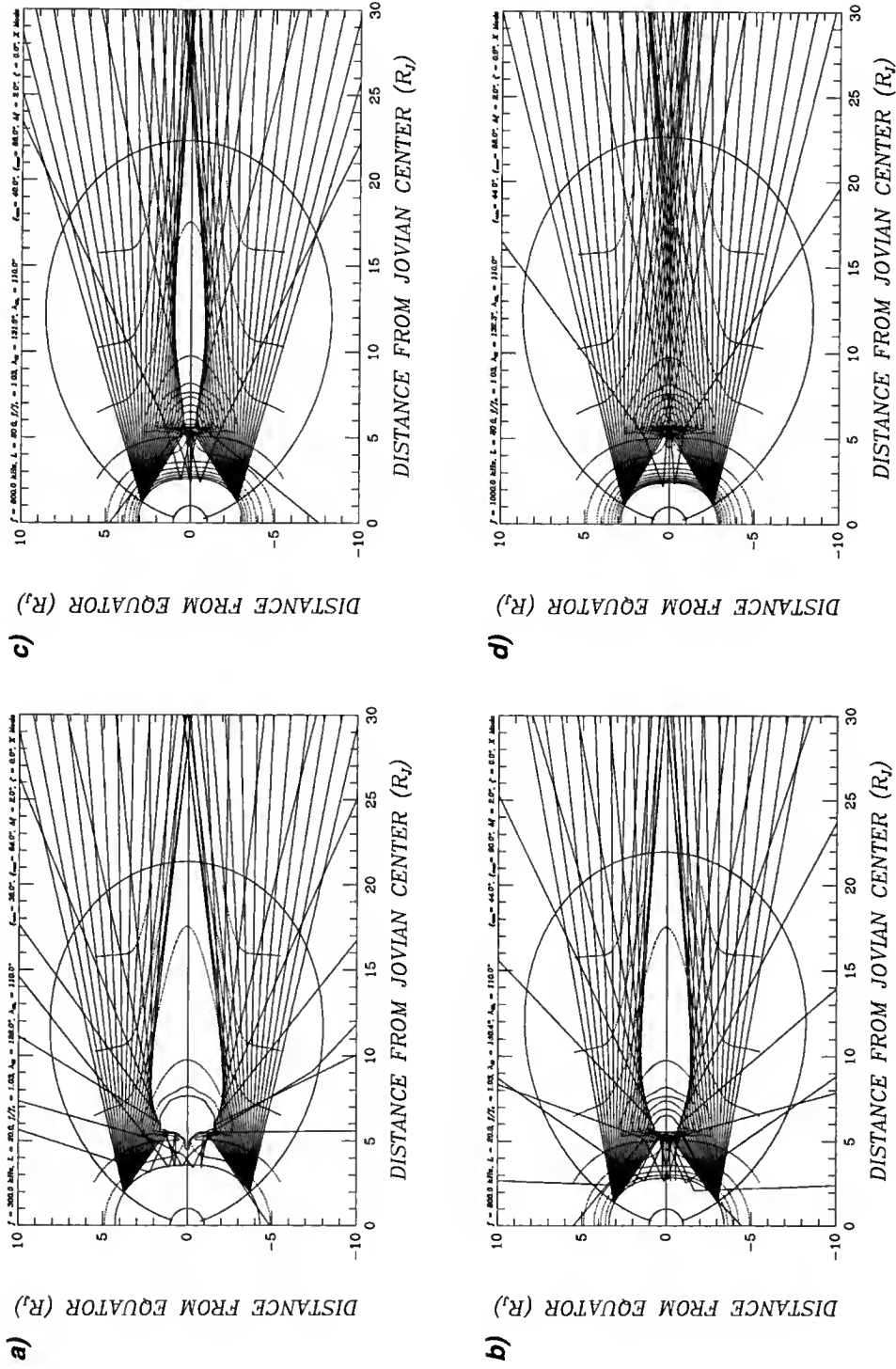


Figure 5.7. Two-dimensional raytracing of the HOM emission in the R-X mode at frequencies of 300 kHz (panel a), 600 kHz (panel b), 800 kHz (panel c), and 1000 kHz (panel d) from the  $L=20$  field line close to the meridian plane whose longitude is  $110^\circ$ . The electron density in the Io plasma torus has been enhanced 3 times higher than the *Divine and Garrett* [1983] model.

will be blocked out by the torus. These results indicate that the Io plasma torus cannot be the source which alters the propagation direction of the radio emission in the entire HOM frequency range. It is worth noting that even a highly enhanced torus is assumed, radio waves at all HOM frequencies, provided they are emitted at relatively high latitudes (or large  $L$ -shells) and initially propagate toward the equator, still do not suffer any refraction from the torus; instead, they escape straight away from the magnetosphere to reach the observer near the equator.

We have seen that a highly enhanced Io torus does not seem to be the case; it is possible that the plasma density in some longitudinal part of the Io torus has been overestimated. The latest observation by Ulysses basically confirmed the electron density in the Io plasma torus measured by Voyager 1 more than a decade ago: the Io plasma torus seems to be less extended out of the centrifugal equator [Bird *et al.*, 1992]. It is likely that the plasma density distribution in the Io plasma torus is not longitudinally symmetrical, and there are regions at some longitudes for which the plasma density is overestimated. If this is indeed the case, then even the radiation at 500 kHz will be only slightly affected by the torus, as is shown in Figure 5.8, in which the emission at two frequencies (300 kHz and 500 kHz) is traced when the electron density distribution in the torus is reduced 50% from that of the *Divine and Garrett* [1983] model. In this case, the Io plasma torus is virtually transparent to the majority of the HOM emission.

### 5.6.2 L-O Mode

I have investigated above how radio waves in the R-X mode would propagate in the inner Jovian magnetosphere and be affected by the Io plasma torus. The R-X mode wave undoubtedly is the dominant component of the HOM emission; the L-O waves, however, also make an appreciable contribution. For example, the URAP

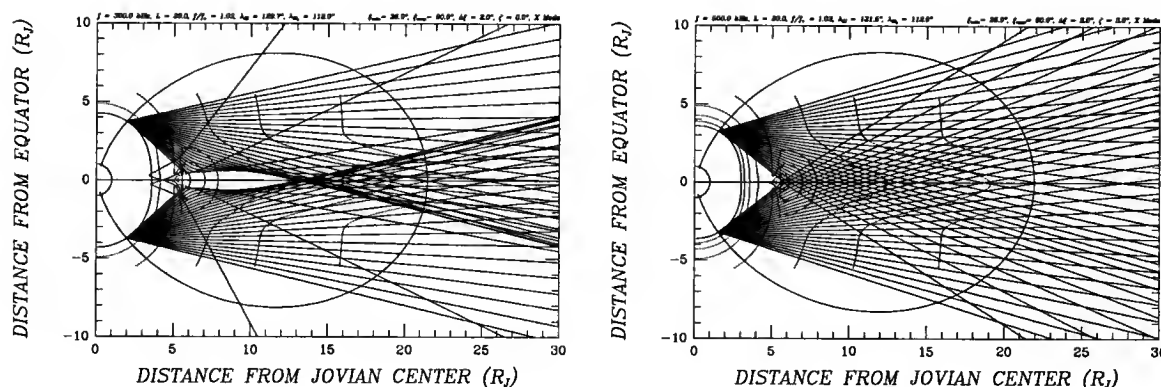


Figure 5.8. Raytracing of the HOM emission at 300 kHz (left panel) and 500 kHz (right panel) for  $L=20$  for a reduced (50%) Io torus plasma density distribution.

experiment of Ulysses observed strong LH polarized emission in the HOM wavelength band when Ulysses was still in the northern hemisphere, in addition to the RH waves that it observed at the same time [Reiner *et al.*, 1993b]. Such LH northern hemisphere emission was in the L-O mode. I investigated the propagation of L-O waves in the inner Jovian magnetosphere for two typical HOM wave frequencies: 500 kHz and 1000 kHz. Notice that the L-O mode waves can be excited anywhere above the altitudes of the  $f_p = f$  surface (for the fundamental mode), especially near the  $f_c = f$  surface (for other harmonic modes) where the R-X mode waves are excited.

At each of the two frequencies, I considered three cases for the L-O mode waves: one for the fundamental emission excited near the  $f_p = f$  surface, one for the second-harmonic emission, and the third one for emission excited at the same place where the R-X waves are excited (*i.e.*, near the  $f = f_c$  surface). The results are shown in Figure 5.9, in which parameters for the source location and initial ray directions are indicated on the top of each panel. In the case of fundamental and second-harmonic emissions (fundamental emission case not shown in the figure), since the source point is not far away from top of the ionosphere, the L-O waves excited from such a place will be quite close to the magnetic equator, and the Io plasma torus is right on their way out. As can be seen from Figure 5.9, waves at frequency 500 kHz or lower

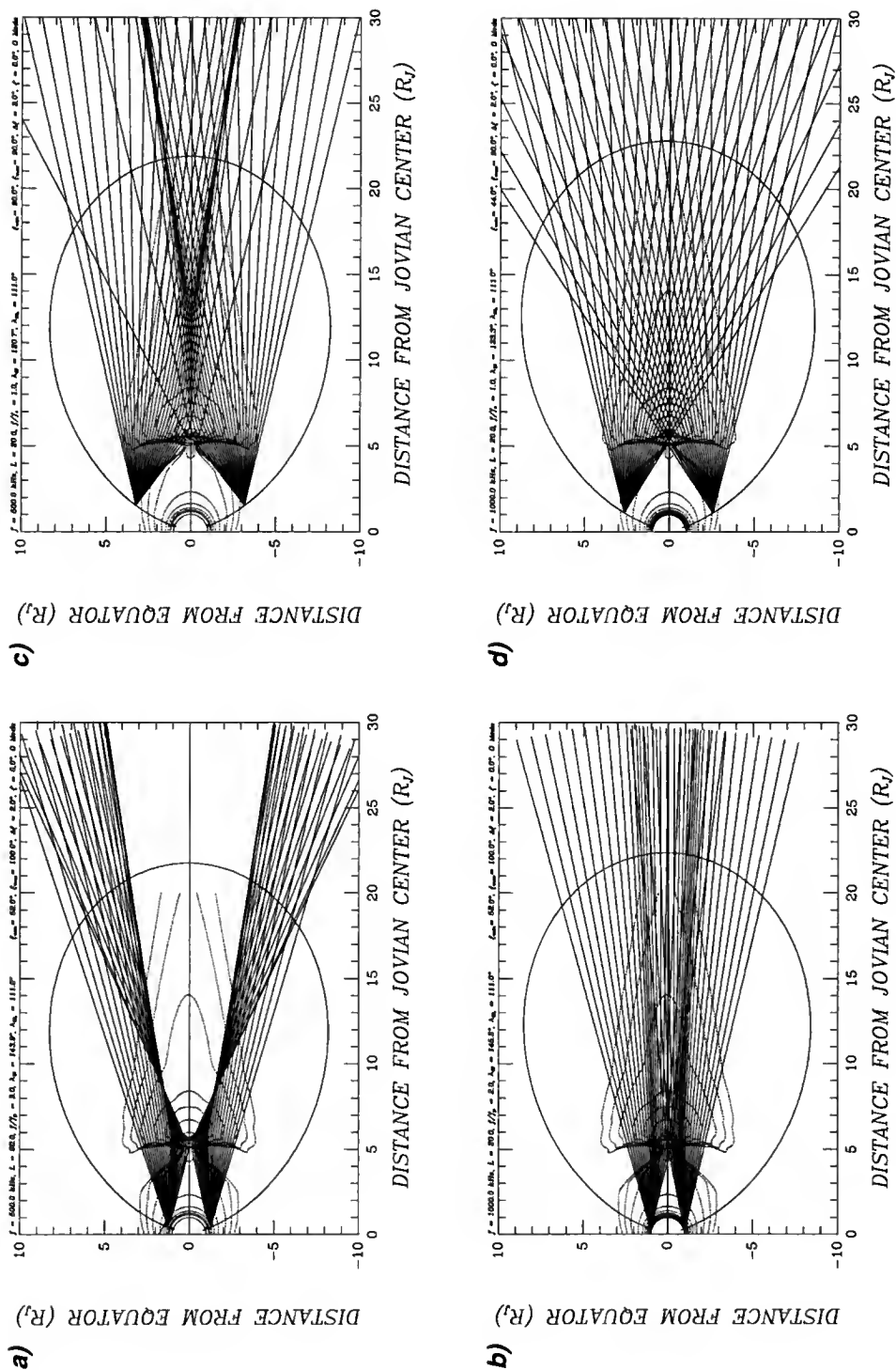


Figure 5.9. Two-dimensional raytracing of the HOM emission in the L-O mode at frequencies of 500 kHz (panels *a* and *c*) and 1000 kHz (panels *b* and *d*) from  $L = 20$  field line close to the meridian plane whose longitude is  $111^\circ$ . Left panels are for the second-harmonic emission (at the altitude where  $f/f_p = 2.0$ ); while right panels are for the radiation excited at the altitude where  $f/f_c = 1.0$  (*i.e.*, near the place where the R-X waves are excited).

propagating toward the equator would be completely blocked out by the Io torus. Waves in the L-O mode at 1 MHz are affected more than those in the R-X mode at the same frequency. It seems unlikely that the L-O waves would come from such a low altitude region. In the case for which the L-O mode waves are excited at the same place as the R-X mode waves, the propagation of the L-O waves is seen similar to that of the R-X waves. In this case, the source regions are very far away above the ionosphere and are further from the magnetic equator. The Io torus affects *only* low frequency ( $\leq 500$  kHz) L-O mode waves that propagate through it, but is unable to reshape the propagation of high frequency ( $\geq 1$  MHz) waves.

So far I have investigated rays launched and propagating near the plane parallel to the meridian plane of the source. Such two-dimensional raytracing results are meaningful for the case where the radiation received by the observer comes from the source region in a CML range similar to that of the observer. In other words, such calculations can only be applied to rays launched from the equatorial edges of the emission cones. Nevertheless, the two-dimensional raytracing provides a good tool which allows us to visualize how the torus affects rays originating at different locations with different initial wave normal angles. In reality, however, the emitted radiation is believed to be beamed in a hollow cone fashion and to propagate toward a wide range of directions. Rays launched along other parts (e.g., leading edges and trailing edges) of the emission cone are often the major contributor of the received radiation, as in the case of Io-A and Io-B sources in the DAM emission, and should also be closely investigated. It is therefore critical to trace radio rays toward any direction that they may go and see how their propagation paths are altered by the Io plasma torus. This would certainly require three-dimensional raytracing, which is discussed in the next section.

### 5.7 Three-dimensional Raytracing Result

In the previous section, two-dimensional raytracing was performed within the Jovian magnetosphere from variety of potential radio source regions at a wide range of HOM frequencies. The results clearly indicate that the Io plasma torus can play a major role in influencing the radio wave propagation *only* for waves that go through the central region of the torus, especially for those at frequencies below about 500 kHz. How the Io torus affects radio waves propagating in any directions is investigated here via the three-dimensional raytracing calculation.

In Chapter 4, a beaming model of the HOM emission was set up, and good results that fit the observations were obtained. According to the model, the HOM emission originates from a pair of magnetically conjugate sources at high latitude (with  $L \geq 15$ ) located at about  $30^\circ$  CML. The radiation is beamed into a hollow cone whose axis is parallel or anti-parallel to the local magnetic field. The opening angle of the hollow cone beam is moderate, somewhere between  $60^\circ$  and  $85^\circ$ . When the leading and trailing edges of the hollow cone beam pass over an observer near the equator, the observer will receive two maxima with a major wide gap centered at  $200^\circ$  CML (when the hollow cone is turned away from the observer), and a minor gap centered around  $30^\circ$  CML (when the observer is inside the hollow cone). A basic assumption of this successful model is that the received waves propagate along straight lines without suffering any refraction from the Io plasma torus. Let us now take the advantage of the three-dimensional raytracing technique to test if such an assumption is valid. Here again the ionosphere model and the Io plasma torus model of *Divine and Garrett* [1983] are assumed.

We launch rays from assumed source points on magnetic field lines with specified  $L$ -shell values ( $\pm 10$  and  $\pm 20$ , where a negative  $L$ -shell value indicates a source in the southern hemisphere) and longitude ( $\lambda_c = 30^\circ$ ). The source is located on the field

line where the local electron cyclotron frequency ( $f_c$ ) is just slightly below the wave frequency. Rays are launched with the same wave normal angles ( $\xi$ ) with respect to the local magnetic field at each of a series of azimuth angles ( $\zeta$ ) separated by  $10^\circ$ . The final direction of a ray is represented by the intersection of the ray with a Jupiter-centered celestial sphere having a large radius ( $200 R_J$  in our case). The positions of these points on the Jovicentric celestial sphere are then plotted in a two-dimension Mercator projected format as a function of latitude and west longitude. Results are shown in Figure 5.10, in which the emission at frequencies of 300, 500, 700, 900, 1100, and 1300 kHz located on the field lines with  $L=10$  and  $L=20$  in both hemispheres is traced. Parameters regarding source location and initial ray direction are shown on the top of each panel. Clearly, these raytracing results are very similar for radiation originating on higher latitudes ( $L \geq 20$ ), except that the initial wave normal angles can be set larger. As is expected and confirmed in the two-dimensional raytracing, low frequency rays that are initially closer to the  $\zeta = 0^\circ$  are heading toward the Io torus, and are therefore refracted by the torus, more or less, depending on how deep these rays can go through the torus. However, rays launched from other part of the hollow cone are not affected by the torus. Notice that for an observer near  $3^\circ \sim 5^\circ$  latitude, the hollow cone beams at all frequencies would be intercepted twice by the observer, one near  $90^\circ$  CML, and the other, near  $330^\circ$  CML (*i.e.*,  $-30^\circ$  CML). This is exactly what was observed by the two Voyager spacecraft, and by Ulysses when its ecliptic latitude was about  $1.5^\circ$  north [Reiner *et al.*, 1993b].

### 5.8 HOM Source Localization via Raytracing

I have shown in Chapter 2 that for the PRA antenna system the surface separating the directions of incident rays, for which the indicated sense of circular polarization is correct from those for which the indicated sense is reversed, is not a single plane,



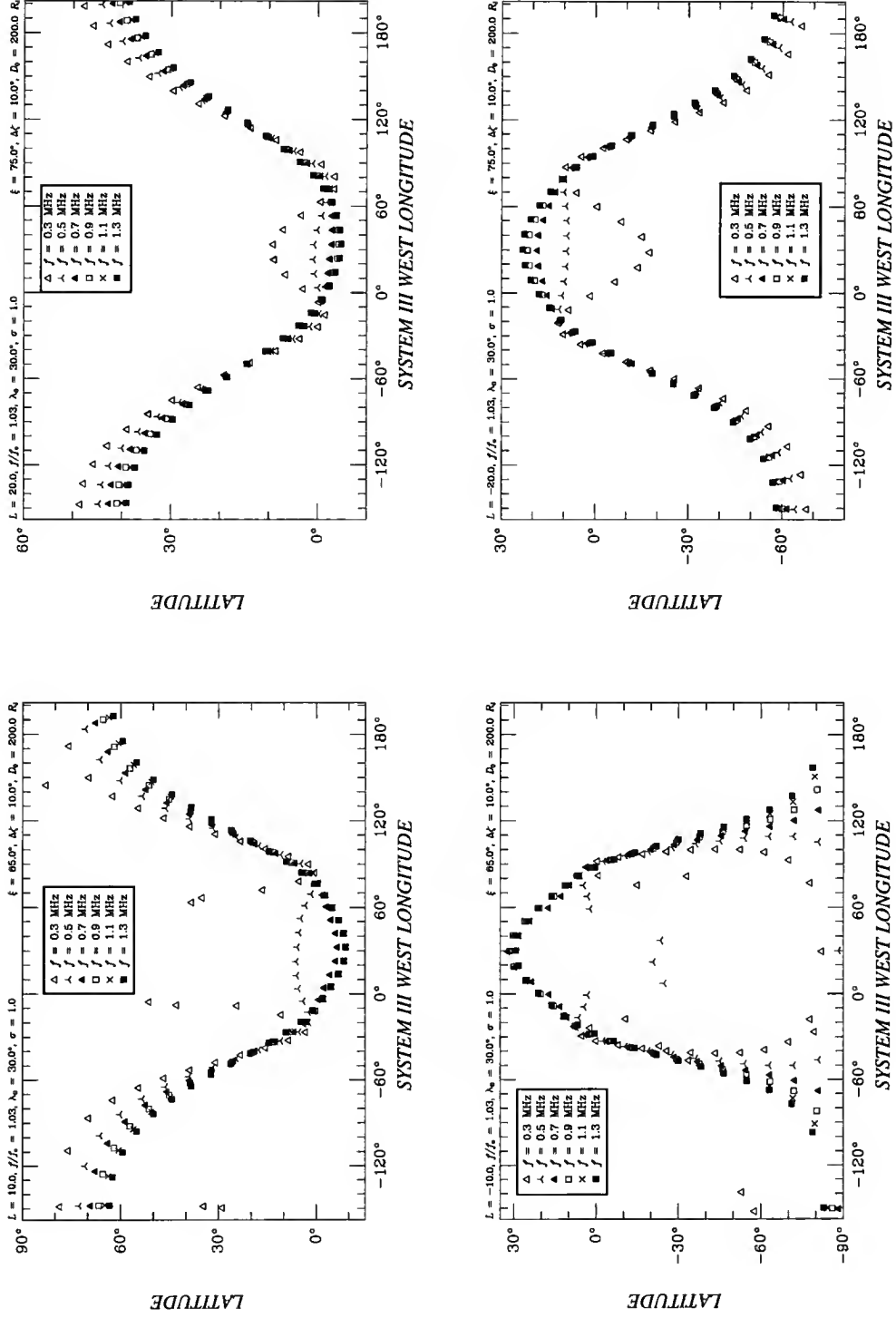


Figure 5.10. Three-dimensional raytracing results for radiation at frequencies of 300, 500, 700, 900, 1100, and 1300 kHz located on  $L = 10$  (left panels) and  $L = 20$  (right panels) in both the northern (upper panels) and southern (lower panels) hemispheres. Sources in the southern hemisphere are represented with negative  $L$ -shell values.

as was previously assumed in the literature. Instead, I have found that if only those rays incident on the front side of the antenna system are considered, there appears to be a single E-plane that is tilted  $27^\circ$  from the monopole plane. For rays incident on the back side of the antenna system, however, the effective E-plane tilt is  $45^\circ$ . The knowledge of these two equivalent E planes enables us to determine the true sense of circular polarization of rays arriving from most directions<sup>1</sup>. Furthermore, when the sudden change in polarization sense occurs a polarization source crosses the appropriate E-plane, we know that the unknown source incident direction would lie somewhere in this plane. In this section I use this feature to put constraints in source localization, together with the raytracing technique in an effort to locate the HOM source observed during a spacecraft-maneuver polarization reversal (SMPR) event and to correct for the ray bending due to refraction.

According to Equations (4.1), (4.2), and (4.5), it is clear that, regardless of the polarization state of the incoming radiation, the apparent degree of its circular polarization  $V_{app}$  will be zero if the source is within the E-plane ( $\Theta = 90^\circ$ ) and the observed polarization sense of the incoming radiation will be true one if the source is above the E-plane. Apparently this feature of the antenna response to circularly polarized radiation can be used to set constraints in localizing the radio sources. The idea is that if the detected incoming radiation undergoes a polarization reversal during the course of a spacecraft maneuver, and at the time when the incoming radiation appears to be unpolarized ( $V_{app} = 0$ ), it must be that the incident direction of the incoming radiation is in the E-plane of the equivalent dipole system. Ideally, if the direction angles of the incoming radiation ( $\Theta, \Phi$ ) with respect to the equivalent dipole system can be determined, then the direction cosines ( $c_1, c_2, c_3$ ) of the radiation at

---

<sup>1</sup>Unfortunately, no other information regarding the polarization of incident radiation could be obtained from the Voyager data.

the spacecraft with respect to the Jovicentric coordinate system can be calculated by

$$\begin{pmatrix} \sin \Theta \cos \Phi \\ \sin \Theta \sin \Phi \\ \cos \Theta \end{pmatrix} = \mathbf{T}_{J2A} \begin{pmatrix} c_1 \\ c_2 \\ c_3 \end{pmatrix} \quad \text{or} \quad \begin{pmatrix} c_1 \\ c_2 \\ c_3 \end{pmatrix} = \mathbf{T}_{A2J} \begin{pmatrix} \sin \Theta \cos \Phi \\ \sin \Theta \sin \Phi \\ \cos \Theta \end{pmatrix}, \quad (5.10)$$

where  $\mathbf{T}_{A2J}$  is the matrix which transforms from the equivalent antenna system (of the spacecraft) to the Jovicentric coordinate system and can be calculated from Equation (C.2) for each given moment of the spacecraft event time.  $\mathbf{T}_{J2A} = \mathbf{T}_{A2J}^T$  is the transpose of  $\mathbf{T}_{A2J}$  which does the inverse transformation as  $\mathbf{T}_{A2J}$ , and is given by Equation (C.7). In reality, for each spacecraft maneuver event that can be used for localizing a radio source, it can only be sure that at the moment of polarization reversal the radio source lies in the E-plane ( $\Theta = 90^\circ$ ), but in no way one can know the azimuthal angle ( $\Phi$ ) of the radio source with respect to the spacecraft. The best one can do is to trace back the radio wave rays, which lie in the ( $\Theta = 90^\circ$ ) plane but with different azimuthal angles, toward the planet and use other means to put constraints on  $\Phi$  and to locate the source.

If there were two sequential maneuver events in a relatively short period of time, during which the same radio source is still active, for one to locate the radio source, one would be able to eliminate the ambiguity of the source location. Of course, such event should occur when the spacecraft is not far away from the planet so that the accuracy of source determination can be retained. Unfortunately, no such double events were found in our data base. The only spacecraft maneuver event that can be used to put constraint on source localization is that occurred at 03:06 on March 6, 1979 right after Voyager 1 encountered with Jupiter (see Figure 2.3). During this event, Jupiter's direction seen from the spacecraft was changed from below the E-plane to above the E-plane, as has been shown in Figure 2.5 (on page 21). Radiation above 500 kHz experienced a polarization reversal from RH (false polarization sense) to LH (true polarization sense). Radiation at lower frequencies experienced an opposite

polarization reversal. I made an effort to locate the radio sources at a broad range of frequencies by using this event.

As a first step, it was assumed that the radiation received during this event is emitted in the R-X mode and is from the place where the local electron cyclotron frequency is just slightly lower than the wave frequency. It was also assumed that radio waves propagate along straight lines, *i.e.*, the refraction effect from Io torus is ignored. We have seen above that the assumption of straight line propagation is basically good enough for emissions above 500 kHz, as long as they are not initially propagating toward the Io plasma torus. Correction was of course made in the next step when raytracing was performed. I searched for rays that are launched from the spacecraft in the E-plane ( $\Theta = 90^\circ$ ) toward Jupiter and are intercepted by the  $f_c = f$  surface. Since during this maneuver event, Jupiter was seen in the back side of the spacecraft, a  $45^\circ$  tilt angle of the E-plane with respect to the monopole plane was used. Emissions at 4 frequency values of 400, 600, 1000, and 1300 kHz were investigated. For radiation at each frequency, rays were launched in the E-plane with a broad range of azimuthal angles (at an interval of  $0.5^\circ$ ), then the Jovigraphic longitude and latitude (or  $L$ -shell) of the intersection point on the  $f_c$  surface were calculated for each ray. Also the direction angle of the ray with respect to the magnetic field at the intersection point was calculated; this angle would be the initial wave normal angle when the ray direction at the source is reversed. The result is listed in Table 5.1 and is displayed in Figure 5.11, in which intersection points in the southern hemisphere are represented with negative  $L$ -shell values. The figure clearly shows that possible radio sources come from the region in the southern hemisphere with a (west) longitude range somewhere between  $280^\circ$  (*i.e.*,  $-80^\circ$ ) and  $40^\circ$ , depending on the latitude (or  $L$ -shell) of the source. The  $L$ -shell range is between 3 and 25. The fact that all possible radio source points at frequencies greater than 500 kHz are in the southern hemisphere is consistent with the observation: During the maneuver event, the detected true

Table 5.1. Source localization via the event of polarization reversal occurred at 03:06 SCET on day 65 (March 6), 1979. Listed are longitudes ( $\lambda_{\text{III}}$ ),  $L$ -shell values, and direction angles ( $\xi$ ) of intersection points on the surface of  $f_c$  at 400, 600, 1000, and 1300 kHz.

[illegible]

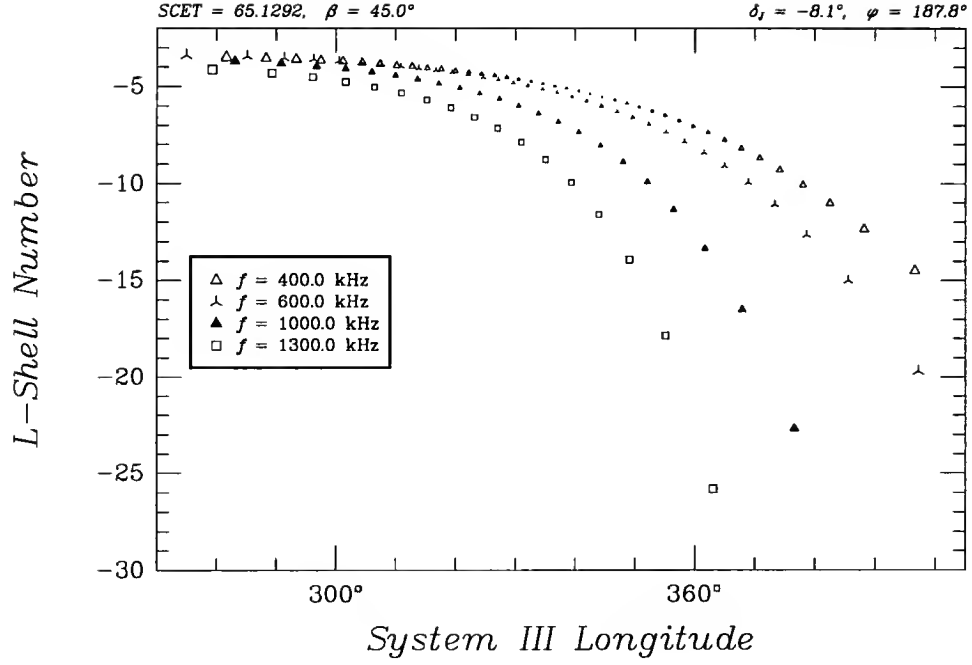


Figure 5.11. Position of intersection points of rays launched from the spacecraft in the E-plane with the  $f_c = f$  surface for radiation at frequencies 400, 600, 1000, and 1300 kHz. Point size is proportional to the direction angle, listed in Table 5.1, of rays with respect to the local magnetic field at the intersection point.

polarization sense is left handed, meaning that the majority of radiation comes from the southern hemisphere, provided that the radiation is emitted and propagate in the R-X mode as has been assumed. Since the azimuthal angle  $\Phi$  of the incoming ray cannot be determined unambiguously, one cannot uniquely determine the  $L$ -shell of the source. One can, however, probably eliminate those points which have small ( $\leq 50^\circ$ ) wave normal angles, because, according to the CMI theory, radio waves are emitted at large wave normal angles with respect to the local magnetic field. When source points with small wave normal angles are eliminated only points around  $310^\circ$  CML with small  $L$ -shells and those with large  $L$ -shells at CML greater than  $0^\circ$  (i.e.,  $360^\circ$ ) are left. Figure 5.11 also shows that if radiation at different frequencies is from the same  $L$ -shell, the source longitude would be different for radiation at different frequencies.

Calculation shown in Figure 5.11 was done with the assumption that waves from the source propagate and reach the spacecraft along straight lines. This is basically true, as has been shown in previous sections, for radiation at frequencies of 700 kHz and up. However, refraction of rays at frequencies below 500 kHz becomes an increasingly serious problem which has not yet been investigated by means of actual raytracing. To do this, a special program was developed that would search for what I call *matched* rays. A matched ray is the one launched from the source point and will eventually reach the spacecraft with a high accuracy. We know that for each ray to be launched from the source point, there are two variables that determine the initial direction of the wave normal: the initial wave normal angle  $\xi$ , and the azimuthal angle  $\zeta$  (see Figure 4.16a on page 85 for illustration). The ray-matching procedure is done like this: at a given time, an initial direction is determined by the direction of the straight line from the source point to the spacecraft. First the azimuthal angle  $\zeta$  is fixed, and an optimized  $\xi$  value is searched that would correspond to a ray which has the minimum angular and linear distance to the receiver (the spacecraft). We then search for an optimized  $\zeta$  value while keeping the  $\xi$  value fixed at the just-found optimized value. Using the optimized  $\zeta$  value, we continue searching for a new optimized  $\xi$  value, and the iteration procedure is repeated until a ray that reaches the receiver is found. The end point of this ray will have zero angular and linear distances from the spacecraft. Usually, this iteration procedure is repeated for 5 to 8 times before such a “matched” ray is found. If after 15 or 20 iterations no matched ray can be found, we would then conclude that no rays from this specific position can reach the receiver. Searching for such matched rays can have several advantages: The initial wave normal direction can be accurately determined, which gives a quantitative measurement of the initial wave angles. Secondly, the incident direction of the ray from the source to the spacecraft can be determined as well, which is useful in source localization.

I applied this ray-matching technique to the polarization reversal event occurred at 03:06 on day 65 (March 5), 1979 to eliminate the ambiguity of HOM source locations determined in the first step. During this event, Voyager 1 was only  $15.5 R_J$  away from Jupiter, and it was oriented such that Jupiter was seen at  $172^\circ 7'$  azimuth and  $130^\circ 2'$  colatitude with respect to the monopole coordinate system. Since at this time Jupiter was on the back side of the antenna system, a  $45^\circ$  tilt angle of the E-plane relative to the monopole plane is assumed. Matched rays are searched for *all* possible source locations that are visible by the spacecraft at that time. Source positions are specified as usual by their longitude values ( $\lambda_{III}$ ),  $L$ -shell values (negative ones indicating sources in southern hemisphere), and wave frequency ( $f$ ) which is close to the local electron cyclotron frequency  $f_c$ . An important constraint in locating a radio source when using the polarization reversal event is that when the radio emission reaches the spacecraft, their incident angle measured from the normal to the E-plane has to be  $90^\circ$ . Thus, during the event of polarization reversal, only those rays that actually reach the spacecraft, and more importantly, that have incident angles of  $90^\circ$  are counted as rays that are received at the spacecraft. In our calculation, only rays that reach the spacecraft with incident angles in the range of  $90^\circ \pm 0^\circ 5'$  are considered to be qualified. Only the source locations from those qualified rays are the possible ones that actually make contributions to the received emission during the event.

Shown in Figure 5.12 are source locations, determined by the matched rays with  $90^\circ \pm 0^\circ 5'$  incident angles, in terms of the west longitude and initial wave normal angle; the wave frequency and the  $L$ -shell number are labeled as pairs of parameters in the parentheses (negative  $L$ -shell values represent sources in the southern hemisphere). Emissions at frequencies of 500, 600, 1000, and 1300 kHz on  $L$ -shells with values from 6 up to 30 were investigated. No rays at 500 and 600 kHz with  $L$ -shell value of  $\pm 6$  were found. No rays at 500 kHz with  $L$ -shell value of  $\pm 10$  were found. Clearly, radiation at low frequencies ( $\leq 600$  kHz) from low  $L$ -shells are deviated by the refraction



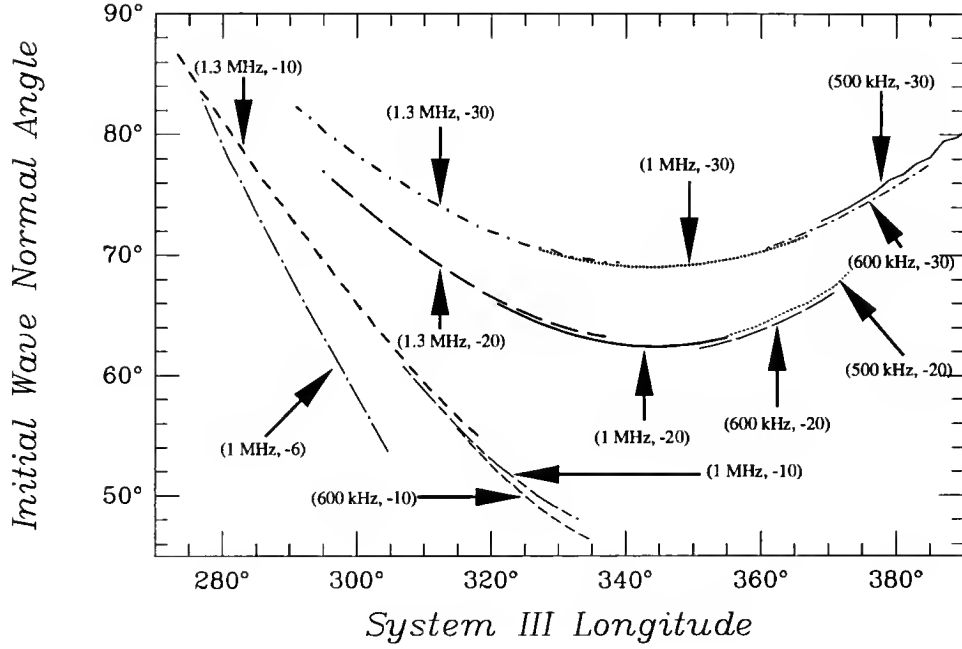


Figure 5.12. Source locations for radiation at frequencies of 500, 600, 1000, and 1300 kHz, determined via three-dimensional raytracing during an event of polarization reversal. Labeled in parentheses are the wave frequency (which is assumed to be approximately equal to  $f_c$ ) and  $L$ -shell value (negative values representing points in the southern hemisphere).

from the Io torus during the polarization reversal event. However, since radiation at these frequencies was clearly observed, it is only possible that the received radiation must have come from high  $L$ -shells. Also, all rays from the northern hemisphere (with positive  $L$ -shells) either cannot reach the observer (*i.e.*, not matched rays), or have incident angles very different from  $90^\circ$ ; they do not meet the constraint we set and are therefore rejected. Results in Figure 5.12 strongly suggest that radiation received during the polarization reversal event come from high  $L$ -shells in the southern hemisphere, in a longitude region between  $300^\circ$  (*i.e.*,  $-60^\circ$ ) and  $30^\circ$  CML. Radiation emitted from these regions initially have wave normal angles between  $65^\circ$  and  $75^\circ$  for  $L = 20$ , and  $72^\circ$  and  $82^\circ$  for  $L = 30$ . It also indicates that the wave normal angle is a function of the wave frequency, with waves at 1 MHz having smallest wave normal angle, and waves at frequencies above or lower 1 MHz have larger wave normal angles.

Notice that the source locations determined via raytracing and the polarization reversal event are consistent with those deduced from the HOM emission modeling presented in Chapter 4. They all suggest that the HOM emission is from the region on the magnetic field lines whose  $L$ -shell value is greater than 20 and whose CML is near  $25^\circ$ . *Reiner et al.* [1993a, 1993b], using the Ulysses observation and the direction finding capabilities of the URAP experiment, found that the HOM sources can be located near  $325^\circ$  CML (determined when Ulysses was far from Jupiter and at low latitude) and  $45^\circ$  CML during an event occurred when Ulysses was at high ( $20^\circ$ ) magnetic latitude. With the observation of the URAP experiment, the incoming wave's direction (both the latitudinal angle and the azimuthal angle with respect to the spacecraft system) can be uniquely determined. In the work of *Reiner et al.* [1993a, 1993b], the source location was determined by measuring the arrival direction of the radiation reaching the Ulysses spacecraft, and then finding the intersection of a straight line extending in the reverse direction with a modeled  $f_c = f$  surface. They concluded that the HOM sources may be confined in a small longitudinal region near  $45^\circ$  CML with very small  $L$ -shells ( $4 \sim 8$ ). Consequently, the initial wave normal angle so determined is very small ( $\leq 28^\circ$ ). Lacking the necessary raytracing for source localization makes their result not very convincing, especially when it comes from the determination of the  $L$ -shell and the wave normal angle. The source longitude region (near  $325^\circ$  and  $45^\circ$  CML) determined by *Reiner et al.* [1993b] is certainly in good agreement with ours. It is obvious that very important and interesting results can be deduced if our raytracing procedure is applied to the study of the Ulysses observation.

## CHAPTER 6

### A MODEL OF NEPTUNE'S SMOOTH RADIO COMPONENT

#### 6.1 Introduction

Observations of Neptune radio emissions by the Voyager PRA experiment [Warwick *et al.*, 1977] revealed a complex time-varying spectrum with a high-frequency cutoff at about 1300 kHz. The most conspicuous and longest-observed components of Neptune's hectometric-kilometric radio emission [Warwick *et al.*, 1989] are the bursty or sharp-burst component at frequencies between about 500 and 1320 kHz, attributed by Farrell *et al.* [1990, 1991] to X-mode emission from the south polar regions, and the smooth component [Sawyer *et al.*, 1990, 1992; Ladreiter *et al.*, 1991], observed on all receiver channels below about 800 kHz. The latter may itself consist of more than one component, but the major part is believed to be X-mode radiation from one or more Neptunian north magnetic polar regions. Radio emission components that were observed only during the close encounter were nonthermal continuum below about 60 kHz [Kurth *et al.*, 1990], and electron cyclotron harmonic waves below 400 kHz [Gurnett *et al.*, 1989]. Disturbances were also observed on most channels during the ring-plane crossing as particles within the ring struck the antenna elements [Pedersen *et al.*, 1991]. We will not be concerned with these close-encounter events. Instead, our focus will be on the smooth component that occurs in almost every rotation during the encounter period.

Neptune's radio emissions were observed to be repetitive as the planet rotates. The smooth component of such emissions is believed to consist of at least two components: (a) Main component which was observed for more than 10 days around the encounter period in a relatively broad range of frequencies (typically from 20 kHz to 500 kHz most of time, and reaching up to 800 kHz near encounter). This component is circularly right-handed polarized at the emission peak when Voyager is north of the magnetic equator (in terms of an OTD magnetic field model). (b) The other component was observed only in a frequency range from about 600 kHz to 800 kHz and only for a few rotations. A typical dynamic spectrum plot is shown in Figure 6.1 for the day of encounter (day 237 or August 25, 1989) for both the LH and RH flux density components. As has been mentioned in Chapter 2, the Neptune PRA data used in this study has been cleaned with all recognizable interference removed.

Figure 6.2 shows typical plots of total flux density and apparent degree of circular polarization (referred to as the polarization ratio) as a function of spacecraft event time (SCET) for the 116-kHz receiver channel over 6 days of observations at encounter that I employed in modeling. The magnetic latitude<sup>1</sup> of the spacecraft as a function of SCET is also shown. The closest approach occurred early on day 237 (August 25). As has been demonstrated in Chapter 2, there are uncertainties in the orientation of the electric plane (E-plane) of the PRA antenna system relative to the spacecraft. Such uncertainties can introduce large errors in the apparent degree of circular polarization; even the sign or sense of the polarization may at times be reversed (*i.e.*, indicated LH elliptical polarization may actually be RH, and vice versa). However, the senses of the apparent degree of circular polarization indicated in Figure 6.2 are known to be

---

<sup>1</sup>For convenience, the OTD field is used to define a Neptunian magnetic longitude and latitude coordinate system. The magnetic longitude is measured along the magnetic equator from the meridian plane toward which the magnetic dipole moment is tilted. For the Neptune magnetic field, this arbitrarily defined system reflects the symmetry of the field only at relatively great distances; there is little symmetry at the distance of the radio source.

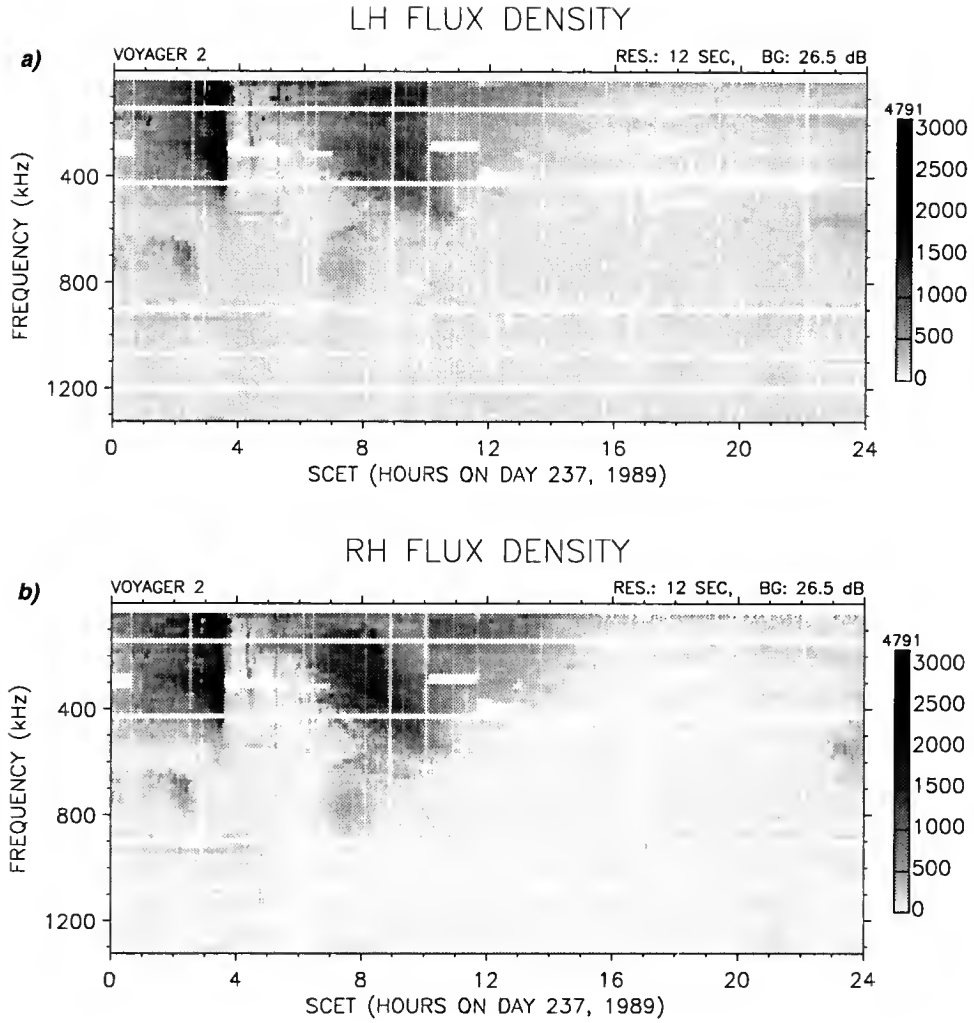


Figure 6.1. Voyager 2 PRA dynamic spectrum on the day of encounter (day 237 or August 25, 1989) displayed as the emission frequency versus spacecraft event time (SCET) for both LH (upper panel) and RH (lower panel) flux density components. Intensities are indicated by the gray level with the scale bar (in units of millibels) shown on the right of each plot.

correct except for an uncertainty during the time interval from 02:00 to 10:00 SCET on day 237. The apparent senses can be therefore used to some extent to separate different emission components. Two distinct components of the emission can be identified from this figure and the dynamic spectrum plot of their Figure 2 in *Warwick et al.* [1989] as follows: (a) A wide-band continuous (smooth) predominantly RH-polarized component that is observed when the spacecraft is in the northern magnetic

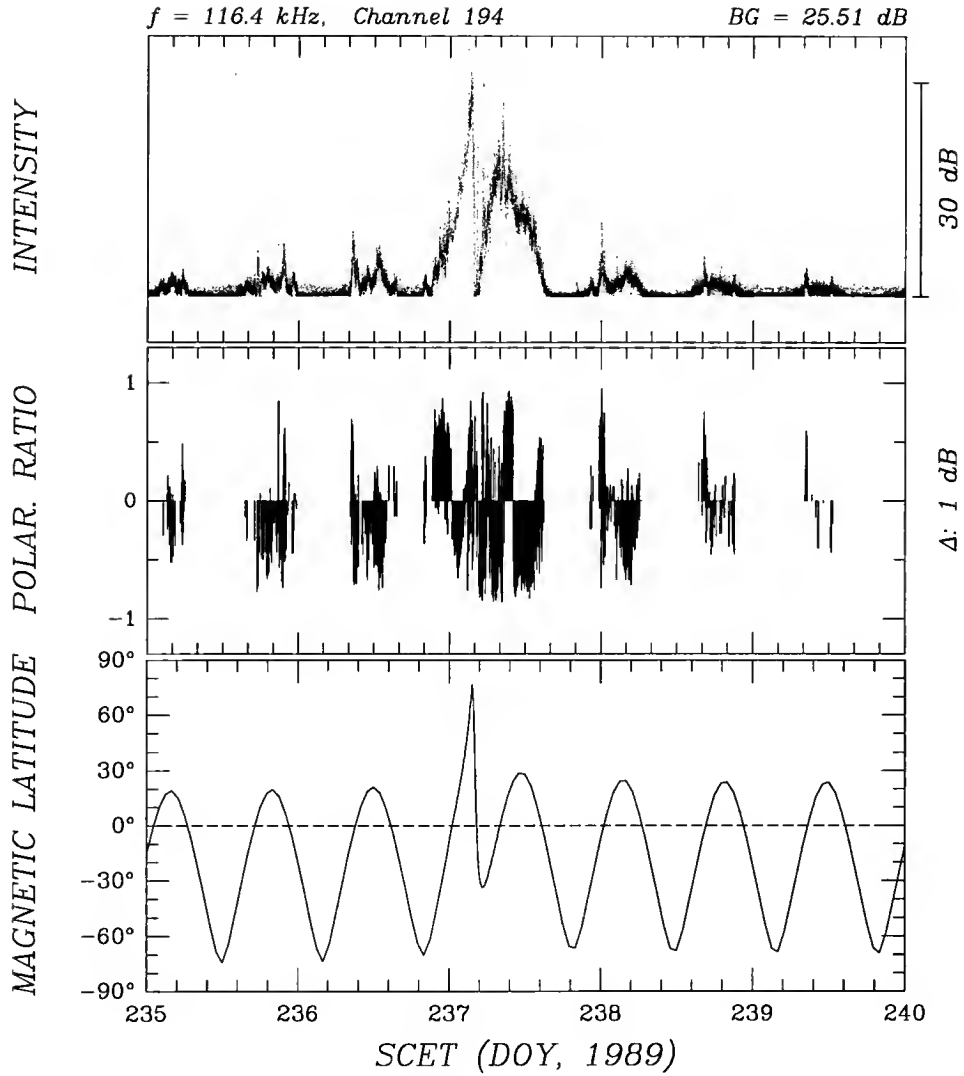


Figure 6.2. Total flux density and apparent degree of circular polarization as function of time for the 116.4 kHz receiver channel. Polarization ratio is the same as the apparent degree of circular polarization. The magnetic latitude of Voyager 2 as a function of SCET is also plotted.

hemisphere. This is the main smooth component; (b) A relatively brief narrow-band (about 30 kHz bandwidth) pulse of predominantly LH-polarized emission that is observed at the same frequency each time the spacecraft crosses a magnetic latitude of approximately 0°. This latter component will be referred to as the narrow band narrow beam (NBNB) component.

Up to date, the cyclotron maser instability (CMI) proposed by *Wu and Lee* [1979] is still believed to be the most probable mechanism responsible for radio emissions from the magnetized planets. Sources of radio emissions are assumed to be located at positions at which the electron cyclotron frequency ( $f_c$ ) is very close but slightly less than the frequency of observation. Radio emission is beamed into a hollow cone with a large angle from the local magnetic field direction. In this sense, a good understanding of a more accurate (or realistic) magnetic field strength and direction can be crucial in localizing and modeling the Neptunian radio emissions. On the other hand, in order for the CMI mechanism to be operative, the ratio of the plasma frequency ( $f_p$ ) to the cyclotron frequency,  $f_p/f_c$ , must be a small value (less than 0.1) in the source region. Modeling radio emission from within the magnetosphere and plasmasphere can lead to important clues for a better understanding the magnetic and plasma environment in the source region.

*Sawyer et al.* [1990] modeled the main component, using a revised OTD magnetic field model [*Ness et al.*, 1989], with an R-X mode emission beamed into a filled cone with angular halfwidth of  $17^\circ$  from the conjugate sources at latitude  $\pm 47^\circ$  distributed over the longitude range from  $-170^\circ$  to  $85^\circ$ . The lack of any physical explanation on how this type of NKR source would be distributed so symmetrically about the equator makes their model unconvincing. *Ladreiter et al.* [1991]<sup>2</sup> achieved limited success in modeling the beaming of the smooth component, using an assumed hollow-cone beam, again together with the OTD model of the Neptunian magnetic field. Their beaming model was able to provide a reasonable match to the observed intensity versus time curve only for a short period near the closest approach. However, their northern source (for which the OTD  $L=6$ ) would have barely been visible to Voyager during

---

<sup>2</sup>I will henceforth refer to the four authors of the *Ladreiter et al.* [1991] paper, and to the paper itself, as LLRR.

the storm (*i.e.*, it is almost occulted by the stop zone), as will be shown in later sections. This makes their model questionable.

Soon after Neptune's magnetic field was modeled by *Ness et al.* [1989] based on the Voyager 2 observation as an offset tilted dipole, it was realized that Neptune's magnetic field, especially in the radio-emitting region of the magnetosphere, is less dipole-like than for any of other giant planets; such an OTD model is a good approximation to the actual field only at radial distances greater than  $4 R_N$  ( $1 R_N = 24,762$  km) and less than  $15 R_N$ ; multipole field components cannot be neglected at closer distances. Later, *Connerney et al.* [1991] developed a more complicated and realistic Neptune magnetic field model, the so-called  $O_8$  model.

*Sawyer et al.* [1992] concluded from the failure of their model based on the OTD field to match the observed radio emissions that the real Neptunian field is highly irregular. They suggested that changes in polarization and intensity of the high-latitude radio emission observed at Neptune was caused by repeated occultations by magnetic hills due to the distorted topography of the iso-magnetic intensity surfaces. In the LLRR paper, on the other hand, the authors stated that they were justified in using the simpler OTD field model, indicating that they believed the result obtained with the  $O_8$  model would not have been greatly different.

I will demonstrate, however, in the next section that the OTD2 model is clearly inadequate for the purpose of modeling Neptune's radio emissions, especially at higher frequencies. Consequently, previously determined source locations and relevant parameters of the beaming cone do not stand on a meaningful physical foundation. I will show in Section 6.3 an improved model to the NKR smooth component, using the same general method as did LLRR, a method that had previously been employed by *Gulkis and Carr* [1987] for modeling the smooth component of the radio emission from Uranus. The most important improvement that I have made over the LLRR modeling and previous modeling efforts is the use of the more realistic  $O_8$  magnetic



field model of *Connerney et al.* [1991] and it will be shown that my beam model not only provides a much better fit, over a longer period of time to the observation, than did that of *Ladreiter et al.* [1991] but the source region it predicts is within the actual area on the  $f_c = f$  surface that is visible during the storm. In Section 6.4 I will consider the implications of my results regarding the plasma distribution in the ionosphere and the magnetosphere. And finally I make a summation and draw my conclusions in Section 6.5.

## 6.2 The Neptunian Magnetic Field Models

Neptune's magnetic field was found, based on the Voyager 2 observation, by *Ness et al.* [1989] to be, to a first approximation, that of a magnetic dipole (with a moment of  $0.133 \text{ Gauss} \cdot R_N^3$ ) tilted  $46^\circ 8'$  with respect to the rotation axis toward  $W79^\circ 5'$  (Neptunian longitude system or NLS) and offset by  $0.546 R_N$  from the center of the planet. Later, a revised Neptune OTD magnetic field model, known as OTD2, was established by its developers leading to a better fit to the observation. In this model, the magnetic dipole was tilted  $45^\circ 2'$  from the rotation axis toward  $W76^\circ 5'$  NLS, and is offset by  $0.55 R_N$  from the Neptune center. Such offset tilted dipole field models can be a good approximation to the actual field only at radial distances greater than  $4 R_N$ ; multipole field components cannot be neglected at closer distances. Because of the extreme offset of the magnetic dipole, the surface field intensity at the OTD south magnetic pole (which is located in the southern hemisphere and is the one toward which the field lines are directed) is higher by an order of magnitude than that of the opposite pole.

A higher-order field expansion led to the  $O_8$  model [*Connerney et al.*, 1991], a 15-coefficient spherical harmonic model containing dipole, quadrupole, and octopole components. This model provides greatly improved accuracy at distances down to

somewhat less than  $1.2 R_N$  from the center of the planet, where the radio sources are located. In this field model the dominant surface pole is still the one in the southern hemisphere, but there are other much weaker poles at other locations. The  $O_8$  model, like the OTD2, has a strong south magnetic pole, but unlike the OTD2 it has several north poles (defined as places on the  $r = 1 R_N$  surface at which  $B$  is perpendicular upward). The surface field strength at these north poles is weaker than that at the south pole by an order of magnitude or more. Although the  $O_8$  model is only a partial solution to a linear system of equations which relates the model parameters to the spacecraft observations, and is accurate probably only at locations in the spacecraft trajectory, it still provides a more realistic basis for initial attempts to model the Neptunian radio emission beam than did the previous offset tilted dipole (OTD) model [*Ness et al.*, 1989].

As has been mentioned in Section 6.1, so far almost all efforts in modeling Neptune radio emissions are based on the OTD (or OTD2) model. It was so because either at the time when those NKR models were made the  $O_8$  model was not available (in case of *Sawyer et al.* [1990]), or OTD model was used for simplicity. In making their NKR model, *Ladreitner et al.* [1991] argued that the difference between the OTD2 model and the  $O_8$  model at the source region (at least for those sources at lower frequencies) is not significant, indicating that they believed the result obtained with the  $O_8$  model would not have been greatly different. I believe that this is incorrect — that the  $O_8$  field model must be used.

A beaming model of planetary radio emissions is often described by several key parameters such as (1) ratio of wave frequency ( $f$ ) to electron cyclotron frequency ( $f_c$ ) which determines how close the radio source is to the  $f_{R=0} = f$  surface; (2) wave normal angle with respect to the local magnetic field direction at the source. The gradient of magnetic field near the source location often affects significantly the propagation of the emitted X-mode radio waves. When higher-order terms are introduced to the

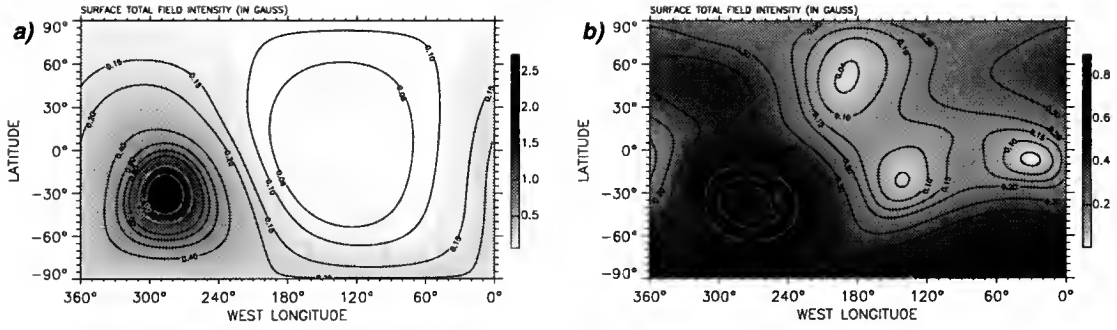


Figure 6.3. Total magnetic field intensity at the Neptunian surface calculated (a) from the OTD field model [Ness *et al.*, 1989], and (b) from the O<sub>8</sub> field model [Connerney *et al.*, 1991].

magnetic field model, the field magnitude and direction at a given point in the field can change dramatically, especially when such higher-order terms are not so small to be ignored, which is the case for the Neptune magnetic field. Differences in both magnitude of the magnetic field strength and magnetic field direction at the source can lead completely different parameter sets for the beaming model. The difference between the O<sub>8</sub> model and the OTD model can also lead difference in determining the radio horizon that controls occultation of radio sources by the planet and by its ionosphere.

The difference of the O<sub>8</sub> model from the OTD model can be seen from Figures 6.3 and 6.4. In Figure 6.3 the total magnetic field intensity at the Neptunian surface (gray level coded) is compared for the OTD and O<sub>8</sub> field models. There is clearly a great difference in magnitude at the surface. A more important comparison, however, is at the  $f_c = f$  surface, *i.e.*, the surface at which the local electron cyclotron frequency as given by the model approximately equals the frequency of observation (116 kHz in the present case). Figures 6.4 shows the global distribution of the differences between the field directions calculated by the O<sub>8</sub> and OTD field models at points on the  $f_c = 116$  kHz surface (the latter being based on the O<sub>8</sub> model). It is seen that the magnetic field direction errors introduced by using the OTD rather than the O<sub>8</sub> field model at

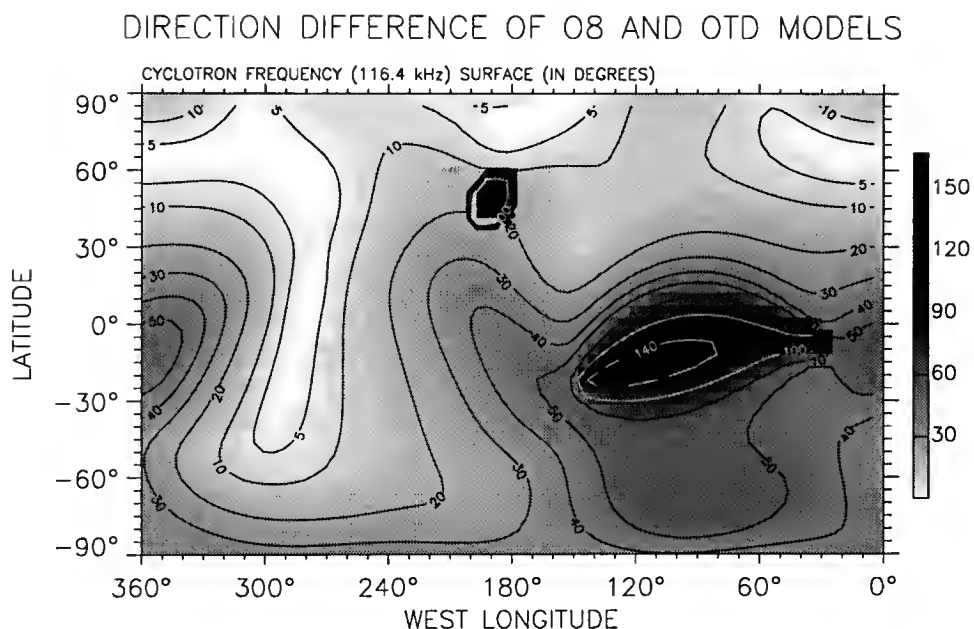


Figure 6.4. Global distribution of the difference between the field directions calculated by the O<sub>8</sub> and OTD field models at points on the  $f_c = 116.4$  kHz surface (the  $f_c$ -surface having been calculated assuming the O<sub>8</sub> model).

points over those source locations suggested by *Ladreiter et al.* [1991] and by me (see Section 6.4 below) would range from about 20° to 40°. In addition, there would be equally severe errors in the magnetic field intensity if the simpler OTD field model were used instead of the O<sub>8</sub> model. Because of these large errors in both the field magnitude and direction at the proposed source locations by LLRR, there can be no doubt that their modeling results for the smooth component source location and beam shape are unrealistic.

The Neptunian magnetic field undoubtedly contains important multipole components that are of higher order than those of the O<sub>8</sub> model. This model is probably about as accurate as can be obtained from the Voyager magnetometer measurements. We have shown, however, that despite its limitations the O<sub>8</sub> field model leads to much more realistic smooth-component radio beam modeling than does its predecessor, the OTD model.

### 6.3 Plasmasphere Model

Neptune's plasmasphere consists of an ionosphere and a magnetosphere as do the plasmaspheres of other giant planets. Neptune's ionosphere was modeled and predicted by *Shinagawa and Waite* [1989] prior to the Voyager encounter with Neptune, based on some early models by *McElroy* [1973] and *Atreya and Donahue* [1975]. It is not yet clear from the Voyager observations how accurate this predicted ionospheric model is.

There exists an important constraint on the modeling of the smooth-component radio emission from Neptune: In order for the CMI to operate, there must be a maximum limit, which is about 0.1, for the ratio of plasma frequency ( $f_p$ ) to electron cyclotron frequency ( $f_c$ ). To search for source locations of smooth NKR where the  $f_p/f_c$  ratio meets the CMI condition and to better understand the Neptunian radio radiation, one needs the information of plasma density distribution in the ionosphere and magnetosphere of Neptune. The present inadequacy of plasma density information is responsible for what is probably the greatest uncertainty in the modeling of Neptune's radio emission processes. During the Voyager 2 encounter with Neptune, various attempts to measure the plasma density in the ionosphere were made. The Voyager 2 plasma instrument made the only direct *in situ* plasma density measurement [*Belcher et al.*, 1989] which suggested a very low plasma density, typically from  $10^{-3}$  to  $10^{-1}$   $\text{cm}^{-3}$  with maximum value around  $1.4 \text{ cm}^{-3}$ . This result is in conflict with the whistler observations [*Gurnett et al.*, 1990] which estimated a minimum electron density to be around from 30 to  $100 \text{ cm}^{-3}$ . Radio occultation measurements [*Tyler et al.*, 1989] clearly show a maximum electron density of  $2 \times 10^3 \text{ cm}^{-3}$  at an altitude of 1400 km, decreasing to several hundred  $\text{cm}^{-3}$  at the altitude of 5000 km (a scale height of about 1800 km). Models based on standard ionospheric theory also give considerably higher electron densities than the ionospheric measurements.

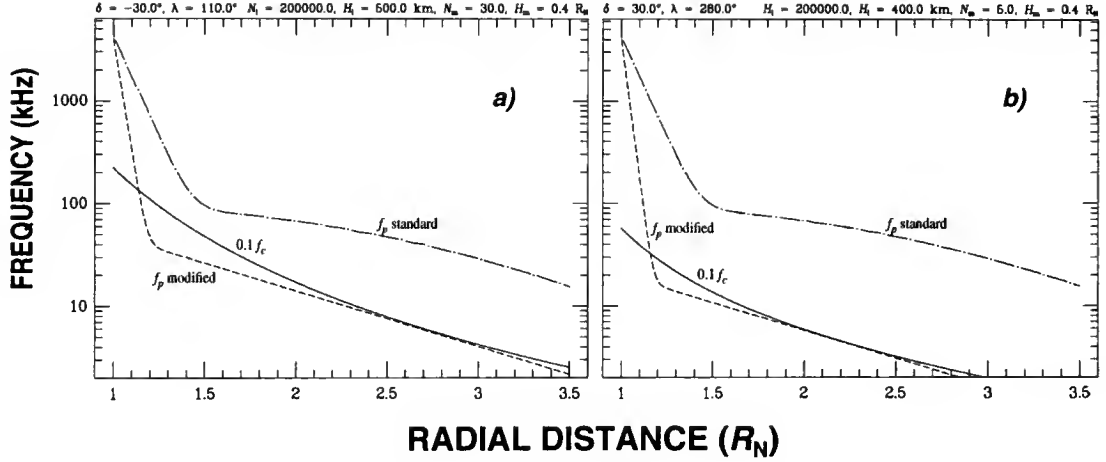


Figure 6.5. Curves of  $f_p$  and  $0.1 f_c$  as a function of radial distance from Neptune's center (a) at our modeled narrow-band narrow-beam source region near the south-magnetic auroral zone, and (b) at our modeled smooth-component radio source region near the principal north-magnetic auroral zone. The solid curves are the plots of  $0.1 f_c$  versus distance; the dot-dashed curves indicate  $f_p$  versus distance as calculated from the plasmaspheric model used by *Menietti et al.* [1991] (i.e., the standard model); the dashed curves are our modifications of the  $f_p$  versus distance curve.

For example, models of Neptune's ionosphere by *Shinagawa and Waite* [1989] give maximum electron densities of  $10^5 \text{ cm}^{-3}$ . The present situation regarding Neptune's ionosphere is obviously confused.

Although the above-mentioned modeling constraint that the  $f_p/f_c$  ratio must be 0.1 or less in the source region relies upon the poorly known spatial distribution of the quantity  $f_p$ , we will make a thorough review of all available information on the plasma density distribution in Neptune's ionosphere and magnetosphere and will test a range of possible models for this distribution for compatibility with observable CMI radio emission from globally distributed candidate locations. The latter process could possibly contribute to our knowledge of the Neptunian plasmaspheric density distribution as well as to that of the radio emission geometry. For example, I illustrate in Figure 6.5 a test of the compatibility of each of two quite different plasmaspheric  $f_p$  distribution models with the above-mentioned tentatively-selected smooth-component radio source location (see next section). The dot-dashed curve in Figure 6.5 is derived for

the radial direction through the plasmasphere at the assumed radio source location from the plasmaspheric model used by *Menietti et al.* [1991]; I shall refer to it as the standard model. It is based on the ionospheric plasma frequency model due to *Shinagawa and Waite* [1989], together with the magnetospheric plasma frequency model derived by *Gurnett et al.* [1990] from the whistler observations. In this standard model, the electron density (in units of  $\text{cm}^{-3}$ ) distributions in the ionosphere and in the magnetosphere are expressed, respectively, as

$$N_{\text{ionos}} = 10^{mr+n_i}$$

$$N_{\text{mag}} = 0.09 + C e^{-k(r/R_N-1)^2},$$

where  $m = -3.16 \times 10^{-4} \text{ km}^{-1}$ ,  $n_i = 13.18$ ,  $C = 99.91 \text{ cm}^{-3}$ ,  $k = 0.567$ , and the radial distance  $r$  is in kilometers. The solid curve in the figure is the quantity  $0.1 f_c$  plotted against the radial distance  $r$  for the same direction, as calculated from the  $\text{O}_8$  magnetic field model. Figure 6.5a is for direction near the south polar region in the southern magnetic hemisphere (I refer to this direction as the southern direction), and Figure 6.5b is for direction toward the auroral zone in the northern magnetic hemisphere (I refer to this direction as the northern direction). It is apparent that the ratio  $f_p/f_c$  greatly exceeds 0.1 for all  $r$  values in all directions, and it can therefore be concluded that the unmodified standard model for the plasma frequency distribution appears to be incompatible with our derived radio source location.

The dashed curves, however, represent a plasma frequency distribution for which  $f_p/f_c < 0.1$  over a considerable range of the radial distances in excess of  $1.07 R_N$ , corresponding to a range of possible CMI emission frequencies covering the observed smooth-component spectrum. I developed these dashed curves by keeping the maximum electron density of the ionosphere and by arbitrarily reducing the peak magnetospheric electron density, the magnetospheric scale height, and the ionospheric scale height for both northern and southern directions. The electron number density

distributions in the ionosphere and the magnetosphere are given (in units of  $\text{cm}^{-3}$ ) by

$$N_{\text{ionos}} = N_i e^{-\frac{r-1}{H_i}}$$

$$N_{\text{mag}} = N_m e^{-\frac{r-1}{H_m}},$$

where  $H_i$  and  $H_m$  are scale heights for the ionosphere and the magnetosphere, respectively, and they take the same unit as  $r$  (*i.e.*, in units of  $R_N$ ). In order to bring down the ratio of  $f_p/f_c$  to 0.1 for a considerable frequency range, the peak magnetospheric electron density has to be reduced to 1/24 that of the standard model, and the magnetospheric and ionospheric scale heights have to be reduced to 1/2 and 1/7 those of the standard model, respectively (see Figure 6.5*a*), for northern direction; for southern direction the peak magnetospheric electron density has to be reduced to 1/4 that of the standard model, and the magnetospheric and ionospheric scale heights have to be reduced to 1/2 and 1/3 those of the standard model, respectively (see Figure 6.5*b*).

In Earth's magnetosphere, the CMI emission at kilometric wavelengths has been observed to originate in the auroral zones within electron-depleted cavities. The reduction of electron density within such a cavity, which is necessary to bring the ratio of  $f_p/f_c$  below 0.1 in order for the CMI emission process to take place, results from the development of a parallel electric field component in association with precipitating auroral particles. I should point out in the above example that, based on the radio horizon calculations, the rather limited region from which one must select the actual source area includes the one I selected by means of trial-and-error hollow-cone beam fitting, and also the principal north magnetic polar auroral zone (see next section). The electron densities in the magnetosphere as calculated from my plasmasphere model for the northern direction are probably too low to be realistic. On the other hand, the electron densities that the standard plasmasphere model describes are too high, which is not realistic either. I tend to believe that my plasmasphere model for



the southern direction is a self-consistent one which provides a suitable environment for radiation to be emitted from places near the southern magnetic polar region, while radiation from the northern magnetic hemisphere has to come from the depleted-electron cavity region, in which the plasma frequency distribution has been reduced from approximately that of the standard plasmaspheric model to the dashed curve in Figure 6.5*b*, resulting in the emission by the CMI process.

#### 6.4 Modeling

There are two steps in my modeling process. First, I search for a set of parameters for the source location and beaming geometry that can best fit the observation, regardless visibility and plasma environment of the source region. Then two major constraints are imposed before starting the final comprehensive search for the radio beam model that best fits the observed data at each of a series of representative frequencies: (1) The final source locations must be within the radio horizon for X-mode emission at the times at which the emission was observed at that frequency, and (2) sources are located in the region for which the plausible estimates of the ratio  $f_p/f_c$  are smaller than 0.1, where  $f_p$  is the plasma frequency.

Let me now briefly outline my first step in modeling the smooth component. The sources are assumed to be located at positions at which the electron cyclotron frequency ( $f_c$ ) based on the O<sub>8</sub> field model is very slightly less than the frequency of observation. For the RH-polarized smooth component, emission from each point of the source region is assumed to be beamed into either a hollow cone or a filled cone that is axially aligned with tangency of the magnetic field line at the source point. The model parameters being used are: (1) magnetic colatitude of the source,  $\theta_m$  (assumed to be a strip of unit width in latitude); (2) opening half-angle of the emission cone,  $\beta$ ; (3) cone wall thickness,  $\Delta\beta$ ; (4) magnetic longitude of center of

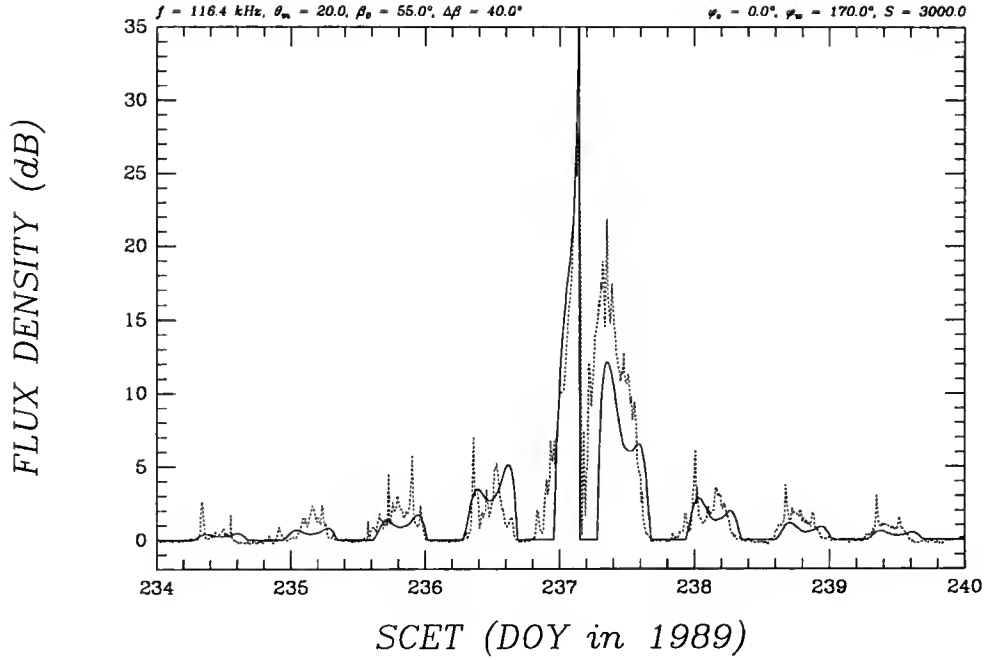


Figure 6.6. Comparison of the modeled intensity (solid curve) as a function of spacecraft event time (SCET) in units of day of year (DOY) with the smoothed observed total intensity (dotted curve) for the 116.4 kHz channel. Source parameters are shown on the top of the plot.

source region,  $\phi_c$ ; (5) source region width in terms of magnetic longitude,  $\phi_w$ ; (6) plot scale constant,  $S$ . In other words, the source was assumed to be of unit width in magnetic latitude while the source location and extent in magnetic longitude were treated as free parameters in the modeling process.

A simulation of the observed intensity versus time was made with the model between day numbers from 234 (August 22) to 240 (August 28) for each of several combinations of the above parameters. A comparison of this modeled intensity with the smoothed observed total intensity versus time for radiation at frequency  $f = 116$  kHz is shown in Figure 6.6. The good fit to the predominantly RH-polarized smooth component of the observed curve of intensity versus time suggests that its source was in the northern hemisphere at magnetic colatitude  $20^\circ$ , within a longitude width of  $170^\circ$  centered at  $0^\circ$  magnetic longitude; and that the beam was the superposition of hollow-cone elements with opening half angles of about  $55^\circ$  each. Although the fit

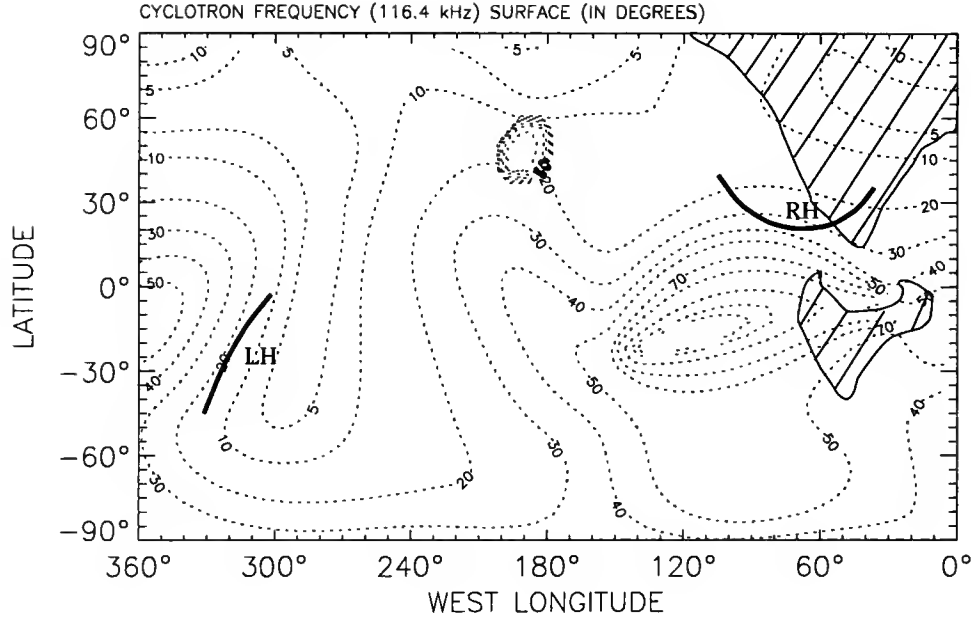


Figure 6.7. Source regions mapped on the  $f_c = 116.4$  kHz surface as calculated by the  $O_8$  field model. Over plotted are contour curves of the distribution of the difference between the field directions calculated by the  $O_8$  and OTD models (see Figure 6.4). The hatched area is the visible radio horizon during the period when the smooth component was observed (see Figure 6.9).

is far from perfect, it is much better than those obtained by LLRR and by others, and is close enough to suggest strongly that important features of our model for this emission component are more or less correct. The model simulates correctly not only the occurrence of the emission in each rotation cycle, but also correctly predicts the dropout of the intensity before the closest approach at SCET 03:56 on day 237 (August 25), believed due to the passage of the spacecraft under the  $f_c = f$  surface. The corresponding source region is mapped in Figure 6.7. The hatched area in the figure is the visible radio horizon during the period when the smooth component was observed (see below). The curved line that lies largely inside the shaded area and is labeled RH is the preliminary source region as determined by the hollow-cone-beam-fitting method. Its  $L$ -shell value (as defined in terms of the OTD magnetic coordinate system) is  $L \sim 17$ . The hollow-cone beam opening half-angle,  $\beta$ , is  $55^\circ$ . Although the LLRR-modelled source region for the RH-polarized smooth component was in

the same general longitude region as mine, it was on the  $L = 6$  OTD  $L$ -shell, far outside our  $L$ -shell value of 17. Contrary to my model, that of LLRR also predicts a conjugate LH-polarized source in a much smaller area than the RH source. However, the existence of a distinctive observed component corresponding to this conjugate source region was not conclusively demonstrated by LLRR, and according to my model it does not exist.

In the above modeling process, no restrictions were put on source locations and conditions of the plasma environment in the source region. The result already clearly suggests that the source of the smooth component is in the northern magnetic hemisphere near the auroral zone as calculated from the  $O_8$  magnetic model. The beaming angle of the radiation is a bit smaller than what one expects from the CMI theory.

The second step I take is to eliminate from further consideration those global regions from within which the observed radiation was unlikely to have originated. I systematically compare plots of received radiation intensity and polarization sense versus time as derived from each of a series of geometrical models with the corresponding plots that were actually observed, until a good match is obtained. In doing so, I select a candidate source area on the  $f_c = f$  surface that is subject to the above restrictions, and I assume that radiation is emitted continuously but incoherently from all the elements of this area into identical hollow-cone beams. Each source element is at the apex of its emission beam, and the axis of this component beam is tangent to the magnetic field line at the source element. The half-angle of the hollow cone beam (which is  $< 90^\circ$ ) and wall thickness of the cone are treated as free parameters in the modeling process. The radiation is assumed to be in the R-X mode and the received intensity at the spacecraft having been reduced inversely as the square of the distance. This modeling process is performed for the smooth-component source location and emission beam characteristics at each frequency from 40 kHz to 400 kHz and all times for which there is sufficient activity.

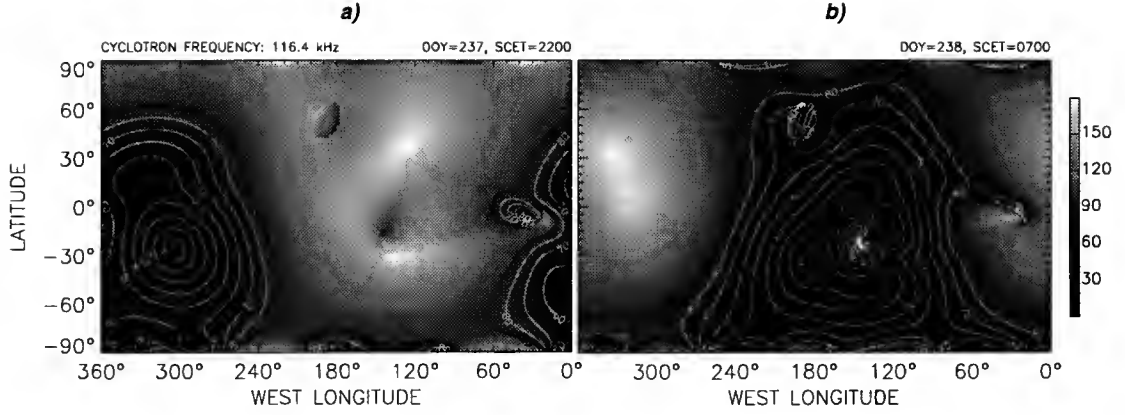


Figure 6.8. Contours of constant spacecraft direction angle with respect to the vector  $-\nabla B$  on the  $f_c = 116$  kHz surface, as calculated with the  $O_8$  magnetic field model, (a) for the starting time of smooth-component activity, and (b) for the time at which the activity ended. The contours for  $10^\circ$  to  $80^\circ$  (at  $10^\circ$  intervals) are white curves, while the  $90^\circ$  curve is black.

All potential R-X mode source locations are at a relatively short distance outside the  $f_c = f$  surface; I incur negligible error by assuming that they are located on this surface. The radio horizon at frequency  $f$  as seen from the spacecraft is defined by the set of directions that are tangent to the  $f_c = f$  surface (refraction neglected); it is also approximately defined by the lines of sight from the spacecraft that are perpendicular to the field gradient vector  $\nabla B$  at the  $f_c = f$  surface. Figure 6.8a is a map of contour curves of constant spacecraft direction angle with respect to the vector  $-\nabla B$  on the contour surface defined by  $f_c = 116$  kHz, for the starting time of smooth-component activity at the frequency 116 kHz. Each contour curve for  $90^\circ$  defines a radio horizon for this time. Notice that the shape of such radio horizon can be very different from that calculated with an OTD magnetic field model, as has been anticipated. At any given time, the direction angle from the  $-\nabla B$  vector to the spacecraft at every point within the part of a radiating region that is *below* the radio horizon must be greater than  $90^\circ$  (because such source region has not yet raised up). Thus in Figure 6.8a, which is for the storm starting time, the direction angle is greater than  $90^\circ$  in the part of the radiating region that will rise above the horizon during the course of the

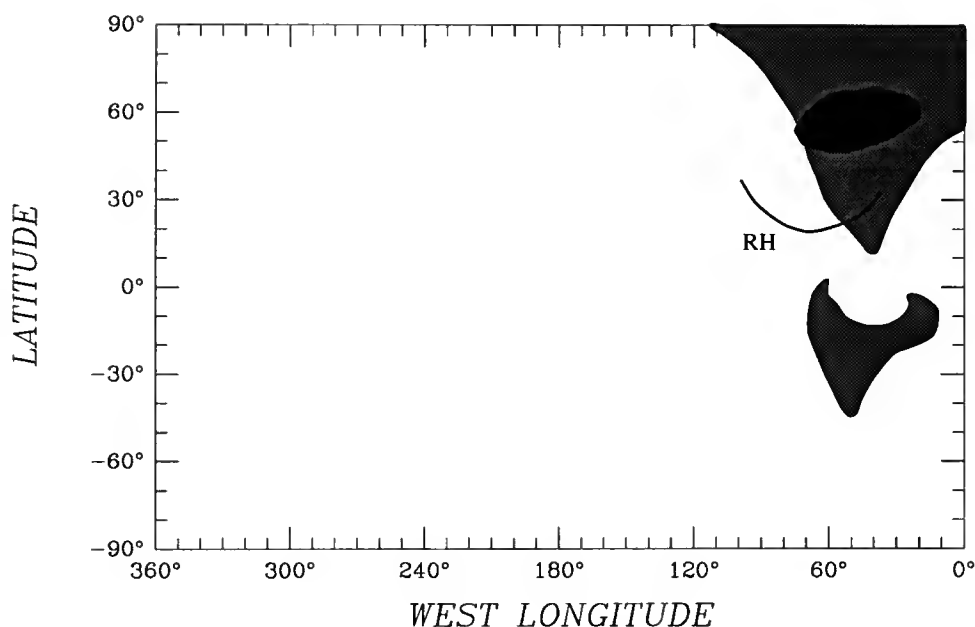


Figure 6.9. The area on the  $f_c = 116$  kHz surface which is visible by the spacecraft during the period of the storm; the curved line inside it is our previously determined location of the source; the darker-shaded region is one of the *Connerney et al.* [1991] auroral zones.

storm, and the regions in which the direction angle is less than  $90^\circ$  are not radiating because the radiation is yet to be received. Figure 6.8*b* is the same type of plot for the time at which the storm just ended; here the angle has become greater than  $90^\circ$  in all of the radiating region, and the area which is above the horizon (direction angle  $< 90^\circ$ ) is not radiating. If one makes the reasonable assumption that the source region remained fixed in East Longitude and Latitude during the observed storm, then the source could have been located only in some area within the region for which the direction angle was greater than  $90^\circ$  at both the starting and ending times (and at all intervening times). This is the shaded region of Figure 6.9; it is the only potential source region that was visible by the spacecraft during the period of the storm. It is reassuring to find that our source location determined in the first step (see Figure 6.7) also lies within this region, as can be seen in Figure 6.9. Also in the region is the

auroral zone associated with the strongest of the north magnetic poles, as determined by *Connerney et al.* [1991] on the basis of the  $O_8$  field model.

In an alternative modeling method, I treat the latitude and longitude of the source region as free parameters so that the derived source region is an area instead of lines. Furthermore, the source region is located by tracing along magnetic field lines upward from their footprints, which originate from a region designated on the “surface” of Neptune, until the  $f_c$  surface is reached. I systematically searched for the source region within the visible radio horizon until the best fit to the observation was obtained. It was found that the most promising source region is located *inside* the auroral zone near the northern magnetic polar region determined with the  $O_8$  model by *Connerney et al.* [1991]. To be more specific, the footprint of the source region is confined in an area with a longitude range from  $10^\circ$  NLS to  $60^\circ$  NLS and a latitude range from  $44^\circ$  to  $60^\circ$ . The beaming angle was found to be around  $85^\circ$  for radiation at lower frequencies (e.g., 116 kHz) and  $65^\circ$  for higher frequencies (above 400 kHz), and the emission beam is thicker at lower frequencies ( $24^\circ$  for 116 kHz) than at higher frequencies ( $7^\circ$  for 250 kHz and above).

An example of modeled intensity curve as a function of SCET for frequencies of 116, 250 and 404 kHz and the corresponding source footprint on the Neptune’s surface are shown in Figure 6.10. Panel (d) in the figure is for source maps, and the rest are for the intensity curves. This figure clearly shows that our model correctly simulates the observed radiation, not just at a single frequency channel, but at a broad frequency range (from about 40 kHz to over 400 kHz). The most convincing support on the good fit of the model to the observation is that source locations are correctly determined to be in the region near the auroral zone (calculated with the  $O_8$  magnetic field model), visible during the radiation is actually observed. It is also the region where intensive particle precipitation along magnetic field lines was found [*Paranicas and Cheng*, 1994]. The association of our modeled NKR smooth component with such

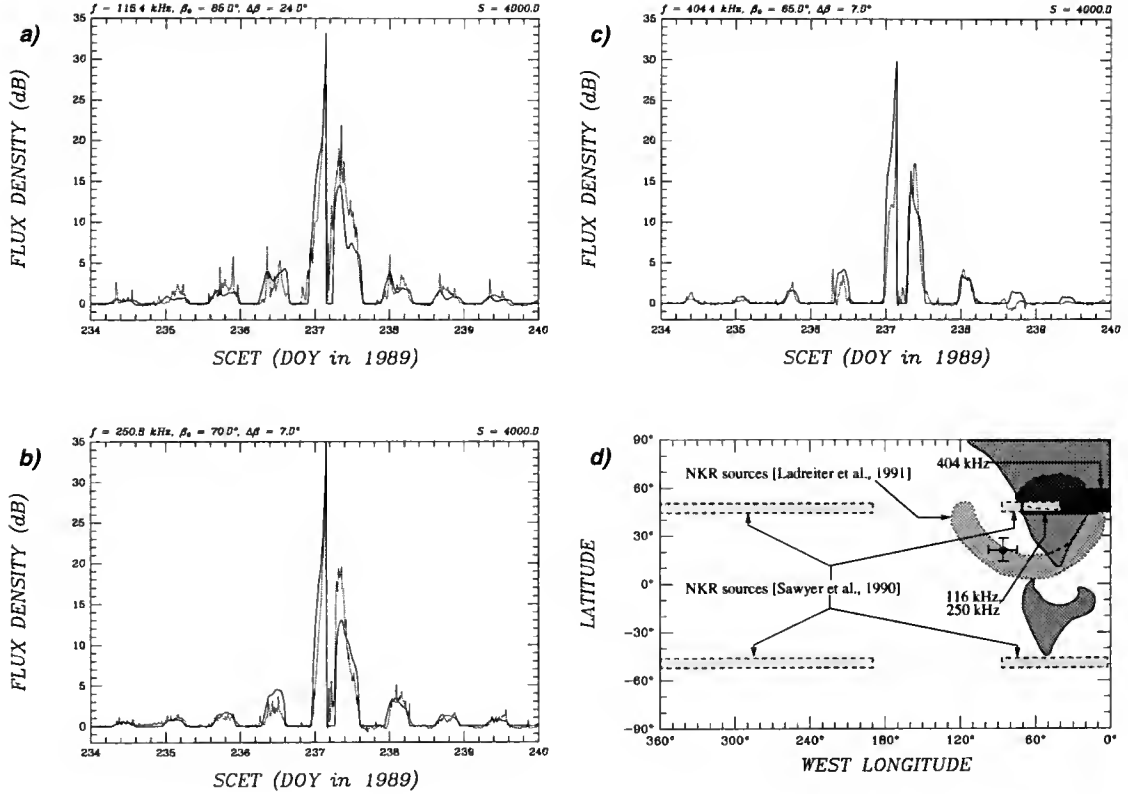


Figure 6.10. Comparison of modeled intensity curves as a function of spacecraft event time (SCET) with observed intensity at frequency of 116 kHz (a), 250 kHz (b), and 404 kHz (c). Footprints of the source regions for radiation at these frequencies are in panel (d). Over-plotted are also footprints of source regions determined by *Sawyer et al.* [1990], *Ladreiter et al.* [1991], and by *Lecacheux and Boischo*t [unpublished report]. The visible  $f_c = 116 \text{ kHz}$  during the storm is calculated with the  $O_8$  model (see Figure 6.9).

electron precipitation is obvious. Since we used the more realistic  $O_8$  field model, the physical parameters such as the opening angle of the beaming cone, wall thickness of the cone, latitude and longitude range of the source region, etc., should be more meaningful than if the OTD magnetic field model had been used.

Plotted in Figure 6.10d are also footprints of source locations determined by early modeling work by *Sawyer et al.* [1990], *Ladreiter et al.* [1991] and *Lecacheux and Boischo*t [unpublished report]. These source regions are considerably far away from the visible  $f_c = f$  surface (shown in Figure 6.10d is the  $f_c = 116 \text{ kHz}$  visible surface).



Much of such regions are occulted by the  $f_c = f$  surface, and consequently source regions determined by the OTD model are very questionable.

### 6.5 Discussion

As has been mentioned in Section 6.3, the magnetic field strength in the northern magnetic hemisphere is so low that the condition for CMI to operate ( $f_p/f_c < 0.1$ ) cannot possibly be met if the standard plasmasphere model is used and if no efficient physical process for depleting electrons in the polar region is involved. I have presented two plasmaspheric models which would bring down the  $f_p/f_c$  ratio in a broad region in which the electron cyclotron frequency range is about that of observed radiation (see Figure 6.5). I tend to believe the plasmaspheric model developed for the southern radio sources is more realistic than other models. I believe a strong electron depletion process is actually happening so that depleted-electron cavities are created in the magnetic north auroral zone. The most probable source regions are in this auroral zone where electron cavity is located and magnetic field strength is relatively stronger than other place in the northern magnetic hemisphere. I am therefore confident about the source locations that I determined above. I did get better modeling result for source regions in the auroral zone than for the source region previously obtained when no constraints were imposed. A larger wave normal angle (or beaming angle of the hollow cone) is favored by the CMI theory.

Before my effort in modeling the Neptunian kilometric radiation, I first demonstrated that, due to the significant contribution from the higher order terms in the expansion of the field model to the actual magnetic field, the simple OTD magnetic field model is not valid in the vicinity of the NKR source regions and therefore cannot be used in the NKR modeling. If the NKR sources are located closed to the  $f = f_c$

surface, as the CMI theory predicted, the OTD model is very different in both magnitude and direction in the source region. Furthermore, as a tool of diagnosing the plasma environment near the source region (and the region between the source and the observer), the fact that the NKR is observed from both magnetic hemispheres suggests that the Voyager 2 radio occultation measurement [Tyler *et al.*, 1989] may have overestimated the plasma density in the ionosphere. Even the whistler observation [Gurnett *et al.*, 1990] may have overestimated the plasma density in the magnetosphere. A consistent ionospheric and magnetospheric model has been established. It is concluded that radiation from the northern magnetic polar region must be from the electron-depleted region.

## CHAPTER 7

### SUMMARY AND CONCLUSIONS

In this dissertation I have dealt with several aspects of radio emissions from the planets Jupiter and Neptune. In the process of analyzing the Voyager PRA data, I found that the previously determined value of the relative orientation of the PRA antenna electric plane was incorrect. A tilt of  $23.3^\circ$  of the E-plane from the monopole plane, which was the previously accepted value based on the work of *Lecacheux and Ortega-Molina* [1987], would lead to impossible results in obtaining directional information from other sources. I have used more than a dozen previously unused spacecraft maneuver events to recalibrate the direction in which the indicated sense of circular polarization reverses itself. The results indicate that the antenna E-surface is not a single plane, and its tilt may vary at different azimuths. The best approximation at present is that the tangent of the E-surface is tilted in one of two directions depending on the incident direction of the incoming waves: it is tilted  $27^\circ$  on the front side of the monopole plane [azimuth angle between  $-45^\circ$  (or  $315^\circ$ ) and  $135^\circ$ ], and  $45^\circ$  on the back side of the antenna plane (azimuth angle between  $135^\circ$  and  $315^\circ$ ). Our analysis confirmed that the polarization sense of the Jupiter hectometric (HOM) and kilometric (KOM) radio emissions observed by Voyager 2 is opposite to the true polarization sense for most of the encounter period. In order to determine the actual polarization sense at any time during the close approach, one must use the newly calibrated antenna response information together with information on the radio source location. The newly calibrated antenna response was also used to determine source

location of the Jupiter HOM emission during a spacecraft maneuver event with the aid of the raytracing technique. The source locations determined in this way were found to be consistent with those predicted with our beaming model.

I have thoroughly reviewed the characteristics of the Jovian HOM emission based on the Voyager observations, and have found many previously undiscovered features. There is a clear evidence that the HOM emission can occur at a frequency as high as 8 MHz. A wide gap near  $200^\circ$  CML in the intensity profile was a most conspicuous feature for the HOM emission in its entire frequency range. A narrow gap around  $30^\circ$  CML is a feature that is dependent on the observer's latitude and frequency. The observed change of the appearance of recorded data before and after encounter is caused by a combination of changes in latitude and local time of the observer. By calculating the average flux density and occurrence probability as a function of frequency and magnetic latitude for both LH and RH components and for data recorded during increasing and decreasing magnetic latitude regions, I showed that the HOM emission is not beamed into a constant magnetic latitude as was previously believed. The magnetic latitude of the beaming center and the beaming widths are all functions of wave frequency. Furthermore, radiation of the LH and RH components at lower HOM frequencies, believed to be emitted from source regions in the southern and northern hemispheres respectively, is beamed more northward and southward. This is an important piece of observational evidence to support our idea that the HOM emission is not subject to the refraction effect of the Io plasma torus.

We explored some models that would lead to a true magnetic equatorial beaming. We demonstrated that widely distributed hollow-cone source models do not form the magnetic equatorial beaming that fits the observation. There appear to be two possible magnetic equatorial beaming models that could form the desired beaming. One locates the HOM sources in a region very close to the magnetic pole (near the cusp region), and radiation is beamed into a single hollow cone with nearly  $90^\circ$  half opening

angle. The other possibility is that the HOM source is distributed over all longitudes on a constant  $L$ -shell where the local magnetic field vector is nearly parallel to the magnetic equator and radiation is confined to a filled cone along the magnetic field direction. By assuming that the HOM emission is generated by the CMI mechanism, I have modeled the beaming of the HOM emission over a broad frequency range. This modeling resulted in several important discoveries. The HOM sources were found to be located on large  $L$ -shell values ( $> 20$ ) at the place where the electron cyclotron frequency is approximately equal to the frequency of observation. The source region was found to be confined to a narrow longitudinal region centered near  $30^\circ$  CML. The radiation is beamed into a hollow cone with a large opening angle (in the range of  $70^\circ$  to  $80^\circ$ ), depending on the frequency. The so-called magnetic latitudinal beaming is actually caused by interception of this hollow cone by the observer near the equator.

The propagation of the radio emission through the Jovian magnetosphere has been investigated in great detail with the two- and three-dimensional raytracing techniques over the entire HOM frequency range. Assuming that the  $O_4$  magnetic field model and the *Divine and Garrett* [1983] plasmaspheric model correctly describe the Jovian magnetospheric environment, it was found by means of raytracing that there can be only a small portion of the HOM emission propagating through the central, dense part of the Io plasma torus, and that such radiation at frequencies higher than 800 kHz will not be appreciably affected by the torus. From the source locations suggested in my beaming model (Chapter 4) and by others in the literature, most HOM emission can reach an observer near the equator without being affected by the Io torus at all. I conclude that the Io plasma torus is *not* a major disturbing influence on the propagation of the HOM emission, nor is it responsible for the possible magnetic equatorial beaming or shadowing of the HOM emission. It is also clear that the broad peak in the power spectrum of the HOM emission is not due to the so-called focusing effect by the Io torus, but rather is an intrinsic property of the emission itself.

Waves propagating in both the R-X and L-O modes were investigated. For the L-O mode wave, as long as they are emitted near the  $f_c \approx f$  surface, they would experience almost the same propagation effect as the R-X mode waves do. It is unlikely that L-O waves are emitted from the altitude where  $f_p \approx f$ , because at such low altitude the rays (especially those at lower frequencies) would be strongly deviated by the Io plasma torus. By using the ray-matching technique in the raytracing calculation and a special spacecraft maneuver event that occurred when Voyager 1 was only  $15 R_J$  away from Jupiter and caused the PRA antenna beam to scan over the HOM source region, I successfully located a HOM source region. The result is in good agreement with what we have found in our beaming model.

In contrast, the Neptunian kilometric radiation (NKR) comes from an entirely different magnetospheric environment than the Jovian HOM emission. We modeled one of several NKR components, the low-frequency smooth component (with a frequency range between about 30 kHz and 500 kHz). We demonstrated that the magnetic field distributions near the NKR source region as previously predicted by the OTD model and as predicted by us with the aid of the more realistic  $O_8$  model are very different in both magnitude and field direction. We concluded that the OTD model is basically invalid for use in modeling NKR source locations. As a tool for the remote sensing the plasma environment in the magnetosphere, radio emissions from the planetary magnetosphere can provide indirect information on plasma density and other physical parameters, provided that the radio emission theory is valid. Assuming that the NKR is generated through the CMI mechanism, we examined models of electron distribution in the Neptunian ionosphere and magnetosphere, and found that in order for CMI to operate, the peak electron density in the magnetosphere must be much lower than what the standard model predicts, and the scale heights for both the ionosphere and the magnetosphere need to be also smaller than those in the standard model. Furthermore, we concluded that the NKR from the northern magnetic

hemisphere in R-X mode must be from the electron-depleted cavity regions. Without considering the actual visibility of the radio source region, our model suggests that the low-frequency smooth NKR is located in the northern magnetic hemisphere on the  $L \approx 17$  shell centered at  $0^\circ$  magnetic longitude, with a longitudinal width of about  $170^\circ$ . The radiation for each subsource is beamed into a hollow cone of  $55^\circ$  opening half angle. This source region is closer to the auroral zone determined by *Connerney et al.* [1991] than that determined by the LLRR model. Due to the complexity of the Neptunian magnetic field described by the  $O_8$  model, the  $f_c \approx f$  surface can take a very irregular shape. By excluding regions on the  $f_c = f$  surface that are visible when no emission is observed and including the region visible when emission is observed, we found a region on the  $f_c = f$  surface inside which the NKR source is located. Incidentally, this region also is partially in the auroral zone determined by *Connerney et al.* [1991]. By systematically changing latitude and longitude values of the footprint on the Neptunian surface of the source region while adjusting other model parameters, we found that the NKR low-frequency smooth source is very close to the northern magnetic pole and partially inside the auroral zone. The radiation was found to be beamed into hollow cones whose opening angle is in the range of  $65^\circ \sim 85^\circ$ , depending on the wave frequency (the lower the wave frequency, the larger the cone opening angle). It is worth noting that the source locations determined by the LLRR model and by *Sawyer et al.* [1990] are virtually invisible most of time when the emission was observed, suggesting that such source locations are very questionable.

## APPENDIX A REFRACTIVE INDEX AND RAY EQUATIONS

### A.1 Refractive Index and the Appleton-Hartree Formula

It is well known that the Maxwell's equations describe the behavior of the electromagnetic wave travelling in a medium. In the vacuum, the electric displacement  $\mathbf{D}$  is in the same direction of the electric field  $\mathbf{E}$ ; in a plasma, however, it is generally associated with  $\mathbf{E}$  via the dielectric tensor  $\mathbf{K}$ :  $\mathbf{D} = \mathbf{K} \cdot \mathbf{E}$ , where  $\mathbf{K}$  is given by (see, e.g., *Stix* [1962])

$$\mathbf{K} = \begin{pmatrix} S & -iD & 0 \\ iD & S & 0 \\ 0 & 0 & P \end{pmatrix},$$

where the quantities  $S$  (for sum),  $D$  (for difference), and  $P$  (for plasma) are functions of the plasma angular frequency  $\Pi_k$  and the cyclotron angular frequency  $\Omega_k$  of all kind of particles involved, and are defined as follows:

$$\left. \begin{aligned} S &= \frac{1}{2}(R + L), & D &= \frac{1}{2}(R - L) \\ R &= 1 - \sum_k \frac{\Pi_k'^2}{\omega^2} \left( \frac{\omega}{\omega + \epsilon_k \Omega_k'} \right) & \text{or} & \quad R = 1 - \sum_k \frac{X_k}{U_k + \epsilon_k Y_k} \\ L &= 1 - \sum_k \frac{\Pi_k'^2}{\omega^2} \left( \frac{\omega}{\omega - \epsilon_k \Omega_k'} \right) & \text{or} & \quad L = 1 - \sum_k \frac{X_k}{U_k - \epsilon_k Y_k} \\ P &= 1 - \sum_k \frac{\Pi_k'^2}{\omega^2} & \text{or} & \quad P = 1 - \sum_k \frac{X_k}{U_k} \end{aligned} \right\}, \quad (\text{A.1})$$



where summations are over all species;  $\epsilon_k = \pm 1$  defines the sign of the electric charge,  $\omega$  is the angular frequency of the wave;  $X_k$  and  $Y_k$  are related with the ratios of  $\Omega_k$  and  $\Pi_k$  to the wave frequency:

$$X_k = \frac{\Pi_k^2}{\omega^2}, \quad Y_k = \frac{\Omega_k}{\omega}. \quad (\text{A.2})$$

$\Omega'_k$  and  $\Pi'_k$  are the cyclotron angular frequency and the plasma angular frequency, respectively, for the  $k$ th type particles when collisions are included, and are defined as

$$\Omega'_k = \frac{\Omega_k}{U_k} = \left| \frac{q_k B}{m_k U_k} \right|, \quad \text{and} \quad \Pi'^2_k = \frac{\Pi_k^2}{U_k} = \frac{N_k q_k^2}{\epsilon_0 m_k U_k}$$

$$U_k = 1 - i \frac{2\pi \nu_k}{\omega} = 1 - i Z_k, \quad Z_k = \frac{2\pi \nu_k}{\omega},$$

where  $q_k$  is the electric charge,  $m_k$  the mass,  $N_k$  the number density,  $\nu_k$  the (effective) collision frequency, all for the particles of the  $k$ th type, and finally  $\epsilon_0$  is the permittivity of free space. For electrons,

$$X_e = X = \frac{\Pi_e^2}{\omega^2} = \frac{f_p^2}{f^2}, \quad Y_e = Y = \frac{\Omega_e}{\omega} = \frac{f_c}{f} \quad (\text{A.3a})$$

$$f_p = \frac{1}{2\pi} \sqrt{\frac{e^2 N_e}{\epsilon_0 m_e}}, \quad f_c = \frac{1}{2\pi} \frac{eB}{m_e}. \quad (\text{A.3b})$$

Solving the Maxwell's equations with Fourier analysis, one gets

$$\mathbf{n} \times (\mathbf{n} \times \mathbf{E}) + \mathbf{K} \cdot \mathbf{E} = 0,$$

where  $\mathbf{n} = \frac{c}{\omega} \mathbf{k}$  is a dimensionless vector whose magnitude (real part)  $n = |\mathbf{n}|$  is the ratio of the velocity of light to the phase velocity and whose direction is the same as that of the wave propagation vector  $\mathbf{k}$ . Substituting the dielectric tensor  $\mathbf{K}$  into the above equation and defining  $\xi$  to be the angle between the magnetic field strength  $\mathbf{B}$

and the vector  $\mathbf{n}$ , we have

$$\begin{pmatrix} S - \tilde{n}^2 \cos^2 \xi & -iD & \tilde{n}^2 \cos \xi \sin \xi \\ iD & S - \tilde{n}^2 & 0 \\ \tilde{n}^2 \cos \xi \sin \xi & 0 & P - \tilde{n}^2 \sin^2 \xi \end{pmatrix} \begin{pmatrix} E_x \\ E_y \\ E_z \end{pmatrix} = 0. \quad (\text{A.4})$$

We use the symbol  $\tilde{n}$  to emphasize that the magnitude of  $\mathbf{n}$  is in general a complex number:

$$\tilde{n} = n + i\chi,$$

where  $n$  and  $\chi$  describe the phase velocity ( $c/n$ ) and the attenuation rate of a wave travelling in the medium, respectively. The condition for a nontrivial solution of Equation (A.4) is that the determinant of the square matrix be zero, which gives the following dispersion relation [Stix, 1962]:

$$A\tilde{n}^4 - B\tilde{n}^2 + C = 0, \quad (\text{A.5})$$

where

$$\left. \begin{aligned} A &= S \sin^2 \xi + P \cos^2 \xi \\ B &= RL \sin^2 \xi + PS (1 + \cos^2 \xi) \\ C &= PRL \end{aligned} \right\}. \quad (\text{A.6})$$

The solution to Equation (A.5) is

$$\tilde{n}^2 = \frac{B \pm F}{2A}, \quad (\text{A.7})$$

where  $F$  satisfies

$$F^2 = B^2 - 4AC = (RL - PS)^2 \sin^4 \xi + 4P^2 D^2 \cos^2 \xi. \quad (\text{A.8})$$

It is often convenient to write Equation (A.7) in other forms which better describe how much the plasma deviates from the vacuum:

$$\begin{aligned} \tilde{n}^2 &= \frac{B \pm F}{2A} = 1 - \left( 1 - \frac{B \pm F}{2A} \right) \\ &= 1 - \left( \frac{2A - B \mp F}{2A} \right) = 1 - \frac{(2A - B)^2 - F^2}{2A(2A - B \pm F)} \end{aligned}$$

$$\therefore \quad \tilde{n}^2 = 1 - \frac{2(A - B + C)}{2A - B \pm \sqrt{B^2 - 4AC}}. \quad (\text{A.9})$$

The two solutions shown in Equations (A.7) and (A.9) correspond to two types of wave modes: the ordinary (O) mode with left hand polarization for the upper sign (+), and the extraordinary (X) mode with right hand polarization for the lower sign (-). The L-O and R-X mode waves are so labeled due to their characteristics at two extreme cases: parallel propagation when  $\xi = 0^\circ$ , and perpendicular propagation when  $\xi = 90^\circ$ . In the case of the parallel propagation ( $\xi = 0^\circ$ ), two of three roots of the dispersion relation correspond to transverse electromagnetic waves with the right hand (for  $\tilde{n}^2 = R$ ) and the left hand (for  $\tilde{n}^2 = L$ ) polarization, respectively (the third root  $P = 0$  corresponds to a longitudinal electrostatic plasma oscillation). In case of the perpendicular propagation ( $\xi = 90^\circ$ ), two roots of the dispersion relation correspond to, respectively, a transverse waves in a cold plasma without a magnetic field ( $\tilde{n}^2 = P$ , the ordinary mode) and the extraordinary mode ( $\tilde{n}^2 = RL/S$ ) that becomes electrostatic at hybrid resonance frequency at which  $S = 0$ .

For radio waves propagating in planetary magnetospheres, the cyclotron and plasma frequencies for particles other than electrons are very small compared with the wave frequency and therefore can be ignored. In this case, only electrons need to be considered, and equations in (A.1) become (note that  $\epsilon_e = -1$ ,  $q_e = e$ ,  $X_e = X$ ,  $Y_e = Y$ ,  $U_e = U$ ,  $Z_e = Z$ ):

$$R = 1 - \frac{X}{U - Y}, \quad L = 1 - \frac{X}{U + Y}, \quad P = 1 - \frac{X}{U}$$

$$S = \frac{1}{2}(R + L) = 1 - \frac{XY}{U^2 - Y^2}$$

$$D = \frac{1}{2}(R - L) = -\frac{XY}{U^2 - Y^2},$$

and equations in (A.6) become

$$\left. \begin{aligned} A &= \frac{(U - X)(U^2 - Y^2) - XY^2 \sin^2 \xi}{U(U^2 - Y^2)} \\ B &= \frac{2U(U - X)^2 - 2Y^2(U - X) - XY^2 \sin^2 \xi}{U(U^2 - Y^2)} \\ C &= \frac{(U - X)^3 - (U - X)Y^2}{U(U^2 - Y^2)} \end{aligned} \right\},$$

which, to the dispersion equation (A.5), is equivalent to:

$$\left. \begin{aligned} A &= U^2(U - X) - Y^2(U - X) - XY^2 \sin^2 \xi \\ B &= 2U(U - X)^2 - 2Y^2(U - X) - XY^2 \sin^2 \xi \\ C &= (U - X)^3 - Y^2(U - X) \end{aligned} \right\}. \quad (\text{A.10})$$

Substituting expressions of  $A$ ,  $B$ , and  $C$  into Equations (A.8) and (A.7), we can write Equation (A.7) as

$$\tilde{n}^2 = \frac{2U(U - X)^2 - 2Y^2(U - X) - XY^2 \sin^2 \xi \pm \sqrt{XY^2 \sin^4 \xi + 4(U - X)^2 \cos^2 \xi}}{2U^2(U - X) - 2Y^2(U - X \cos^2 \xi)}, \quad (\text{A.11})$$

which is, according to Equation (A.9), equivalent to

$$\tilde{n}^2 = 1 - \frac{2X(U - X)}{2U(U - X) - Y^2 \sin^2 \xi \pm \sqrt{Y^4 \sin^4 \xi + 4Y^2(U - X)^2 \cos^2 \xi}}. \quad (\text{A.12})$$

The above two equations are often referred to as the Appleton-Hartree formula, and the latter form is more convenient in numerical calculations. In planetary magnetospheres, the plasma can be treated as “cold” one, meaning the thermal motions of electrons can be ignored. This is to say that collisions of electrons with other particles can be ignored ( $\nu = 0$ , or  $U = 1$ ). In this case,  $\tilde{n}$  is either a real or an imaginary quantity but not a complex one, and the Appleton-Hartree formula becomes:

$$\tilde{n}^2 = 1 - \frac{2X(1 - X)}{2(1 - X) - Y^2 \sin^2 \xi \pm \sqrt{Y^4 \sin^4 \xi + 4Y^2(1 - X)^2 \cos^2 \xi}}. \quad (\text{A.13})$$

In a region in which the electromagnetic waves can still propagate,  $\tilde{n}$  must be pure real ( $\tilde{n} = n$ ).

## A.2 Ray Equations and Relevant Terms

The ray equations that we used in Chapter 5 were first developed by *Haselgrove* [1954]. They describe the motion of energy in electromagnetic waves propagating in an anisotropic medium in three dimensions of a spherical coordinate system. Conventionally, this coordinate system is chosen to be the same as the planetocentric coordinate system. Under such spherical coordinate system, the ray equations can be written:

$$\left. \begin{aligned} \dot{r} &= \frac{c}{\tilde{n}^2} \left( n_r - \tilde{n} \frac{\partial \tilde{n}}{\partial n_r} \right) \\ \dot{\theta} &= \frac{c}{r \tilde{n}^2} \left( n_\theta - \tilde{n} \frac{\partial \tilde{n}}{\partial n_\theta} \right) \\ \dot{\varphi} &= \frac{c}{r \sin \theta \tilde{n}^2} \left( n_\varphi - \tilde{n} \frac{\partial \tilde{n}}{\partial n_\varphi} \right) \end{aligned} \right\}, \quad (\text{A.14})$$

$$\left. \begin{aligned} \dot{n}_r &= \frac{c}{\tilde{n}} \frac{\partial \tilde{n}}{\partial r} + n_\theta \dot{\theta} + n_\varphi \dot{\varphi} \sin \theta \\ \dot{n}_\theta &= \frac{1}{r} \left( \frac{c}{\tilde{n}} \frac{\partial \tilde{n}}{\partial \theta} - n_\theta \dot{r} + n_\varphi r \dot{\varphi} \cos \theta \right) \\ \dot{n}_\varphi &= \frac{1}{r \sin \theta} \left( \frac{c}{\tilde{n}} \frac{\partial \tilde{n}}{\partial \varphi} - n_\varphi \dot{r} \sin \theta - n_\varphi r \dot{\theta} \cos \theta \right) \end{aligned} \right\}, \quad (\text{A.15})$$

where  $n_r$ ,  $n_\theta$  and  $n_\varphi$  are three components of the refractive index  $n$  in the spherical coordinate system:

$$\mathbf{n} = n_r \mathbf{e}_r + n_\theta \mathbf{e}_\theta + n_\varphi \mathbf{e}_\varphi, \quad (\text{A.16})$$

where  $\mathbf{e}_r$ ,  $\mathbf{e}_\theta$ , and  $\mathbf{e}_\varphi$  are unit vectors of the orthogonal curvilinear coordinate system.

$n_r$ ,  $n_\theta$  and  $n_\varphi$  give the direction of the wave normal,  $\mathbf{n} = \frac{c}{\omega} \mathbf{k}$ , and they satisfy the

normalization relation:

$$n_r^2 + n_\theta^2 + n_\varphi^2 = \text{real} \{ \tilde{n}^2 \} = n^2. \quad (\text{A.17})$$

The refractive index  $\tilde{n}$  appeared in the ray equations (A.14) and (A.15) is given by the Appleton-Hartree formula, Equation (A.12) or (A.13), for the cold plasma environment. We now define another vector,  $\mathbf{Y}$ , whose magnitude represents  $Y = f_c/f$  and whose direction is that of the magnetic field  $\mathbf{B}$ :

$$\mathbf{Y} = Y_r \mathbf{e}_r + Y_\theta \mathbf{e}_\theta + Y_\varphi \mathbf{e}_\varphi = \frac{e}{2\pi m_e f} \mathbf{B}. \quad (\text{A.18})$$

The three components of  $\mathbf{Y}$  can be expressed in terms of the three components of  $\mathbf{B}$ :

$$\left. \begin{aligned} Y_r &= \frac{e}{2\pi m_e f} B_r \\ Y_\theta &= \frac{e}{2\pi m_e f} B_\theta \\ Y_\varphi &= \frac{e}{2\pi m_e f} B_\varphi \end{aligned} \right\}. \quad (\text{A.19})$$

We can also resolve  $\mathbf{Y}$  with respect to  $\mathbf{n}$  (or  $\mathbf{k}$ ) into two components, one is the longitudinal component ( $Y_L$ ) parallel to  $\mathbf{n}$ , and the other the transverse component ( $Y_T$ ) perpendicular to  $\mathbf{n}$ :

$$Y_T = Y \sin \xi, \quad Y_L = Y \cos \xi. \quad (\text{A.20})$$

They are related through:

$$\frac{\partial Y_L}{\partial \xi} = -Y \sin \xi = -Y_T \quad (\text{A.21})$$

and

$$\frac{\partial Y_T}{\partial \xi} = Y \cos \xi = Y_L. \quad (\text{A.22})$$

We now can rewrite the Appleton-Hartree formula (A.12) in another form:

$$\tilde{n}^2 = 1 - \frac{2X(U - X)}{2U(U - X) - Y_T^2 \pm \sqrt{Y_T^4 + 4Y_L^2(U - X)^2}}. \quad (\text{A.23})$$

When electron collision can be ignored,  $Z = 0$ ,  $U = 1$ , and  $\tilde{n}$  becomes a pure real or imaginary number.

We now derive terms of  $\tilde{n} \frac{\partial \tilde{n}}{\partial n_r}$ ,  $\tilde{n} \frac{\partial \tilde{n}}{\partial n_\theta}$ , and  $\tilde{n} \frac{\partial \tilde{n}}{\partial n_\varphi}$  in ray equations of (A.14), and  $\frac{\partial \tilde{n}}{\partial r}$ ,  $\frac{\partial \tilde{n}}{\partial \theta}$ , and  $\frac{\partial \tilde{n}}{\partial \varphi}$  in ray equations of (A.15), in terms of a given magnetic field distribution  $\mathbf{B}(r, \theta, \varphi)$  and an electron density distribution  $N_e(r, \theta, \varphi)$ . For convenience, let

$$\mathbf{n} \cdot \mathbf{Y} = G = n_r Y_r + n_\theta Y_\theta + n_\varphi Y_\varphi = n Y \cos \xi \quad (\text{A.24})$$

$$\cos \xi = \frac{\mathbf{n} \cdot \mathbf{Y}}{n Y} \quad (\text{A.25})$$

$$Y \cos \xi = \frac{\mathbf{n} \cdot \mathbf{Y}}{n} = \frac{G}{n} = Y_L \quad (\text{A.26})$$

$$\frac{Y_L}{n} = \frac{\mathbf{n} \cdot \mathbf{Y}}{n^2} = \frac{G}{n^2} \quad (\text{A.27})$$

$$Y_L^2 = \frac{G^2}{n^2}, \quad Y_T^2 = Y^2 - Y_L^2, \quad Y_T^4 = (Y_T^2)^2. \quad (\text{A.28})$$

Also, let 
$$W = \pm \sqrt{Y_T^4 + 4Y_L^2 (U - X)^2} \quad (\text{A.29})$$

$$D = 2U (U - X) - Y_T^2 + W. \quad (\text{A.30})$$

We then can abbreviate Equation (A.23) in the following form:

$$\tilde{n}^2 = 1 - \frac{2X(U - X)}{D}. \quad (\text{A.31})$$

Equation (A.13) suggests that  $\tilde{n} = \tilde{n}(X, Y, Z, \xi)$ , but only  $\xi$  is a function of  $(n_r, n_\theta, n_\varphi)$ . We therefore have

$$\frac{\partial \tilde{n}}{\partial n_r} = \frac{\partial \tilde{n}}{\partial \xi} \frac{\partial \xi}{\partial n_r} \quad \text{or} \quad \tilde{n} \frac{\partial \tilde{n}}{\partial n_r} = \tilde{n} \frac{\partial \tilde{n}}{\partial \xi} \frac{\partial \xi}{\partial n_r}. \quad (\text{A.32})$$

From Equation (A.25),

$$\begin{aligned}
 -\sin \xi \frac{\partial \xi}{\partial n_r} &= \frac{\mathbf{n} \cdot \mathbf{Y}}{Y} \left( \frac{-1}{n^2} \right) \frac{\partial n}{\partial n_r} + \frac{1}{nY} \frac{\partial}{\partial n_r} (\mathbf{n} \cdot \mathbf{Y}) \\
 &= -\frac{\mathbf{n} \cdot \mathbf{Y}}{n^2 Y} \frac{n_r}{n} + \frac{1}{nY} \frac{\partial}{\partial n_r} (n_r Y_r + n_\theta Y_\theta + n_\varphi Y_\varphi) \\
 &= -\frac{Y_L}{nY} \frac{n_r}{n} + \frac{Y_r}{nY}
 \end{aligned}$$

$$Y_T \frac{\partial \xi}{\partial n_r} = -\frac{Y_r}{n} + \left( \frac{n_r}{n^2} \right) Y_L$$

$$\begin{aligned}
 \tilde{n} \frac{\partial \tilde{n}}{\partial n_r} &= \frac{\tilde{n}}{Y_T} \frac{\partial \tilde{n}}{\partial \xi} \cdot Y_T \frac{\partial \xi}{\partial n_r} = \frac{1}{Y_T} \tilde{n} \frac{\partial \tilde{n}}{\partial \xi} \left[ -\frac{Y_r}{n} + \left( \frac{n_r}{n^2} \right) Y_L \right] \\
 &= \frac{1}{Y_T Y_L} \tilde{n} \frac{\partial \tilde{n}}{\partial \xi} \left[ -\left( \frac{Y_L}{n} \right) Y_r + \frac{Y_L^2}{n^2} n_r \right]
 \end{aligned}$$

$$\therefore \tilde{n} \frac{\partial \tilde{n}}{\partial n_r} = \frac{1}{Y_T Y_L} \tilde{n} \frac{\partial \tilde{n}}{\partial \xi} \left[ \left( \frac{Y_L}{n} \right)^2 n_r - \left( \frac{Y_L}{n} \right) Y_r \right]. \quad (\text{A.33})$$

Similarly, 
$$\tilde{n} \frac{\partial \tilde{n}}{\partial n_\theta} = \frac{1}{Y_T Y_L} \tilde{n} \frac{\partial \tilde{n}}{\partial \xi} \left[ \left( \frac{Y_L}{n} \right)^2 n_\theta - \left( \frac{Y_L}{n} \right) Y_\theta \right], \quad (\text{A.34})$$

$$\tilde{n} \frac{\partial \tilde{n}}{\partial n_\varphi} = \frac{1}{Y_T Y_L} \tilde{n} \frac{\partial \tilde{n}}{\partial \xi} \left[ \left( \frac{Y_L}{n} \right)^2 n_\varphi - \left( \frac{Y_L}{n} \right) Y_\varphi \right]. \quad (\text{A.35})$$

The term  $\left( \frac{Y_L}{n} \right)$  has been given by Equation (A.27);  $Y_r$ ,  $Y_\theta$ , and  $Y_\varphi$  are directly related, respectively, via (A.19) to  $B_r$ ,  $B_\theta$ , and  $B_\varphi$  which are given by (B.10), (B.11), and (B.14). The term  $\frac{\tilde{n}}{Y_L Y_T} \frac{\partial \tilde{n}}{\partial \xi}$  can be solved from (A.31) and (A.30):

$$2\tilde{n} \frac{\partial \tilde{n}}{\partial \xi} = 2X(U - X) \frac{1}{D^2} \frac{\partial D}{\partial \xi}, \quad (\text{A.36})$$

where  $\frac{\partial D}{\partial \xi}$  can be obtained from Equation (A.30):

$$\frac{\partial D}{\partial \xi} = -2Y_T \frac{\partial Y_T}{\partial \xi} + \frac{\partial W}{\partial \xi} = 2Y_T Y_L \left[ \frac{Y_T^2 - 2(U - X)^2}{W} - 1 \right]. \quad (\text{A.37})$$



Thus 
$$2\tilde{n} \frac{\partial \tilde{n}}{\partial \xi} = 2X(U-X) \frac{1}{D^2} \cdot 2Y_T Y_L \left[ \frac{Y_T^2 - 2(U-X)^2}{W} - 1 \right].$$

$$\therefore \frac{\tilde{n}}{Y_T Y_L} \frac{\partial \tilde{n}}{\partial \xi} = \frac{2X(U-X)}{D^2} \left[ \frac{Y_T^2 - 2(U-X)^2}{W} - 1 \right]. \quad (\text{A.38})$$

Terms of  $\frac{\partial \tilde{n}}{\partial r}$ ,  $\frac{\partial \tilde{n}}{\partial \theta}$ , and  $\frac{\partial \tilde{n}}{\partial \varphi}$  in ray equations in (A.15) are much more complicated:

$$\frac{\partial \tilde{n}}{\partial r} = \frac{\partial \tilde{n}}{\partial X} \frac{\partial X}{\partial r} + \frac{\partial \tilde{n}}{\partial Y} \frac{\partial Y}{\partial r} + \frac{\partial \tilde{n}}{\partial Z} \frac{\partial Z}{\partial r} + \frac{\partial \tilde{n}}{\partial \xi} \frac{\partial \xi}{\partial r} \quad (\text{A.39})$$

$$\tilde{n} \frac{\partial \tilde{n}}{\partial r} = \tilde{n} \frac{\partial \tilde{n}}{\partial X} \frac{\partial X}{\partial r} + \tilde{n} \frac{\partial \tilde{n}}{\partial Y} \frac{\partial Y}{\partial r} + \tilde{n} \frac{\partial \tilde{n}}{\partial Z} \frac{\partial Z}{\partial r} + \frac{\tilde{n}}{Y_L Y_T} \frac{\partial \tilde{n}}{\partial \xi} \cdot Y_L Y_T \frac{\partial \xi}{\partial r}. \quad (\text{A.40})$$

Similarly,

$$\tilde{n} \frac{\partial \tilde{n}}{\partial \theta} = \tilde{n} \frac{\partial \tilde{n}}{\partial X} \frac{\partial X}{\partial \theta} + \tilde{n} \frac{\partial \tilde{n}}{\partial Y} \frac{\partial Y}{\partial \theta} + \tilde{n} \frac{\partial \tilde{n}}{\partial Z} \frac{\partial Z}{\partial \theta} + \frac{\tilde{n}}{Y_L Y_T} \frac{\partial \tilde{n}}{\partial \xi} \cdot Y_L Y_T \frac{\partial \xi}{\partial \theta}, \quad (\text{A.41})$$

$$\tilde{n} \frac{\partial \tilde{n}}{\partial \varphi} = \tilde{n} \frac{\partial \tilde{n}}{\partial X} \frac{\partial X}{\partial \varphi} + \tilde{n} \frac{\partial \tilde{n}}{\partial Y} \frac{\partial Y}{\partial \varphi} + \tilde{n} \frac{\partial \tilde{n}}{\partial Z} \frac{\partial Z}{\partial \varphi} + \frac{\tilde{n}}{Y_L Y_T} \frac{\partial \tilde{n}}{\partial \xi} \cdot Y_L Y_T \frac{\partial \xi}{\partial \varphi}. \quad (\text{A.42})$$

In the above three equations, terms of  $\frac{\partial X}{\partial r}$ ,  $\frac{\partial X}{\partial \theta}$ , and  $\frac{\partial X}{\partial \varphi}$  are calculated from the given electron density model; while terms of  $\frac{\partial Y}{\partial r}$ ,  $\frac{\partial Y}{\partial \theta}$ , and  $\frac{\partial Y}{\partial \varphi}$  are calculated from the given magnetic field model. The term  $\frac{\tilde{n}}{Y_L Y_T} \frac{\partial \tilde{n}}{\partial \xi}$  has been given in Equation (A.38).

Now let us solve for  $Y_T Y_L \frac{\partial \xi}{\partial r}$ ,  $Y_T Y_L \frac{\partial \xi}{\partial \theta}$ , and  $Y_T Y_L \frac{\partial \xi}{\partial \varphi}$  in Equations (A.40), (A.41), and (A.42). Let us bear in mind that  $n$  (*not*  $\tilde{n}$ ) and  $n_r, n_\theta, n_\varphi$  are not a function of  $(r, \theta, \varphi)$ . From Equation (A.25), we have,

$$\begin{aligned} -\sin \xi \frac{\partial \xi}{\partial r} &= \frac{\partial}{\partial r} \left( \frac{\mathbf{n} \cdot \mathbf{Y}}{nY} \right) = \frac{1}{nY} \frac{\partial (\mathbf{n} \cdot \mathbf{Y})}{\partial r} + (\mathbf{n} \cdot \mathbf{Y}) \frac{\partial}{\partial r} \left( \frac{1}{nY} \right) \\ &= \frac{1}{nY} \left( \mathbf{n} \cdot \frac{\partial \mathbf{Y}}{\partial r} \right) - \frac{\mathbf{n} \cdot \mathbf{Y}}{nY^2} \frac{\partial Y}{\partial r} \end{aligned}$$

$$= \frac{1}{nY} \left( \mathbf{n} \cdot \frac{\partial \mathbf{Y}}{\partial r} \right) - \frac{nY_L}{nY^2} \frac{\partial Y}{\partial r}$$

$$Y \sin \xi \frac{\partial \xi}{\partial r} = \frac{Y_L}{Y} \frac{\partial Y}{\partial r} - \frac{1}{n} \left( \mathbf{n} \cdot \frac{\partial \mathbf{Y}}{\partial r} \right)$$

$$Y_T \frac{\partial \xi}{\partial r} = \frac{Y_L}{Y} \frac{\partial Y}{\partial r} - \frac{1}{n} \left( \mathbf{n} \cdot \frac{\partial \mathbf{Y}}{\partial r} \right).$$

Thus,

$$Y_L Y_T \frac{\partial \xi}{\partial r} = \frac{Y_L^2}{Y} \frac{\partial Y}{\partial r} - \frac{Y_L}{n} \left( \mathbf{n} \cdot \frac{\partial \mathbf{Y}}{\partial r} \right). \quad (\text{A.43})$$

Similarly,

$$Y_L Y_T \frac{\partial \xi}{\partial \theta} = \frac{Y_L^2}{Y} \frac{\partial Y}{\partial \theta} - \frac{Y_L}{n} \left( \mathbf{n} \cdot \frac{\partial \mathbf{Y}}{\partial \theta} \right), \quad (\text{A.44})$$

$$Y_L Y_T \frac{\partial \xi}{\partial \varphi} = \frac{Y_L^2}{Y} \frac{\partial Y}{\partial \varphi} - \frac{Y_L}{n} \left( \mathbf{n} \cdot \frac{\partial \mathbf{Y}}{\partial \varphi} \right), \quad (\text{A.45})$$

where

$$\left. \begin{aligned} \mathbf{n} \cdot \frac{\partial \mathbf{Y}}{\partial r} &= n_r \frac{\partial Y_r}{\partial r} + n_\theta \frac{\partial Y_\theta}{\partial r} + n_\varphi \frac{\partial Y_\varphi}{\partial r} \\ \mathbf{n} \cdot \frac{\partial \mathbf{Y}}{\partial \theta} &= n_r \frac{\partial Y_r}{\partial \theta} + n_\theta \frac{\partial Y_\theta}{\partial \theta} + n_\varphi \frac{\partial Y_\varphi}{\partial \theta} \\ \mathbf{n} \cdot \frac{\partial \mathbf{Y}}{\partial \varphi} &= n_r \frac{\partial Y_r}{\partial \varphi} + n_\theta \frac{\partial Y_\theta}{\partial \varphi} + n_\varphi \frac{\partial Y_\varphi}{\partial \varphi} \end{aligned} \right\}, \quad (\text{A.46})$$

or

$$\left. \begin{aligned} \mathbf{n} \cdot \frac{\partial \mathbf{Y}}{\partial r} &= \frac{e}{2\pi m_e f} \left( n_r \frac{\partial B_r}{\partial r} + n_\theta \frac{\partial B_\theta}{\partial r} + n_\varphi \frac{\partial B_\varphi}{\partial r} \right) \\ \mathbf{n} \cdot \frac{\partial \mathbf{Y}}{\partial \theta} &= \frac{e}{2\pi m_e f} \left( n_r \frac{\partial B_r}{\partial \theta} + n_\theta \frac{\partial B_\theta}{\partial \theta} + n_\varphi \frac{\partial B_\varphi}{\partial \theta} \right) \\ \mathbf{n} \cdot \frac{\partial \mathbf{Y}}{\partial \varphi} &= \frac{e}{2\pi m_e f} \left( n_r \frac{\partial B_r}{\partial \varphi} + n_\theta \frac{\partial B_\theta}{\partial \varphi} + n_\varphi \frac{\partial B_\varphi}{\partial \varphi} \right) \end{aligned} \right\}. \quad (\text{A.47})$$

Terms of  $\frac{\partial B_r}{\partial r}$ ,  $\frac{\partial B_\theta}{\partial r}$ , and  $\frac{\partial B_\varphi}{\partial r}$  can be calculated from Equations (B.15), (B.18), and

(B.22);  $\frac{\partial B_r}{\partial \theta}$ ,  $\frac{\partial B_\theta}{\partial \theta}$ , and  $\frac{\partial B_\varphi}{\partial \theta}$  can be calculated from Equations (B.16), (B.19), and

(B.23); and finally  $\frac{\partial B_r}{\partial \varphi}$ ,  $\frac{\partial B_\theta}{\partial \varphi}$ , and  $\frac{\partial B_\varphi}{\partial \varphi}$  can be calculated from Equations (B.17), (B.21), and (B.25).

Terms of  $\tilde{n} \frac{\partial \tilde{n}}{\partial X}$ ,  $\tilde{n} \frac{\partial \tilde{n}}{\partial Y}$ , and  $\tilde{n} \frac{\partial \tilde{n}}{\partial Z}$  in Equations (A.40), (A.41), and (A.42) can be solved as follows:

$$\begin{aligned}
 2\tilde{n} \frac{\partial \tilde{n}}{\partial X} &= -\frac{\partial}{\partial X} \left[ \frac{2X(U-X)}{D} \right] \\
 &= -\frac{2}{D} [(U-X) - X] - 2X(U-X) \left( \frac{-1}{D^2} \right) \frac{\partial D}{\partial X} \\
 &= -\frac{2(U-2X)}{D} + \frac{2X(U-X)}{D^2} \left[ \frac{8Y_L^2(U-X)(-1)}{2W} - 2U \right] \\
 \tilde{n} \frac{\partial \tilde{n}}{\partial X} &= -\frac{U-2X}{D} - \frac{X(U-X)}{D^2} \left[ \frac{4Y_L^2(U-X)}{W} + 2U \right] \\
 &= -\frac{1}{D^2} \left[ 2U(U-X)^2 - (U-2X)Y_T^2 + \right. \\
 &\quad \left. \frac{(U-2X)Y_T^4 + 4Y_L^2(U-X)^2(U-2X+X)}{W} \right] \\
 \tilde{n} \frac{\partial \tilde{n}}{\partial X} &= -\frac{1}{D^2} \left[ 2U(U-X)^2 - (U-2X)Y_T^2 + \frac{(U-2X)Y_T^4 + 4Y_L^2(U-X)^3}{W} \right].
 \end{aligned} \tag{A.48}$$

Also,

$$2\tilde{n} \frac{\partial \tilde{n}}{\partial Y} = \frac{2X(U-X)}{D^2} \frac{\partial D}{\partial Y}, \tag{A.49}$$

but,

$$\begin{aligned}
 \frac{\partial D}{\partial Y} &= -2Y_T \frac{\partial Y_T}{\partial Y} + \frac{\partial W}{\partial Y} \\
 &= -2Y_T \sin \xi + \frac{1}{2W} \left[ 4Y_T^3 \frac{\partial Y_T}{\partial Y} + 8(U-X)^2 Y_L \frac{\partial Y_L}{\partial Y} \right] \\
 &= -\frac{2Y_T^2}{Y} + \frac{1}{W} \left[ 2Y_T^3 \sin \xi + 8(U-X)^2 Y_L \cos \xi \right]
 \end{aligned}$$

$$= \frac{2}{Y} \left[ -Y_T^2 + \frac{Y_T^4 + 2(U-X)^2 Y_L^2}{W} \right]$$

$$\therefore \tilde{n} \frac{\partial \tilde{n}}{\partial Y} = \frac{2X(U-X)}{D^2 Y} \left[ -Y_T^2 + \frac{Y_T^4 + 2(U-X)^2 Y_L^2}{W} \right]. \quad (\text{A.50})$$

And,

$$2\tilde{n} \frac{\partial \tilde{n}}{\partial Z} = \frac{2Xi}{D} - 2X(U-X) \left( \frac{-1}{D^2} \right) \frac{\partial D}{\partial Z}$$

$$\tilde{n} \frac{\partial \tilde{n}}{\partial Z} = \frac{Xi}{D} + \frac{X(U-X)}{D^2} \frac{\partial D}{\partial Z}. \quad (\text{A.51})$$

But,

$$\begin{aligned} \frac{\partial D}{\partial Z} &= \frac{\partial}{\partial Z} (2U^2 - 2UX - Y_T^2 + W) \\ &= 4U(-i) - 2X(-i) + \frac{\partial W}{\partial Z} = 2Xi - 4Ui + \frac{\partial W}{\partial Z}, \end{aligned}$$

and

$$\frac{\partial W}{\partial Z} = \frac{1}{2W} 8Y_L^2 (U-X)(-i) = -\frac{4Y_L^2 (U-X)i}{W}$$

$$\begin{aligned} \frac{\partial D}{\partial Z} &= 2Xi - 4Ui - \frac{4Y_L^2 (U-X)i}{W} \\ &= 2i \left[ X - 2U - \frac{2Y_L^2 (U-X)}{W} \right] \end{aligned}$$

$$\begin{aligned} \tilde{n} \frac{\partial \tilde{n}}{\partial Z} &= \frac{Xi}{D} + \frac{X(U-X)}{D^2} (2i) \left[ X - 2U - \frac{2Y_L^2 (U-X)}{W} \right] \\ &= \frac{Xi}{D^2} \left\{ D + 2(U-X) \left[ X - 2U - \frac{2Y_L^2 (U-X)}{W} \right] \right\} \\ &= \frac{Xi}{D^2} \left\{ (U-X)[2U + 2(X-2U)] - Y_T^2 + \frac{W^2 - 4Y_L^2 (U-X)^2}{W} \right\} \\ &= \frac{Xi}{D^2} \left[ (U-X)(2U + 2X - 4U) - Y_T^2 + \frac{Y_T^4 + 4Y_L^2 (U-X)^2 - 4Y_L^2 (U-X)^2}{W} \right] \end{aligned}$$

$$\therefore \tilde{n} \frac{\partial \tilde{n}}{\partial Z} = \frac{Xi}{D^2} \left[ -2(U-X)^2 - Y_T^2 + \frac{Y_T^4}{W} \right]. \quad (\text{A.52})$$

## APPENDIX B THE JOVIAN AND NEPTUNIAN MAGNETIC FIELD MODELS

Generally, for a region where there is no local current ( $\nabla \times \mathbf{B} = 0$ ), the magnetic field  $\mathbf{B}$  can be determined by the magnetic scalar potential  $V$  which represents the contributions of internal (or the planetary field) and external sources to the region:

$$\mathbf{B}(r, \theta, \varphi) = -\nabla V(r, \theta, \varphi) = -\nabla (V^e + V^i), \quad (\text{B.1})$$

where

$$V(r, \theta, \varphi) = V^e + V^i = a \sum_{n=1}^{\infty} \left[ \left( \frac{r}{a} \right)^n T_n^e + \left( \frac{a}{r} \right)^{n+1} T_n^i \right]$$

$$T_n^e(\theta, \varphi) = \sum_{m=0}^n P_n^m(\cos \theta) [G_n^m \cos(m\varphi) + H_n^m \sin(m\varphi)]$$

$$T_n^i(\theta, \varphi) = \sum_{m=0}^n P_n^m(\cos \theta) [g_n^m \cos(m\varphi) + h_n^m \sin(m\varphi)] .$$

Here  $P_n^m(\cos \theta)$  are Schmidt quasi-normalized associated Legendre functions of degree  $n$  and order  $m$ , defined by

$$P_n^m(x) = \left[ \frac{2(n-m)!}{(n+m)!} \right]^{\frac{1}{2}} (1-x^2)^{\frac{m}{2}} \frac{d^m}{dx^m} P_n(x) \quad (\text{B.2})$$

and  $P(x)$  is a polynomial solution of the Legendre equation:

$$(1-x^2) \frac{d^2 y}{dx^2} - 2x \frac{dy}{dx} + n(n+1)y = 0 \quad (n = 0, 1, 2, \dots)$$

$$P_n(x) = \frac{1}{2^n n!} \frac{d^n}{dx^n} (x^2 - 1)^n = \frac{(-1)^n}{2^n n!} \frac{d^n}{dx^n} (1 - x^2)^n .$$

Table B.2 lists expressions of  $P_n^m(x)$  for  $n \leq 4$ .

### B.1 Models Without External Terms

For most planetary magnetic field models, it is usually assumed that there are no external current sources that make contribution to the magnetic field distribution, *i.e.*,  $V^e = 0$ . Therefore,

$$V(r, \theta, \varphi) = V^i(r, \theta, \varphi) = a \sum_{n=1}^{\infty} \left(\frac{a}{r}\right)^{n+1} \sum_{m=0}^n A_n^m(\varphi) P_n^m(\cos \theta), \quad (\text{B.3})$$

where we have defined

$$\left. \begin{aligned} A_n^m(\varphi) &= g_n^m \cos(m\varphi) + h_n^m \sin(m\varphi) \\ B_n^m(\varphi) &= g_n^m \sin(m\varphi) - h_n^m \cos(m\varphi) \end{aligned} \right\}. \quad (\text{B.4})$$

The relations between  $A_n^m(\varphi)$  and  $B_n^m(\varphi)$  are

$$\frac{dA_n^m(\varphi)}{d\varphi} = -mB_n^m(\varphi), \quad \frac{dB_n^m(\varphi)}{d\varphi} = mA_n^m(\varphi). \quad (\text{B.5})$$

In our study, various magnetic field models for Jupiter and Neptune are used. In those models, terms up to octopole ( $n_{\max} = 3$ ) are included. The spherical harmonic coefficients  $g_n^m$  and  $h_n^m$  for Jupiter's O<sub>4</sub> and O<sub>6</sub> models and Neptune's O<sub>8</sub> model are listed in Table B.1.

The magnetic field distribution is

$$\mathbf{B} = -\nabla V = -\frac{\partial V}{\partial r} \mathbf{e}_r - \frac{1}{r} \frac{\partial V}{\partial \theta} \mathbf{e}_\theta - \frac{1}{r \sin \theta} \frac{\partial V}{\partial \varphi} \mathbf{e}_\varphi, \quad (\text{B.6})$$

*i.e.*,

$$\left. \begin{aligned} B_r &= -\frac{\partial V}{\partial r} \\ B_\theta &= -\frac{1}{r} \frac{\partial V}{\partial \theta} \\ B_\varphi &= -\frac{1}{r \sin \theta} \frac{\partial V}{\partial \varphi} \end{aligned} \right\}, \quad (\text{B.7})$$

Table B.1. Spherical harmonic coefficients for the Jovian  $O_4$  magnetic field model [Acuña and Ness, 1976], the Jovian  $O_6$  magnetic field model [Connerney, 1992], and the Neptunian  $O_8$  magnetic field model [Connerney et al., 1991].

Planet	Jupiter		Neptune
Radius	71,372 km		24,765 km
Model	$O_4$	$O_6$	$O_8$
$g_1^0$	+4.218	+4.24202	+0.09732
$g_1^1$	+0.664	−0.65929	+0.03220
$h_1^1$	+0.264	+0.24116	−0.09889
$g_2^0$	−0.203	−0.02181	+0.07448
$g_2^1$	−0.735	−0.71106	+0.00664
$h_2^1$	−0.469	−0.40304	+0.11230
$g_2^2$	+0.513	+0.48714	+0.04499
$h_2^2$	+0.088	+0.07179	−0.00070
$g_3^0$	−0.233	+0.07565	−0.06592
$g_3^1$	−0.076	−0.15493	+0.04098
$h_3^1$	−0.580	−0.38824	−0.03669
$g_3^2$	+0.168	+0.19775	−0.03581
$h_3^2$	−0.487	+0.34243	+0.01791
$g_3^3$	−0.231	−0.17958	+0.00484
$h_3^3$	−0.294	−0.22439	−0.00770
Dipole moment $\mathcal{M}$	4.28 $G \cdot R_J^3$	4.29972 $G \cdot R_J^3$	0.142 $G \cdot R_N^3$
OTD tilt angle $\beta$	−9°6	−9°4	−46°9
OTD tilt longitude $\alpha$	201°7	200°1	72°0
OTD offset	0.07 $R_J$	0.11874 $R_J$	0.55 $R_N$

and

$$B = |\mathbf{B}| = \sqrt{B_r^2 + B_\theta^2 + B_\varphi^2}. \quad (\text{B.8})$$

The gradient of  $B(r, \theta, \varphi)$  is

$$\nabla B = \frac{\partial B}{\partial r} \mathbf{e}_r + \frac{1}{r} \frac{\partial B}{\partial \theta} \mathbf{e}_\theta + \frac{1}{r \sin \theta} \frac{\partial B}{\partial \varphi} \mathbf{e}_\varphi. \quad (\text{B.9})$$

We now derive expressions of  $B_r$ ,  $B_\theta$ , and  $B_\varphi$ , starting from their definition equations in (B.7) and the expression for the scalar potential, Equation (B.3). For  $B_r$ , we have

$$B_r = -\frac{\partial V}{\partial r} = -a \sum_{n=1}^{\infty} (n+1) \left(\frac{a}{r}\right)^n \left(-\frac{a}{r^2}\right) \sum_{m=0}^n A_n^m(\varphi) P_n^m(\cos \theta)$$

$$\therefore B_r = \sum_{n=1}^{\infty} (n+1) \left(\frac{a}{r}\right)^{n+2} \sum_{m=0}^n A_n^m(\varphi) P_n^m(\cos \theta). \quad (\text{B.10})$$

Similarly, for  $B_\theta$  we have

$$B_\theta = -\frac{1}{r} \frac{\partial V}{\partial \theta} = -\frac{a}{r} \sum_{n=1}^{\infty} \left(\frac{a}{r}\right)^{n+1} \sum_{m=0}^n A_n^m(\varphi) \frac{dP_n^m(\cos \theta)}{d\theta}$$

$$\therefore B_\theta = -\sum_{n=1}^{\infty} \left(\frac{a}{r}\right)^{n+2} \sum_{m=0}^n A_n^m(\varphi) U_n^m(\cos \theta), \quad (\text{B.11})$$

where we have let

$$U_n^m(\cos \theta) = \frac{d}{d\theta} P_n^m(\cos \theta) = \frac{dP_n^m(\cos \theta)}{d\cos \theta} \frac{d\cos \theta}{d\theta}$$

or

$$U_n^m(x) = -\sqrt{1-x^2} \frac{dP_n^m(x)}{dx} \quad (x = \cos \theta).$$

From the recurrence relation of the associated Legendre polynomial

$$(1-x^2) \frac{dP_n^m}{dx} = (n+1)xP_n^m - K_n^m P_n^m,$$

where  $K_n^m = \sqrt{(n-m+1)(n+m+1)}$ , we have

$$(1-x^2)^{1/2} \frac{dP_n^m}{dx} = \frac{(n+1)x}{\sqrt{1-x^2}} P_n^m - \frac{K_n^m}{\sqrt{1-x^2}} P_{n+1}^m.$$

Let

$$S_n^m(\cos \theta) = S_n^m(x) = \frac{1}{\sqrt{1-x^2}} P_n^m(x) = \frac{P_n^m(\cos \theta)}{\sin \theta} \quad (m \neq 0), \quad (\text{B.12})$$



we can then have

$$U_n^m(x) = K_n^m S_{n+1}^m(x) - (n+1)xS_n^m(x) \quad (m \neq 0). \quad (\text{B.13})$$

Expressions of  $S_n^m(x)$  and  $U_n^m(x)$  for  $n \leq 4$  are given in Table B.2. Note that  $|x|=1$  is not a singularity point for  $S_n^m(x)$  as long as  $m \neq 0$ , because  $P_n^m(x)$  has a factor of  $\sqrt{1-x^2}$  when  $m \neq 0$  which cancels out the same factor in the denominator of  $S_n^m(x)$ . For the case of  $m=0$ ,

$$U_n^0(x) = -\sqrt{1-x^2} \frac{dP_n}{dx},$$

and  $\frac{dP_n}{dx}$  can be calculated by

$$P'_{n+1}(x) = xP'_n(x) + (n+1)P_n(x).$$

Now, for  $B_\varphi$ :

$$\begin{aligned} B_\varphi &= -\frac{1}{r \sin \theta} \frac{\partial V}{\partial \varphi} = -\frac{a}{r \sin \theta} \sum_{n=1}^{\infty} \left(\frac{a}{r}\right)^{n+1} \sum_{m=0}^n P_n^m(\cos \theta) \frac{dA_n^m}{d\varphi} \\ &= -\sum_{n=1}^{\infty} \left(\frac{a}{r}\right)^{n+2} \sum_{m=0}^n \frac{[-mB_n^m(\varphi)]}{\sin \theta} P_n^m(\cos \theta) \\ &= \sum_{n=1}^{\infty} \left(\frac{a}{r}\right)^{n+2} \sum_{m=0}^n mB_n^m(\varphi) S_m^n(\cos \theta) \end{aligned}$$

$$\therefore B_\varphi = \sum_{n=1}^{\infty} \left(\frac{a}{r}\right)^{n+2} \sum_{m=1}^n mB_n^m(\varphi) S_m^n(\cos \theta). \quad (\text{B.14})$$

Expressions of  $\frac{\partial B}{\partial r}$ ,  $\frac{\partial B}{\partial \theta}$ , and  $\frac{\partial B}{\partial \varphi}$  have to be derived from Equation (B.8):

$$\left. \begin{aligned} \frac{\partial B}{\partial r} &= \frac{1}{B} \left( B_r \frac{\partial B_r}{\partial r} + B_\theta \frac{\partial B_\theta}{\partial r} + B_\varphi \frac{\partial B_\varphi}{\partial r} \right) \\ \frac{\partial B}{\partial \theta} &= \frac{1}{B} \left( B_r \frac{\partial B_r}{\partial \theta} + B_\theta \frac{\partial B_\theta}{\partial \theta} + B_\varphi \frac{\partial B_\varphi}{\partial \theta} \right) \\ \frac{\partial B}{\partial \varphi} &= \frac{1}{B} \left( B_r \frac{\partial B_r}{\partial \varphi} + B_\theta \frac{\partial B_\theta}{\partial \varphi} + B_\varphi \frac{\partial B_\varphi}{\partial \varphi} \right) \end{aligned} \right\}.$$

Let us get  $\frac{\partial B_r}{\partial r}$ ,  $\frac{\partial B_r}{\partial \theta}$ , and  $\frac{\partial B_r}{\partial \varphi}$  first. From Equation (B.10), we have

$$\frac{\partial B_r}{\partial r} = \sum_{n=1}^{\infty} (n+1)(n+2) \left(\frac{a}{r}\right)^{n+1} \left(-\frac{a}{r^2}\right) \sum_{m=0}^n A_n^m(\varphi) P_n^m(\cos \theta),$$

$$\therefore \frac{\partial B_r}{\partial r} = -\frac{1}{a} \sum_{n=1}^{\infty} (n+1)(n+2) \left(\frac{a}{r}\right)^{n+3} \sum_{m=0}^n A_n^m(\varphi) P_n^m(\cos \theta). \quad (\text{B.15})$$

$$\frac{\partial B_r}{\partial \theta} = \sum_{n=1}^{\infty} (n+1) \left(\frac{a}{r}\right)^{n+2} \sum_{m=0}^n A_n^m(\varphi) \frac{dP_n^m(\cos \theta)}{d\theta},$$

$$\therefore \frac{\partial B_r}{\partial \theta} = \sum_{n=1}^{\infty} (n+1) \left(\frac{a}{r}\right)^{n+2} \sum_{m=0}^n A_n^m(\varphi) U_n^m(\cos \theta). \quad (\text{B.16})$$

$$\frac{\partial B_r}{\partial \varphi} = \sum_{n=1}^{\infty} (n+1) \left(\frac{a}{r}\right)^{n+2} \sum_{m=0}^n P_n^m(\cos \theta) \frac{dA_n^m(\varphi)}{d\varphi},$$

$$\therefore \frac{\partial B_r}{\partial \varphi} = -\sum_{n=1}^{\infty} (n+1) \left(\frac{a}{r}\right)^{n+2} \sum_{m=1}^n m B_n^m(\varphi) P_n^m(\cos \theta). \quad (\text{B.17})$$

From Equation (B.11), we can easily get expressions of  $\frac{\partial B_\theta}{\partial r}$ ,  $\frac{\partial B_\theta}{\partial \theta}$ , and  $\frac{\partial B_\theta}{\partial \varphi}$ :

$$\frac{\partial B_\theta}{\partial r} = -\sum_{n=1}^{\infty} (n+2) \left(\frac{a}{r}\right)^{n+1} \left(-\frac{a}{r^2}\right) \sum_{m=0}^n A_n^m(\varphi) U_n^m(\cos \theta),$$

$$\therefore \frac{\partial B_\theta}{\partial r} = \frac{1}{a} \sum_{n=1}^{\infty} (n+2) \left(\frac{a}{r}\right)^{n+3} \sum_{m=0}^n A_n^m(\varphi) U_n^m(\cos \theta). \quad (\text{B.18})$$

$$\frac{\partial B_\theta}{\partial \theta} = -\sum_{n=1}^{\infty} \left(\frac{a}{r}\right)^{n+2} \sum_{m=0}^n A_n^m(\varphi) \frac{dU_n^m(\cos \theta)}{d\theta},$$

$$\therefore \frac{\partial B_\theta}{\partial \theta} = -\sum_{n=1}^{\infty} \left(\frac{a}{r}\right)^{n+2} \sum_{m=0}^n A_n^m(\varphi) V_n^m(\cos \theta), \quad (\text{B.19})$$

where 
$$V_n^m(\cos \theta) = \frac{d}{d\theta} U_n^m(\cos \theta) = \frac{d^2}{d\theta^2} P_n^m(\cos \theta), \quad (\text{B.20})$$

its expressions for  $n \leq 4$  are given in Table B.2.

$$\begin{aligned} \frac{\partial B_\theta}{\partial \varphi} &= - \sum_{n=1}^{\infty} \left(\frac{a}{r}\right)^{n+2} \sum_{m=0}^n U_n^m(\cos \theta) \frac{dA_n^m(\varphi)}{d\varphi}, \\ \therefore \quad \frac{\partial B_\theta}{\partial \varphi} &= \sum_{n=1}^{\infty} \left(\frac{a}{r}\right)^{n+2} \sum_{m=1}^n m B_n^m(\varphi) U_n^m(\cos \theta). \end{aligned} \quad (\text{B.21})$$

Finally,  $\frac{\partial B_\varphi}{\partial r}$ ,  $\frac{\partial B_\varphi}{\partial \theta}$ , and  $\frac{\partial B_\varphi}{\partial \varphi}$  can be derived from Equation (B.14):

$$\begin{aligned} \frac{\partial B_\varphi}{\partial r} &= \sum_{n=1}^{\infty} (n+2) \left(\frac{a}{r}\right)^{n+1} \left(-\frac{a}{r^2}\right) \sum_{m=0}^n m B_n^m(\varphi) S_n^m(\cos \theta), \\ \therefore \quad \frac{\partial B_\varphi}{\partial r} &= -\frac{1}{a} \sum_{n=1}^{\infty} (n+2) \left(\frac{a}{r}\right)^{n+3} \sum_{m=1}^n m B_n^m(\varphi) S_n^m(\cos \theta). \end{aligned} \quad (\text{B.22})$$

$$\begin{aligned} \frac{\partial B_\varphi}{\partial \theta} &= \sum_{n=1}^{\infty} \left(\frac{a}{r}\right)^{n+2} \sum_{m=1}^n m B_n^m(\varphi) \frac{dS_n^m(\cos \theta)}{d\theta}, \\ \therefore \quad \frac{\partial B_\varphi}{\partial \theta} &= \sum_{n=1}^{\infty} \left(\frac{a}{r}\right)^{n+2} \sum_{m=1}^n m B_n^m(\varphi) T_n^m(\cos \theta), \end{aligned} \quad (\text{B.23})$$

$$\text{where} \quad T_n^m(\cos \theta) = \frac{dS_n^m(\cos \theta)}{d\theta}, \quad (\text{B.24})$$

and its expressions for  $n \leq 4$  are given in Table B.2.

$$\begin{aligned} \frac{\partial B_\varphi}{\partial \varphi} &= \sum_{n=1}^{\infty} \left(\frac{a}{r}\right)^{n+2} \sum_{m=1}^n m S_n^m(\cos \theta) \frac{dB_n^m(\varphi)}{d\varphi}, \\ \therefore \quad \frac{\partial B_\varphi}{\partial \varphi} &= \sum_{n=1}^{\infty} \left(\frac{a}{r}\right)^{n+2} \sum_{m=1}^n m^2 A_n^m(\varphi) S_n^m(\cos \theta). \end{aligned} \quad (\text{B.25})$$

## B.2 Models With External Terms

If a planetary magnetic model also contains external terms in its scalar potential expression, we need to add those terms for the calculation of the field distribution

and its gradient. One of the Jovian magnetic field models, the so-called P11(3,2)A model developed at the JPL by *Davis et al.* [1975] is such a model that contains external terms up to  $n=2$  (quadrupole). In this case, we need to add contributions from these external sources as well.

The scalar potential contributed from the external sources is:

$$V^e(r, \theta, \varphi) = a \sum_{n=1}^{\infty} \left[ \left( \frac{r}{a} \right)^n T_n^e(\theta, \varphi) \right], \quad (\text{B.26})$$

where 
$$T_n^e(\theta, \varphi) = \sum_{m=0}^n P_n^m(\cos \theta) [G_n^m \cos(m\varphi) + H_n^m \sin(m\varphi)].$$

Similar to what we have done with the internal sources, we can let

$$\left. \begin{aligned} C_n^m(\varphi) &= G_n^m \cos(m\varphi) + H_n^m \sin(m\varphi) \\ D_n^m(\varphi) &= G_n^m \sin(m\varphi) - H_n^m \cos(m\varphi) \end{aligned} \right\}. \quad (\text{B.27})$$

The relations between  $C_n^m(\varphi)$  and  $D_n^m(\varphi)$  are

$$\frac{dC_n^m(\varphi)}{d\varphi} = -mD_n^m(\varphi), \quad \frac{dD_n^m(\varphi)}{d\varphi} = mC_n^m(\varphi). \quad (\text{B.28})$$

The three components of  $\mathbf{B}$  (from the external sources only) are:

$$B_r = - \sum_{n=1}^{\infty} n \left( \frac{r}{a} \right)^{n-1} \sum_{m=0}^n C_n^m(\varphi) P_n^m(\cos \theta) \quad (\text{B.29})$$

$$B_\theta = - \sum_{n=1}^{\infty} \left( \frac{r}{a} \right)^{n-1} \sum_{m=0}^n C_n^m(\varphi) U_n^m(\cos \theta) \quad (\text{B.30})$$

$$B_\varphi = \sum_{n=1}^{\infty} \left( \frac{r}{a} \right)^{n-1} \sum_{m=1}^n m D_n^m(\varphi) S_m^n(\cos \theta). \quad (\text{B.31})$$

The corresponding terms  $\frac{\partial B_r}{\partial r}$ ,  $\frac{\partial B_\theta}{\partial r}$ , and  $\frac{\partial B_\varphi}{\partial r}$  from the external sources are:

$$\frac{\partial B_r}{\partial r} = -\frac{1}{a} \sum_{n=1}^{\infty} n(n-1) \left( \frac{r}{a} \right)^{n-2} \sum_{m=0}^n C_n^m(\varphi) P_n^m(\cos \theta) \quad (\text{B.32})$$

$$\frac{\partial B_\theta}{\partial r} = -\frac{1}{a} \sum_{n=1}^{\infty} (n-1) \left(\frac{a}{r}\right)^{n-2} \sum_{m=0}^n C_n^m(\varphi) U_n^m(\cos \theta) \quad (\text{B.33})$$

$$\frac{\partial B_\varphi}{\partial r} = -\frac{1}{a} \sum_{n=1}^{\infty} (n-1) \left(\frac{r}{a}\right)^{n-2} \sum_{m=1}^n m D_n^m(\varphi) S_n^m(\cos \theta) . \quad (\text{B.34})$$

Terms of  $\frac{\partial B_r}{\partial \theta}$ ,  $\frac{\partial B_\theta}{\partial \theta}$ , and  $\frac{\partial B_\varphi}{\partial \theta}$  from the external sources are:

$$\frac{\partial B_r}{\partial \theta} = -\sum_{n=1}^{\infty} n \left(\frac{r}{a}\right)^{n-1} \sum_{m=0}^n C_n^m(\varphi) U_n^m(\cos \theta) \quad (\text{B.35})$$

$$\frac{\partial B_\theta}{\partial \theta} = -\sum_{n=1}^{\infty} \left(\frac{r}{a}\right)^{n-1} \sum_{m=0}^n C_n^m(\varphi) V_n^m(\cos \theta) \quad (\text{B.36})$$

$$\frac{\partial B_\varphi}{\partial \theta} = \sum_{n=1}^{\infty} \left(\frac{r}{a}\right)^{n-1} \sum_{m=1}^n m D_n^m(\varphi) T_n^m(\cos \theta) . \quad (\text{B.37})$$

Similarly, terms of  $\frac{\partial B_r}{\partial \varphi}$ ,  $\frac{\partial B_\theta}{\partial \varphi}$ , and  $\frac{\partial B_\varphi}{\partial \varphi}$  from the external sources are:

$$\frac{\partial B_r}{\partial \varphi} = \sum_{n=1}^{\infty} n \left(\frac{r}{a}\right)^{n-1} \sum_{m=1}^n m D_n^m(\varphi) P_n^m(\cos \theta) \quad (\text{B.38})$$

$$\frac{\partial B_\theta}{\partial \varphi} = \sum_{n=1}^{\infty} \left(\frac{r}{a}\right)^{n-1} \sum_{m=1}^n m D_n^m(\varphi) U_n^m(\cos \theta) \quad (\text{B.39})$$

$$\frac{\partial B_\varphi}{\partial \varphi} = \sum_{n=1}^{\infty} \left(\frac{r}{a}\right)^{n-1} \sum_{m=1}^n m^2 C_n^m(\varphi) S_n^m(\cos \theta) . \quad (\text{B.40})$$

Table B.2. Expressions of  $P_n^m(x)$ ,  $S_n^m(x)$ ,  $U_n^m(x)$ ,  $V_n^m(x)$  and  $T_n^m(x)$  for  $n$  up to 4.

$(n, m)$	$P_n^m(x)$	$S_n^m(x)$	$U_n^m(x)$	$V_n^m(x)$	$T_n^m(x)$
(1, 0)	$x$	$x/\sqrt{1-x^2}$	$-\sqrt{1-x^2}$	$-x$	$-1/(1-x^2)$
(1, 1)	$(1-x^2)^{1/2}$	1	$x$	$-\sqrt{1-x^2}$	0
(2, 0)	$\frac{1}{2}(3x^2-1)$	$\frac{1}{2\sqrt{1-x^2}}(3x^2-1)$	$-3x\sqrt{1-x^2}$	$3(1-2x^2)$	$\frac{1}{2(1-x^2)}(3x^3-5x)$
(2, 1)	$x\sqrt{3(1-x^2)}$	$\sqrt{3}x$	$\sqrt{3}(1-2x^2)$	$-4x\sqrt{3(1-x^2)}$	$-\sqrt{3(1-x^2)}$
(2, 2)	$\frac{\sqrt{3}}{2}(1-x^2)$	$\frac{1}{2}\sqrt{3(1-x^2)}$	$x\sqrt{3(1-x^2)}$	$\sqrt{3}(2x^2-1)$	$\frac{\sqrt{3}}{2}x$
(3, 0)	$\frac{1}{2}(5x^3-3x)$	$\frac{1}{2\sqrt{1-x^2}}(5x^3-3x)$	$-\frac{3}{2}(5x^2-1)\sqrt{1-x^2}$	$\frac{3}{2}(11x-15x^3)$	$\frac{10x^4-15x^2+3}{2(1-x^2)}$
(3, 1)	$\frac{5x^2-1}{2}\sqrt{\frac{3}{2}(1-x^2)}$	$\sqrt{\frac{3}{2}}(5x^2-1)$	$-\sqrt{\frac{3}{2}}(11x-15x^3)$	$(11-45x^2)\sqrt{\frac{3}{2}(1-x^2)}$	$-5x\sqrt{\frac{3}{2}(1-x^2)}$
(3, 2)	$\frac{\sqrt{15}}{2}x(1-x^2)$	$\frac{1}{2}x\sqrt{15(1-x^2)}$	$-(1-3x^2)\sqrt{\frac{15}{4}(1-x^2)}$	$\frac{\sqrt{15}}{2}(9x^3-7x)$	$\frac{\sqrt{15}}{2}(2x^2-1)$
(3, 3)	$\sqrt{\frac{5}{8}}(1-x^2)^{3/2}$	$\sqrt{\frac{5}{8}}(1-x^2)$	$\sqrt{\frac{45}{8}}x(1-x^2)$	$3(3x^2-1)\sqrt{\frac{5}{8}(1-x^2)}$	$x\sqrt{\frac{5}{2}(1-x^2)}$
(4, 0)	$\frac{1}{8}(35x^4-30x^2+3)$	$\frac{1}{8\sqrt{1-x^2}}(35x^4-30x^2+3)$	$-\frac{5}{2}(7x^3-3x)\sqrt{1-x^2}$	$\frac{5}{2}(27x^2-28x^4-3)$	$\frac{105x^5-170x^3+57x}{8(1-x^2)}$
(4, 1)	$\sqrt{\frac{5}{8}}(1-x^2)(7x^3-3x)$	$\sqrt{\frac{5}{8}}(7x^3-3x)$	$-\sqrt{\frac{5}{8}}(27x^2-28x^4-3)$	$(27x-56x^3)\sqrt{\frac{5}{2}(1-x^2)}$	$3(1-7x^2)\sqrt{\frac{5}{8}(1-x^2)}$
(4, 2)	$\frac{\sqrt{5}}{4}(1-x^2)(7x^2-1)$	$\frac{1}{4}(7x^2-1)\sqrt{5(1-x^2)}$	$(7x^3-4x)\sqrt{5(1-x^2)}$	$\sqrt{5}(28x^4-29x^2+4)$	$\frac{3\sqrt{5}}{4}(7x^3-5x)$
(4, 3)	$\sqrt{\frac{35}{8}}x(1-x^2)^{3/2}$	$\sqrt{\frac{35}{8}}x(1-x^2)$	$-\sqrt{\frac{35}{8}}(1-x^2)(1-4x^2)$	$(5x-8x^3)\sqrt{\frac{35}{2}(1-x^2)}$	$(3x^2-1)\sqrt{\frac{35}{8}(1-x^2)}$
(4, 4)	$\frac{\sqrt{35}}{8}(1-x^2)^2$	$\frac{\sqrt{35}}{8}(1-x^2)^{3/2}$	$\frac{\sqrt{35}}{2}x(1-x^2)^{3/2}$	$\frac{35}{2}(4x^2-1)(1-x^2)$	$\frac{\sqrt{35}}{8}3x(1-x^2)$

## APPENDIX C

### TRANSFORMATION OF SPACECRAFT COORDINATE SYSTEMS

In the process of calibration of the PRA antenna system, the position (*i.e.*, direction) of an object (radio source or center of the planet) with respect to a spacecraft coordinate system (the monopole antenna system or the equivalent dipole antenna system) is required. Positional information for an object is usually given in terms of a reference system consisting of a true prime meridian and equator of date of the planet, while information on the spacecraft's position and orientation is given in terms of Earth mean ecliptic and equinox system at a specified epoch. On the other hand, when using the raytracing technique to search for the HOM emission source by tracing rays from the spacecraft toward a given direction, we need to convert positional and orientational vectors from the spacecraft reference frame into the planetary reference frame. However, no direct transformation information of this type was provided by NASA for the Voyager mission. It was necessary for me to make these transformational calculations from the data provided for describing spacecraft's position and orientation throughout the encounter period. The latter information is given in the *Supplementary Experiment Data Record* (SEDR) file distributed by the Jet Propulsion Laboratory.

Among much useful information, the SEDR file provides the following quantities needed in our study: (1) Cartesian state vectors (position and velocity) of the spacecraft and some satellites of the planet in the frame *Earth mean ecliptic and equinox of 1950.0* (referred to as the E system) with the origin centered at the planet; (2)

Cartesian state vectors (position and velocity) of the spacecraft and those planetary satellites in the frame of the planet's true prime meridian and equator of date, also with its origin centered at the planet; (3) Cartesian unit vectors of three axes of the spacecraft, spacecraft centered, Earth mean ecliptic and equinox of 1950.0. For convenience, we refer to the spacecraft system defined by the pitch, yaw, and roll axes [*i.e.*, the  $X, Y, Z$  axes in Figure 2.2)] as the S system; the reference system composed by the equivalent dipole antenna (the  $x, y, z$  axes in Figure 2.2) as the A system; and the reference system of *Jupiter System III true prime meridian and equator of date* with Jupiter centered as the J system.

### C.1 Transformation at a Given Catalog Time

We already know that the matrix which transforms the A system to the S system is:

$$\begin{aligned}\mathbf{T}_{A2S} &= \mathbf{R}_1[90^\circ - (40^\circ - \beta)] \mathbf{R}_3(135^\circ) \\ &= \mathbf{R}_1(50^\circ + \beta) \mathbf{R}_3(135^\circ),\end{aligned}\tag{C.1}$$

where  $\beta$  is the tilt angle of the equivalent dipole plane (*i.e.*, the E-plane) from the actual monopole plane,  $\mathbf{R}_1$  and  $\mathbf{R}_3$  are rotation matrices about the  $x$  and  $z$  axes, respectively. According to the PRA antenna recalibration result presented in Chapter 2,  $\beta = 27^\circ$  for the front side of the antenna, and  $\beta = 45^\circ$  for the back side of the antenna.

What we are looking for is the transformation relation that transforms vectors from the A system to the J system or vice versa. Suppose the transformation from the E system to the J system is  $\mathbf{T}_{E2J}$ , then the transformation from the A system to the J system,  $\mathbf{T}_{A2J}$ , should be:

$$\mathbf{T}_{A2J} = \mathbf{T}_{E2J} \mathbf{T}_{S2E} \mathbf{T}_{A2S},\tag{C.2}$$

where  $\mathbf{T}_{S2E}$  is the matrix which transforms the S system to E system and can be constructed from the unit vectors of spacecraft's  $X, Y, Z$  axes (expressed with respect



to the E system) as follows: Let  $\mathbf{x}$ ,  $\mathbf{y}$ , and  $\mathbf{z}$  be unit vectors of the  $X, Y, Z$  axes of the spacecraft, respectively:

$$\left. \begin{aligned} \mathbf{x} &= a_1\mathbf{i} + a_2\mathbf{j} + a_3\mathbf{k} \\ \mathbf{y} &= b_1\mathbf{i} + b_2\mathbf{j} + b_3\mathbf{k} \\ \mathbf{z} &= c_1\mathbf{i} + c_2\mathbf{j} + c_3\mathbf{k} \end{aligned} \right\} ,$$

then 
$$\mathbf{T}_{S2E} = (\mathbf{x}, \mathbf{y}, \mathbf{z}) = \begin{pmatrix} a_1 & b_1 & c_1 \\ a_2 & b_2 & c_2 \\ a_3 & b_3 & c_3 \end{pmatrix} . \quad (\text{C.3})$$

Apparently, since the spacecraft is moving and may constantly change its orientation via all kinds of maneuvers, all of the above transformation matrices except  $\mathbf{T}_{A2S}$  are functions of time.

Now the key part of this problem is to obtain the transformation matrix  $\mathbf{T}_{E2J}$ . Fortunately, the SEDR file provides us Cartesian positional vectors of at least three concerned celestial bodies in both E system and J system during the Voyager's encounter period. We can use them to solve for  $\mathbf{T}_{E2J}$ .

Obviously, there are nine unknown elements for determining  $\mathbf{T}_{E2J}$ :

$$\mathbf{T}_{E2J} = \begin{pmatrix} t_{11} & t_{12} & t_{13} \\ t_{21} & t_{22} & t_{23} \\ t_{31} & t_{32} & t_{33} \end{pmatrix} ,$$

which means we need at least three independent observations or positional vectors of the spacecraft and two other celestial bodies with respect to both the E system and the J system to solve for  $\mathbf{T}_{E2J}$ . We can use positional vectors of the spacecraft, and we will use the positional vectors of the Jovian satellites Io and Callisto for the Jupiter mission and of the Neptunian satellites Triton and Nereid for the Neptune mission.

Let  $v_1$ ,  $v_2$ , and  $v_3$  be positional vectors of the spacecraft, and the two planetary satellites in E system, and  $V_1$ ,  $V_2$ , and  $V_3$  in J system, respectively, and

$$v_i = \begin{pmatrix} x_i \\ y_i \\ z_i \end{pmatrix}, \quad V_i = \begin{pmatrix} X_i \\ Y_i \\ Z_i \end{pmatrix}, \quad (i = 1, 2, 3);$$

$v_i$  and  $V_i$  ( $i = 1, 2, 3$ ) should be related through the transformation matrix  $\mathbf{T}_{E2J}$ :

$$V_i = \mathbf{T}_{E2J} \cdot v_i \quad \text{or} \quad v_i = \mathbf{T}_{J2E} \cdot V_i \quad (i = 1, 2, 3), \quad (\text{C.4})$$

where  $\mathbf{T}_{J2E}$  is the inverse matrix of  $\mathbf{T}_{E2J}$ , and since  $\mathbf{T}_{E2J}$  is a normalized orthogonal matrix,  $\mathbf{T}_{J2E}$  is simply the transpose of  $\mathbf{T}_{E2J}$ . One of the above two equations actually corresponds to nine linear equations:

$$\begin{pmatrix} x_1 & y_1 & z_1 & 0 & 0 & 0 & 0 & 0 & 0 \\ 0 & 0 & 0 & x_1 & y_1 & z_1 & 0 & 0 & 0 \\ 0 & 0 & 0 & 0 & 0 & 0 & x_1 & y_1 & z_1 \\ x_2 & y_2 & z_2 & 0 & 0 & 0 & 0 & 0 & 0 \\ 0 & 0 & 0 & x_2 & y_2 & z_2 & 0 & 0 & 0 \\ 0 & 0 & 0 & 0 & 0 & 0 & x_2 & y_2 & z_2 \\ x_3 & y_3 & z_3 & 0 & 0 & 0 & 0 & 0 & 0 \\ 0 & 0 & 0 & x_3 & y_3 & z_3 & 0 & 0 & 0 \\ 0 & 0 & 0 & 0 & 0 & 0 & x_3 & y_3 & z_3 \end{pmatrix} \begin{pmatrix} t_{11} \\ t_{12} \\ t_{13} \\ t_{21} \\ t_{22} \\ t_{23} \\ t_{31} \\ t_{32} \\ t_{33} \end{pmatrix} = \begin{pmatrix} X_1 \\ Y_1 \\ Z_1 \\ X_2 \\ Y_2 \\ Z_2 \\ X_3 \\ Y_3 \\ Z_3 \end{pmatrix}. \quad (\text{C.5})$$

(This is actually a set of three 3-element linear equation systems.) Solving these linear equations simultaneously should give the transformation matrix  $\mathbf{T}_{E2J}$  we want. The transformation matrix from the J system to the E system,  $\mathbf{T}_{J2E}$ , is simply the transpose of  $\mathbf{T}_{E2J}$ :

$$\mathbf{T}_{J2E} = \mathbf{T}_{E2J}^T. \quad (\text{C.6})$$

Solution of Equation (C.5), together with Equations (C.1) and (C.3) will give the transformation from the A system to the J system via Equation (C.2). Consequently, the transformation from the J system back to the A system can be obtained through the transposes of matrices  $\mathbf{T}_{E2J}$ ,  $\mathbf{T}_{S2E}$ , and  $\mathbf{T}_{A2S}$ :

$$\mathbf{T}_{J2A} = \mathbf{T}_{A2S}^T \mathbf{T}_{S2E}^T \mathbf{T}_{E2J}^T. \quad (\text{C.7})$$

Equations (C.2) and (C.7) give transformation between the A system and the J system at any catalog time given in the SEDR file. The SEDR catalog time is given at an interval of about 1.6 minutes, which is much longer than the sampling time of the POLLO mode of the PRA experiment. In our study, we need to know the position of a presumed source or the orientation of the spacecraft with respect to the planetary system at any time. Thus transformation between the A system and the J system at any given time will be needed. During the period when the spacecraft remains in a “stable” orientation, the matrices  $\mathbf{T}_{J2A}$  and  $\mathbf{T}_{A2J}$  calculated at a catalog time which is close to the given time would be accurate enough; but during a period of spacecraft maneuver, the spacecraft’s orientation changes rapidly, we will need a more accurate way to calculate  $\mathbf{T}_{J2A}$  and  $\mathbf{T}_{A2J}$  at any time during such a period. We deal with this problem in the next section.

### C.2 Transformation at any Given Time

The transformation matrices  $\mathbf{T}_{J2A}$  and  $\mathbf{T}_{A2J}$  allow us to transform any vector from the J system to the A system, or vice versa. This can be done for any catalog time listed in the SEDR file. To make such transformation at any other given time, we need to know the corresponding matrix for that time. Apparently, to get transformation matrix  $\mathbf{T}_{J2A}(t)$  or  $\mathbf{T}_{A2J}(t)$  valid at any given time  $t$ , we need to know the matrix at several consecutive times  $t_1, t_2, \dots, t_k$ , where  $t_1 \leq t \leq t_k$ , and we can then get the matrix  $\mathbf{T}_{J2A}(t)$  through interpolation. However, such interpolation can not be applied directly to the matrices, otherwise significant computation error can be introduced.

We now introduce a more practical method of interpolation among normalized orthogonal matrices. Suppose we have two coordinate systems with the same origin,  $(X, Y, Z)$  and  $(x, y, z)$ , respectively, whose three unit vectors are  $(\mathbf{I}, \mathbf{J}, \mathbf{K})$  and  $(\mathbf{i}, \mathbf{j},$

$\mathbf{k}$ ). Obviously,  $(\mathbf{i}, \mathbf{j}, \mathbf{k})$  can be expressed in terms of  $(\mathbf{I}, \mathbf{J}, \mathbf{K})$ , and vice versa:

$$\left. \begin{aligned} \mathbf{i} &= a_1 \mathbf{I} + a_2 \mathbf{J} + a_3 \mathbf{K} \\ \mathbf{j} &= b_1 \mathbf{I} + b_2 \mathbf{J} + b_3 \mathbf{K} \\ \mathbf{k} &= c_1 \mathbf{I} + c_2 \mathbf{J} + c_3 \mathbf{K} \end{aligned} \right\},$$

*i.e.*, the transformation from the  $(x, y, z)$  system to the  $(X, Y, Z)$  system can be accomplished via the following matrix ( $\mathbf{M}$ ):

$$\mathbf{M} = \begin{pmatrix} a_1 & b_1 & c_1 \\ a_2 & b_2 & c_2 \\ a_3 & b_3 & c_3 \end{pmatrix}. \quad (\text{C.8})$$

This is a normalized orthogonal matrix, and therefore there are only three independent variables for the matrix; In general, such a transformation can be achieved by three independent rotations to the frame system. Naturally the three Eulerian angles,  $(\theta, \phi, \psi)$ , shown in Figure C.1, can be used for such purpose; and the transformation matrix  $\mathbf{M}$  can be expressed by these Eulerian angles:

$$\mathbf{M} = \mathbf{R}_3(-\phi) \mathbf{R}_1(-\theta) \mathbf{R}_3(-\psi). \quad (\text{C.9})$$

The change ranges of the Eulerian angles are:  $0 \leq \theta \leq \pi$ ,  $0 \leq \phi \leq 2\pi$ , and  $0 \leq \psi \leq 2\pi$ . Expanding the above equation, we have

$$\mathbf{M} = \begin{pmatrix} \cos \phi \cos \psi - \sin \phi \cos \theta \sin \psi & -\cos \phi \sin \psi - \sin \phi \cos \theta \cos \psi & \sin \phi \sin \theta \\ \sin \phi \cos \psi + \cos \phi \cos \theta \sin \psi & -\sin \phi \sin \psi + \cos \phi \cos \theta \cos \psi & -\cos \phi \sin \theta \\ \sin \theta \sin \psi & \sin \theta \cos \psi & \cos \theta \end{pmatrix}. \quad (\text{C.10})$$

By equating corresponding elements in the matrices given by (C.8) and (C.10), we can uniquely solve for the three Eulerian angles. First,  $\theta$  is determined by

$$\cos \theta = c_3.$$

If  $\theta \neq 0$  (*i.e.*,  $c_3 \neq 1$ ), one can then solve for  $\psi$  from

$$\left. \begin{aligned} \sin \theta \sin \psi &= c_1 \\ \sin \theta \cos \psi &= c_2 \end{aligned} \right\},$$

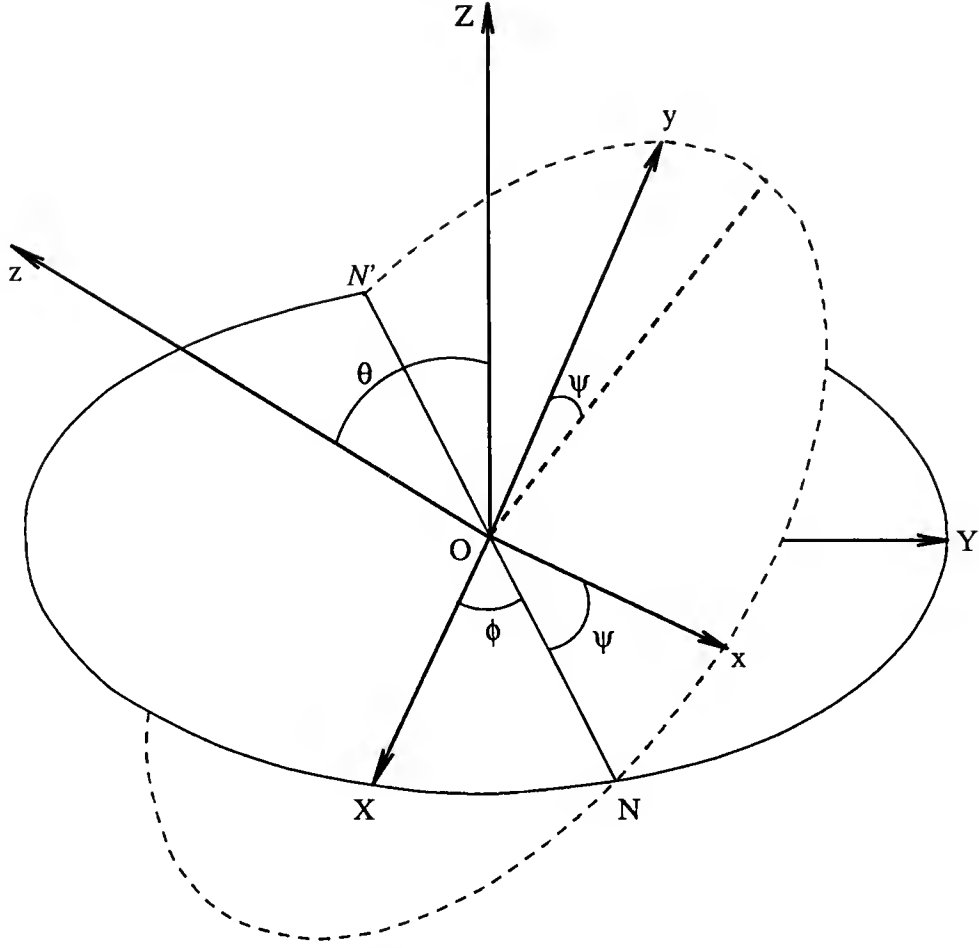


Figure C.1. Definition of Eulerian angles  $\theta, \phi, \psi$ .

and solve for  $\phi$  from

$$\left. \begin{aligned} \sin \theta \sin \phi &= a_3 \\ -\sin \theta \cos \phi &= b_3 \end{aligned} \right\}.$$

If  $\theta=0$  (i.e.,  $c_3=1$ ), only one rotation is needed to obtain the transformation matrix  $\mathbf{M}$ . In this case, Equation (C.9) becomes

$$\mathbf{M} = \mathbf{R}_3(-\phi) \mathbf{R}_3(-\psi) = \mathbf{R}_3(-\phi') = \begin{pmatrix} \cos \phi' & -\sin \phi' & 0 \\ \sin \phi' & \cos \phi' & 0 \\ 0 & 0 & 1 \end{pmatrix}, \quad (\text{C.11})$$

where  $\phi' = \phi + \psi$ , and it can be solved by

$$\left. \begin{array}{l} \cos \phi' = a_1 \\ \sin \phi' = a_2 \end{array} \right\}.$$

By using the Eulerian angles to express a transformation matrix, we will be able to describe a time varying transformation matrix by three angular functions:

$$\mathbf{M}(t) \Longleftrightarrow \{\theta(t), \phi(t), \psi(t)\}.$$

Once the transformation matrix  $\mathbf{M}(t)$  as a function of time is obtained, the corresponding Eulerian angles as functions of time are also determined. The corresponding Eulerian angles at any time can then be obtained by interpolation, which eventually gives the transformation matrix at that given time.

## REFERENCES

- Acuña, M. H., K. W. Behannon, and J. E. P. Connerney, Jupiter's magnetic field and magnetosphere, in *Physics of the Jovian Magnetosphere*, edited by A. J. Dessler, Chapter 1, pp. 1–50, Cambridge University Press, New York, 1983.
- Acuña, M. H., and N. F. Ness, The main magnetic field of Jupiter, *J. Geophys. Res.*, **81**, 2917–2922, 1976.
- Alexander, J. K., T. D. Carr, J. R. Thieman, J. J. Schauble, and A. C. Riddle, Synoptic observations of Jupiter's radio emissions: Average statistical properties observed by Voyager, *J. Geophys. Res.*, **86**, 8529–8545, 1981.
- Alexander, J. K., M. D. Desch, M. L. Kaiser, and J. R. Thieman, Latitudinal beaming of Jupiter's low frequency radio emissions, *J. Geophys. Res.*, **84**, 5167–5174, 1979.
- Atreya, S. K., and T. M. Donahue, Ionospheric models of Saturn, Uranus, and Neptune, *Icarus*, **24**, 358, 1975.
- Bagenal, F., R. L. McNutt, Jr., J. W. Belcher, H. S. Bridge, and J. D. Sullivan, Revised ion temperatures for Voyager plasma measurements in the Io plasma torus, *J. Geophys. Res.*, **90**, 1755, 1985.
- Bagenal, F., and J. D. Sullivan, Direct plasma measurements in the Io torus and inner magnetosphere of Jupiter, *J. Geophys. Res.*, **86**, 8447–8466, 1981.
- Bagenal, F., J. D. Sullivan, and G. L. Siscoe, Spatial distribution of plasma in the Io torus, *Geophys. Res. Lett.*, **7**, 41–44, 1980.
- Barrow, C. H., Emission cones in Jupiter's hectometric radiation, *Astron. Astrophys.*, **250**, 245–252, 1991.
- Barrow, C. H., and M. D. Desch, Solar wind control of Jupiter's hectometric radio emission, *Astron. Astrophys.*, **213**, 495–501, 1989.
- Belcher, J. W., H. S. Bridge, F. Bagenal, B. Coppi, O. Divers, A. Eviatar, G. S. Gordon, Jr., A. J. Lazarus, R. L. McNutt, Jr., K. W. Ogilvie, J. D. Richardson, G. L. Siscoe, E. C. Sittler, Jr., J. T. Steinberg, J. D. Sullivan, A. Szabo, L. Villanueva, V. M. Vasyliunas, and M. Zhang, Plasma observations near Neptune: Initial results from Voyager 2, *Science*, **246**, 1478–1483, 1989.

- Berge, G. L., and S. Gulkis, Earth-based radio observations of Jupiter: Millimeter to meter wavelengths, in *Jupiter*, edited by T. Gehrels, pp. 830–847, University of Arizona Press, Tucson, Arizona, 1976.
- Bigg, E. K., Influence of the satellite Io on Jupiter's decametric radiation, *Nature*, *203*, 1008–1010, 1964.
- Bird, M. K., S. W. Asmar, J. P. Brenkle, P. Edenhofer, O. Funke, M. Pätzold, and H. Volland, Ulysses radio occultation observations of the Io plasma torus during the Jupiter encounter, *Science*, *257*, 1531–1535, 1992.
- Brown, L. W., Jupiter emission observed near 1 MHz, *Astrophys. J.*, *192*, 547–550, 1974*a*.
- Brown, L. W., Spectral behaviour of Jupiter near 1 MHz, *Astrophys. J.*, *194*, L159–L162, 1974*b*.
- Burke, B. F., and K. L. Franklin, Observations of a variable radio source associated with the planet Jupiter, *J. Geophys. Res.*, *60*, 213–217, 1955.
- Carr, T. D., Radio frequency emission from the planet Jupiter, *Astron. J.*, *64*, 39–41, 1959.
- Carr, T. D., Jupiter's decametric rotation period and the source A emission beam, *Phys. Earth Planet. Int.*, *6*, 21–28, 1972.
- Carr, T. D., and M. D. Desch, Recent decametric and hectometric observations of Jupiter, in *Jupiter*, edited by T. Gehrels, pp. 693–737, University of Arizona Press, Tucson, 1976.
- Carr, T. D., M. D. Desch, and J. K. Alexander, Phenomenology of magnetospheric radio emissions, in *Physics of the Jovian Magnetosphere*, edited by A. J. Dessler, Chapter 7, pp. 226–284, Cambridge University Press, New York, 1983.
- Carr, T. D., and S. Gulkis, The auroral kilometric radiation from Uranus and its magnetospheric implications, in *Planetary Radio Emission II*, edited by H. O. Rucker, S. J. Bauer, and B. M. Pedersen, pp. 223–235, Austrian Academy of Sciences Press, Vienna, 1987.
- Carr, T. D., J. J. Schauble, and C. C. Schauble, Pre-encounter distributions of Saturn's low frequency radio emission, *Nature*, *292*, 745–747, 1981.
- Carr, T. D., A. G. Smith, F. F. Donovan, and H. I. Register, The twelve-year periodicities of the decametric radiation of Jupiter, *Radio Science*, *5*, 495–503, 1970.
- Carr, T. D., and L. Wang, Auroral origin of jovian hectometric emission, in *Third Neil Brice Memorial Symposium on the Magnetospheres of the Outer Planets*, Katlenburg-Lindau, FRG, 1988.
- Carr, T. D., and L. Wang, The origin of Jupiter's hectometric radio emission, in *Res. Rep. 89*, Dept. of Astro., Univ. of Florida, Gainesville, Florida, 1989.



- Carr, T. D., and L. Wang, Monitoring Jupiter's hectometric emission, in *Low Frequency Astrophysics from Space*, edited by N. E. Kassim, and K. W. Weiler, pp. 113–117, Lecture Notes in Physics, 362, Springer-Verlag, Berlin, 1990.
- Connerney, J. E. P., The magnetic field of Jupiter: A general inverse approach, *J. Geophys. Res.*, *86*, 7679–7693, 1981.
- Connerney, J. E. P., Doing more with Jupiter's magnetic field, in *Planetary Radio Emission III*, edited by H. O. Rucker, S. J. Bauer, and M. L. Kaiser, pp. 13–33, Austrian Academy of Sciences Press, Vienna, 1992.
- Connerney, J. E. P., M. H. Acuña, and N. F. Ness, Modeling the Jovian current sheet and inner magnetosphere, *J. Geophys. Res.*, *86*, 8370–8384, 1981.
- Connerney, J. E. P., M. H. Acuña, and N. F. Ness, The magnetic field of Neptune, *J. Geophys. Res.*, *96*, 19023–19042, 1991.
- Davis, L., Jr., D. E. Jones, and E. J. Smith, The magnetic field of Jupiter, in *AGU Fall Meeting*, San Francisco, 1975.
- Desch, M. D., Evidence for solar wind control of Saturn radio emission, *J. Geophys. Res.*, *87*, 4549, 1982.
- Desch, M. D., and C. H. Barrow, Direct evidence for solar wind control of Jupiter's hectometer-wavelength radio emission, *J. Geophys. Res.*, *89*, 6819, 1984.
- Desch, M. D., and T. D. Carr, Dekametric and hectometric observations of Jupiter from the RAE-1 satellite, *Astrophys. J.*, *194*, L57–L59, 1974.
- Desch, M. D., and T. D. Carr, Modulation of the Jovian emission below 8 MHz, *Astrophys. J.*, *83*, 828–837, 1978.
- Desch, M. D., and H. O. Rucker, The relationship between Saturn kilometric radiation and the solar wind, *J. Geophys. Res.*, *88*, 8999, 1983.
- Divine, N., and H. B. Garrett, Charged particle distributions in Jupiter's magnetosphere, *J. Geophys. Res.*, *88*, 6889–6903, 1983.
- Douglas, J. N., and H. J. Smith, Presence and correlation of fine structure in Jovian decametric radiation, *Nature*, *192*, 741, 1961.
- Douglas, J. N., and H. J. Smith, Interplanetary scintillation in Jovian decametric radiation, *Astrophys. J.*, *148*, 885–903, 1967.
- Dulk, G. A., Apparent changes in the rotation rate of Jupiter, *Icarus*, *7*, 173–182, 1967.
- Dulk, G. A., A. Lecacheux, and Y. Leblanc, The complete polarization state of a storm of millisecond bursts from Jupiter, *Astron. Astrophys.*, *253*, 292–306, 1992.

- Farrell, W. M., M. D. Desch, and M. L. Kaiser, Field-independent source localization of Neptune's radio bursts, *J. Geophys. Res.*, **95**, 143–148, 1990.
- Farrell, W. M., M. D. Desch, and M. L. Kaiser, Evidence of auroral plasma cavities at Uranus and Neptune from radio burst observations, *J. Geophys. Res.*, **96**, 19049–19059, 1991.
- Franklin, K. L., and B. F. Burke, Radio observations of Jupiter, *Astron. J.*, **61**, 177, 1956.
- Gallagher, D. L., and N. D'Angelo, Correlations between solar wind parameters and auroral kilometric radiation intensity, *Geophys. Res. Lett.*, **8**, 1087, 1981.
- Genova, F., M. G. Aubier, and A. Lecacheux, Modulations in Jovian decametric spectra: Propagation effects in terrestrial ionosphere and Jovian environment, *Astron. Astrophys.*, **104**, 229–239, 1981.
- Genova, F., P. Zarka, and C. H. Barrow, Voyager and Nançay observations of the Jovian radio emission at different frequencies, *Astron. Astrophys.*, **182**, 159, 1987.
- Goldreich, P., and D. Lynden-Bell, Io, a Jovian unipolar inductor, *Astrophys. J.*, **156**, 59–78, 1969.
- Goldstein, M. L., A. Eviatar, and J. R. Thieman, A beaming model of the Io-independent Jovian decameter radiation based on multipole models of the Jovian magnetic field, *Astrophys. J.*, **229**, 1186–1197, 1979.
- Green, J. L., The Io decametric emission cone, *Radio Sci.*, **19**, 556–570, 1984.
- Green, J. L., and D. A. Gurnett, Ray tracing of Jovian kilometric radiation, *Geophys. Res. Lett.*, **7**, 65–68, 1980.
- Green, J. L., D. A. Gurnett, and S. D. Shawhan, The angular distribution of auroral kilometric radiation, *J. Geophys. Res.*, **82**, 1825, 1977.
- Green, J. L., J. R. Thieman, C. A. Higgins, Jr., L. Aist-Sagara, and S. F. Fung, Lane features in Jovian hectometric radio emissions, in *Planetary Radio Emissions III*, edited by H. O. Rucker, S. J. Bauer, and M. L. Kaiser, pp. 91–103, Austrian Academy of Sciences Press, Vienna, 1992.
- Gulkis, S., and T. D. Carr, The main source of radio emission from the magnetosphere of Uranus, *J. Geophys. Res.*, **92**, 15159–15168, 1987.
- Gurnett, D. A., The Earth as a radio source: Terrestrial kilometric radiation, *J. Geophys. Res.*, **79**, 4227, 1974.
- Gurnett, D. A., W. S. Kurth, I. H. Cairns, and L. J. Granroth, Whistlers in Neptune's magnetosphere: Evidence of atmospheric lightning, *J. Geophys. Res.*, **95**, 20967–20976, 1990.

- Gurnett, D. A., W. S. Kurth, R. L. Poynter, L. J. Granroth, I. H. Cairns, W. M. Macek, S. L. Moses, F. V. Coroniti, C. F. Kennel, and D. D. Barbosa, First plasma wave observations at Neptune, *Science*, *246*, 1494, 1989.
- Hamming, R. W., Stable predictor corrector methods for ordinary differential equations, *J. Assoc. Comp. Mach.*, *6*, 37–47, 1959.
- Haselgrove, J., Ray theory and a new method for ray tracing, in *The Physics of the Ionosphere*, pp. 355–364, Physical Society, London, 1954.
- Hashimoto, K., A reconciliation of propagation modes of auroral kilometric radiation, *J. Geophys. Res.*, *89*, 7459–7466, 1984.
- Hashimoto, K., and M. L. Goldstein, A theory of the Io phase asymmetry of the Jovian decametric radiation, *J. Geophys. Res.*, *88*, 2010–2020, 1983.
- Higgins, C. A., Jr., J. L. Green, J. R. Thieman, S. F. Fung, R. M. Candey, and L. Aist-Sagara, Structure within Jovian hectometric radiation, in *AGU Fall Meeting*, San Francisco, 1993.
- Hill, T. W., A. J. Dessler, and C. K. Goertz, Magnetospheric models, in *Physics of the Jovian Magnetosphere*, edited by A. J. Dessler, Chapter 10, pp. 353–394, Cambridge University Press, New York, 1983.
- Imai, K., L. Wang, and T. D. Carr, Origin of Jupiter's decametric modulation lanes, in *Planetary Radio Emissions III*, edited by H. O. Rucker, S. J. Bauer, and M. L. Kaiser, pp. 69–90, Austrian Academy of Sciences Press, Vienna, 1992.
- Jones, D., Latitudinal beaming of planetary radio emissions, *Nature*, *288*, 225–229, 1980.
- Jones, D., Radio wave emission from the Io torus, *Adv. Space Res.*, *1*, 333, 1981.
- Jones, D., and R. J. L. Grard, Propagation characteristics of electromagnetic waves in the magnetosphere, in *The Scientific Satellite Programme During the International Magnetospheric Study*, edited by K. Knott, and B. Battrock, p. 293. D. Reidel Publishing Company, 1976.
- Jones, R. M., and J. J. Stephenson, A versatile three-dimensional ray tracing computer program for radio waves in the ionosphere, in *OT-Report 75-76*, Dept. of Comm., 1976.
- Kaiser, M. L., and M. D. Desch, Saturnian kilometric radiation: Source locations, *J. Geophys. Res.*, *87*, 4555, 1982.
- Kaiser, M. L., M. D. Desch, A. C. Riddle, A. Lecacheux, J. B. Pearce, J. K. Alexander, J. W. Warwick, and J. R. Thieman, Voyager spacecraft radio observations of Jupiter: Initial cruise results, *Geophys. Res. Lett.*, *6*, 507, 1979.
- Kurth, W. S., D. D. Barbosa, D. A. Gurnett, R. L. Poynter, and I. H. Cairns, Low-frequency radio emissions at Neptune, *Geophys. Res. Lett.*, *17*, 1649, 1990.

- Ladreiter, H. P., *The Jovian Hectometric Radiation*. PhD thesis, Univ. of Graz, Graz, Austria, 1990.
- Ladreiter, H. P., The cyclotron maser instability: Application to low-density magnetoplasmas, *Astrophys. J.*, **370**, 419–426, 1991.
- Ladreiter, H. P., and Y. Leblanc, Jovian hectometric radiation: Beaming, polarization, source extension, and solar wind control, *Astron. Astrophys.*, **226**, 297, 1989.
- Ladreiter, H. P., and Y. Leblanc, Modeling of the Jovian hectometric radiation: A three-dimensional study, *Annales Geophysicae*, **8**, 477–488, 1990a.
- Ladreiter, H. P., and Y. Leblanc, Source location of the Jovian hectometric radiation via ray tracing technique, *J. Geophys. Res.*, **95**, 6423–6435, 1990b.
- Ladreiter, H. P., Y. Leblanc, G. K. F. Rabl, and H. O. Rucker, Emission characteristics and source location of the smoothed Neptunian kilometric radiation, *J. Geophys. Res.*, **96**, 19101–19110, 1991.
- Lang, G. J., and R. G. Peltzer, Planetary radio astronomy receiver, *IEEE Trans.*, **AES13**, 466, 1977.
- Le Quéau, D., R. Pellat, and A. Roux, Direct generation of the auroral kilometric radiation by the maser synchrotron instability: An analytical approach, *Phys. Fluids*, **27**, 247–265, 1984a.
- Le Quéau, D., R. Pellat, and A. Roux, Direct generation of the auroral kilometric radiation by the maser synchrotron instability: Physical mechanism and parametric study, *J. Geophys. Res.*, **89**, 2831–2841, 1984b.
- Leblanc, Y., M. G. Aubier, A. Ortega-Molina, and A. Lecacheux, Overview of the Uranian radio emissions: Polarization and constraints on source locations, *J. Geophys. Res.*, **92**, 15125–15138, 1987.
- Leblanc, Y., and G. Daigne, The broadband Jovian kilometric radiation. Statistical properties and source model, in *Planetary Radio Emissions*, edited by H. O. Rucker, and S. J. Bauer, pp. 112–147, Austrian Academy of Sciences Press, Vienna, 1984.
- Lecacheux, A., G. A. Dulk, and M. Y. Boudjada, The elliptical polarization of the Jovian decametric emission and the magnetosphere of Jupiter, in *Planetary Radio Emissions III*, edited by H. O. Rucker, S. J. Bauer, and M. L. Kaiser, pp. 147–154, Austrian Academy of Sciences Press, Vienna, 1992a.
- Lecacheux, A., and F. Genova, Source localization of Saturn kilometric radio emission, *J. Geophys. Res.*, **88**, 8993–8998, 1983.
- Lecacheux, A., N. Meyer-Vernet, and G. Daigne, Jupiter's decametric radio emission: A nice problem of optics, *Astron. Astrophys.*, **94**, L9–L12, 1981.

- Lecacheux, A., and B. Møller-Pedersen, Some spectral characteristics of the hectometric Jovian emission, *J. Geophys. Res.*, *85*, 6877–6882, 1980.
- Lecacheux, A., and A. Ortega-Molina, Polarization and localization of the Uranian radio sources, *J. Geophys. Res.*, *92*, 15148–15158, 1987.
- Lecacheux, A., B. M. Pedersen, P. Zarka, M. G. Aubier, M. D. Desch, W. M. Farrell, M. L. Kaiser, R. J. MacDowall, and R. G. Stone, In ecliptic observations in Jovian radio emissions by Ulysses comparison with Voyager results, *Geophys. Res. Lett.*, *19*, 1307–1310, 1992b.
- Lee, L. C., and C.-S. Wu, Amplification of radiation near cyclotron frequency due to electron population inversion, *Phys. Fluids*, *23*, 1348–1354, 1980.
- Luoarn, P., A. Roux, H. de Feraudy, D. Le Quéau, M. Andre, and L. Matson, Trapped electrons as a free energy source for the AKR, *J. Geophys. Res.*, *95*, 5983, 1989.
- Lyons, L. R., and D. J. Williams, *Quantitative Aspects of Magnetospheric Physics*, D. Reidel, Dordrecht, 1984.
- Mayer, C. H., T. P. McCullough, and R. M. Sloanaker, Observations of Mars and Jupiter at a wavelength of 3.15 cm, *Astrophys. J.*, *127*, 11–16, 1958.
- McClain, E. F., A test for nonthermal radiation from Jupiter at a wavelength of 21 cm, *Astron. J.*, *64*, 339–340, 1959.
- McElroy, M. B., The ionospheres of the major planets, *Space Sci. Rev.*, *14*, 460, 1973.
- Menietti, J. D., J. L. Green, S. Gulkis, and N. F. Six, Three-dimensional ray tracing of the Jovian magnetosphere in the low-frequency range, *J. Geophys. Res.*, *89*, 1489–1495, 1984.
- Menietti, J. D., D. Tsintikidis, and D. A. Gurnett, Modeling of whistler ray paths in the magnetosphere of Neptune, *J. Geophys. Res.*, *96*, 19117–19122, 1991.
- Ness, N. F., M. H. Acuña, L. F. Burlaga, J. E. P. Connerney, R. P. Lepping, and F. M. Neubauer, Magnetic fields at Neptune, *Science*, *246*, 1473–1478, 1989.
- Omidi, N., C.-S. Wu, and D. A. Gurnett, Generation of auroral kilometric and Z mode radiation by the cyclotron maser mechanism, *J. Geophys. Res.*, *89*, 883, 1984.
- Ortega-Molina, A., and G. Daigne, Polarization response of two crossed monopoles on a spacecraft, *Astron. Astrophys.*, *130*, 301–310, 1984.
- Ortega-Molina, A., and A. Lecacheux, Polarization response of the Voyager-PRA experiment at low frequencies, *Astron. Astrophys.*, *229*, 558–568, 1990.
- Ortega-Molina, A., and A. Lecacheux, Polarization of Jovian hectometric emission, *J. Geophys. Res.*, *96*, 11441–11453, 1991.

- Paranicas, C., and A. F. Cheng, Drift shells in the octupole field model ( $O_8$ ) at Neptune, *Geophys. Res. Lett.*, submitted, 1994.
- Pedersen, B. M., A. Lecacheux, P. Zarka, M. G. Aubier, M. L. Kaiser, and M. D. Desch, Phenomenology of Neptune's radio emissions observed by the Voyager planetary radio astronomy experiment, *J. Geophys. Res.*, *97*, 19201, 1992.
- Pedersen, B. M., N. Meyer-Vernet, M. G. Aubier, and P. Zarka, Dust distribution around Neptune: Grain impacts near the ring plane measured by the Voyager planetary radio astronomy experiment, *J. Geophys. Res.*, *96*, 19187–19196, 1991.
- Pilcher, C. B., J. S. Morgan, J. H. Fertel, and C. C. Avis, A movie of the Io plasma torus, *Bull. Amer. Astro. Soc.*, *13*, 731, 1981.
- Rabl, G. K. F., C. H. Barrow, and H. O. Rucker, Solar wind dependence of the Jovian hectometric radio emission: Comparison between Voyager 1 and 2 observations, *Astron. Astrophys.*, *232*, 242, 1990.
- Ralston, A., Numerical integration methods for the solution of ordinary differential equations, in *Mathematical Methods for Digital Computers, Volume 1*, edited by A. Ralston, and H. S. Wiff, Chapter 8, pp. 95–109, John Wiley & Sons, Inc., New York, 1960.
- Reiner, M. J., J. Fainberg, and R. G. Stone, Source characteristics and locations of hectometric radio emissions from the northern Jovian hemisphere, *Geophys. Res. Lett.*, *20*, 321–324, 1993a.
- Reiner, M. J., J. Fainberg, and R. G. Stone, Source characteristics of Jovian hectometric emissions, *J. Geophys. Res.*, *98*, 18767–18777, 1993b.
- Riihimaa, J. J., Structured events in the dynamic spectra of Jupiter's decametric radio emission, *Astron. J.*, *73*, 265–270, 1968.
- Riihimaa, J. J., Modulation lanes in the dynamic spectra of Jovian L bursts, *Astron. Astrophys.*, *4*, 180–188, 1970.
- Roux, A., and R. Pellat, Coherent generation of the auroral kilometric radiation by nonlinear beatings between electrostatic waves, *J. Geophys. Res.*, *84*, 5189–5198, 1979.
- Sawyer, C. B., K. L. Neal, and J. W. Warwick, Polarization model applied to Uranian radio emission, *J. Geophys. Res.*, *96*, 5575–5590, 1991.
- Sawyer, C. B., J. W. Warwick, and J. H. Romig, The effect of magnetic topography on high-latitude radio emission at Neptune, *J. Geophys. Res.*, *97*, 1–9, 1992.
- Sawyer, C. B., J. W. Warwick, and J. H. Roming, Smooth radio emission and a new emission at Neptune, *Geophys. Res. Lett.*, *17*, 1645–1648, 1990.
- Sayre, E., Characteristics of the Planetary Radio Astronomy antenna, in *Res. Rep.*, Contract NAS5-24008, MOD-21, Avco Corporation, 1976.

- Shinagawa, H., and J. H. Waite, Jr., The ionosphere of Neptune, *Geophys. Res. Lett.*, *16*, 945–948, 1989.
- Smith, E. J., L. Davis, Jr., and D. E. Jones, Jupiter's magnetic field and magnetosphere, in *Jupiter*, edited by T. Gehrels, pp. 788–829, Univ. of Arizona, Tucson, Arizona, 1976.
- Stix, T. H., *The Theory of Plasma Waves*, McGraw-Hill, New York, 1962.
- Stone, R. G., B. M. Pedersen, C. C. harvey, P. Canu, N. Cornilleau-Wehrlin, M. D. Desch, C. de Villedary, J. Fainberg, W. M. Farrell, K. Goetz, R. A. Hess, S. Hoang, M. L. Kaiser, P. J. Kellogg, A. Lecacheux, N. Lin, R. J. MacDowall, R. Manning, C. A. Meetre, N. Meyer-Vernet, M. Moncuquet, V. Osherovich, M. J. Reiner, A. Tekle, J. Thiessen, and P. Zarka, Ulysses radio and plasma wave observations in the Jupiter environment, *Science*, *257*, 1524–1531, 1992.
- Thieman, J. R., and A. G. Smith, Detailed geometrical modeling of Jupiter's Io-related decametric radiation, *J. Geophys. Res.*, *84*, 2666–2674, 1979.
- Trafton, L., The Jovian SII torus: Its longitudinal asymmetry, *Icarus*, *42*, 111, 1980.
- Tyler, G. L., *et al.*, Voyager radio science observations of Neptune and Triton, *Science*, *246*, 1466, 1989.
- Wang, L., and T. D. Carr, Monitoring and modeling of Jupiter's hectometric radiation, in *The Fred Scarf memorial symposium: Magnetospheres of the Outer Planets*, Annapolis, Maryland, 1990.
- Wang, L., T. D. Carr, and F. Reyes, Voyager radio investigations of Neptune and Uranus, in *Res. Rep. 91*, Dept. of Astro., Univ. of Florida, Gainesville, Florida, 1991.
- Warwick, J. W., J. K. Alexander, M. D. Desch, T. D. Carr, S. Gulkis, A. Boischot, C. C. Harvey, and B. M. Pedersen, Voyager 1 planetary radio astronomy observations near Jupiter, *Science*, *204*, 995–998, 1979a.
- Warwick, J. W., J. K. Alexander, M. D. Desch, T. D. Carr, S. Gulkis, A. Boischot, Y. Leblanc, B. M. Pedersen, and D. H. Staelin, Planetary radio astronomy observations from Voyager 2 near Jupiter, *Science*, *206*, 991–995, 1979b.
- Warwick, J. W., D. R. Evans, G. R. Peltzer, R. G. Peltzer, J. H. Romig, C. B. Sawyer, A. C. Riddle, A. E. Schweitzer, M. D. Desch, M. L. Kaiser, W. M. Farrell, T. D. Carr, I. de Pater, D. H. Staelin, S. Gulkis, R. L. Poynter, A. Boischot, F. Genova, Y. Leblanc, A. Lecacheux, B. M. Pedersen, and P. Zarka, Voyager planetary radio astronomy at Neptune, *Science*, *246*, 1498–1501, 1989.
- Warwick, J. W., J. B. Pearce, R. G. Peltzer, and A. C. Riddle, Planetary radio astronomy experiment for Voyager missions, *Space Sci. Rev.*, *21*, 309–327, 1977.

- Wong, H. K., C.-S. Wu, F. J. Ke, R. S. Schneider, and L. F. Ziebell, Electromagnetic cyclotron loss-cone instability associated with weakly relativistic electrons, *J. Plasma Phys.*, *28*, 503, 1982.
- Wu, C.-S., and L. C. Lee, A theory of the terrestrial kilometric radiation, *Astrophys. J.*, *230*, 621–626, 1979.
- Wu, C.-S., H. K. Wong, D. J. Gorney, and L. C. Lee, Generation of the auroral kilometric radiation, *J. Geophys. Res.*, *87*, 4476–4488, 1982.
- Zarka, P., Remote sensing of auroral plasmas, in *Planetary Radio Emissions III*, edited by H. O. Rucker, S. J. Bauer, and M. L. Kaiser, pp. 351–369, Austrian Academy of Sciences Press, Vienna, 1992.



## BIOGRAPHICAL SKETCH

Liyun Wang was born on January 25, 1960 in Kunming, the capital city of Yunnan Province, People's Republic of China. He happily married his sweetheart Bin Zong in 1984; they now have a lovely four-year old daughter, Christine.

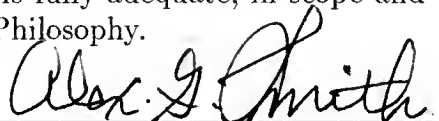
Upon graduation from the First High School of Kunming in 1976, Liyun worked at the Bureau of Telecommunication of Kunming City. He later attended the Yunnan University where, in January 1982, he received a Bachelor of Science in physics and a minor in applied optics. After graduating from the Yunnan University, he accepted employment as a course lecturer at the same university where he taught courses in general physics for two and half years. He began his graduate studies at the Yunnan Observatory, Chinese Academy of Sciences, in August 1984, where he participated in a research project on stellar evolution. In August 1985 he transferred to the Department of Astronomy at the University of Florida, and began to pursue research in radio astronomy. He was involved in processing and analyzing data of the Voyager Planetary Radio Astronomy (PRA) experiment from Jupiter, Uranus, and Neptune. He was also responsible for developing and maintaining software packages for the Voyager PRA project. Meanwhile, he focused on development of theoretical models to account for radio emissions from the outer planets. He received his degree of Master of Science in April 1988. The degree of Doctor of Philosophy was awarded to him in August 1994 by the University of Florida.

I certify that I have read this study and that in my opinion it conforms to acceptable standards of scholarly presentation and is fully adequate, in scope and quality, as a dissertation for the degree of Doctor of Philosophy.



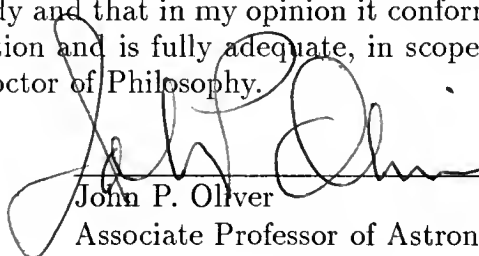
Thomas D. Carr, Chairman  
Professor of Astronomy and Physics

I certify that I have read this study and that in my opinion it conforms to acceptable standards of scholarly presentation and is fully adequate, in scope and quality, as a dissertation for the degree of Doctor of Philosophy.



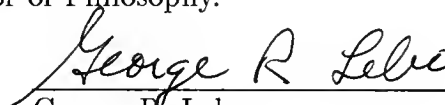
Alex G. Smith  
Distinguished Service Professor  
of Astronomy and Physics

I certify that I have read this study and that in my opinion it conforms to acceptable standards of scholarly presentation and is fully adequate, in scope and quality, as a dissertation for the degree of Doctor of Philosophy.



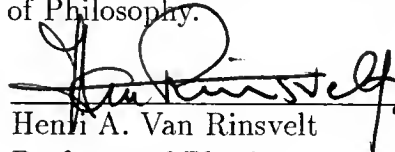
John P. Oliver  
Associate Professor of Astronomy

I certify that I have read this study and that in my opinion it conforms to acceptable standards of scholarly presentation and is fully adequate, in scope and quality, as a dissertation for the degree of Doctor of Philosophy.



George R. Lebo  
Associate Professor of Astronomy

I certify that I have read this study and that in my opinion it conforms to acceptable standards of scholarly presentation and is fully adequate, in scope and quality, as a dissertation for the degree of Doctor of Philosophy.



Henri A. Van Rinsvelt  
Professor of Physics

This dissertation was submitted to the Graduate Faculty of the Department of Astronomy in the College of Liberal Arts and Sciences and to the Graduate School and was accepted as partial fulfillment of the requirements for the degree of Doctor of Philosophy.

August 1994

---

Dean, Graduate School

LD  
1780  
1994  
.W2461

